Universität Stuttgart

Institut für Wasser- und Umweltsystemmodellierung

Mitteilungen

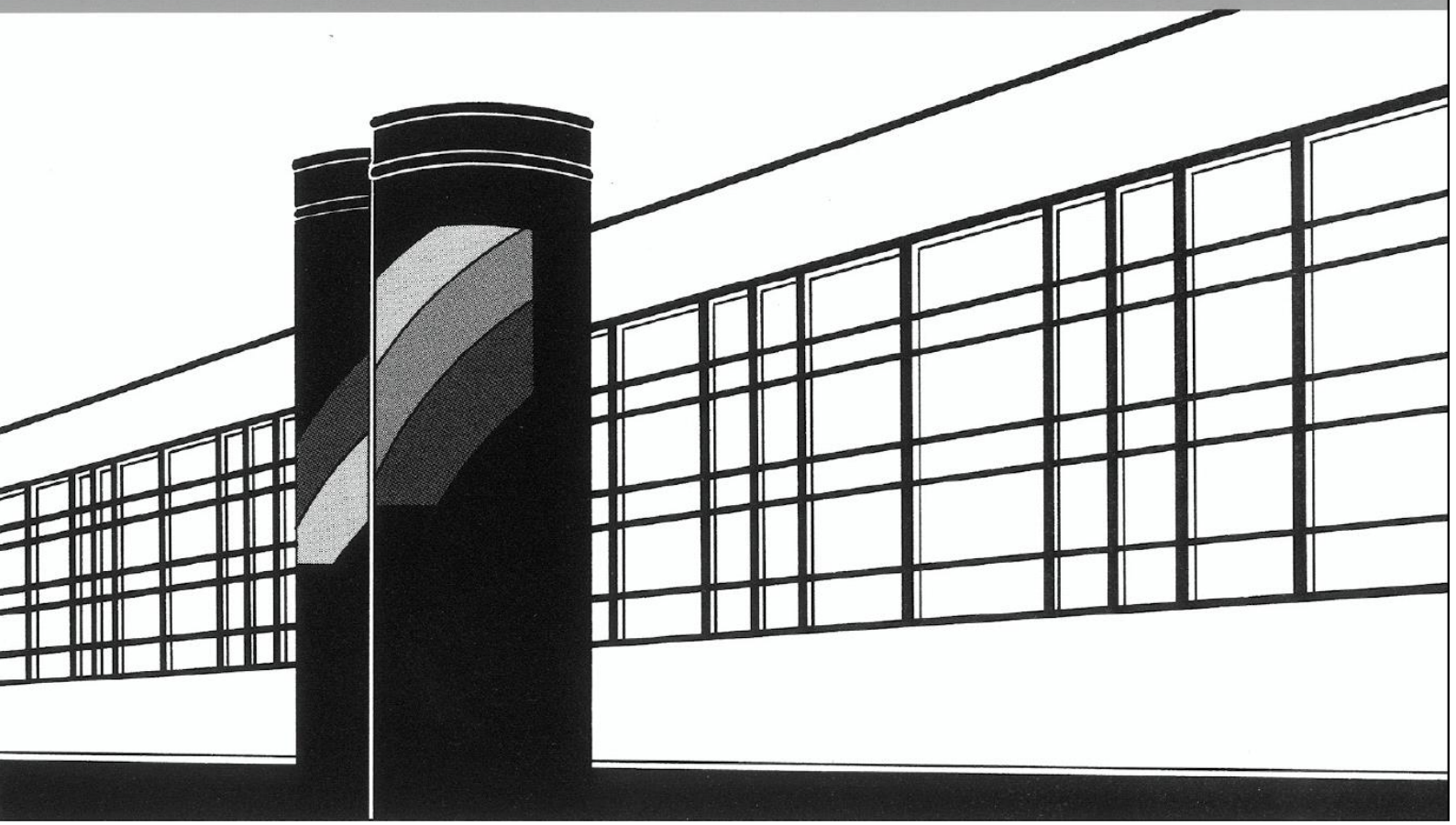

Heft 302 Jan Görtz

Coupled modeling approach for physico-chemical processes during the deterioration of cement-based structures

Coupled modeling approach for physico-chemical processes during the deterioration of cement-based structures

von der Fakultät Bau- und Umweltingenieurwissenschaften der Universität Stuttgart zur Erlangung der Würde eines Doktor-Ingenieurs (Dr.-Ing.) genehmigte Abhandlung

vorgelegt von
Jan Görtz
aus Aachen

Hauptberichter:	Prof. Dr.-Ing. Silke Wieprecht
Mitberichter:	Prof. Dr.-Ing. Harald Garrecht

Tag der mündlichen Prüfung: 28. November 2022

Institut für Wasser- und Umweltsystemmodellierung
der Universität Stuttgart
2023

Heft 302

Coupled modeling approach for physico-chemical processes during the deterioration of cement-based structures

von
Dr.-Ing.
Jan Görtz

Eigenverlag des Instituts für Wasser- und Umweltsystemmodellierung
der Universität Stuttgart

D93 Coupled modeling approach for physico-chemical processes during the deterioration of cement-based structures

Bibliografische Information der Deutschen Nationalbibliothek
Die Deutsche Nationalbibliothek verzeichnet diese Publikation in der Deutschen Nationalbibliografie; detaillierte bibliografische Daten sind im Internet über http://www.d-nb.de abrufbar

Görtz, Jan:
Coupled modeling approach for physico-chemical processes during the deterioration of cement-based structures, Universität Stuttgart. - Stuttgart: Institut für Wasser- und Umweltsystemmodellierung, 2023

(Mitteilungen Institut für Wasser- und Umweltsystemmodellierung, Universität Stuttgart: H. 302)
Zugl.: Stuttgart, Univ., Diss., 2023
ISBN 978-3-910293-06-9
NE: Institut für Wasser- und Umweltsystemmodellierung <Stuttgart>: Mitteilungen

Herausgegeben 2023 vom Eigenverlag des Instituts für Wasser- und Umweltsystem-modellierung

Druck: P+K Solutions GmbH & Co. KG, Stuttgart

Acknowledgements

I would like to take this opportunity to thank all my supervisors, colleagues, friends and collaborators who have supported me throughout the whole process of creating this work. First and foremost I am grateful to my supervisor, Prof. Silke Wieprecht who gave me the opportunity and supported my work from start to finish. Very special thanks belong to Dr. Kristina Terheiden who supported me during the whole time with scientific discussions and suggestions and ensured a motivational and positive working atmosphere. I would also like to thank Prof. Harald Garrecht for being the co-reporter and helping me through the progress of this thesis.

As the work on this thesis was mainly conducted and written during my time at the Institute for Modelling Hydraulic and Environmental Systems, major thanks also belong to everybody working. You all made sure that my time there was not only fruitful but also joyful and inspiring. This particularly includes Daniel Stolz with our countless discussions, our sometimes crazy ideas outside the beaten track and our funny encounters during our trips. Similarly, all members of the working group, the staff at the institute workshop, the IT team, the student assistants and all colleagues who joined me for our scientific meet-ups also contributed largely to the overall great work experience. The list of names is too long to be fully listed here but you know how grateful I am for meeting all of you.

Last but not least thanks are due to my girlfriend and my family that always supported, encouraged and helped me during this whole time. Thank you for standing with me!

> 'Exactly!' said Deep Thought. 'So once you do know what the question actually is, you'll know what the answer means.'
>
> -Douglas Adams, The Hitchhiker's Guide to the Galaxy

Contents

List of Figures

List of Tables

Acronyms

Notation	Description
AAR	Alkali-aggregate reaction
ACR	Alkali-carbonate reaction
AFm	Monosulfate
AFt	Ettringite
ASR	Alkali-silica reaction
CBM	Cement-based material
CBS	Cement-based structures
CH	Portlandite
CSH	Calcium silicate hydrate
DEF	Delayed ettringite formation
FVM	Finite volume method
GGBS	Ground granulated blast-furnace slag
ITZ	Interfacial Transition Zone
LMA	Law of mass action
MBE	Mass balance equation
MRC	Moisture retention curves
MVG	Mualem Van Genuchten model
PSD	Pore size distribution
RCC	Roller compacted concrete

Notation	Description
REV	Representative elementary volume
SCM	Supplementary cementitious material
STaC	Stress-Transport-and-Chemistry - developed numerical framework

List of symbols

Sign	Description	Unit
A	Area	m^2
a	Activity of species s	$-$
$A_{f,e}$	Intersecting fracture area in element	m^2
A_γ	First coefficient for extended Davies' relation	$-$
A_r	Activity of species s	m^2
A_s	Surface area	m^2
b	Biot coefficient	$-$
$\mathbf{b_f}$	Body force vector	Pa/m
B_γ	Second coefficient for extended Davies' relation	$-$
b_i	Species parameter in the extended Davies' relation	m
M	Biot modulus	m
$\boldsymbol{C}$	Fourth-order stiffness tensor	Pa
c	Molar concentration of species in the liquid phase	mol/m^3
C_l	Volumetric heat capacity of the liquid phase	$J/(m^3K^1)$
C_m	Specific moisture capacity	m^{-1}
C_s	Total volumetric heat capacity of the solid phases	$J/(m^3K^1)$
c_s	Molar concentration of species	mol/m^3
C_v	Volumetric heat capacity of the vapor phase	$J/(m^3K^1)$
φ_r	Relative humidity	$-$
D_s	Diffusion coefficient for certain species s	m^2/s
Dq	Damköhler number	$-$
D_e	Effective diffusion coefficient	m^2/s
D_v	Differential pore size distribution	m^2
e_0	Electric charge of one electron	C
E	Young's modulus	Pa
E_f	Enthalpy of fusion	J/m^3
F	Farraday constant = 9.64e+4	C/mol
f_c	Uniaxial compressive strength	Pa

Sign	Description	Unit
f_t	Uniaxial tensile strength	Pa
f_y	Yield function	Pa
G	Shear modulus	Pa
g	Gravitational acceleration	m/s^2
G_F	Fracture energy	N/m
$\boldsymbol{g}_n$	Unit vector in upwards gravity direction	–
h_c	Capillary pressure head	mH_20
h_l	Liquid pressure head	mH_2O
h_{mois}	Moisture transfer coefficient	m/s
$\boldsymbol{I}_3$	Third-order identity tensor	–
I	Ionic strength	mol/m^3
J	Compliance function	Pa^{-1}
K	Bulk modulus	Pa
$\boldsymbol{K}$	Hydraulic permeability	m
$\boldsymbol{k}$	Hydraulic conductivity	m/s
k_b	Stefan Boltzman Constant = 1.380649e-23	J/K
K_c	Chemical equilibrium constant	–
k_r	Reaction rate coefficient of nth order	$(l/mol)^{n-1}/s^1$
$k_{r,e}$	Effective reaction rate coefficient	s^{-1}
K_S	Bulk modulus of the solid grains	Pa
K_s	Chemical solubility constant	–
$\boldsymbol{k_s}$	Hydraulic conductivity of saturated material	m/s
K_T	Bulk modulus of the solid skeleton	Pa
κ	Compressibilitiy	Pa^{-1}
l	Internal length parameter of fracture element	m
l_e	Length of an element in fracture direction	m
L_v	Volumetric latent heat capacity of the vapor phase	J/m^3
$\mathbf{M_{ev}}$	Eigenvector matrix	–
$\boldsymbol{n_{bc}}$	Boundary normal vector	–
n	Eulerian porosity	–
n_{vg}	Second coefficient for Van Genuchten sorptions isotherm	–
n_{vg}	Second Genuchten coefficient	–
p_{atm}	Atmospheric pressure	Pa
p_c	Capillary pressure in matrix	Pa

Sign	Description	Unit
p_{cryst}	Crystallisation pressure	Pa
p_g	Gas phase pressure in matrix	Pa
p_{ice}	Ice phase pressure	Pa
p_l	Liquid pressure in matrix	Pa
p	Pressure	Pa
r_p	Pore radius	m
P_S	Solid pressure	Pa
p_v	Vapor pressure	Pa
$p_{v,sat}$	Saturated vapor pressure	Pa
$\boldsymbol{q}_a$	Advective heat flux density	$\mathrm{W/m^2}$
$\boldsymbol{q}_c$	Conductive heat flux density	$\mathrm{W/m^2}$
q_{cnv}	Convective heat flux density	$\mathrm{W/m^2}$
q_l	Source/ sink or liquid water	$-$
$\boldsymbol{q}_r$	Heat flux density caused by radiation	$\mathrm{W/m^2}$
$q_{r,l}$	Heat flux density caused by longwave radiation	$\mathrm{W/m^2}$
$q_{r,s}$	Heat flux density caused by shortwave radiation	$\mathrm{W/m^2}$
q_s	Source/ sink of species	$\mathrm{mol/(m^3 s^1)}$
q_v	Source/ sink or vapor	$-$
R_s	Specific gas constant	J/(kgK)
R_u	Universal gas constant	J/(molK)
s_p	Solid phase concentration	$\mathrm{mol/m^3}$
S_s	Specific surface area	$\mathrm{m^2/m^3}$
$s_{storage}$	Storativity	$\mathrm{m^{-1}}$
S_{total}	Total amount of heat stored	$\mathrm{J/m^3}$
T	Temperatur	K
t	Time	s
T_m	Melting temperature	K
$T_{m,p}$	Melting temperature in pores	K
t_r	Characteristic reaction time	s
t_t	Characteristic transport time	s
$\boldsymbol{u}$	Displacement vector	m
V	Volume	$\mathrm{m^3}$
$\boldsymbol{v}_{a,s}$	Advective solute flux density	$\mathrm{mol/(m^2 s)}$
$\boldsymbol{v}_{a,v}$	Advective vapor flux density	m/s

Sign	Description	Unit
V_{b0}	Initial bulk volume	m^3
V_b	Bulk volume	m^3
$\boldsymbol{v}_{d,v}$	Diffusive flux density	m/s
$\boldsymbol{v}_g$	Gas phase flux density	m/s
V_{dsp}	Volume density of strength defying solid phases	m^3/m^3
V_e	Volume of element	m^3
$\boldsymbol{v}_f$	Fluid velocity / fluid flux density	m/s
V_l	Liquid water volume	m^3
$\boldsymbol{v}_l$	Darcy velocity / liquid flux density	m/s
V_m	Molar volume	m^3/mol
$\boldsymbol{v}_s$	Flux density of species	mol/(m^2s)
$\boldsymbol{v}_{d,s}$	Diffusive flux density of species	mol/(m^2s)
$\boldsymbol{v}_{m,s}$	Migration flux density for species s	mol/(m^2s)
v_r	Reaction rate	mol/s
V_v	Vapor volume	m^3
V_v	Void volume	m^3
$\boldsymbol{v}_v$	Vapor flux density	m/s
V_w	Total water volume	m^3
w	Fracture aperture	m
$\boldsymbol{x_{bc}}$	Location of the boundary condition	–
z_s	Electric charge of species	–
α	Thermal expansion coefficient	K^{-1}
α_{al}	Albedo coefficient	–
α_c	Contact angle	rad
α_{vg}	First coefficient for Van Genuchten sorptions isotherm	m^{-1}
$\delta_{c,a}$	Absolute convergence value	–
$\delta_{c,r}$	Relative convergence value	–
δ	Degree of leaching	–
$\boldsymbol{\epsilon}$	Strain	mm^{-1}
$\boldsymbol{\epsilon}_c$	Creep strain	m/m
$\boldsymbol{\epsilon}_{el}$	Elastic strain	m/m
ϵ	Directional engineering strain	m/m
$\boldsymbol{\epsilon}_{inel}$	Inelastic strain	m/m

Sign	Description	Unit
Ψ	Electrical potential	V
ϵ_m	Permittivity of the material	F/m
ϵ_{p1}	First principal plastic strain	m/m
$\boldsymbol{\epsilon}_p$	Plastic strain	m/m
ϵ_{sf}	Surface emissivity	–
$\boldsymbol{\epsilon}_{sw}$	Swelling strain vector	m/m
$\boldsymbol{\epsilon}_t$	Total strain	m/m
$\boldsymbol{\epsilon}_{th}$	Thermal strain	m/m
$\boldsymbol{\epsilon}_{th}$	Thermal strain vector	m/m
γ	Specific weight	$\mathrm{N/m^3}$
Γ_l	Liquid moisture exchange coefficient	$\mathrm{s^{-1}}$
Γ_s	Solute species exchange coefficient	mol/s
κ_p	Internal damage parameter	–
λ	Thermal conductivity	W/(mK)
λ_p	Plastic multiplier	–
λ_L	1st Lame parameter	Pa
μ_L	2nd Lame parameter	Pa
$\mu^0_{c,s}$	Standard chemical potential of a species	J/mol
$\mu_{c,s}$	Chemical potential of a species	J/mol
μ_d	Dynamic viscosity	$\mathrm{m^2/s}$
ν	Poisson ratio	–
ν_k	Kinematic viscosity	$\mathrm{Ns/m^2}$
ϕ	Lagrangian porosity	–
ω_l	Moisture transfer coefficient	$\mathrm{m^{-2}}$
ω_s	Solute transfer coefficient	$\mathrm{m^{-2}}$
ρ_c	Charge density	$\mathrm{C/m^3}$
ρ_{ice}	Density of ice	$\mathrm{kg/m^3}$
ρ_l	Density of liquid	$\mathrm{kg/m^3}$
ρ_{mol}	Molar density of a species	$\mathrm{mol/m^3}$
ρ_t	Density of the composite material	$\mathrm{kg/m^3}$
ρ_v	Density of vapor	$\mathrm{kg/m^3}$
$\boldsymbol{\sigma}$	Total stress tensor	Pa
$\sigma_{s,c-l}$	Surface tension between crystal and liquid	N/m
$\boldsymbol{\sigma'}$	Effective stress tensor	Pa

Sign	Description	Unit
σ	Total directional stress	Pa
$\sigma_{s,i-l}$	Surface tension between ice crystal and liquid	N/m
σ'_{p1}	First principle effective plastic stress	Pa
$\boldsymbol{\sigma}'_{\mathbf{p}}$	Effective plastic stress	Pa
$\sigma_{s,s-l}$	Surface tension between solid and liquid	N/m
θ	Volumetric water content	m^3/m^3
τ	Tortuosity of the pore space	m/m
θ_l	Volumetric liquid water content	m^3/m^3
$\Theta_{l,f}$	Dimensionless liquid saturation in fracture	–
Θ_l	Dimensionless liquid saturation in matrix	–
$\theta_{l,r}$	Residual volumetric liquid water content	m^3/m^3
$\theta_{l,sat}$	Saturated volumetric liquid water content	m^3/m^3
θ_v	Volumetric vapor content	m^3/m^3
χ_B	Bishop parameter	–
$\chi_{l,s}$	Fraction of skeleton area in contact with liquid	–
γ_s	Activity coefficient of species s	–
ζ_f	Fracture roughness coefficient	–
ζ_s	Fracture surface coefficient	–

Abstract

The maintenance of cement-based structures plays a decisive role in structures' long-term safety and service life. The costs for maintenance as well as any restrictions in use can also induce considerable financial costs to the owners and shareholders of the structure. As part of the scheduled maintenance of structures, the actual structural condition is regularly monitored during inspections, and, in the case of identified defects, appropriate countermeasures are taken.

However, selecting and evaluating possible maintenance measures is complex because the relevant aging processes influence each other in multiple ways. Thus, possible long-term effects are challenging to predict as only limited solution options exist. To improve the prediction and thus the evaluation of possible maintenance alternatives, a holistic, general modeling concept for the description of aging processes is developed in the present work. With the help of the developed concept, the holistic calculation of aging processes can be improved, and a well-founded selection of the most economic planning variant can be made.

The model is derived by evaluating the physico-chemical properties of cement-based building materials and determining their relevance concerning aging processes. In addition to the building material, the construction-related characteristics and their impact on aging are discussed. Based on the identified building material and structural properties, the known aging processes for cement-based building materials are described and classified concerning their similarities in modeling. For this, the processes are divided into weakening processes, which reduce the material resistance based on the chemical changes, and processes, which induce internal stresses. In addition to the description of the material deterioration by reducing the mechanical resistance, the simultaneously occurring changes in the pore space are also modeled. Similarly, the pore space's transformation during the cracks' initiation and growth is introduced. These changes in the pore space are relevant for describing the material and energy fluxes connected to each aging process. Therefore, the decisive transport mechanisms are included to capture the aging rates. In particular, the moisture transport is described under consideration of the pore structure as well as of the influence of discontinuities like cracks and joints. As cracks play a decisive role during deterioration, the modeling approach also

includes the description of their initiation and growth. Furthermore, the advective and diffusive transport of solutes in the fluid phases and the simultaneously occurring heat transport are implemented. The change in the material's chemical composition is described with the help of the dissolution and precipitation processes of the cement phases. The modeling is carried out by taking the activities of the already dissolved ions in the liquid phase as well as the available solid cement paste components into account.

In order to validate the developed modeling approach, the individual domains are used to re-simulate published and newly collected experimental data. A good agreement with the published measured data is found for all data sets. Furthermore, the modeling approach is compared with analytical and comparable numerical simulations with good agreement. The combined overall model is applied to a set of benchmark cases to demonstrate its applicability to structures. Here, the strength reduction throughout the structure is computed based on the changes in chemical composition. These changes are also studied for the block-wise construction process' effects on the deterioration rate. It is found that the variance of material properties has a notable impact but does not change the service life of the structure significantly. In contrast, the service life can be significantly changed when construction joints or cracks are present. This is found in the second set of comparisons when the effect of these inhomogeneities is studied. In particular, the transport of water from the joints and cracks towards the matrix and joint-matrix diffusion are found to impact the deterioration rates greatly. While the former increases the rate of deterioration in the joint and matrix by increasing the flow rates, the latter induces a broader spread of material reduction around the joint and thus reduces the rate of decay for the joint.

Finally, the developed modeling approach is applied to evaluate a structure's different durability measures. When comparing the effects of using a surface sealing to the impact of improving the construction joints, cracking is found to have a decisive influence on the results. While the cracking of the surface sealing increases the rate of deterioration even beyond the initial level, the joint treatment is found to improve the service life even when cracks are formed. By combining appropriate formulations and new coupling options, the model allows the quantification of a structure's service life. Therefore, the developed approach can be used to predict aging as well as curing processes and their related decisive mechanisms during the service life of structures. Hence, it is an essential new tool for a wide range of research and development applications.

Zusammenfassung

Die Alterung und Instandhaltung von Bauwerken aus zementbasierten Baustoffen spielt eine entscheidende Rolle sowohl für die Langzeitsicherheit als auch für die Lebensdauer der Bauwerke. Die damit verbundenen Kosten und etwaige Nutzungsausfälle im Falle von größeren Schäden können dabei ganz erhebliche finanzielle Kosten für die Bauwerkseigentümer bedeuten. Im Rahmen der planmäßigen Instandhaltung von Bauwerken wird daher regelmäßig der Ist-Zustand bei Inspektionen erfasst und im Falle von ermittelten Mängeln entsprechende Gegenmaßnahmen ergriffen.

Die Auswahl und Bewertung von möglichen Instandhaltungsmaßnahmen ist allerdings komplex, da sich die maßgeblichen Alterungsprozesse auf vielfältige Weise gegenseitig beeinflussen und die zu erwartende Langzeitauswirkung der Maßnahmen mit den verfügbaren Berechnungsmöglichkeiten nur schwer abzuschätzen ist. Um die Vorhersagemöglichkeit und damit auch die Bewertung von möglichen Instandsetzungsalternativen zu verbessern, wird in der vorliegenden Arbeit ein ganzheitliches, generalisierbares Modellierungskonzept zur Beschreibung von Alterungsprozessen entwickelt.

Zur Herleitung der benötigten Modellierungsgrundlagen werden die physio-chemischen Eigenschaften von zementbasierten Baustoffen zusammengestellt und ihre Relevanz für Alterungsprozesse bewertet. Neben den Eigenschaften des Baustoffs selbst werden auch die herstellungsbedingten Besonderheiten mit ihrer Bedeutung für die Alterung als Einflussfaktor ermittelt. Basierend auf den Baustoff- und Bauwerkseigenschaften werden die bekannten Alterungsprozesse für zementbasierte Bauwerkstoffe beschrieben und bezüglich ihrer Gemeinsamkeiten bei der Modellierung klassifiziert. Neben der Beschreibung der Materialentfestigung durch Reduktion der mechanischen Widerstände wird dabei aber auch die gleichzeitig stattfindende Veränderung des Porenraums modelliert. Die modellierte Veränderung im Porenraum ist dabei im Speziellen für die Beschreibung der zu jedem Alterungsprozess gehörenden Stoff- und Energieströme relevant, welche analog zu den Schädigungsprozessen ermittelt werden. Zu den Transportmechanismen zählen der Feuchtetransport in der homogenen Porenstruktur, aber auch der Feuchtransport im Bereich von Diskontinuitäten wie Rissen und Fugen. Darüber hinaus

wird der advektive und diffusive Transport von gelösten Stoffen in der Flüssigkeitsphase, aber auch der zeitgleich stattfindende Wärmetransport dargestellt. Die Veränderung der chemischen Zusammensetzung wird mithilfe der zugrundeliegenden Lösungs- und Ausfällungsprozesse der festigkeitsinduzierenden Zementphasen beschrieben. Diese Modellierung erfolgt dabei unter Berücksichtigung der Aktivitäten der bereits gelösten Ionen sowie der verfügbaren Zementsteinphasen. Um die Veränderung im Verformungs- und Spannungszustand des Bauwerks erfassen zu können, wird ein kombiniertes elastisch-plastisches mechanisches Modell genutzt, welches auch für die Beschreibung der zugehörigen Porenraumveränderungen günstig ist.

Der entwickelte Modellierungsansatz wird anhand der einzelnen implementierten Teilmodelle verifiziert. Die Validierung erfolgt durch die Simulation und den Vergleich mit in der Literatur verfügbaren und neu erhobene Versuchsdaten. Hierbei wird insgesamt eine gute Übereinstimmung der Ergebnisse mit veröffentlichten Messdaten gefunden. Die Anwendungsmöglichkeit des Gesamtmodells wird anhand einiger Berechnungsbeispiele an der Koynastaumauer demonstriert. Neben der Veränderung des Verformungszustands des Bauwerks über die Standzeit wird dabei auch die Reduktion der Bauwerksfestigkeiten und die Veränderung der Verteilung der chemischen Zusammensetzung für die Struktur dargestellt. In diesem Zuge wird auch der Einfluss der Blockbauweise auf die Alterung untersucht. Hierbei zeigt sich, dass ungünstige Materialeigenschaften einzelner Blöcke zwar einen deutlich erkennbaren Einfluss haben, aber die Lebensdauer nicht signifikant beeinflussen. Sobald allerdings Risse oder Fugen berücksichtigt werden, kann die Alterungsrate deutlich verändert werden. Dies zeigt eine weitere Serie von Berechnungen an der Staumauer, wobei vor allem der Effekt des Flüssigkeitsaustausches zwischen Riss und Fuge mit der umliegenden Matrix, aber auch die Diffusion zwischen Fuge und Matrix entscheidende Einflüsse darstellen. Hierbei vergrößert der erhöhte Flüssigkeitsaustausch von Riss oder Fuge die Alterungsrate deutlich, während die Diffusion für eine breitere Alterungfront und einen langsameren Fortschritt in der Fuge sorgt.

In einer letzten Serie von Berechnungen wird der Einfluss verschiedener Maßnahmen zur Verbesserung der Dauerhaftigkeit verglichen. Dabei wird die Auswirkung des Aufbringens einer Oberflächendichtung einer Verbesserung der Fugeneigenschaften entgegengestellt. Es zeigt sich, dass das Auftreten von Rissen eine große Rolle spielt und die Alterungsrate im Falle der Oberflächendichtung sogar noch erhöht. Im Gegenteil dazu bleibt das Verbessern der Fugen auch mit dem Auftreten von Rissen eine Maßnahme, welche die Dauerhaftigkeit nachhaltig erhöht. Es kann daher gezeigt werden, dass der entwickelte Ansatz sowohl zur Quantifizierung möglicher Lebensdauern als auch zur Ermittlung entscheidender Schädigungsprozesse eingesetzt werden kann und daher in Forschung sowie in der Technik viele Anwendungsmöglichkeiten hat.

1 Introduction

Nowadays, significant global economic challenges arise from aging structures and infrastructures. Especially for concrete/cement-based structures, the aging processes are initiated by diverse sources and thus get evident in a wide range of civil structures worldwide e.g. at bridges (Bhattacharya et al. 2008; Akiyama et al. 2014), harbour piers (Polder et al. 2005), dams (Dolen et al. 2003; Bettzieche et al. 2004) and even at critical structures like nuclear power plants (Braverman et al. 2004; Arel et al. 2017). Since each of these structures is designed for a specific purpose, the deteriorative processes need to be regularly counteracted by maintenance and repairs to preserve the designated function of the structure (Val et al. 2009). However, these works are usually associated with an additional budget; thus, maintaining structures and infrastructure is related to high costs. Furthermore, with the increasing share of new cement-based civil structures as well as the increasing age of structures worldwide, the costs for maintenance are expected to rise, independent of the fact that the current costs are already significant for the national economy (Cusatis et al. 2015; Gjørv 2011).

As one of the main drivers of deterioration of cement-based materials is their thermodynamic imbalance with the surrounding media (Ulm et al. 1999), deterioration generally is inevitable in most cases. However, the rate of the deterioration process can be changed by different measures. For new constructions, these measures include the change of the chemical composition of the material, selecting adequate construction techniques and a precise, durable technical design that accounts for each service load. Similarly, many different repair and improvement options are available for existing structures. Therefore, accurate planning of each measure and structure is needed to reduce future maintenance costs. Such planning requires well-founded understanding as well as accurate predictions of the deterioration processes and their sources. Thus, if this knowledge and the necessary predictive tools are available, a structure's durability can be significantly improved. Therefore, this thesis aims to increase the understanding of different aging processes as well as their interdependencies while also improving the modeling and prediction of these processes. This consequently reduces maintenance costs, decreases resource usage and guarantees a sustainable interaction with the built environment.

1.1 Deterioration of cement-based structures

The aging or deterioration of cement-based structures is governed by environmental conditions, such as physical, chemical and biological effects, that alter the structure's material (Tang et al. 2015). Based on the material's properties changes, the aging processes then influence the structure's response to its mechanical loads, potentially resulting in severe deformations or even cracking. However, the description of the deterioration processes in the material is complex since multiple interdependent factors cause them. These factors include a large set of mechanical, moisture, thermal and chemical loads, which are the driving potentials for the deterioration. For example, such loads can be aggressive chemical environmental conditions like sulfuric soils and acidic waters or increased water pressures and humidities for subsurface and hydraulic structures.

Nevertheless, when the long-term durability of a structure is assessed, these gradients are not decisive by themselves but the observed rate of change in the material (Basheer et al. 2001). Hence, each load must be linked to transport and exchange processes that govern the observed deterioration. Here, material-dependent factors also control transport processes in addition to the applied driving potentials. These factors include properties like the material's permeability, which controls the fluid flow in the material and thus also the exchange rates towards the environment. However, material properties can rarely be assumed homogeneous across a structure, as the construction processes cannot be executed with such precision. Therefore, heterogeneities and interfaces are introduced during construction. These heterogeneities are particularly evident when poor material quality, unreliable construction techniques, or careless on-site practice are applied. In addition, the complexities for modeling are increased further, as material properties are also subject to continuous changes. Thus, by changing the material's properties, deterioration and deformation also impact the rate of deterioration by itself.

Consequently, the deterioration of each structure is unique and based on the set of imposed loads and the distribution of material properties. As a result, the description and prediction of deterioration processes cannot be generalized, as each structure's unique factors must be determined and considered.

1.2 Predicting and controlling durability

In current construction practice, durability is considered during the design phase of cement-based structures when the common construction standards, as DIN EN 1992 (2011), ACI 318

(2019) or DIN EN 206 (2021) are selected. Those standards include durability concepts which are based on prescriptive design. This means that the parameters of material properties, such as the selection of raw materials, the applied batching and mixing and on-site measures like curing and placing, are specified according to standards. Similarly, cracks and deformations are limited during the design phase. Within these standards, aggressive environments are implemented based on the exposure condition of each structural component, representing a simplified measure of the deterioration potential of the environment. For example, if a component is subjected to marine chlorides, certain minimum cement contents and maximum water to cement ratios must be fulfilled.

However, the prescriptive concept is often criticized by researchers and engineers, as the prescribed values of mixture properties do not sufficiently account for cement types, aggregates and construction methods on-site (Sangoju et al. 2021; Alexander et al. 2019; Beushausen et al. 2019; Alexander et al. 2008; Becker 2008; Walraven 2008; Day 2005). Thus, even if the prescribed properties are considered by following the specification, different results for structural durability are observed. This is induced by the unique set of constraints and parameters of each site and structure, which cannot be fully considered during the planning phase. For historic structures built with different methods, fulfilling the current safety standards is also hard to achieve when a prescriptive design concept is applied (Torero 2019; Spyrakos 2018). Given these limitations of prescriptive design, performance-based concepts receive increasing attention. While for prescribed concepts, the variability of parameters is evaluated statistically during the design phase, performance-based methods predict the durability originating from the measured material parameters. Based on the observed values, the lifetime and safety of the structure are then predicted by using adequate physico-chemical and (numerical) models (Baroghel-Bouny et al. 2009). Hence, the availability of models describing the deterioration processes is vital for performance-based design. Consequently, a shift toward performance-based models not only increases the scientific community's interest in improving the understanding and modeling of deterioration processes but also requires improving the modeling in the sector of applied engineering and construction.

Much detailed research has been conducted on understanding each individual process for modeling and describing the structural deterioration. The models derived for each process are then applied for modeling specific aspects or combined actions of the different domains. Based on the complexity of the interactions of each model, combined effects are usually only taken into account within a few processes. An example is the chemical modeling domain, which governs the dissolution and precipitation of the solid phase composition. Given the

impact of the phase composition on durability, it is evident that many approaches have been developed to model and understand the chemical dissolution of the cement phases. As the dissolution rates are closely linked to a solvent, these chemical models are often already coupled with solute and moisture transport. These models and studies are applied to model the influence of reactive transport, including chemical and transport processes like calcium leaching (Mainguy et al. 2000; Gaitero et al. 2014; Huang et al. 2018; Isgor et al. 2019). Likewise, the effect of the formation of expansive solids like ettringite or the effects of alkali-aggregate reaction (AAR) are also computed in a similar manner (Farage et al. 2004; Grimal et al. 2010; Guthrie et al. 2015; Kim et al. 2015). Given the modeled solid phases' expansive nature, some of the above studies also include the induced swelling effects and the structure's mechanical response. However, in these cases, the moisture transport is usually only included in a simplified form, neglecting the pore structure changes. In addition, the interaction of cracks on moisture transport and the changes in pore pressure during cracking is not considered.

Within another field of studies of cement-based materials, the moisture or gas flow is modeled in detail based on a detailed description of the pore structure (Mayer et al. 1992; Baroghel-Bouny et al. 1999; Navarro et al. 2006; Baroghel-Bouny 2007; Julnipitawong 2011). While this field of research is more focused on the details of liquid and vapor transport as well as adsorption and exchange with the surrounding matter, chemical and mechanical aspects are usually not taken into account.

In fracture mechanics, the focus is rather on a detailed and precise description of the structure's response to mechanical loads. This field applies and continuously improves models that determine the structure's failure process. The modeling is based on the description of crack initiation and growth for different materials, including cement-based materials. Within the multitude of developed models, improving the description of the material's response during ultimate loading has always been one of the main objectives. This response can be obtained by using the more classical modeling approaches like the discrete crack model (Braun et al. 2014; Paluszny et al. 2009), the elasto-plastic descriptions (Wei et al. 2008; Tauzowski 2021) or combined and damage-based approaches (Qi et al. 2013; Nechnech et al. 2002). More recently, modeling approaches like the cohesive crack (Barpi et al. 2010; Shi et al. 2013))or phase fields models (Santillán et al. 2017) have been applied in this field to allow more robust modeling of the material failure. Nevertheless, this field focuses on the description of the mechanical response even though the interaction with moisture transport is accounted for more often in recent research (Sha et al. 2017; Rahal et al. 2017; Javanmardi et al. 2005; Chong-Shi et al. 2005; Lai et al. 2008).

However, the interaction with moisture transport is usually only considered in a more simplified way compared to the specialized domains. In almost all mechanical cases, the fluid is mainly treated as a load within the mechanical description. Thus, these models do not consider the effect of solute transport.

Even though each model description is precise and valid within its field, the long-term modeling of the structures requires contributions from all research fields and multi-directional coupling between different factors and solutions techniques. This trend is also evident in the increasing amount of multi-domain coupled models which are presented recently (Zhao et al. 2020; Zhou et al. 2017; Gasch et al. 2016; Du et al. 2016; Zhang et al. 2016; Jendele et al. 2014). However, even though the approaches are multi-disciplinary, they currently still lack the capability to fully describe the deterioration of a cement-based structure over its service life. Thus, despite the increase in efforts for developing holistic modeling approaches, still great effort is needed to describe the long-term deterioration of concrete structures with comprehensive models as concluded by Alexander (2018).

1.3 Outline and structure

In order to get closer to a holistic modeling approach for the evaluation of the service life of a structure, a combined approach is developed and implemented into a flexible framework. The model description is developed to allow better planning of new structures while also improving the prediction of the effects of maintenance and repairs. Therefore, a general description of the relevant aging factors and processes is selected. The approach is implemented in a generalized, adjustable numerical toolbox, which allows for simulation and evaluation of the response of different structures while considering all relevant physical domains over the whole life cycle of the structure.

In order to derive the approach, the characteristics of cement-based materials that are relevant for modeling and deterioration are identified first. This includes the description of the hardening process, the chemical composition, the porous properties and the construction-related factors of the material. Based on these characteristics, the relevant processes for describing deterioration are displayed and evaluated for moisture, thermal and solute transport processes. As the description of the alteration of the chemical composition is closely linked, this alteration is also discussed. The alteration of the material imposes effects on the mechanical and transport properties, as will be shown. Concluding on the identified descriptions and the

material factors, adequate modeling approaches for the transport as well as the chemical and structural change are selected and developed. Finally, the possible interactions are chosen and formulated. The modeling approach is implemented within a numerical framework which is presented, evaluated and discussed. As the framework is adjustable, further implementation of other model descriptions is still possible even though specific approaches are selected within this work. Each physical domain is evaluated against experiments as well as analytical and experimental results from the literature. Lastly, the developed approach is applied to predicting the deterioration processes of a gravity dam. Within different sets of comparative cases, the impacts of structural heterogeneities and the effects of joints and cracks on deterioration rates are evaluated. Eventually, the outcomes of different maintenance measures for the gravity dam are compared.

2 Cement-based structures

Cement-based structures (CBS) arise in a multitude of different designs, shapes, construction principles and purposes, each with its own set of constraints and hence deterioration factors. Nevertheless, this diversity of the structural design is rivaled by the cement-based material (CBM) compositions, as different mixtures, compounds and supplementary additives change the strength and durability of the material significantly. Hence, each structure's unique response to loads is governed by many factors, including the selected technical design, the mechanical and chemical properties of the material, and possible flaws and heterogeneity induced during construction.

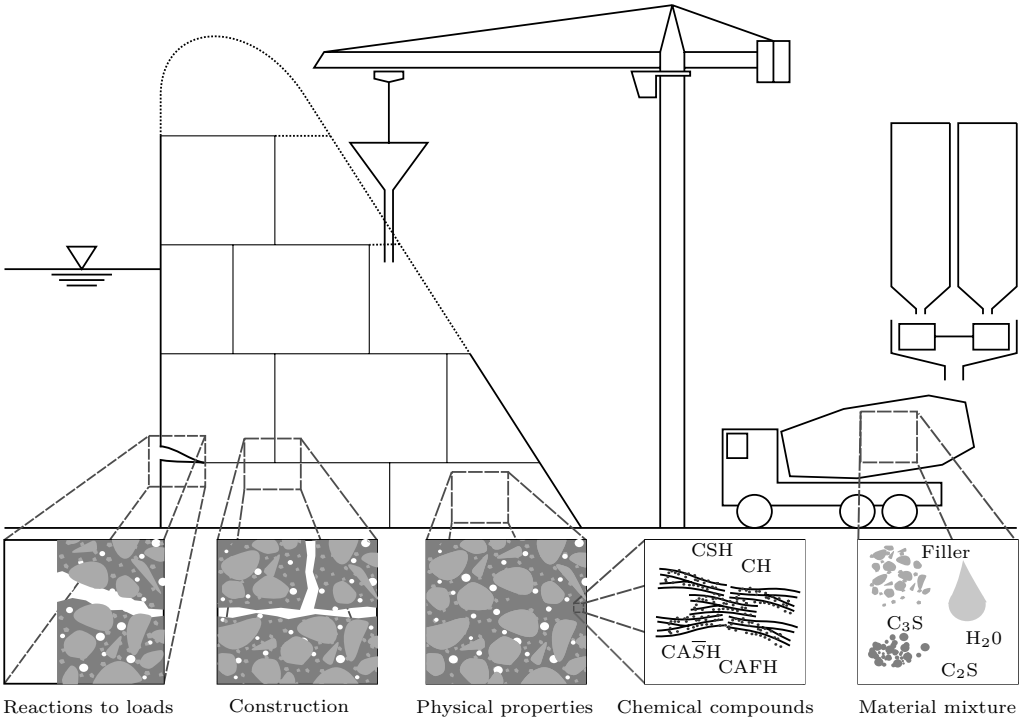

Fig. 2.1: Factors influencing the durability of a cement-based structure

Different factors affecting the structure's durability are illustrated in Fig. 2.1 for a gravity dam under construction. One factor affecting the durability is the design of the cementitious mixture of the material, which governs the material's chemical composition and the material's strength and pore structure. Discontinuities and other flaws can occur at interfaces and surfaces

of the material during the placing and hydration, which also affect the local strength and pore structure. Thus, the resistance to loads can be decreased significantly at these locations. Mechanical, thermal, creep and shrinkage processes induced by mechanical, moisture or thermal loads can weaken the material locally when (micro) cracking or sliding occurs. All these local changes impact the structure's durability and thus have to be discussed for holistic modeling. A description of these different factors and properties is presented in the following chapters to identify the most critical aspects. The wide variety of cement-based materials is first described in terms of chemical and physical composition. Then the physical properties relevant to aging are presented and the effect of construction methods is discussed.

2.1 Chemical composition

Cement-based materials can be generalized as a mixture of inert filler material held together by the hardened cement acting as a binder. The binder is activated by adding water to the mixture, as the initially anhydrous cement reacts with the provided water forming the hydration products and yielding the hardened cement paste. As this inclusion of water into the chemical structure is an exothermic reaction, hydration heat is released. This hardening process can be rather fast while producing a relatively high-strength material within hours, but, depending on the cement and material mixture, it is also possible that it can take years to reach the final strength of the paste. Nevertheless, most hydration heat is usually released within a few days, even for slow-hardening mixtures. The lapse of this hardening is influenced by the mixture proportions of the materials as well as the addition of supplementary cementing materials (SCMs), such as fly ash or furnace slag, which can speed up or slow down the hardening process or reduce the released hydration heat(Kosmatka et al. 2011). In order to adjust specific attributes of the mixture, further chemical admixtures can be added.

The most common cement-based materials are concrete and mortar, whose main difference is the size of aggregates or inclusions used for the material mixture. However, this seemingly small difference has a large impact during construction, as the sizes of the aggregates greatly influence the workability and hence the possible applications of the materials (Bureau of Reclamation 1975). In addition to mortar and concrete, masonry is another commonly used construction technique, sometimes also debated as a cement-based material. For this technique, a layer of mortar is used to bind a set of larger bricks or stones. Even though this is an ancient technique, it is still being applied to modern construction.

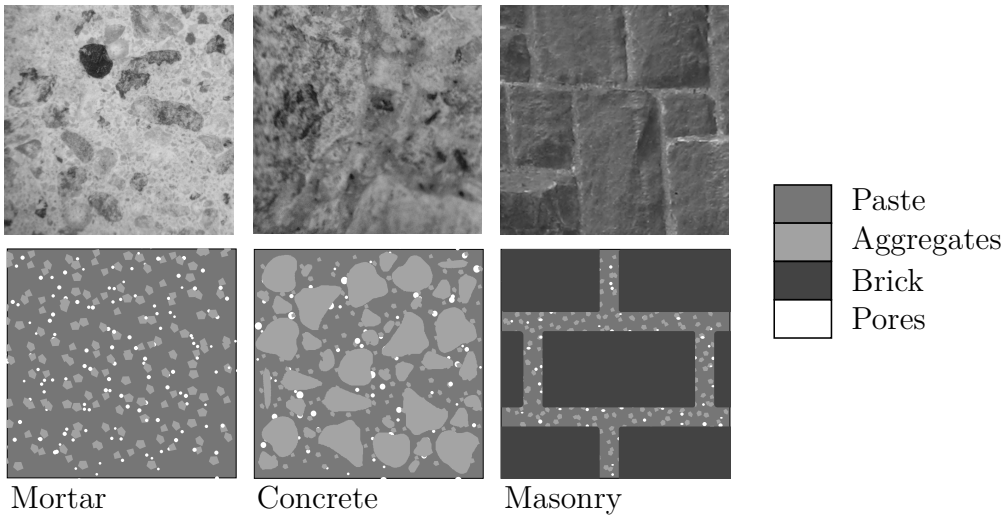

Fig. 2.2: Most common cement-based materials

For concrete, the most commonly applied form in structures is reinforced concrete. Here additional steel elements are embedded into the material as reinforcement. Even though this is the most common form, the description of the reinforcement within the material is not explicitly discussed within this work, as the interaction and bonding between the steel and concrete add an additional layer of complexity to the deterioration. Thus, this topic is left out to allow a more explicit focus on the plain material. Nevertheless, most of the described mechanisms also apply to reinforced structures; thus, there is only a slight limitation to applying the described methods.

Even without considering additional reinforcements, the material is heterogeneous and contains pores of multiple length scales independent of the applied material composition. The sizes and connectivities of the pores affect the resistance to permeation of fluids and thus durability. The pore structure is strongly impacted by the applied cement types, aggregates, admixtures and SCMs. Therefore, a short overview of cement-based materials and their mixture ingredients such as cement, SCMs, admixtures and aggregates is given.

2.1.1 Cement

The European standard DIN EN 197-1 (2011) describes cement as a fine-grained inorganic hydraulic binder material. This definition combines many different cement types with different mineralogical compositions. However, portland clinker-based cement types are the most used.

The raw Portland clinker phase mainly consists of two calcium silicate phases, tricalcium silicate (alit) and dicalcium silicate (belit). The remainder contains tricalcium aluminate,

Tab. 2.1: Range of clinker phase contributions in different Portland cements surveyed between 1950 and 2004 composition according to Bhatty et al. (2008)

Clinker phase	**Chemical formula**	**CCN**	**Mass fraction**
Alite (Tricalcium silicate)	$3CaO{\cdot}SiO_2$	C_3S	40-70 %
Belite (Dicalcium silicate)	$2CaO{\cdot}SiO_2$	C_2S	10-45 %
Tricalcium aluminate	$3CaO{\cdot}Al_2O_3$	C_3A	0-15 %
Tetracalcium aluminoferrite	$4CaO{\cdot}Al_2O_3{\cdot}Fe_2O_3$	C_4AF	5-15 %

tetracalcium alumina ferrite and parts of free lime. Within this general description, the range of applied clinker phase compositions for Portland cement is broad, as displayed in Tab. 2.1. As the molecular formulas of the phases are long and contain repetitions, a short-form notation (CCN - Cement chemists notation) of the chemical components is commonly applied in cement chemistry (see Appendix A.1).

2.1.2 Supplementary cementitious materials and chemical admixtures

Supplementary cementitious materials (SCMs) are natural materials or industrial byproducts that are used as additives within the cement. The SCMs can be included during the cement manufacturing or added to the cement-based material upon mixture. Depending on the selected SCMs, the properties of the cement-based material are changed by the additives' pozzolanic or hydraulic properties. SCMs also change the rate of strength gain, the amount and the rate of hydration heat, as well as the resistance to permeation and aggressive media. Given these potential positive effects on the properties of the paste, using cheap industrial byproducts can also improve the costs as well as the energy used during production.

Like SCMs, chemical admixtures can be added to the material during or before mixing. Admixtures are used to control specific properties, the workability and applicability of the mixture under certain conditions, and to overcome difficulties upon mixing and economic reasons. SCMs and chemical admixtures, therefore, do not only influence the immediate chemical and mechanical properties of the material, but they also have a significant influence on the durability of the material (see Appendix A.2) as those changes also impact the pore structure and resistance to chemical attacks.

2.1.3 Aggregates or filler

The second base ingredient of cement-based materials is the filler material, also called aggregates. Aggregates are granular solid materials that are bonded by the cement paste during hydration.

Aggregates should be inert in order not to influence the hardening as well as the durability of the cementitious paste. However, as aggregates are not always completely nonreactive, the soluble contents of chloride, sulfates and silicas should be minimized according to application (DIN EN 12620 2008). As cementitious materials contain large quantities of aggregates, usually between 70% to 80% of the mass of the concretes and mortars, their composition and properties influence the possibility of pumping and working the fresh material (Obi 2017). Based on the number of aggregates contained in the material, some properties of the composite material can be precisely derived by accounting for the contributions of the aggregates. Hence, normal, lightweight and heavyweight concrete can be produced by selecting a specific aggregate density. However, averaged contributions do not fully reflect the observed macroscopic properties for all quantities, such as the tensile strength (Tasong et al. 1998) discussed later in Sec. 2.2.1.

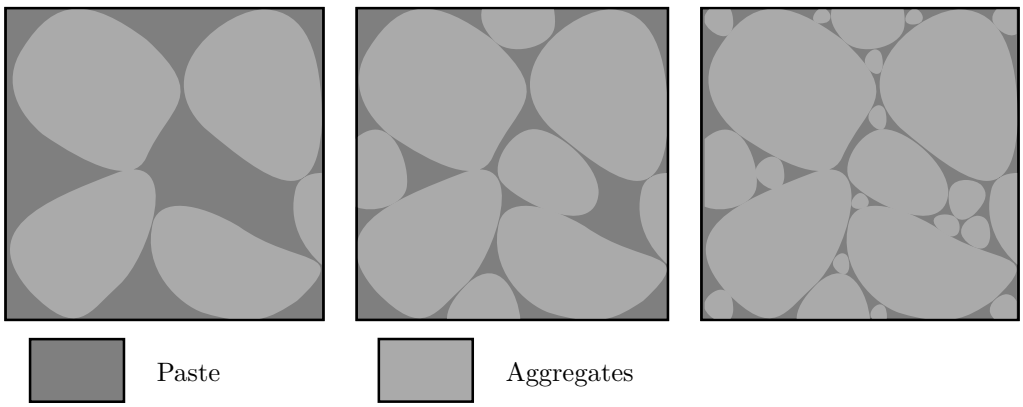

Fig. 2.3: Illustration of the effect of the aggregate grading on the compaction of the cement paste

In addition to the physical properties such as Young's modulus or the density of the pure aggregate material, the size, the form of the aggregates and their size distribution (grading) play an essential role in the properties and durability of the cementitious material. As the distribution and composition of the aggregate sizes govern the ability of the compaction of the aggregates, as displayed in Fig. 2.3, it is evident that aggregate affects different macroscopic properties. Since a wider spread of aggregate sizes can be compacted more efficiently than distributions of more uniform sizes, higher mechanical strength values are observed for these "well rounded" size distributions (Meddah et al. 2010). As the compaction and material also affect the pore space of the material, the selection of aggregates also changes the pore structure and thus the moisture and solute transport rates (Fabien et al. 2017).

2.1.4 Cement hydration

Cement hydration is the hardening process that is initiated with the addition of water to the unreacted cement. During the hydration process, the supplied water reacts with the hydraulic components of the clinker phases by forming their hydrated counterparts. This exact sequence of the hydration process and the hydration phases are complex and the governing, rate-controlling mechanism are still being discussed in current research (Scrivener et al. 2019). However, it is agreed that the chemical composition of cement influences the hydration process significantly. Hence, apart from the initial clinker phase composition, the amount of included supplementary cementitious materials is of importance. In addition, the amount of water that is supplied, the aggregates and potentially admixtures also influence the hardening process of the paste.

Descriptive models of the hydration process have been developed over the last decades. These models compile the complexity of the hydration process into a set of primary reaction equations. The underlying chemical reaction process, nonetheless, is not a "simple incorporation of water into the solid" but is a combination of several sequential processes and phases. The first phase is the dissolution of the solid phase resulting in an oversaturated solution of hemihydrates, a phase of nucleation of the cement phases and finally, a phase of crystal growth (Kurdowski 2014). This whole process is simplified within most hydration models, where only a general reaction path is displayed, which does not entirely account for each intermediate step. One of the commonly applied descriptive models is the Tennis model (Tennis et al. 2000), which describes the hydration of cement as a set of prime reactions for each clinker phase:

$$\begin{aligned}
2C_3S + 10.6H &\rightarrow C_{3.4} - S_2 - H_8 + 2.6CH \\
2C_2S + 8.6H &\rightarrow C_{3.4} - S_2 - H_8 + 0.6CH \\
C_3A + 3C\overline{S}H_2 + 26H &\rightarrow C_6A\overline{S}_3H_{32} \\
2C_3A + C_6A\overline{S}_3H_{32} + 4H &\rightarrow 3C_4A\overline{S}H|_{12} \\
C_3A + CH + 12H &\rightarrow C_4AH_{13} \\
C_4AF + 2CH + 10H &\rightarrow 2C_3\left(A,F\right)H_6
\end{aligned} \tag{2.1}$$

The first two equations of the model describe the reactions of the two primary clinker phases, alite and belite, which are usually regarded as the most important phases. Those two reactions govern the amount of CSH formed, which is the hardened paste's primary strength source. For ordinary cement, the mass fraction of CSH in the paste is around 50 %, with an additional quantity of 15 % - 25 % being CH (portlandite), which is also formed by the two primary reactions

(Kosmatka et al. 2011). The third reaction path describes the reaction of the supplied aluminate with gypsum if present. The result is ettringite, which subsequently is consumed by follow-up reactions forming monosulfate (fourth reaction). However, if additional sulfates are available, ettringite can form again. If aluminates remain, ettringite is consumed by forming monosulfate, while the remaining aluminates are then hydrated, forming calcium aluminate hydrate. The ferrite phase can also react with gypsum, similar to aluminates, but the reaction is generally slower. For this reason, hydrogarnet is often formed (sixth equation). The temporal succession of these steps is displayed in Fig 2.4 by the amount of each solid phase formed during hydration.

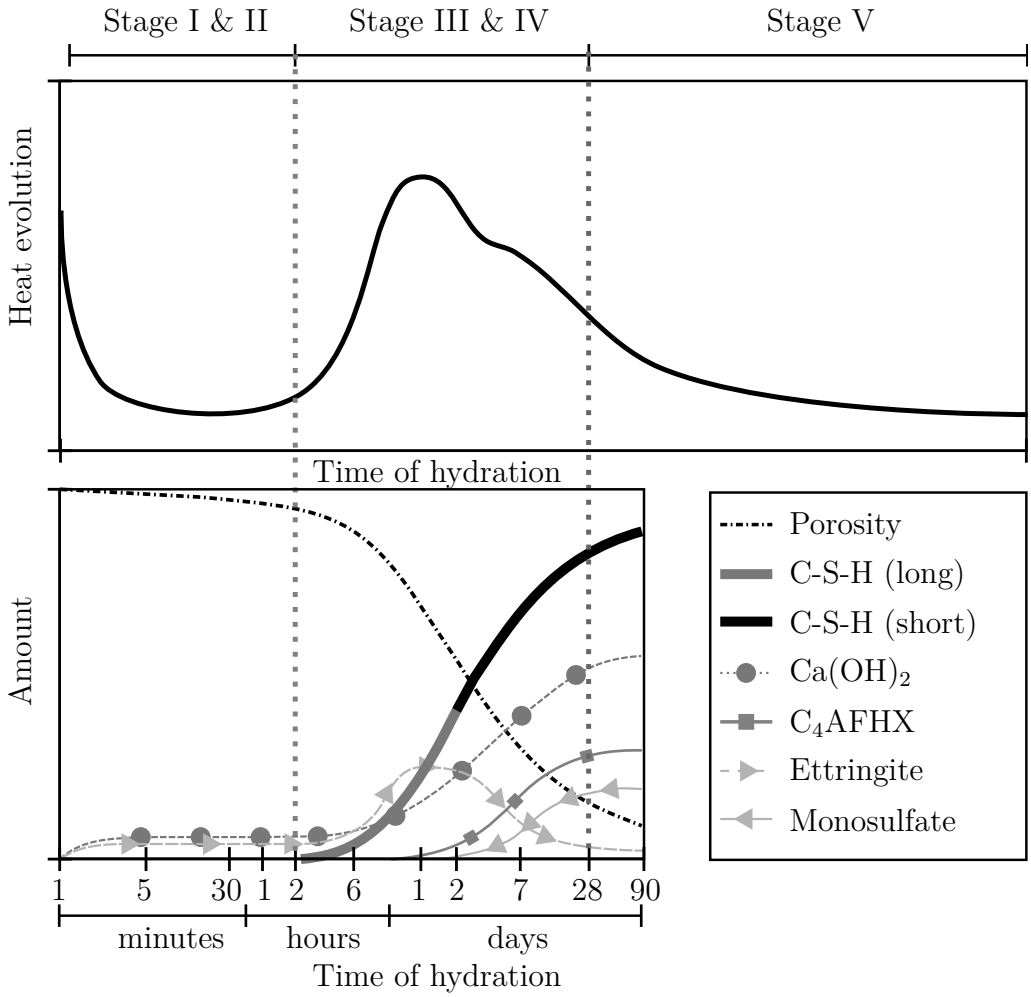

Fig. 2.4: Top: Evolution of hydration heat (Kosmatka et al. 2011), Bottom: relative volumes of the cement phases and hydration products as a function of time adapted from Locher et al. (1976)

If the rate of released heat in the hydration process is measured, the process can be distinguished into different stages, as displayed on top of Fig 2.4. The initial reaction and first

deceleration, a phase of slow reaction (induction II), a phase of acceleration of the hydration rate and a final phase of decreasing hydration speed (Bensted et al. 2002).

The initial phase is controlled by the immediate exothermic reaction of the surface of the alite with the supplied water. However, in addition to this reaction, simultaneous dissolution of alite also contributes to the released heat (Bullard et al. 2011). The deceleration of the heat release after the first reaction phase is explained by two different theories. The older hypothesis states that a meta-stable CSH hydrate forms at the reactive surface, preventing a faster dissolution of the phases (Jennings et al. 1979). More recently, this deceleration has been explained by decreased dissolution rates. This decrease in rate is governed by the increasing saturation of alite and the formation of shallow pits, which both reduce the reaction kinetics (Juilland et al. 2017). After reaching the minimum dissolution rates, the hydration rate increases again in Stage III as precipitation and dissolution rates rise. This period is usually described as "nucleation and free growth," which can be modeled by exponential laws. The outward growth of the fibrous CSH phases initiating from the C_3S surface of this phase is displayed in Fig. 2.5. This growth process is not only important for the achieved strength of the hardened paste but also defines the remaining void space after hydration. The exact sequence of this stage is still not fully understood as multiple models are still discussed in current research (Scrivener et al. 2019).

After reaching the maximum hydration rates, the hydration process is slowed as the available space for new hydration products reduces and becomes a key factor. Here the available space, water availability, as well as the distribution of hydration products become significant aspects even though more research is needed to describe the interaction of these processes fully. During this deceleration phase stage, the formation of monosulfate can induce a short phase of increased growth which is indicated by a third peak.

During the whole process of hydration, CSH phases are formed by consuming alite and belite as described before. As the paste exhibits a very low crystallinity, the ratios of calcium to silicate within the CSH phases vary over an extensive range (between 0.5-3), as discussed by Richardson (2008). Hence, the chemical composition within the hardened CSH phases is strongly influenced by the initial composition, water supply during hydration and available temperatures. The hydration product with the second-highest quantity, portlandite, forms large crystalline aggregates during hydration.

As described in Sec. 2.1.2, the availability of SCMs can initiate secondary reactions, which consume the formed portlandite while producing additional CSH or similar phases. The amount

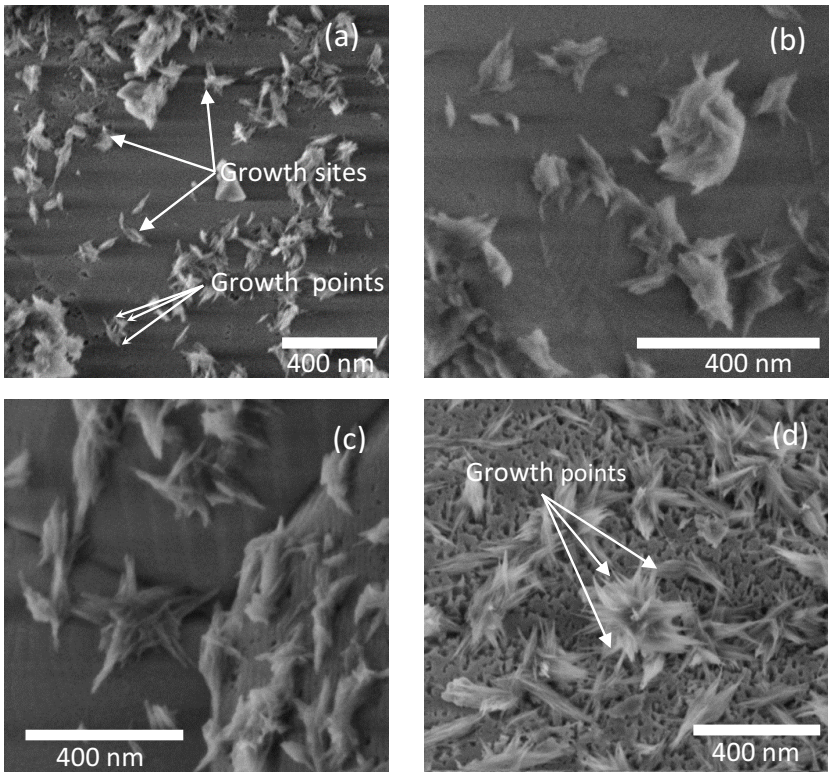

Fig. 2.5: Nucleation and growth of the CSH phases during the third stage hydration after 2, 4, 5, and 6 h after hydration (Nguyen-Tuan et al. 2020)

of aluminate and ferrite phases produced during hydration can be predicted more easily by accounting for the initial amount of ferrite and aluminate components in the clinker as the reactions are less interdependent.

Based on the description of the hydration process, it is clear that the hardened paste is not a homogeneous material. This is especially evident in the period of growth around the reaction products, where pits of somewhat heterogeneous mixtures of chemically active and inert components are formed. The result is a heterogeneous mixture of newly formed hydration products, aggregates, unreacted cement educts and excess water. Given the heterogeneous result of hydration, the resulting geometrical setup and interconnections of the void space in the hardened paste are also complex. The remaining void space includes the space between the solid parts that is mostly filled with water after hydration. This region does not significantly contribute to the material's strength as water is interchangeable and thus reacts less stiffly. Nevertheless, this zone is still decisive for the durability and general response of the material based on its potential for fluid flow and exchange. The void space of cement-based materials is therefore discussed in the following sections.

2.1.5 Void structure of cement-based materials

During the cement paste's mixing and hardening, the hydration products are formed and bonded to the aggregates. At the same time, voids within the cement paste and at the phase interfaces remain inevitably. As voids in the cement paste can originate from different processes, they are often classified according to their origin. In addition, voids are not only found in the cement paste but also within aggregates or at the interfaces between both regions.

Pores in the cement paste

During the third stage of hydration (see Sec 2.1.4), the cement paste gains most of its strength and durability governing properties. The outward growth of the hydration products at this stage does not occur on the whole surface simultaneously but only on a few growth sites, as displayed previously in Fig. 2.5. Here, it is evident that the heterogeneous distribution of educts governs the growth. Voids can then be classified into interlayer, gel, capillary, hollow-shell pores and air voids depending on the formation process. Based on the difference in origin, the size of the pores also varies over multiple magnitudes, ranging from the large macropores over capillary to gel pores and interlayer voids in the CSH.

The smallest scale of the void structure is displayed in Fig. 2.6. In between the silicate-rich layers of solid CSH, small (<1 nm) poorly interconnected pores are formed. Given their size and low connectivity to other voids, water molecules within the interlayer space are usually not removed before reaching very low (11-20 %) relative humidities (Jennings 2008). Multiple layers of CSH layers form a globule, which leaves gel pores with sizes of a few nanometers between them. Given their size and location, determining their quantity is complicated as the water kept in the CSH interlayers is removed simultaneously with the water in the gel pores upon drying. As gel pores account for large quantities of the surface area of the CSH phase, they play an essential role during shrinkage and creep (Jennings et al. 2008).

The larger scales of pores in cementitious materials are displayed in Fig. 2.7. Here the biggest pores, the macro pores and air voids are displayed as well as the smaller capillary pores and the even smaller hollow-shell pores.

Hadley et al. (2000) identified pores formed during the gel phases' outward growth towards the initial water-filled cavities. Here, the space that initially is filled with the unhydrated cement grains will not be fully filled with cementitious products in some cases. As a result, relatively large (1-15 µm) grain-shaped "hollow-shell" pores arise.

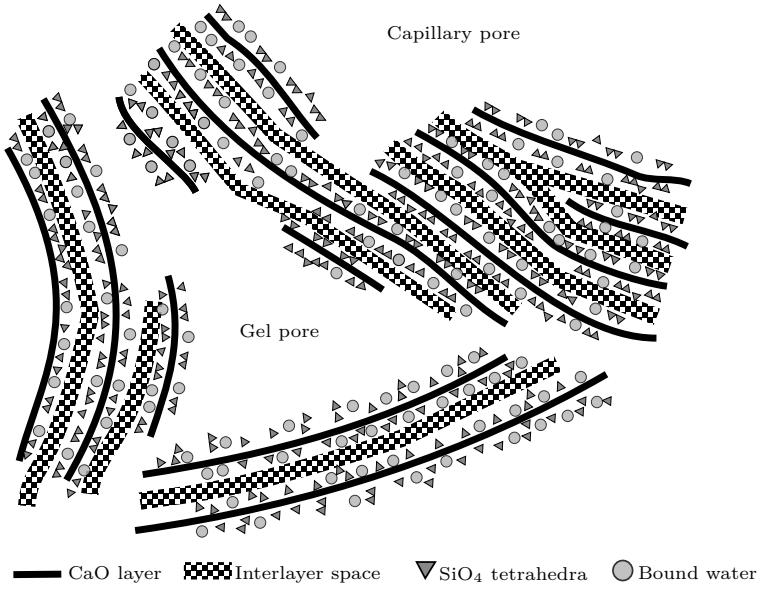

Fig. 2.6: CSH gel structure according to Pinson et al. (2015)

The capillary pores are larger pores that arguably affect the macroscopic behavior like strength and permeability the most (Powers 1958). Capillary pores are defined as the void space that remains filled with water after the hydration. At the beginning of hydration, the unhydrated clinker phases are supplied with water for the reaction from their surrounding. As not all the water is used for reaction, water-filled voids remain after hydration, forming a more or less connected network of voids. Given the complex and heterogeneous formation process, capillary pores are very irregular in shape and size (2 nm up to 10 µm). For these reasons, they are often divided into small, medium and large capillary pores. As the unreacted water initially fills these pores, it is evident that the amount of capillary pores in the material is mainly dependent on the amount of water supplied for hydration.

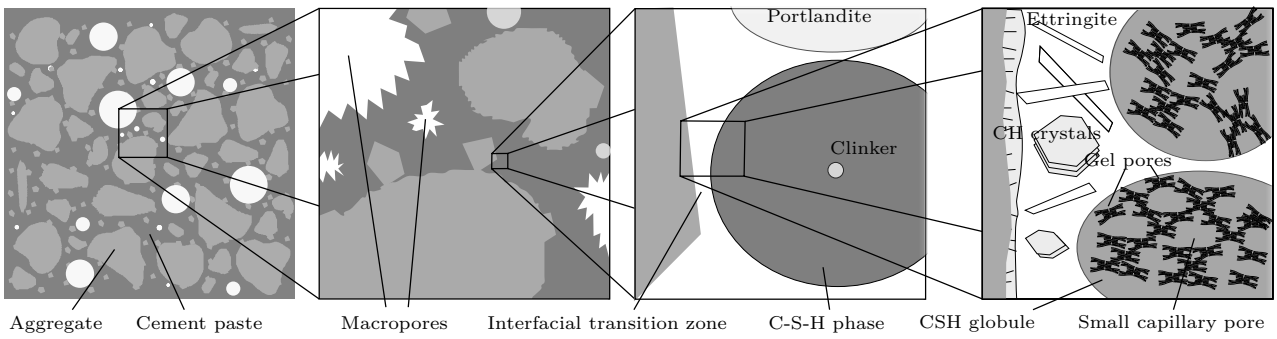

Fig. 2.7: Different pore types in the cement paste according to Jennings et al. (2008) and De Rooij et al. (1998)

Air voids can also be found within the cement paste. Air voids are usually induced during the mixing and placing process of the material. Given the wide variety of origin, air voids also have an extensive range of sizes and can reach up to sizes of several millimeters. Air voids are usually not well connected and form individual voids. This can be beneficial for the freeze-thawing resistance of the material since air-filled voids allow deformation and hence can release stress locally. For this reason, adding air-entraining admixture during hardening can be beneficial to introducing air voids deliberately (see Sec. 3.5.5).

Pores in the aggregates

Pores are not only formed during the hydration of the cement paste; the aggregates and other inclusions like the masonry blocks can also be more or less porous by themselves. Hence, dependent on the material used as aggregate, the increase in porosity differs. Common aggregates are expected to have 0-6 % porosity (Lamichhane 2005). However, if sandstones are used, a larger amount of void space is included in the composite material. As some inclusions can also have larger pore diameters, they also reduce the material's resistance to permeation. Nevertheless, most aggregates can be regarded as almost impermeable compared to cement paste. Powers (1958) found the hydraulic conductivity of aggregates to range between 10^{-11}-10^{-14} m/s for most common rocks with sandstones being the only more conductive material reaching hydraulic conductivities of 10^{-10} m/s.

Voids at the phase interfaces

At the interfaces between inclusions and the cement paste, additional voids are caused by the distinct change in local properties. Within this category, the "Interfacial Transition Zone" (ITZ), which is formed during hydration, is the focus of many researchers. This zone is found to have significantly different properties compared to the properties of the pure paste as well as the aggregates (Scrivener et al. 2004).

The difference between the ITZ and the raw paste is induced by a set of distinct factors. One key factor is the water film around the aggregates which increases the water to cement ratio locally and allows cement components to dissolve and hydration products to crystallize during hydration. Different authors report a duplex film composed of fine CSH and portlandite crystals perpendicular to the surface (Barnes et al. 1978; De Rooij et al. 1998). Around this layer, crystalline portlandite, as well as CSH particles, are found. This composition is also illustrated in Fig. 2.7. Even though the properties of the ITZ are still the subject of current research and are not fully understood, a few properties of the ITZ are agreed upon by multiple authors as

summarized in Diamond et al. (1998). It is concluded that a large number of capillary pores connected to a network as well as less unreacted clinker phases are present. In addition, an increased amount of portlandite and ettringite as well as a generally lower mechanical strength is observed. Based on this lower strength, it is recognized that the ITZ's contribution to the material's macroscopic behavior is one of the main reasons for the differences observed between the pure cement paste and the composite cement-based material (Scrivener et al. 2004). The macroscopic response is also displayed later in Fig. 3.5. Apart from the effect on the structural strength, the durability is also impacted by the ITZ as connections of the voids around the aggregates can form a network of pores that is more accessible to liquids than the homogeneous paste.

Similar zones also form along other phase boundaries. One example is the ITZ-like zone that can be observed around the added steel for reinforced materials (Kenny et al. 2012). The formation principle of the ITZ also applies at interfaces to larger blocks and stones within masonry structures, as these stones can be understood as larger aggregates. A similar process occurs when cement-based materials are placed at subsequent times, as the bond between the already hardened paste and the fresh, plastic paste cannot achieve the same bond properties compared to materials that are being placed simultaneously (see Sec. 2.3).

2.2 Macroscopic properties of cement-based materials

The macroscopic physical properties of the material govern the observable reactions of the structures to environmental impacts such as mechanical, moisture and temperature loads. Hence, they are the critical design factors influencing the structure's durability as they govern the structural response to loads on the macroscale. Given the described complex microstructure of cement-based materials, it is clear that the chemical composition of the paste, the multiscale mixture and arrangement, the aggregates, the voids and the partially included fluids govern the macroscopic properties of the material together.

Thus, the material's response can be described by the sum of each phase when considering their mutual interaction. A direct description and modeling of the contribution of each mineral, aggregate and liquid phase can be applied in research to obtain and derive the macroscopic response on a bigger scale (Haecker et al. 2005). However, such small-scale modeling remains unpractical for larger structures as the exact mineralogical and void composition is not known precisely. In addition, the computational effort is not reasonable on a structural scale. In order to still accurately describe the macroscopic behavior of composite materials, theories have

been developed to allow an upscaling based on the behavior observed on the microscale. Based on each phase's assumed and computed microscopic contribution and the modeled interactions, a macro scale response can be derived this way. These theories and concepts rely on applying spatial (and sometimes temporal) averages over specific volumes and phases of the composite material.

A commonly applied concept is the representative elementary volume (REV; Bear et al. 1987). The concept of the REV assumes that the response of composite material, which is assessed at a size much larger than the scale of the contributing particle or phases, converges to an "average" behavior. This means a representative volume size can be found, where the material's properties remain identical, independent of the selected location. This is possible when averages sufficiently express the impact of small-scale heterogeneities at this scale.

This concept of the REV is illustrated in Fig.2.8, where the effect of the selected averaging scale is displayed for the computed average void fraction. It is shown that the computed void fraction fluctuates on smaller REV scales as either voids or solid phases fill large portions of the averaging volume.

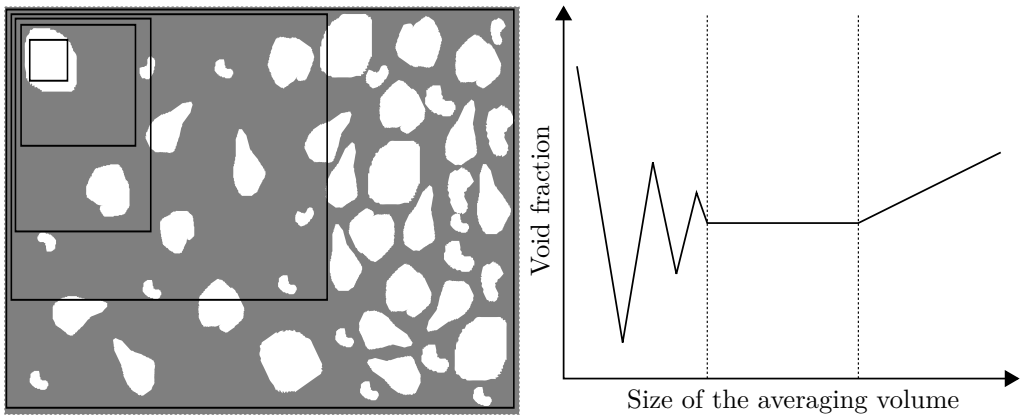

Fig. 2.8: Illustration of the effect of the size of the representative elementary volume on the average void fraction (void volume / total volume)

However, after reaching a certain size, the ratio of voids and solid phases included in the volume is no longer affected by the volume's position. In this case, the value of the material parameter (void fraction) converges. This size is referred to as the minimum representative elementary volume. If the volume is increased much further, this representative value can change again as a result of larger scale heterogeneity (e.g. different material sections). This effectively represents an upper bound for the averaging volume. Consequently, the averaging

length scale has to be much greater than the sizes of the microscale while still being small enough to capture the relevant large-scale heterogeneities of the structure.

For the modeling, this concept implies that macroscopic material properties can be derived that allow for computing the structural response when the structure is sufficiently large. Given the small size of the pores and the large size of the structures, this is almost always the case for cement-based structures.

As a consequence of averaging, information regarding the local material composition is lost. While initially, each point in space can be assigned to a specific phase, e.g., being located in void space, this information is not included anymore after averaging. Hence, the void space is ultimately only described by the total volume fraction after averaging. However, sometimes further information on the local sizes, phase- and pore volumes as well as interface properties need to be recovered to allow a detailed description of the macroscopic response.

Different theories have been developed to recover information from the microscale within the macroscopic formulation. Gray et al. (2013) discussed multiple theories and has shown that they can be related and expressed as universal notation within the representative averaging theory.

Macroscopic characterization of the void space

The void space of cement-based materials is an important factor for their macroscopic mechanical response but also for their transport properties. Therefore, different quantities of the voids are usually preserved when the microscopic composition of the material is averaged.

One of the most commonly used parameter is the porosity, which relates the volume occupied by voids to the total bulk volume of the material and thus gives a general quantification of the available void space. However, if the material bulk volume is changed due to loading, it is essential to distinguish between the Eulerian n and Lagrangian porosity ϕ, which relate the void volume V_v to the current bulk volume V_b or the initial bulk volume (at t =0) V_{b0}:

$$n = \frac{V_v}{V_b} \text{ respectively } \phi = \frac{V_v}{V_{b0}} \tag{2.2}$$

Hence, the Eulerian porosity does not capture a reduction in total void space due to loading if the void ratio remains unchanged. In addition, the porosity is often divided into effective (or

open) and total porosity, where the effective porosity refers to the number of interconnected pores, while the total porosity also includes disconnected voids.

Another macroscopic void parameter is the specific surface area of the pore space. This parameter is given by the ratio of the total area of all pore surfaces and the bulk volume

$$S_s = \frac{A_s}{V_b} \tag{2.3}$$

It can also be reasonable to preserve the information of the actual path length of a molecule through the connected void space. In order to recover this information, the tortuosity τ can be computed

$$\tau = \frac{l_{curved}}{l_{straight}} \tag{2.4}$$

where the length of the connected path through the pores l_{curved} is compared to the length of the direct connection $l_{straight}$ on the macroscale. The tortuosity then can be applied to resemble microscopic properties for processes like diffusion.

As most of the void space parameters are just averaged to scalar values on the macro scale, the information on their distribution is lost. In order to recover the information on pore sizes, a pore size distribution (PSD) can be evaluated for the representative volume. The pore size distribution then describes the number of pores per size fraction within the void space. The typical forms for pore size distributions are the differential and the cumulative form, where the cumulative form displays the amount of void space $V_v(r_p)$ covered by pores that are smaller than a particular diameter r_p. The differential form $D_v(r_p)$ accounts for the change of this void volume per change in pore radius and thus describes the density of the distribution:

$$D_v(r_p) = \frac{\mathrm{d}V_v(r_p)}{\mathrm{d}r_p} \tag{2.5}$$

The information on the microscopic pore sizes is displayed as a pore size distribution in Fig. 2.9 for three different concretes.

Depending on the application and selected modeling approach, additional information on the shape and size of the pores and the pore structure need to be recovered similarly to improve the description of the macroscopic behavior.

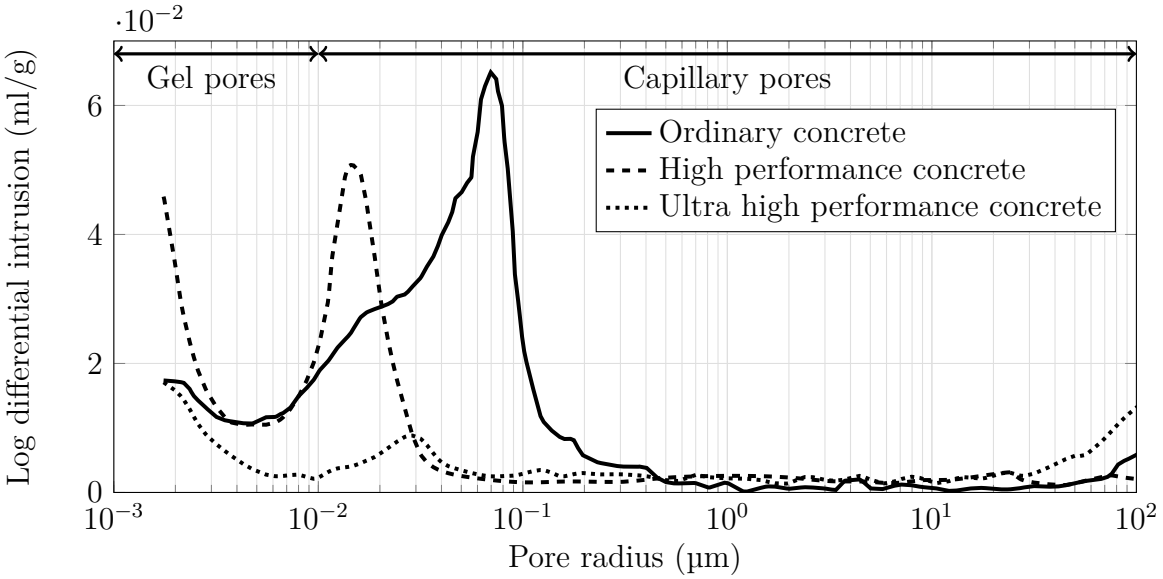

Fig. 2.9: Pore size distribution of different concretes according to Fehling et al. (2005)

2.2.1 Macroscopic physical properties

By applying the REV concept, the material's macroscopic mechanical properties can be obtained similar to the properties of the void space. However, depending on the material property, the interaction of the contributions of the micro and mesostructure are only trivial in some cases but quite complex in others. For properties like the macroscopic density of the material, it is clear that this property can easily be derived by adding up the volume-fraction weighted densities of each phase. Similarly, other properties such as the solid fraction of the material or the specific heat capacity can be calculated by the weighted contributions of each component.

Nevertheless, for many other properties, a more complex relation is obtained. For example, the tensile or compressive strength as well as Young's modulus cannot be evaluated by adding up each phase's weighted contribution. Primarily, parameters like the yield strength are governed by the "weakest link" in the composition (Scrivener et al. 2004) rather than the volumetric averages. Hence, the bond strength between the different phases and the transition zone's size is essential. This is illustrated in Fig. 2.10, where the stress-strain diagrams for the raw aggregates, the pure cement paste as well as the concrete as a combination of both components are displayed.

It is evident that the composite material, the concrete, responds differently than the average response of both contributors. This difference is explained by the mechanically weaker and more porous ITZ. The weak bonds at the ITZ's interfaces are more likely to split first and thus

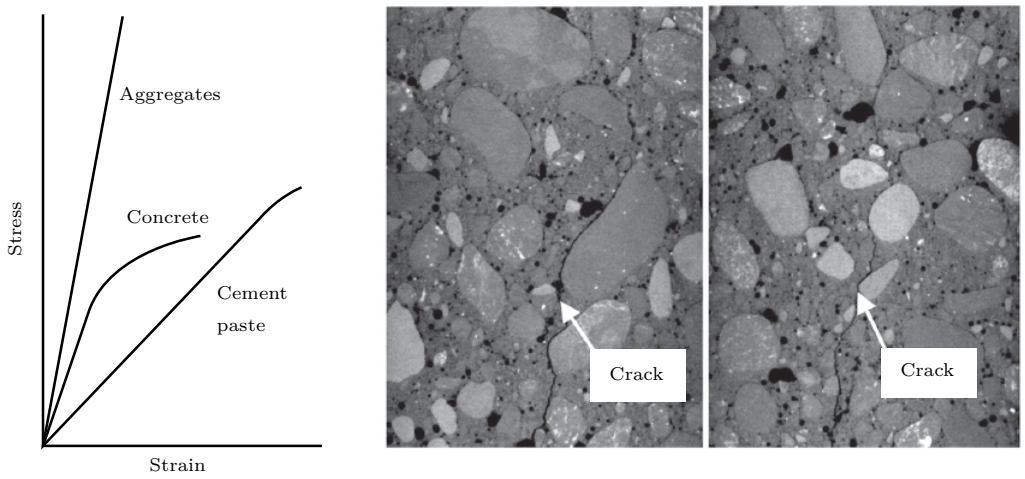

Fig. 2.10: Left: Stress-strain relation for concrete, aggregates and cement paste under compression according to Scrivener et al. (2004) Right: Crack patterns in concrete from Skarżyński et al. (2016)

are a preferential location for crack initiation and growth, as shown on the right-hand side of Fig. 2.10. Hence, the combined response cannot be predicted easily when just the responses of both base materials are known. Numerical simulations can explicitly model the splitting of the ITZ's bonds on the mesoscale (Wang et al. 2020; Eliáš et al. 2015) so that the results can be used for improving the understanding of the response and upscaling capabilities of CBMs. However, applying these models is not feasible on a structural scale as these macroscopic properties have to be known precisely and the computational effort outweighs the little benefits in most cases. Thus, the macroscopic response is more efficiently captured by macroscale experiments, while additional relations can introduce the crucial effects of the mesoscale.

The hydraulic conductivity, a measure of resistance to permeation of liquids (see Sec. 3.1), can also not be simplified by describing the sum of the contribution of each phase. Like the tensile strength, the observed hydraulic conductivity is mainly influenced by the weakest link. This means the averaged macroscopic value mainly depends on larger pores forming connected paths of low resistance through the material. Therefore the ITZ also contributes to the hydraulic conductivity by forming a preferential path for percolating water (Winslow et al. 1994). The influence of the ITZ is less decisive for permeation than for cracking, as the connectivity of the whole pore network is of even more significant impact, as shown by simulations of pore networks extracted by X-ray computed microtomography (Zhang 2017; Sun et al. 2014). Given their size and high connectivity, the amount of capillary pores is thus the most decisive factor for the resistance to flow. The pore diameter and hydraulic conductivity are related with a power equation, while the pore connectivity also increases with porosity.

Thus, it is evident that a decrease in resistance by multiple magnitudes can be observed when the total amount of capillary pores is changed, as shown in Fig. 2.11 (Powers 1958).

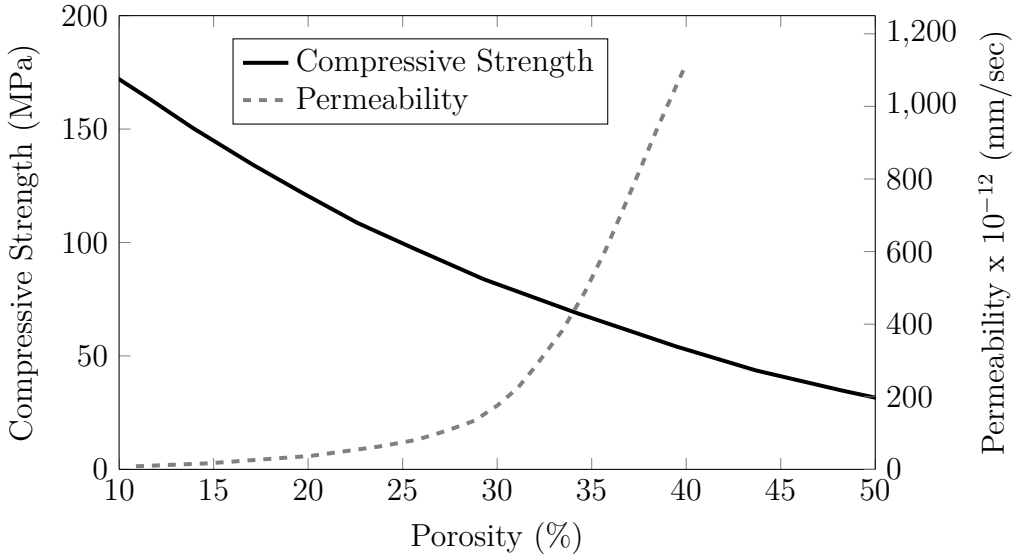

Fig. 2.11: Dependency of the macroscopic properties on the porosity adapted from Powers (1958)

2.3 Construction of cement-based structures

Cement-based structures differ not only by the cement-based material's composition but also deviate in their purpose, applied design concept, expected service loads and environmental impacts during their service life. Based on these different constraints and limitations in materials and methods, cement-based structures are built with many different construction techniques and schedules in addition to the already different material compositions. Different construction techniques and schedules influence the contractor's planning, but more importantly, they can also impact the durability of the structures. This means that the durability of the structures can be affected by human mistakes, carelessness or simple inaccuracies during the mixing and placing of the material, initiating flaws in the material. As there are other impacts such as weather, delays and factors beyond the contractor's control, it is evident that the achieved material properties on-site differ significantly from those observed in laboratory experiments (Gjørv 2011). Consequently, even perfect planning does not prevent the impacts of the selected construction method and the environment on the achieved durability of the structures. Nevertheless, profound construction planning and precise manufacturing are always crucial for achieving durable structures (Hooton et al. 2014).

Potential construction-related factors for durability are discussed in the following. The factors are divided into the manufacturing of the material, the construction steps and other durability-affecting measures (see Appendix A.3).

2.3.1 Manufacturing cement-based materials for construction

Depending on the size of the structure, availability of raw materials and construction site constraints, the cement-based materials are manufactured in multiple ways. In all cases, the cement-based material must be batched and mixed within the first step. Hence, the first potential error can occur during the batching and mixing. In particular, the mixing location influences the achieved quality during this process as on-site mixtures tend to be less reproducible than ready-mix concrete manufactured in factories. Special care must also be taken during the placing and compaction of the material. Insufficient mixing or de-mixing can yield a significantly lower material strength than a precisely produced reference (Juradin et al. 2013). After placing the concrete, increased moisture exchanged with the surrounding air and subsequent quick drying of the material can induce additional adverse effects during the hardening of the material (Santamaria et al. 2019; Idowu et al. 2017).

2.3.2 Step-wise construction

A structure can rarely be built within one step of concreting. This is caused by the size of the formwork, the required scheduling and labor, as well as the available construction methods. In addition, the release of hydration heat can hardly be achieved safely for larger monolithic structures. Consequently, discontinuities between materials of subsequent construction steps arise. The effect of different construction steps can be evident by construction joints between the different concreting steps, connections between precast parts, masonry or roller-compacted concrete joints. Most of the time, joints are even necessary to allow safe deformation while reducing potential cracking. Thus, in many cases, joints are then induced deliberately. All these aspects indicate the formation of additional discontinuities between different parts of the structure. The adverse effects of these joints, which form a plane of weakness, are evident in different experimental studies (e.g. Clark et al. 1985; Hwang et al. 2016) even though their drawback can be reduced by appropriate treatment.

2.3.3 Additional durability measures

In addition to the previously discussed factors, a multitude of non-material-related measures can be conducted to improve or change the durability of a structure. These measures include surface sealing of the material using waterproof materials or drainage systems that can release excess water from the structure. Similarly, ingress of water can also be reduced by grouting. In addition, precise monitoring of the structure, as well as quality checks, are required to achieve high durability. An overview of the potential durability measures and aspects of a gravity dam is displayed in Fig. 2.12.

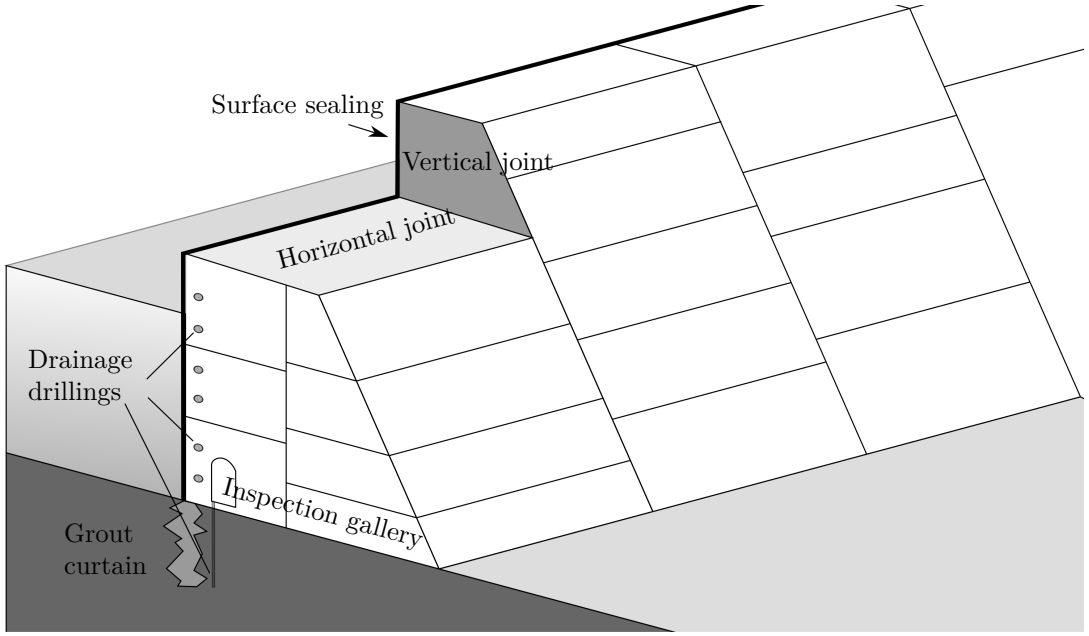

Fig. 2.12: Constructional techniques and measures that improve the durability of a gravity dam

For dams, surface sealings and groutings, drainage systems as well as monitoring systems installed in the inspection gallery are standard measures. Given the size of most structures, horizontal and vertical construction joints are often inevitable. Based on the distinct local changes, it is clear that the material can only be described by a REV approach up to a particular scale, while other sections are subjected to significantly different material properties. Hence, larger structures can never be considered homogeneous as the construction methods, schedule, and other construction effects induce variance and flaws. Therefore, the effects of the construction process should be considered when assessing the durability with increased accuracy, which is also postulated within performance-based methods (Alexander 2018).

3 Durability and transport in cement-based materials

First and foremost, the durability of any structure is governed by its technical design, as structures that are designed inappropriately concerning their expected service loads can undergo excessive cracking and large deformation already within a short period after construction. If these cracks and damages are not kept in check, they limit the structure's lifetime significantly up to causing a complete failure. As the achieved strength of the material governs the cracking and deformation of the structure, the durability is initially influenced by the selected design strength. However, these macroscopic material properties are not constant over time but undergo changes as they are affected by the continuous transformation of the microscopic composition of the material. Hence, even if a failure due to the initial mechanical loads is unlikely based on appropriate technical design, failure can still occur based on the material changes. Here the amount of accumulated strength reduction is vital until the structure is finally unable to fulfill its original function and either reaches the end of its service life or needs to be restored. Thus, in the later stages of a structure's life, the resistance to changes and thus the rate of change becomes decisive.

The change and deterioration of the material are not governed by one single process but are caused by a wide variety of factors involving numerous reactants and changes in the solid phases of the composite material. Deterioration can be induced by contact with liquids, gases and solid substances such as sulfates, acids, and nitrates, but also contact with neutral water is sufficient to cause changes. While some changes can also increase the strength of the material, generally, a weakening is observed. Deterioration processes can be grouped into two main groups by compiling their baseline similarities.

The first group can be identified as processes where parts of the materials are being removed by dissolution, exchange reactions or abrasion. As a result, these processes weaken the material by removing strength-inducing phases and components. The second group of deterioration processes is defined by processes that form new solid components based on local precipitation or reactions. Even though this formation of additional solid components can also strengthen

the material in some cases, limited available space for the new solids phases usually causes an increase in internal stress and potential (micro-) cracking, which again weakens the material.

In order to maintain the deterioration process, each mechanism must be coupled with the transport of reactive or removed material, as deterioration would otherwise be stopped once equilibrium is obtained. The process stops at equilibrium until transport processes introduce a new disequilibrium to resume deterioration. In consequence, the rate of deterioration is affected by two factors, the rate of achieving equilibrium when disequilibrium is present and the rate which introduces the disequilibrium. The interaction of deterioration processes with their transport processes is displayed in Fig. 3.1.

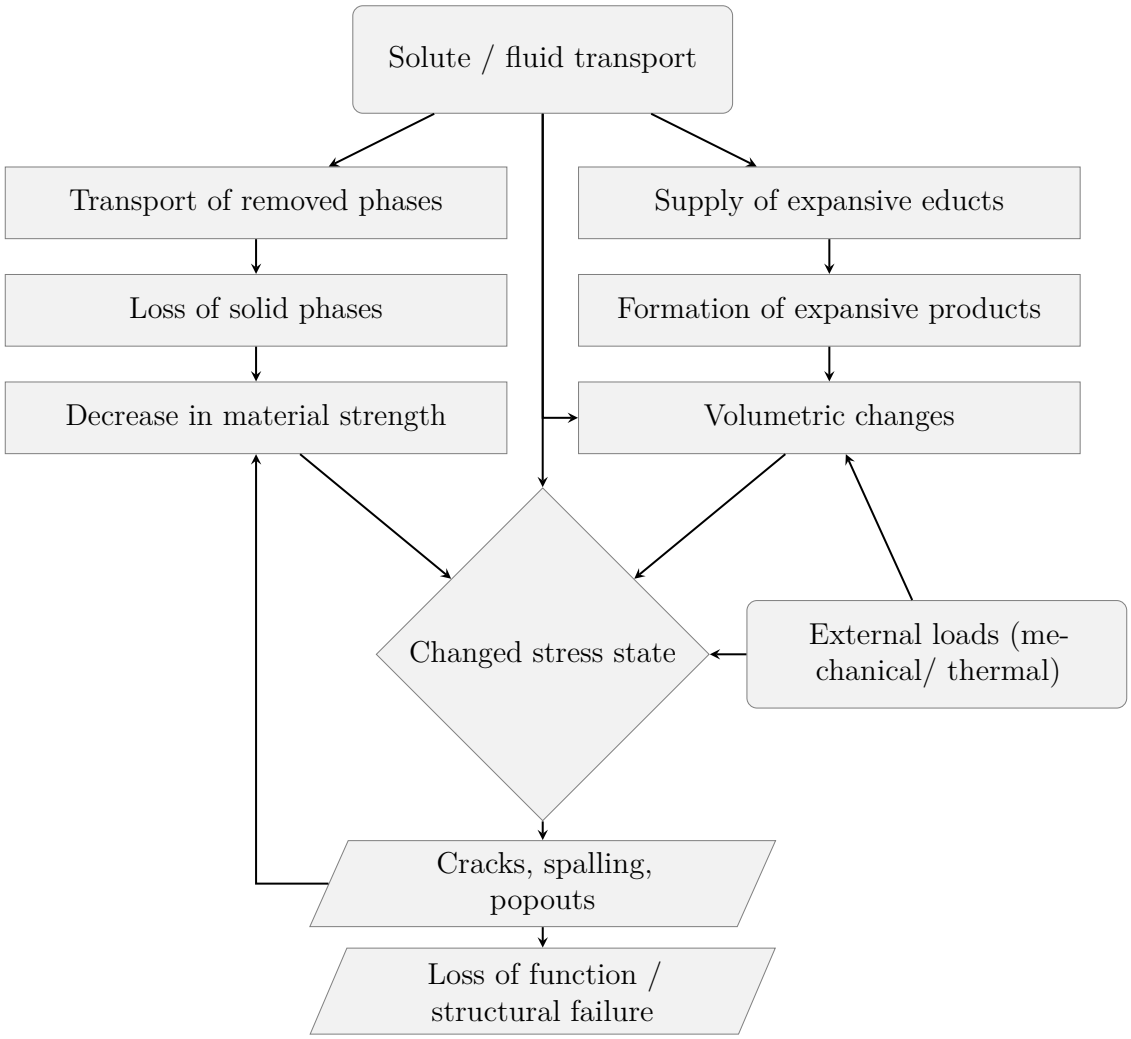

Fig. 3.1: Interaction of transport, deterioration and structural failure

The flow chart is split into the two main deterioration types. For processes where parts of the solids are removed by dissolution, exchange or abrasion, the removed material must be

transported to continue the reaction. Similarly, if new solid components are formed, the supply of educts also affects the formation rate, since the educts consumed or exchanged within a reactive zone cannot be used for further reactions.

In cases where continuous removal of solid phases occurs, the strength and stiffness of the material are directly affected. These changes affect the stress and strain in the material up to causing cracks, spalling and popouts. As flaws like local (micro) cracks further reduce the observed stiffness and strength, more cracks and flaws can be induced in the following. In cases where expansive products are formed, internal pressure is induced if the available pore space is insufficient. This increase in stress can lead to cracking or similar, which again decreases the strength of the material at the same time.

As both groups of deterioration processes require transport and exchange to continue, it is evident that transport rates are one of the critical factors for determining the service life of a structure. Transport through the porous material that supplies educts and removes products is usually the decisive process compared to achieving local equilibrium. This is caused by the rate of achieving local equilibrium, which is usually much faster than the transport rates, rendering the external transport the bottleneck for most deterioration processes. The rate for this transport and exchange depends on the amount of surface in contact with the fluids in disequilibrium (e.g. surrounding air or water), where less exchange occurs if less surface is exposed. In addition, the flow rate across the external and internal surfaces within the pore space is essential. Given the complex hardening process of the cement phase itself and the resulting complex heterogeneous void structure, the available surface area is significantly larger than for most other construction materials. Nevertheless, the flow rates in the materials are relatively low, since the resistance against the fluid flow is also low as induced by the relatively small voids of the material.

This close link between fluid flow rates and the rate of deterioration is also observed in many research studies. When the depth of carbonation, as a direct measure of deterioration induced by carbonates, is studied, the recorded depth can be related quite well to the fluid permeability of the material. Here, a decrease in flow resistance can be linked to faster carbonation rates and increased carbonation depths (Burieke et al. 1993). Similarly, the carbonation depth can be related to the measured water adsorption of the cement-based material, where a material with an increased amount of water adsorbed is also subject to increased carbonation depths (Parrott 1992; Dhir et al. 1994). Another deterioration process commonly studied under laboratory conditions is freeze-thaw resistance, where the loss in macroscopic stiffness is associated with

the amount of freeze and thaw cycles. For this deterioration process, the rate of stiffness loss can also be linked to the material's permeability (Hilsdorf 1997; Gräf et al. 1990) as well as the water adsorption (Dhir et al. 1994). Again, increased permeability or water sorption rate results in faster rates of material stiffness loss.

Based on this interrelation between resistance to flow and durability, the measurement techniques used to indicate the material's durability are mostly based on measurements of fluid flow resistance. This is evident in the RILEM state-of-the-art report (Bjegović et al. 2016), where all listed durability indicators either rely on quantifying the material's resistance to fluid flow directly or its porous properties. The latter, then again, can also be related to fluid resistance, as discussed before (see Fig. 2.11). Thus, durability indicators can be related to an estimate of service life, which is generally more time-effective than tests that directly measure a specific deterioration mechanism. The RILEM report lists three durability indicator classes given by the resistance to fluid flow based on:

- Adsorption: fluid flow governed by capillary forces
- Permeation: fluid flow induced by a pressure gradient
- Diffusion: fluid or ion movement induced by a concentration gradient

For each set of these indicators, multiple measurement techniques have been developed. With these measurements, either gas- or liquid permeation can be directly measured on extracted cored samples, as described in RILEM (1999), or on-site, as presented by Figg (1973) and Schonlin et al. (1987) to only mention a few methods.

Based on the identified importance of transport and flow processes for the deterioration of cement-based materials, any modeling approach for deterioration has to cover the details and rate of deterioration processes as well as their associated transport processes. In order to discuss the basic transport processes as well as deterioration processes, the following section is divided into two topics with the description of the transport processes, namely the transport:

- Moisture transport
- Solute transport
- Heat transport

and the deterioration processes based on the description of:

- Mechanical stress, straining and cracking
- Chemical deterioration
- Physico-mechanical deterioration

3.1 Moisture in cement-based materials

For most cement-based structures, the primary transport process is moisture flow. The flow can be either in the liquid or vapor phase, while the magnitude of each flow rate depends on the environmental conditions. As most natural waters are not pure, it is clear that the transport of potentially dissolved, dispersed or suspended substances and particles occurs simultaneously within the fluid. In addition, the thermal energy stored within the water can also induce and heat flux simultaneously.

As transport takes place within pores of different sizes, within the vapor and liquid phase while also being in contact with different solid phases, the detailed description of the transport processes on the pore scale is also not feasible when modeling an entire structure. Hence, the transport and storage principles described in the latter are based on the REV averaging principle described earlier in Sec. 2.2.1. As a result, the quantities like the liquid flow velocity $\boldsymbol{v}_l$ are to be interpreted as volume averaged quantities. This means that the liquid flow velocity $\boldsymbol{v}_l$ is averaged over the whole volume, including the non-void solid parts. In order to obtain the average fluid velocity in the void space $\boldsymbol{v}_{l,void}$, the ratio of the actual fluid-filled volume compared to the total volume θ_l has to be applied as $v_{l,void} = \boldsymbol{v}_l/\theta_l$. For the actual velocity of the fluid, the tortuosity also has to be considered.

3.1.1 Moisture sorption and storage behavior in CBMs

Two main aspects govern the moisture sorption and storage behavior of CBMs, one being the heterogeneous pore structure that covers multiple size magnitudes as described in Sec. 2.1.5 and the generally hygroscopic nature of the CBMs. Based on both aspects, CBMs store moisture within their pores based on different physical phenomena.

As water is supplied during the hydration of the cement, most of the pores and voids are initially saturated. However, all outer or internal (pore) surfaces that are exposed to (moist) air are in continuous exchange with the vapor contained in the air. This means that if an initially saturated surface of the CBM comes in contact with moist air, water molecules are

transferred between air and surface until the same amount of molecules is emitted back and forth. This state of local thermodynamic equilibrium is often reached for CBM since other moisture transport rates are usually slow in comparison to achieving this equilibrium state. Given this continuous exchange, the initially saturated paste is usually dried after hydration as air is rarely saturated with vapor.

However, not all water molecules in the material can be evaporated as chemical-bound molecules remain bonded under typical conditions. Similarly, gel pores and interlayer space are usually not removed until very low humidities are reached (Jennings 2008). The bound to the surface is governed by the van der Waals forces and, given the high surface ratios, the hydrophilic CSH phase and the low connectivity of these pores. As a result, these small voids remain saturated in most environmental conditions.

Based on the constant exchange of molecules between surface and gas, water is also adsorbed to the surfaces of dry pores. It is generally agreed that a monolayer of water already covers the whole porous surface area at relative humidities of 25 % (Pinson et al. 2015), while additional molecular layers are added when humidities increase further (Badmann et al. 1981). The configuration of the cement phase with the saturated smaller pores and adsorbed water on pore surfaces of larger pores is displayed in Fig. 3.2.

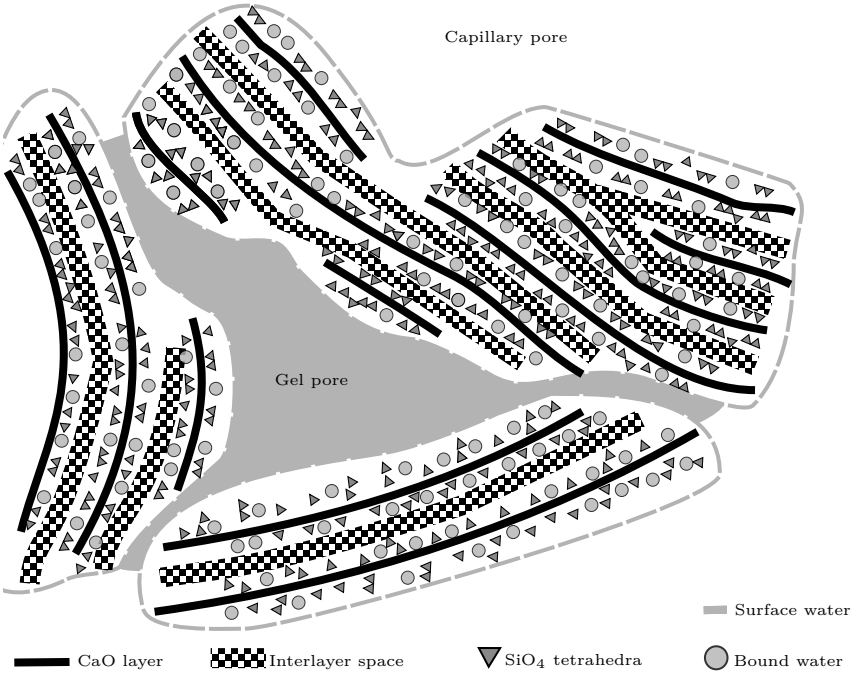

Fig. 3.2: Wetting of the CSH gel structure according to Pinson et al. (2015)

As the total amount of water adsorbed on the pore surfaces at equilibrium with air at a specific humidity depends on the surface forces as well as the available surface area, the phenomenon can be described by surface adsorption theories (e.g. Brunauer et al. 1938).

In addition to surface adsorption, the small diameter and hygroscopic surface of the pores also propels the formation of menisci in pores at the liquid-gas interface. As the formation of the menisci increases the interface area between the liquid and gaseous phase, the pressure required for changes against the curved interface is increased based on the liquid's surface tension $\sigma_{s,s-l}$. The Young-Laplace equation can describe the increase in pressure across the liquid-gas interface:

$$p_g - p_l = p_c = \frac{2\sigma_{s,s-l}}{r_{men}} \tag{3.1}$$

where r_{men} represents the radius of the sphere associated with the meniscus. This radius can be calculated by accounting for the contact angle between solid and liquid α_c and the radius of the pore r_p:

$$r_{men} = \frac{r_p}{\cos(\alpha_c)} \tag{3.2}$$

As the contact angle α_c in the above equations is a measure of the ratio of surface forces between the solid, liquid and gaseous phase, the hygroscopic or hydrophobic properties of the materials are implicitly taken into account. Therefore, the small contact angles for CBMs ($<90°$) in contact with water are a measure of the hygroscopic nature and result in relatively large pressure drops across the interface. This pressure drop is referred to as capillary pressure p_c most of the time. For the description of the above model, the adsorbed water can also be taken into account. If pore surfaces are already covered with a film of water, the contact angle reduces to zero, while the thickness of the adsorbed layers also reduces the available pore radius (Pinson et al. 2015). Capillary forces also propel the redistribution of water in partially saturated pore space. As the capillary pressure within smaller pores is higher than the pressure in larger pores, water from larger pores is transported into smaller pores. Therefore, it is usually assumed that smaller pores are being filled with moisture first, while increasingly larger pores are filled with increasing saturation.

The formation of a meniscus also changes the equilibrium vapor pressure over the curvature. For concave curvatures ($\alpha_c < 90°$) in the pores the equilibrium vapor pressure decreases to a point where vapor precipitates as liquid. This is the case when the partial pressure of the vapor

over the curvature is above the local vapor pressure. The relation between the radius of the maximum pore radius $r_{p,max}$ that is filled by condensation at a specific partial vapor pressure can be described by the Kelvin equation, a particular form of the Gibbs energy equation at constant temperature:

$$\ln(\varphi_r) = \frac{2\sigma_{s,s-l}}{r_{p,max}\rho_l R_{s,v} T} \tag{3.3}$$

where the relative humidity φ_r is the dimensionless measure of local vapor pressure p_v:

$$\varphi_r = \frac{p_v}{p_{v,sat}(T)} \tag{3.4}$$

The Kelvin equation is derived for cylindrical pores under the assumption of local thermodynamic equilibrium and is generally well supported by experiments (Fisher et al. 1981).

This phenomenon, known as capillary condensation, is decisive for the saturation of a large amount of pores within CBMs at higher humidities. This is caused by the sizeable number of pores with diameters between 1 nm-0.1 µm in CBMs, for which capillary condensation is significant at relative humidity above 40 % (Adolphs et al. 2002). For smaller pores and lower humidities, the previously described surface adsorption process prevails. However, large pores with diameters above 0.1 µm are not completely saturated by neither surface adsorption nor capillary condensation and remain to be (super) saturated by different transport processes.

Pores that are not fully saturated also contain water as vapor in the gaseous phase in addition to the liquid water. In order to quantify the moisture conditions within the concept of the REV, the total amount of water volume V_w per bulk volume V_b, denoted as volumetric water content θ or saturation, can be used to describe the moisture condition:

$$\theta = \frac{V_w}{V_b} \tag{3.5}$$

Here, it is clear that the total amount of water is the sum of the water in the liquid V_v and vapor V_v state. Therefore, the total volumetric water content θ can be expressed as the sum of volumetric liquid (V_l) as well as volumetric vapor (V_v) content:

$$\theta = \theta_l + \theta_v \tag{3.6}$$

$$\theta_l = \frac{V_l}{V_b} \text{ and } \theta_v = \frac{V_v}{V_b} \tag{3.7}$$

Similarly, a relative liquid content can be obtained if the current volumetric liquid content Θ_l is compared to the volumetric liquid content when the material is fully saturated $\theta_{l,sat}$:

$$\Theta_l = \frac{\theta_l}{\theta_{l,sat}} \tag{3.8}$$

The above quantities can be used to display the previously described sorption processes on the macroscopic scale. The combined macroscopic sorption behavior of the material can then be described with sorption isotherms, as displayed in Fig. 3.3.

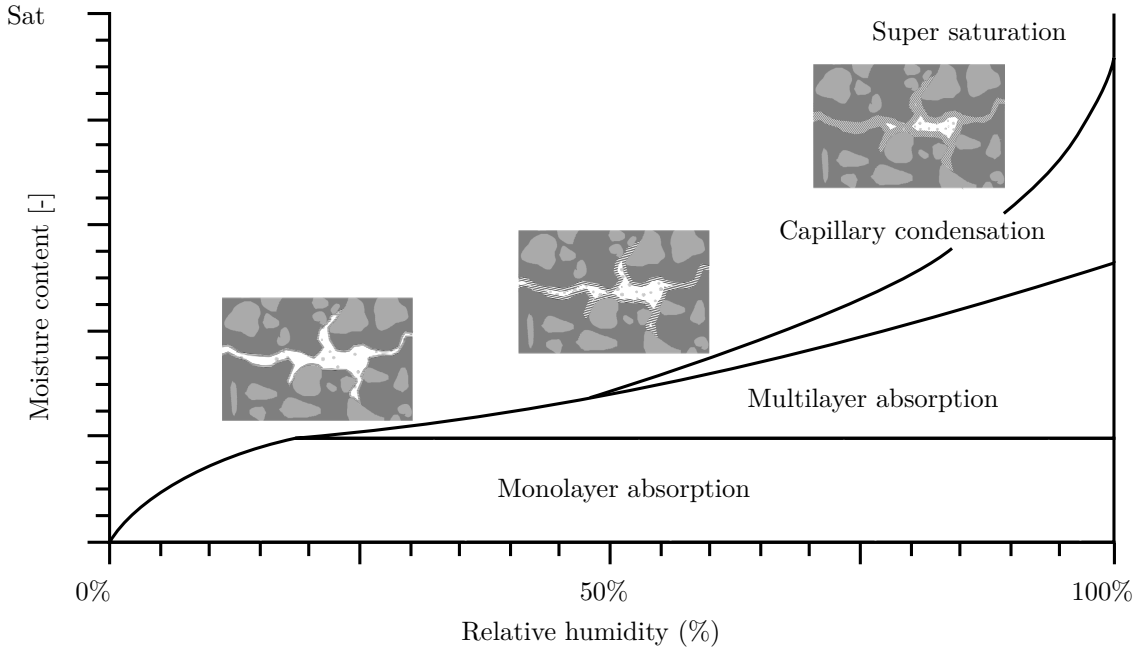

Fig. 3.3: Sorption isotherm and characteristic of cement-based materials as derived from Dubois (2014)

The sorption isotherm relates the amount of water content θ in equilibrium to a specific relative humidity. Hence, this relation describes the combined effects of each process without distinguishing between them. This means the absorption as a monolayer is included at low humidities and the increasing size of the adsorbed film contributes at higher humidities. With a further increase in relative humidity, the capillary condensation also decisively affects the material's saturation. However, macro pores remain to be filled with pressurized water. Given the close relation of the adsorption and capillary condensation to the pore size and surface area,

it is possible to estimate the sorption behavior based on the pore size distribution (Fig. 2.9) and vice versa (Gong et al. 2014; Jiang et al. 2019).

For CBMs with larger discontinuities like joints and cracks, the homogeneity of the material at the REV scale cannot always be assumed across different sections. Hence, even though these discontinuities only occupy a small amount of the total structure, they can provide hydraulic properties, like their hydraulic conductivity, which are greater by magnitudes compared to the surrounding material (Shin et al. 2017; Kim et al. 2014). As a result, cracks and joints are repeatedly observed as sources of significant leakage (Bruce et al. 1991). Therefore, it can be reasonable to distinguish further between the liquid and vapor contents in the matrix and their contents in the discontinuity ($\theta_{l,fracture}$ and $\theta_{v,fracture}$) to describe the flow processes within these voids in greater detail (Görtz et al. 2021b):

$$\theta = \theta_l + \theta_v + \theta_{l,fracture} + \theta_{v,fracture} \tag{3.9}$$

3.1.2 Moisture transport processes

Different driving potentials govern the transport of moisture within the material. They can be summarized within the following categories (Bažant et al. 2018b):

- Diffusion and effusion
- Surface diffusion
- Pressure induced flow/ capillary flow
- Advective transport

For diffusion and effusion, concentration differences of the vapor in the gas phase induce moisture transport. Nevertheless, the hygroscopic properties of CBMs induce different transport mechanisms based on the previously described sorption characteristics. As water is generally adsorbed to the surface, a difference in the amount of water adsorbed to the surface also induces a diffusive flux. For pressurized flow, the driving force is a pressure difference within the liquid phase, while advective transport is governed by the flow of a gaseous phase which transports contained vapor. These different processes are displayed in Fig.3.4 with their governing potentials.

Vapor transport processes only occur in the partially saturated zone, since no gaseous phase exists in the saturated material. In contrast, liquid transport and vapor transport take place at

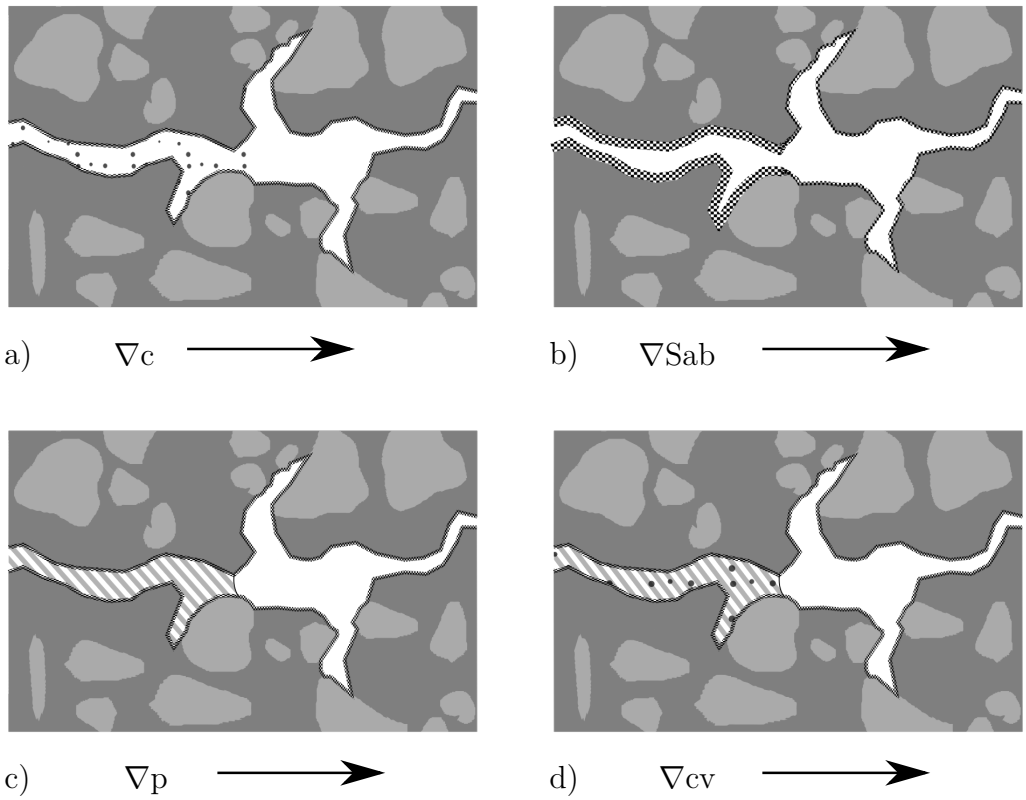

Fig. 3.4: Different moisture transport mechanisms and their driving potential a) Diffusion and effusion b) Surface diffusion c) Pressure flow d) Advective transport

the same time within partially saturated conditions. A description of these transport processes is given in the following sections.

Flow induced by concentration gradients

Concentration gradients propel diffusion within gaseous or aqueous phases. This process is generally governed by the random "Brownian" motion inherent in all atoms, ions and molecules at temperatures above zero Kelvin. Even though this motion is random in direction, concentration gradients can induce a net flux. This is caused by higher fluxes of particles from zones with higher concentrations that are not fully counteracted by the random fluxes from zones of lower concentration. As a result, a net flux is obtained.

Diffusion processes can be described very well in the gaseous phases and larger void spaces; however, in smaller pores of cement-based materials, water molecules interact not only with each other but also colloid with the pore walls. For ambient conditions at 297.15 K and 1 bar pressure, the average travel distance between collisions of molecules in the air is 65 nm

(Jennings 1988). Hence, for pores smaller than this size, water molecules collide more regularly with the pore walls than other molecules. Thus, the effective diffusion coefficient D_e in porous media is related to the pore diameter and not only to the mean free path as in the air. Diffusive processes where collisions with walls occur regularly are termed effusion or Knudsen diffusion. However, in practice, effusion and diffusion cannot be distinguished for CBMs, which is why both processes are often taken into account as combined effusion/diffusion coefficient. In addition to the pore diameter, the influence of the tortuosity τ on the diffusive flux has to be considered when computing diffusion within pore space, as the path length of the diffusive process is changed as well.

The diffusive flux density $\boldsymbol{v}_{d,v}$ of vapor in the gaseous phases is governed by the gradient in vapor pressure p_v as described by Fick's law:

$$\boldsymbol{v}_{d,v} = -D_e \nabla p_v \tag{3.10}$$

where the porous nature of the material, as well as the mobility of the molecule, is taken into account within the effective diffusion coefficient D_e. As the local vapor pressure can be linked to the capillary pressure or saturation, it can be described by using Eq. 3.15 and Eq. 3.3. This assumption is only valid at local equilibrium, which is a valid assumption in most cases for cement-based materials.

When this assumption can be applied, the gradient in vapor pressure can be derived by the gradients of the saturation. Hence, the formulation of the diffusive flux can also be formulated by applying differences in saturation. Similarly, the dependence of the liquid properties like surface tension as well as the density of the temperature can be accounted for by splitting the gradient in vapor pressure (Eq. 3.10) into the different contributions:

$$\boldsymbol{v}_{d,v,x} = -D_e \frac{\partial p_v}{\partial \boldsymbol{x}} = -D_e \frac{\partial p_v}{\partial \theta_l} \frac{\partial \theta_l}{\partial \boldsymbol{x}} - D_e \frac{\partial p_v}{\partial T} \frac{\partial T}{\partial \boldsymbol{x}} \tag{3.11}$$

Surface diffusion

Like diffusion in the gas phase, gradients within the moisture adsorbed on the pore surface can induce a net flow. Again, the "Random Walk" of liquid molecules on the surface propels the movement towards lower concentrations. Consequently, surface diffusion can also be described with Fick's law (Eq. 3.10) by adjusting the flow rate according to pore parameters. Similar to diffusion, pore parameters like tortuosity and the thickness of the adsorbed layer (Hwang et al. 1966) have to be taken into account. As the amount of the adsorbed liquid depends on

the vapor content within the gas phase, surface diffusion flows in the same direction as the vapor diffusion (at local equilibrium). Given this close relation, diffusion, effusion and surface diffusion rates are hard to distinguish during measurements.

Flow induced by pressure gradients

Pressure gradients can impose flow within the liquid or gas phase. For materials exposed to water in the liquid state (e.g. hydraulic structures), the pore space can even be completely saturated. In this case, liquid moisture transport is the prevailing transport. In particular for structures exposed to water at increased pressure (e.g. hydrostatic pressure in reservoirs or subsurface structures), substantial amounts of water pressure within the pore space are reached. However, if the surfaces of a structure are less exposed to liquid water and only subjected to moist air, as in most apartment buildings, the transport of liquids is less intense and only occurs in combination with vapor transport.

When the fluid pressure gradient is considered as the driving potential, the pore properties of the material are taken into account by a coefficient (or tensor) describing the (directional) flow resistance to gases or liquids of the pore space. The flow rate of liquids within the porous material then is described with Darcy's law (Darcy 1856):

$$\boldsymbol{v}_l = -\boldsymbol{k}_s(\nabla h_l + \boldsymbol{g}_n) \tag{3.12}$$

which relates the Darcy flow velocity $\boldsymbol{v}_l$ to the pressure head gradient by applying the saturated hydraulic conductivity of the material $\boldsymbol{k}_s$. The unit vector $\boldsymbol{g}_n$ points in the upward direction and accounts for the effect of gravity. Darcy's law was initially found empirically by experiments, but it can be shown that Darcy's law is a particular form of the Navier-Stokes equation (Whitaker 1986). Here, Darcy's law is derived if incompressible, Newtonian fluids and low flow velocities with neglectable inertia effects are considered. Hence the validity of the above assumptions has to be ensured for application. As a general measure for the ratio of inertia compared to viscous forces, the Reynolds number can be evaluated when assessing the validity of the law. Hassanizadeh et al. (1987) derived an approximate Reynolds number of 10 as a criterion for applying Darcy's law in the pore space. Given the small pore sizes and resulting low flow velocities, Darcy's law is valid in most cases within cement-based structures.

As the hydraulic conductivity in Darcy's law is obtained for a specific liquid, the liquid properties are included in this formulation. This covers properties like the specific weight γ_l and the dynamic viscosity μ_d, which also can be taken directly into account when the

permeability $\boldsymbol{K}$ formulation is used instead:

$$\boldsymbol{k_s} = \boldsymbol{K}\frac{\gamma_l}{\mu_d} \text{ with } \gamma_l = g\rho_l \tag{3.13}$$

The liquid permeability can also be used to estimate the gas resistance. However, the difference between gas and liquid molecules, the Klinkenberg effect (Klinkenberg 1941), has to be considered. The Darcy equation (Eq. 3.12) is commonly formulated for the liquid pressure head h_l. The liquid pressure head can be computed based on the liquid pressure p_l while considering the specific weight of the liquid γ:

$$h_l = \frac{p_l}{\gamma_l} \tag{3.14}$$

Capillary flow

The liquid pressure drop across the meniscus (Eq. 3.1) can also induce a pressure gradient that propels liquid flow. As the meniscus is formed across the air-liquid interface, this flow only occurs during partially saturated conditions. Given the dependence of the capillary pressure on adhesion between the liquid and solid (contact angle), this process is also fundamentally governed by surface forces. Thus, water can rise against gravity to minimize its energy state based on the material's adhesion. The rise continues until a balance between surface- and gravitational forces ($h_c g \rho_l$) is reached. This potential rise against the gravitational forces in a cylindrical pore is described by the use of Eq. 3.1 and accounting for the gravitational forces as formulated in Jurin's law:

$$h_c = \frac{2\sigma_{s,s-l}\cos(\alpha_c)}{\rho_l g r_p} \tag{3.15}$$

This phenomenon is also termed capillary suction since the water pressure drops below its outside pressure within these capillaries. Since the capillary suction also induces a gradient in liquid water pressure, the transport of water induced by capillary forces can also be modeled with Darcy's law (Eq. 3.12) when the pressure description is extended to negative values (-h_c), accounting for capillary suction.

Similar to the effect of temperature on the vapor pressure, the surface tension as well as the contact angle change with the liquid's temperature. As a result, thermal gradients can impose a capillary flow. Thus, capillary flow can be divided into flow driven by the direct hydraulic gradient and flow as a result of a thermal gradient:

$$\boldsymbol{v}_{lcap,x} = \boldsymbol{k}(h_c)\frac{\partial h_c}{\partial \boldsymbol{x}} = \boldsymbol{k}(h_c)\frac{\partial h_c}{\partial \theta_l}\frac{\partial \theta_l}{\partial \boldsymbol{x}} + \boldsymbol{k}(h_c)\frac{\partial h_c}{\partial T}\frac{\partial T}{\partial \boldsymbol{x}} \tag{3.16}$$

As moisture flow is observed towards lower saturations for both capillary and surface forces, both processes can hardly be distinguished when measuring CBMs. Hence, their effect is often described as combined matric potential (Tuller et al. 2005), which is displayed in a water retention curve.

Advective transport

If water is only part of another liquid or gaseous phase, flow also occurs by being transported within the base phase. Hence, if the gaseous phase is in motion, e.g. air is moved by a pressure gradient, the partially contained vapor is transported. This means not only diffusive transport of vapor takes place within the gas phase of a CBM, but also the flux of the air phase induces moisture transport. This process can be described for a given flux of gaseous $\boldsymbol{v}_g$ or liquid phase $\boldsymbol{v}_l$. For a gaseous phase, the advective transport of vapor can be described by using volumetric vapor content θ_v:

$$\boldsymbol{v}_{a,v} = \theta_v \boldsymbol{v}_g \tag{3.17}$$

Combined moisture transport

If the assumption of local equilibrium between vapor and liquid is valid for all pores, the combined transport of all processes can be described using only a few variables. This is possible since the flow direction of all processes follows the same gradient from higher saturation (pressure) to lower saturation. As a result, the combined moisture transport can be computed by using the relations between moisture contents and pressure. An overview of the applied formulations within research is given in Bažant et al. (2018b). Depending on the selected formulation, the moisture transport is described by using one or up to four primary variables from adsorbed water density, the air, vapor, liquid, capillary pressure or the relative humidity and hydraulic head. The number of variables depends on the amount of applied (equilibrium-) assumptions for the system.

Relative transport coefficients

For all moisture flow processes in CBMs, transport rates are derived from different transport coefficients (e.g. hydraulic conductivity $\boldsymbol{k}$ or diffusion coefficient D_e) that account for the flow resistance of the pore structure. As the transport processes take place within different pore sizes depending on the degree of saturation, they are commonly used in a formulation that can account for the degree of saturation. This means the permeability is reduced for a lower saturation, as smaller pores are filled at that state. Thus $\boldsymbol{k}$ is described as a function of

saturation $\boldsymbol{k}(\theta_l,\boldsymbol{k_s})$ based on the intrinsic hydraulic conductivity $\boldsymbol{k_s}$.

3.2 Heat in cement-based materials

Moisture transport is of primary importance for deterioration reaction as the transport of educts and products can be directly affected. However, moisture transport also depends on the temperature as described in the previous section. This is caused by the change in moisture properties with thermal changes, which can also induce moisture flow. In addition, the temperature controls the rate of chemical reactions, while straining due to thermal expansion also impacts the mechanical response. Therefore, a structure's temperature distribution must be known when describing its deterioration.

3.2.1 Heat storage in CBMs

The cementitious material's porous nature governs the material's heat storage. Since multiple phases of water, air and solid are present, the total amount of heat stored in the CMB can be calculated when the amount of heat stored within each component is considered. The total amount of heat stored in a CBM can be expressed as:

$$S_{total} = (1-\phi)C_sT + \theta_vC_vT + \theta_lC_lT + \theta_vL_v \tag{3.18}$$

with C_s, C_v and C_l being the specific volumetric heat capacities of the solid the vapor and liquid phases while L_v represents the latent heat stored in the vapor phase. The amount of heat stored in the air phase, excluding the vapor, is often neglected since the specific heat capacity of air is comparatively low. Even though the above description is purely based on the theoretical balance, this averaged response can also be observed in experiments (dos Santos 2003).

3.2.2 Heat transport on CBMs

The macroscopic transport of heat within the CBM does not differ from other solid materials, as heat is primarily transported as conductive flow induced by temperature gradients. However, advective heat transport is also possible based on the porous structure and the potential for fluid flow within the material. In addition, external faces are subjected to heat flows induced by radiation and heat exchange with the water and the air around a structure.

Conductive heat transport

Conductive heat transport is the common transport mechanism for heat. Heat transport is induced by interactions of atoms and molecules with their neighbors, much like diffusion, transferring heat from hotter to colder regions. This means that local temperature differences are the driving potential, as the energy of the molecule or atom at a higher temperature is exchanged partially with its adjacent neighbor via contact or electron transfer. The transfer increases the neighbor's energy state and finally also its temperature. Fourier's law can express the process labeled conductive heat transport:

$$\boldsymbol{q}_c = -\lambda(\theta)\nabla T \tag{3.19}$$

where the heat flux density $\boldsymbol{q}_c$ is related to the temperature gradient by using the material's thermal conductivity λ. Since thermal conduction occurs within the whole material, the macroscopic thermal conductivity depends not only on the contributions of the solid phases but also on the air and water content θ (dos Santos 2003).

Advective heat transport

Advective heat transport describes the transport of heat within a flowing fluid phase. In contrast to conductive transport, energy is not exchanged by interactions between particles, but particles at a specific energy state are transported with the flowing fluid. The advective heat flux density $\boldsymbol{q}_a$ is related to the transport of liquid and vapor when the energy state of the transported volume is considered:

$$\boldsymbol{q}_a = \boldsymbol{v}_l C_l T + \boldsymbol{v}_{a,v} C_v T + \boldsymbol{v}_{a,v} L_v \tag{3.20}$$

Convective heat transfer

Fluid phases like water or air are usually present on the exterior faces of the material or structure. As the fluids are subjected to a particular flow, advective transport occurs within the surrounding fluid phase, while at the same time, conductive transport processes occur within the fluid and at the interface between the CBM and the fluid. As both processes are occurring simultaneously, they are generally lumped together as convective heat transfer. The convective transport then described the heat flow at the macroscale without describing the fluid flow in detail. The convective heat flux density q_{cnv} is then governed by the temperature

difference of the fluid and the material's surface scaled by the heat transfer coefficient h_c:

$$q_{cnv} = h_c(\boldsymbol{v}_f)(T_{Surface} - T_{Fluid}) \tag{3.21}$$

In order to account for the effect of the fluid flow, the heat transfer coefficient is selected according to the fluid flow rate $\boldsymbol{v}_f$. As the flow field around a structure depends on its geometry, surface roughness and the flow field far from the structure, the applied relation between heat transfer coefficient and fluid velocity has to be selected carefully as many models exist for different setups (Mirsadeghi et al. 2013).

Radiation

Every solid, liquid and gas above zero kelvin also emits heat as radiation. As objects emit but also receive radiative heat from their surroundings, this does not necessarily induce a temperature change. In order to change the temperature of an object, a net flow between objects is required. In the pore space, heat exchange also occurs between pore surfaces, but given the pores' size and the small thermal gradients across each pore, the flow rates are negligibly low. Hence, the radiative heat flow is of importance on the external surfaces of the material. Especially if the temperatures of these surfaces are increased, radiative heat transport rates rise significantly. Nevertheless, the incoming radiation from the surrounding bodies has to be considered to evaluate if the emitted heat flux can cause significant cooling. These external sources do not only include terrestrial objects but also objects like the sky and the sun. The radiative heat flow at surfaces expressed by the emitted radiative heat flux density $\boldsymbol{q}_r$ is generally proportional to the quartic of the temperature of the material. In order to derive the quantity of the heat flux, the temperature potential is scaled by the Stefan-Boltzman constant k_b, and the material's surface emissivity ϵ_{sf}. Here the latter accounts for the differences in the surface in comparison to a 'black' radiator which represents the highest potential emission. The Stefan-Boltzmann's law can describe the radiative flux:

$$\boldsymbol{q}_r = \epsilon_{sf} k_b T^4 \tag{3.22}$$

In addition, not only the heat flux is scaled with the temperature, but also the emitted wavelength depends on the surface temperature, as stated in Planck's law. This is especially important for the sun, given its high temperature. Based on its temperature, the sun induces a radiative heat flow in a significantly shorter wavelength than terrestrial objects. Given this difference in wavelength, the total radiative flux on structures is often split into the shortwave flux $q_{r,s}$, originated from the sun, and the longwave components as emitted by all other objects

$q_{r,l}$. When computing the incoming radiative heat flux, the reflectiveness of the surface has to be considered, as not all of the incoming radiative flux is absorbed. This reflection of the material can be described by using the albedo coefficient α_{al}:

$$\boldsymbol{q}_{r,reflected} = \alpha_{al}\boldsymbol{q}_{r,incoming} \tag{3.23}$$

3.3 Solutes in CMBs

Solutes within the pore space govern the material's potential and rate of deterioration. Especially the transport of ions, atoms and molecules that are removed from the solid material or particles that are able to form new solids phases are of importance for aging processes. Here not only the concentration of the solutes is critical but also their transport rates and local temperatures as they govern the state of each species.

3.3.1 Solute solutions in CBMs

Similar to the moisture being adsorbed and emitted from the solid's surfaces, the compounds of a solid's chemical structure dissolve partially into ions and molecules when solvents like water are available. However, solid phases are not only dissolve, but they also precipitate and form new solids on the surface depending on the ionic composition. This two-way interaction of dissolution and precipitation of a solid phase A_aB_b composed of the ions A^{b+} and B^{a-} can be described as:

$$A_aB_{b(s)} \downarrow\rightleftharpoons aA^{b+}_{(aq)} + bB^{a-}_{(aq)} \tag{3.24}$$

Both reaction directions take place simultaneously, each with its own rate. By using the mass action principle, the reaction rate for the backward and the forward reaction can be formulated as:

$$v_{r\,AB} = \frac{\partial c_{AB}}{\partial t} = k_{r,back} \cdot {c_A}^a {c_B}^b \tag{3.25}$$

$$v_{r\,B} = \frac{\partial c_B}{\partial t} = b \cdot k_{r,for} \cdot c_{AB} \tag{3.26}$$

where the reaction rate v_r of a species can be linked to the concentration c of its educts by making use of the specific reaction rate constant k_r. It is worth noting that the reaction order is equal to the stoichiometric coefficients a, b within this formulation but generally can be determined more precisely with experiments. If sufficient time for both reactions is available, an equilibrium state is found, where forward and backward ration rates coincide. This state can be described by combining the above Eqs. 3.25-3.26 to derive the law of mass action (LMA):

$$K_c(T) = \frac{{c_A}^a {c_B}^b}{c_{AB}} \tag{3.27}$$

with K_c being the equilibrium constant for this reaction. The concentration of the solid phase c_{AB} is generally set to unity. This way, the solubility product K_s can be obtained:

$$K_s(T) = {c_A}^a \cdot {c_B}^b \tag{3.28}$$

When the solid concentration is equal to unity, the kinetic dissolution rate also becomes a constant. In this case, the dissolution rate is governed by the available surface area of the solid. Therefore, the rate constant k_r is commonly replaced by the effective rate $k_{r,e} = k_r A_r$, which accounts for the available reactive surface A_r of the solid.

Given the slow fluid velocities in most CBMs, this equilibrium between the solid phases and the solutes is often reached. In these cases, the pore solution is saturated according to the solid phases' maximum solubility, and thus the ions' transport rates govern further dissolution. The assumption of time-independent saturation of the pore solution with respect to the solid phase solubility is termed local equilibrium assumption (LEA). For this state, the solid and the solutes are in thermodynamic equilibrium as stated by the law of mass action (Eq. 3.28) at all times. This assumption only holds if the time and length scales are large enough to neglect the time needed to dissolve the required amount of solid. However, in most applications, transport rates are slow enough to apply this assumption. Nevertheless, in cases where advective transport is dominant, the assumption of a saturated pore solution might not always be valid for CBMs. In this case, the Damköhler number can be evaluated to assess the validity of the local equilibrium assumption:

$$Dq = \frac{t_t}{t_r} \tag{3.29}$$

where the characteristic time for transport t_t (diffusive or advective) is related to the characteristic reaction time $t_r{=}{k_{r,e}}^{-1}$ (MacQuarrie et al. 2005). Generally, values greater than

one indicate that the transport rates govern the dissolution rate, while values much greater than 1 (e.g. 800; Samson et al. 2007a) have to be reached to ensure the validity of the local equilibrium assumption. However, the minimum Damköhler number required for the equilibrium assumption depends on the case and assumptions, as sometimes values of 10 are discussed to be already sufficient (Grathwohl et al. 2009).

If the liquid within the pores of the CBM is in equilibrium with the solid phases, the total concentration of ions in the solvent is high enough to consider the interactions of ions with each other. While at low concentrations of solutes, the interactions between the ions are negligible, effects like Coulomb, Van-der-Waals forces, as well as hydrogen bonds reduce the mobility of ions at higher concentrations. Hence, the concentrations in Eqs. 3.25-3.28 have to be replaced by the activity a to represent the mobility for highly ionic solutions. Activity generally is described by applying an activity coefficient γ_s, which scales the molar concentration to an "effective" concentration as activity:

$$a = \gamma_s c_s \tag{3.30}$$

As the interactions between ions and molecules are complex and depend on the ions involved, multiple models for calculating activity coefficients for different mixtures have been developed. Even though the approaches are different in their details, most are based on the total ionic strength I of the solution as proposed in the Debye Hückel theory (Debye et al. 1923). The ionic strength is a measure of the total ionicity of the solution, which accounts for the molar concentration of all ionic species c_s as well as their respective ionic charge z_s:

$$I = 0.5 \sum_s {z_s}^2 c_s \tag{3.31}$$

Independent of the applied model, a general mobility reduction for each ionic species is computed with increasing ionic strength, reflecting the increased interaction.

The charge of a species affects the ionic strength of the solution, but charged species can also induce a local electric field in the CBM. This is the case if cations and anions move at different velocities and a charge imbalance is introduced. The imposed field then counteracts the different movements of both charges. These local charge differences can be computed by calculating the local charge density ρ_c by using Farrady's constant F:

$$\rho_c = F \sum_s z_s c_s \tag{3.32}$$

If the local charge densities are known, the resulting local electric potential Ψ field can be computed. Similar to all other transport processes in the CBMs, the flow path's tortuosity must be considered. By using the permittivity ϵ_m and the tortuosity of the material, the Poisson equation for the porous solid material can be assembled (Yu et al. 2015) to compute the electrical potential:

$$\nabla \cdot (\theta_l \tau \nabla \Psi) = \frac{\theta_l}{\epsilon_m} \cdot \rho_c \tag{3.33}$$

3.3.2 Solute transport

The flow of moisture changes the pore pressure and saturation while also propelling the transport of solutes. Like thermal transport, the main solute transport mechanisms are based on diffusive and advective transport processes. In addition, the local activity of the ions and the electrical fields can also induce ionic movement. The total gradients of these potentials for the solute transport are described by the gradient of the electrochemical potential of the species $\mu_{c,s}$ given as:

$$\mu_{c,s} = \mu_{c,s}^0 + R_u T \ln(\gamma_{ss} c_s) + F z_s \Psi \tag{3.34}$$

The relation between the electrochemical potential and flux density of a species $\boldsymbol{v}_s$ is given by (Bockris et al. 1970):

$$\boldsymbol{v}_s = -\frac{D_s c_s}{R_u T} \nabla \mu_{c,s} \tag{3.35}$$

This overall flow equation then can be split into the contributions of each mechanism as discussed in the following.

Diffusive transport

The diffusive part of the transport process based on the electrochemical potential (Eq. 3.34) can be split into the activity and the concentration-related transport. The diffusive (first term) and activity contribution (second term) are derived in Glasser et al. (2008):

$$\boldsymbol{v}_{d,s} = -D_s \theta_l c_s - D_s \theta_l c_s \nabla \ln(\gamma_s) \tag{3.36}$$

Similar to vapor diffusion, the diffusion coefficient for each species D_s depends on the material's pore structure. In order to incorporate these dependencies, the diffusion coefficient of each ionic species obtained in the pure fluid phase has to be scaled to an effective diffusion

coefficient by accounting for the porosity, the connectivity and the tortuosity of the pores as well as Knudsen effects when interacting with the pore walls (Sun et al. 2011, Mu et al. 2008). Like other transport properties, the material's porosity can be used to derive a reasonable initial estimate for the effective diffusion coefficient (Yang et al. 2006). The effect of temperature on the diffusion rates can be added by using the derivative according to (Glasser et al. 2008):

$$\boldsymbol{v}_{d,sT} = \frac{D_s c_s \nabla \ln(\gamma_s)}{T} \nabla \theta_l T \tag{3.37}$$

Solute migration

The contribution of the species transport governed by an electric field (migration flux density $\boldsymbol{v}_{m,s}$) can be derived by the last term of the electrochemical potential Eq. 3.34:

$$\boldsymbol{v}_{m,s} = \frac{D_s \theta_l z_s F}{R_u T} \nabla \Psi \tag{3.38}$$

As described before, this transport process termed solute migration does not only take place in cases when an external electrical field is applied but also within environments not subjected to external electrical potentials. In these cases, a local electrical potential arises (according to Eq. 3.33) based on the different transport rates of cations and anions, which induces an electrical potential by itself.

Advective transport in CBMs

In addition to the transport induced by electrochemical potential, solutes are also transported based on the flow velocity $\boldsymbol{v}_l$ of the solvent phase in the pore space. The advective flux density of a species $\boldsymbol{v}_{a,s}$ can be described as:

$$\boldsymbol{v}_{a,s} = c_s \theta_l \boldsymbol{v}_l \tag{3.39}$$

3.4 Stress and strain in cement-based materials

The occurrence of stresses and strains in CBMs might not always be considered a deterioration mechanism, but it is clear that both quantities govern the local and structural failure of cement-based structures. As stresses and strains result from the applied loads related to the strength of the material, it is clear that changes in the material's composition and structure affect the stress and strain state. When computing stress and strain state, moisture ingress into the material also acts as a load in the pore system, in addition to inducing potential

deterioration due to transport. Therefore, moisture ingress can induce elastic strains, shrinkage, swelling, creep and permanent deformations.

The material's mechanical response also induces changes to the void space, which also affects the transport rates. Based on this, the mechanical state affects the rate of deterioration, especially when cracking occurs or macroscopic voids are formed across the interface. In both cases, it is clear that the hydraulic conductivity is changed significantly (Shin et al. 2017; Rastiello et al. 2014). Hence, the interaction of the stress and strain state with the material and the transport rates needs to be evaluated to estimate and model deterioration rates. Given this interrelation, the importance of implementing the mechanical response into a holistic modeling approach is evident.

3.4.1 Stress and strain in an isotropic linear elastic solid

Strain $\boldsymbol{\epsilon}_t$ is a measure of relative geometric change of a material, while the absolute change of a solid body with respect to an initial spatial configuration (x_0, y_0, z_0) is expressed as displacement vector $\boldsymbol{u}$:

$$\boldsymbol{u} = \begin{bmatrix} x \\ y \\ z \end{bmatrix} - \begin{bmatrix} x_0 \\ y_0 \\ z_0 \end{bmatrix} \tag{3.40}$$

The observed displacement is composed of contributions of the rigid body movement and the changes in the material's geometry. Rigid body movement generally occurs without any internal stress since the body is just moved to a new location. In contrast, when the geometry is changed (strained), a body is stressed. Strain expresses the rate of change in displacement per unit and can be obtained from the derivative of the displacement for each direction:

$$\epsilon_{xx} = \frac{\partial u_x}{\partial x} \quad \text{and} \quad \epsilon_{xy} = \frac{1}{2}\left(\frac{\partial u_y}{\partial x} + \frac{\partial u_x}{\partial y}\right) \tag{3.41}$$

with ϵ_{xx} being the strain normal to the x-coordinate and ϵ_{xy} representing the shear strain, which accounts for a change in the angular relation of the body in the xy-plane.
For a three-dimensional body, the total strain tensor then can be derived for three dimensions from the displacement vector:

$$\boldsymbol{\epsilon}_t = \frac{1}{2}(\nabla \boldsymbol{u} + \nabla \boldsymbol{u}^T) \tag{3.42}$$

with the symmetric strain tensor defined as:

$$\boldsymbol{\epsilon}_t = \begin{pmatrix} \epsilon_{xx} & \epsilon_{xy} & \epsilon_{xz} \\ \epsilon_{xy} & \epsilon_{yy} & \epsilon_{yz} \\ \epsilon_{xz} & \epsilon_{yz} & \epsilon_{zz} \end{pmatrix} \tag{3.43}$$

For a homogeneous single-phase solid, this description of strain can be related to a stress $\boldsymbol{\sigma}$ for a pure elastic, continuous body subjected to small deformations by Hooke's law:

$$\boldsymbol{\sigma} = \boldsymbol{C}\boldsymbol{\epsilon}_{el} \tag{3.44}$$

with $\boldsymbol{C}$ being the fourth-order symmetric stiffness tensor, which represents the elastic properties of the material and $\boldsymbol{\sigma}$ being the symmetric stress tensor:

$$\boldsymbol{\sigma} = \begin{pmatrix} \sigma_{xx} & \sigma_{xy} & \sigma_{xz} \\ \sigma_{xy} & \sigma_{yy} & \sigma_{yz} \\ \sigma_{xz} & \sigma_{yz} & \sigma_{zz} \end{pmatrix} \tag{3.45}$$

Given the symmetric nature of $\boldsymbol{\sigma}$ and $\boldsymbol{\epsilon}_{el}$, only six independent entries exist for each tensor. Thus, they can be rewritten as six components vector (Voigt notation). For an isotropic material, Eq. 3.44 can then be expressed in Voigt notation as:

$$\begin{bmatrix} \sigma_{xx} \\ \sigma_{yy} \\ \sigma_{zz} \\ \sigma_{yz} \\ \sigma_{xz} \\ \sigma_{xy} \end{bmatrix} = \frac{E}{(1+\nu)(1-2\nu)} \begin{bmatrix} 1-\nu & \nu & \nu & 0 & 0 & 0 \\ \nu & 1-\nu & \nu & 0 & 0 & 0 \\ \nu & \nu & 1-\nu & 0 & 0 & 0 \\ 0 & 0 & 0 & \frac{1-2\nu}{2} & 0 & 0 \\ 0 & 0 & 0 & 0 & \frac{1-2\nu}{2} & 0 \\ 0 & 0 & 0 & 0 & 0 & \frac{1-2\nu}{2} \end{bmatrix} \begin{bmatrix} \epsilon_{xx} \\ \epsilon_{yy} \\ \epsilon_{zz} \\ 2\epsilon_{yz} \\ 2\epsilon_{xz} \\ 2\epsilon_{xy} \end{bmatrix} \tag{3.46}$$

which then relates stress and strain to the typical material properties like Young's modulus E and the Poisson ratio ν.The above equation can be written more conveniently for an isotropic material by making use of the Lame parameters:

$$\boldsymbol{\sigma} = 2\mu_L\boldsymbol{\epsilon}_{el} + \lambda_L \operatorname{tr}(\boldsymbol{\epsilon}_{el})\boldsymbol{I}_3 \tag{3.47}$$

where λ_L and μ_L are the first and second Lame parameter. This formulation allows for a simple description and implementation of Hook's equation. In order to relate to the displacement,

this equation can also be expressed by making use of Eq. 3.42:

$$\boldsymbol{\sigma} = \left[\mu_L \nabla \boldsymbol{u} + \mu_L (\nabla \boldsymbol{u})^T + \lambda_L \boldsymbol{I}_3 tr\,(\nabla \boldsymbol{u})\right] \tag{3.48}$$

When describing an elastic isotropic material, the mechanical properties are always uniquely determined by only two parameters. Thus, the Lame parameter can also be related to Young's modulus E, Poisson ratio ν or shear modulus G:

$$\lambda_L = \frac{\nu}{1-2\nu} \cdot \frac{1}{1+\nu} \cdot E \text{ and } \mu_L = G = \frac{1}{2} \cdot \frac{1}{1+\nu} \cdot E \tag{3.49}$$

Another mechanical parameter that is applied to describe the mechanical response is the bulk modulus. The bulk modulus K can be applied to directly calculate the volumetric change of a material when subjected to a uniform change in pressure dp:

$$K = \frac{1}{\kappa} = \frac{-V}{dV} dp = -\frac{dp}{\mathrm{tr}(\boldsymbol{\epsilon}_{el})} \tag{3.50}$$

The solid bulk modulus, therefore, is the inverse of the compressibility κ commonly applied to fluids. Quantifying volumetric change $\mathrm{tr}(\boldsymbol{\epsilon}_{el})$ is essential when the change in void space is of interest. As the bulk modulus is in the same class of elastic properties, it can also be related to any other two independent elastic properties (e.g. E and ν):

$$K = \frac{E}{3(1-2\nu)} \tag{3.51}$$

In addition to the direct mechanical loads, temperature changes also affect the strain and stress state of CBMs. When the temperature of the CBM is changed with respect to a reference temperature T_{ref}, a thermal strain $\boldsymbol{\epsilon}_{th}$ is observed in comparison to the reference configuration:

$$\boldsymbol{\epsilon}_{th} = \alpha (T - T_{ref}) \tag{3.52}$$

where the thermal expansion coefficient α of the material relates the temperature change to a change in strain.

Non-linear material response

Generally, the total strain $\boldsymbol{\epsilon}_t$ of the material that is observed on the macro scale is induced by the contributions of the multiple sources of strain. This includes the reversible elastic $\boldsymbol{\epsilon}_{el}$ and

thermal $\boldsymbol{\epsilon}_{th}$ strain components, moisture-dependant swelling and shrinkage $\boldsymbol{\epsilon}_{sw}$ and all further inelastic $\boldsymbol{\epsilon}_{inel}$ strains. The latter includes effects like (micro) cracking:

$$\boldsymbol{\epsilon}_t = \boldsymbol{\epsilon}_{el} + \boldsymbol{\epsilon}_{th} + \boldsymbol{\epsilon} + \boldsymbol{\epsilon}_{sw} + \boldsymbol{\epsilon}_c + \boldsymbol{\epsilon}_{inel} \tag{3.53}$$

As stated before, Hooke's law (e.g. Eq. 3.47) only partially reflects the solid materials' behavior, as cracking, large strains and temporal behavior need to be considered to describe a material's response in greater detail. In particular cracking is an important process that needs to be modeled when assessing structural failure. Micro-cracks are already contained in the material's structure initially after hardening. These cracks are primarily formed at the interfaces between the aggregates and the binder, partially as a result of different local material properties (Neville et al. 2010).

With an increase in stress level in the material, the pores are initially subjected to linear straining with respect to a linear increase in applied stress. However, with the continuous increase in stress, a deviation from the linear relationship is observed, resulting from irreversible changes within the material's structure. This is induced by the localization of strains which happens when strains are not equally divided over the solid volume. Consequently, only smaller, increasingly weakened parts of the material are affected when (micro-) cracks are formed. The localization of strains, therefore, impacts the local void space as well as the stiffness properties of the materials significantly.

For cement-based materials, this cracking behavior differs between tensile and compressive cracking. The common response for tensile loading of a cement-based material is displayed in Fig. 3.5. Up to around 60-70 % (Chen et al. 2013) of the peak tensile strength, the material shows a linear elastic response. When the load is increased further, new micro-cracks are formed or enlarged. These cracks are often located at the ITZ until they potentially coalesce with other micro-cracks. After reaching the peak tensile strength of the material, cracks localize further by forming more connected, larger cracks while reducing the macroscopic stiffness of the material significantly (softening). With the continuous increase in strain, the material is finally split and macro-cracks are formed. These cracks prevail even if the load is reduced again, as only the elastic strains can be recovered.

During compressive loading, cracks are also initiated at the interfaces around the aggregates (Nemati et al. 1998). Similar to the tensile failure, the material is strained linearly during

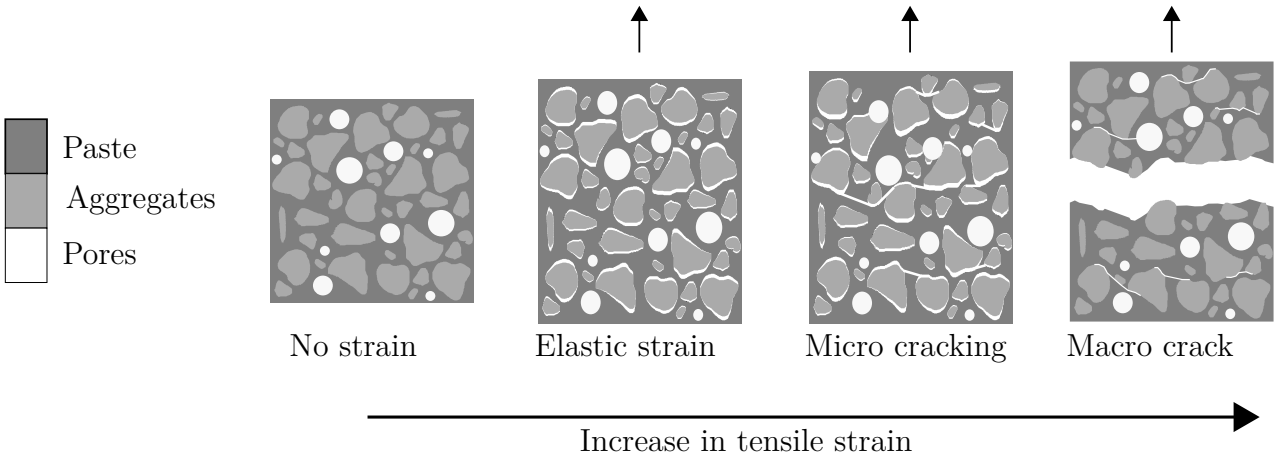

Fig. 3.5: Change of pore structure during tensile loading (Görtz et al. 2021a)

the first phase, while increasingly non-linear behavior can be observed before reaching the peak stress (Carreira et al. 1985). Again this is explained by the formation and growth of micro-cracks. After reaching the peak stress, cracks can connect with each other while forming inclined shear plane(s) (Cusson et al. 1996). As the material is sheared along these planes with continuous loading, their friction properties control the further cracking process. Given the increased roughness of this shear plane based on the heterogeneous structure, it is clear that the compressive failure of cement-based materials is less brittle than the tensile failure while also achieving peak strengths that are greater by one magnitude.

Two effects of cracks on the structural response are usually included when modeling the effects of cracks on the structural response. The stiffness reduction upon cracking by changing the stiffness tensor $\boldsymbol{C}$ and the description of irreversible deformations. For the latter, the strain $\boldsymbol{\epsilon}_t$ can be split into the irreversible (plastic) parts of the strain $\boldsymbol{\epsilon}_p$ and the reversible elastic strain component $\boldsymbol{\epsilon}_{el}$:

$$\boldsymbol{\epsilon}_t = \boldsymbol{\epsilon}_{el} + \boldsymbol{\epsilon}_p \tag{3.54}$$

A more general relation between stress and the elastic and inelastic strains in the system then can be described by also using a damage state variable κ_p, which accounts for stiffness changes as:

$$\boldsymbol{\sigma'} = \boldsymbol{C}(\kappa_p)(\boldsymbol{\epsilon}_t - \boldsymbol{\epsilon}_p) \tag{3.55}$$

The description of the initiation and growth of cracks and the material's failure depends on

many material-dependent factors. Nevertheless, the general cracking behavior can be modeled with a yield criterion f_y, which describes the beginning of non-elastic behavior and a flow rule g which controls the amount of inelastic strain occurring during this phase. In addition, hardening and softening rules are applied to model the change of the yield criterion f_y in agreement with the load history. If stiffness changes are taken into account, a relation between the stiffness tensor and the load history is also required.

As the interaction of directional stresses is generally required for a detailed description of cracking in cement-based materials, a formulation accounting for the whole three-dimensional stress state yields the highest accuracy. If this is omitted, effects like the increased cracking resistance of concrete during bi-axial loading cannot be modeled.

Not only is cracking an evident deviation from an elastic material response but also time-dependent behavior is observed for CBMs. This is evident by the temporal change in deformation at a constant stress level. Similarly, the stress induced by a constant strain on the material does not stay constant but may decrease with the continuation of straining. This decrease is commonly termed relaxation, while the first process is known as creep. Both processes originate in the same viscous deformation processes arising in the material's microstructure.

As this structure is heterogeneous and quite complex, the origin of this behavior is not easily identified. Nevertheless, it is indicated in current research that creep and relaxation (partly) are induced by the rearranging and packing of CSH particles with different structures during loading (Vandamme et al. 2009). In this regard, CBMs are believed to behave, even though otherwise quite different in many regards, similar to soils during these processes (Vandamme et al. 2013). The macroscopic response of the CBM under constant stress (creep) and constant strain (relaxation) is displayed in Fig. 3.6. For the first case, the strain increases with increasing time due to these nanoscale rearrangements. When the material is strained in the second scenario, the arising stress is reduced over time, which is induced by the same (CSH) particle rearrangement.

When creep and relaxation are modeled, time-dependent relations between stress and strain are needed. A general description for this material response is presented in (Bažant et al. 2018a):

$$\boldsymbol{\epsilon}(t) = \boldsymbol{\sigma} J(t,t') \; ; \; \boldsymbol{\epsilon} = \int_0^t J(t,t') d\boldsymbol{\sigma} \tag{3.56}$$

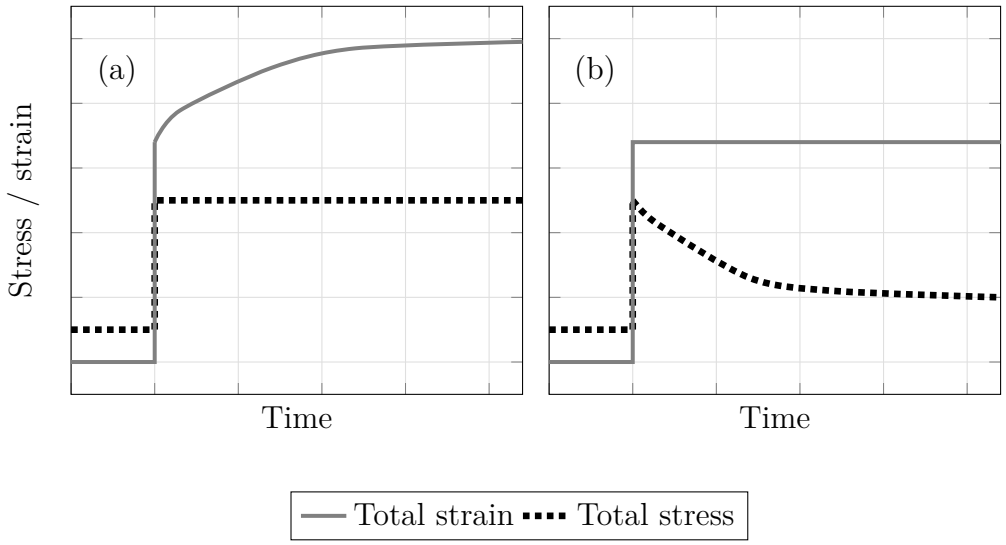

Fig. 3.6: Time dependency of the stress and strain response of solid materials as creep (a) and relaxation (b)

where a stress-strain relation similar to Hooke's law (Eq. 3.47) is described. A compliance function J is introduced to relate the stress to the strains at a certain time t concerning the time of loading t'. It is evident, that for the linear elastic case, $J(t,t')$ coincides with $1/\boldsymbol{C}$. For the general case of creep and relaxation, the compliance function is described with a representative relation of the CBM, e.g. by using a rheologic model scheme such as the complete microprestress-solidification theory described by Bažant et al. (1989) or empirical relations like the Double Power law (Bažant et al. 1976). The time-dependent solution then can be described by the principle of superposition as inherent in the integral relation in Eq. 3.56. The change in the strain as a result of relaxation and creep can also be described as a specific part of the total strain $\boldsymbol{\epsilon}_t$:

$$\boldsymbol{\epsilon}_t = \boldsymbol{\epsilon}_{el} + \boldsymbol{\epsilon}_c + ... = \boldsymbol{\epsilon}_{el} + \boldsymbol{\epsilon}_{cv} + \boldsymbol{\epsilon}_{cf} + ... \tag{3.57}$$

with $\boldsymbol{\epsilon}_c$ being the creep strain developing as a result of the changes in the material's structure. The creep strain can be distinguished even further in "fluid-like" irreversible creep strain $\boldsymbol{\epsilon}_{cf}$ and reversible but time-dependent viscoelastic strains $\boldsymbol{\epsilon}_{cv}$.

In addition, stress and strain in a porous material like CBMs are not necessarily continuous over solid, liquid and gaseous phases, the formulation of a macroscopic stress-strain relation has to be adjusted in comparison to the homogeneous single solid phase described in this section.

3.4.2 Poroelastic stress and strain in a multiphase solid

While the description in the last sections covers a single-phase solid, the complexity of the mechanical response is increased when a porous solid is filled with fluid phases, each at its stress state. In this case, the macroscopic response is governed by the interaction between the deformation of the individual solid particles, the solid skeleton formed by them and the fluids within the voids.

This is illustrated in Fig 3.7, where the local forces applied to the solid by a wetting fluid, commonly water, and a non-wetting fluid, usually air, are displayed. The stress in the displayed solid is the sum of stresses transferred by the solid itself, the pressure of the wetting and non-wetting liquid, and the contribution of the interface between them.

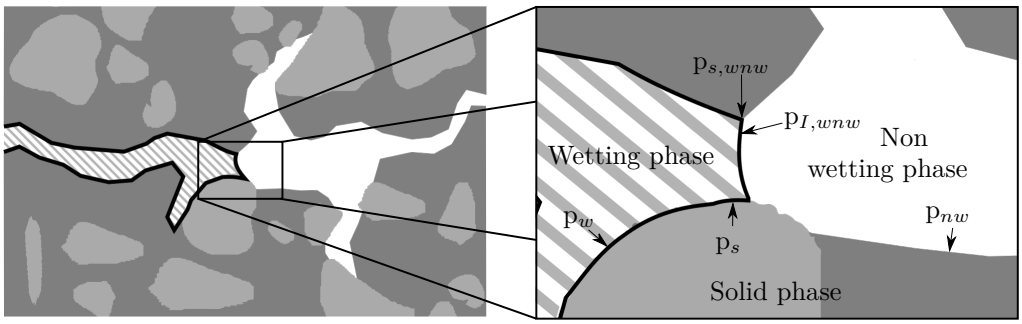

Fig. 3.7: Interaction of the wetting p_w, non-wetting p_{nw}, solid p_s and interface $p_{I,wnw}$ pressures within a porous material

The macroscopic response of the multi-phase solid as a result of these interactions is usually described by making use of coupling relations. Averaged contributions of each phase are then applied to substitute the microscopic contributions. Multiple theories with increasing complexity have been developed over the last 100 years. Almost all of them are based on the principle of effective stress, introduced by Terzaghi (Terzaghi 1925), which has been continuously extended by the works of Biot, Bishop, Skempton, Coussy, Schrefler and Gray (e.g. Biot 1956; Bishop 1959; Skempton 1961; Coussy 2010; Gray et al. 2009).

The effective stress is introduced as the part of the total stress that can be linked to the observed macroscopic deformation of the porous material. The description of the effective stress is based on a measure of an averaged solid phase pressure P_S, which by itself is a combined pressure of all fluids occupying the pore space.

The common and general form of the effective stress $\boldsymbol{\sigma'}$ reads as (Gray et al. 2009):

$$\boldsymbol{\sigma} = \boldsymbol{\sigma'} - bP_S\boldsymbol{I}_3 \tag{3.58}$$

where the Biot-Willis coefficient b describes the ratio between the bulk modulus of the solid skeleton K_T and the solid grains K_S:

$$b = 1 - \frac{K_T}{K_S} \tag{3.59}$$

The above expression is usually named after Biot and Willis, even though it has been obtained by several authors based on similar observations. The first expression for the solid pressure was expressed by Terzaghi (1925) for saturated soils as:

$$P_S = p_l \tag{3.60}$$

where the compressibility of the solid grains was assumed to be zero and hence no specific coefficient was implemented. Thus, the contribution was multiplied with unity within this work. One of the first theories for the solid phase pressure accounting for multiple fluid phases was developed by Bishop (1959):

$$P_S = \left[\chi_B p_l + (1 - \chi_B)p_g\right]\boldsymbol{I}_3 \tag{3.61}$$

which used the Bishop coefficient χ_B as a measure of the contributions of both fluid phases. Lewis et al. (1982) extended Biot's theory by accounting for the contribution of both phases by using the relative saturation Θ_l of both phases:

$$P_S = \left[\Theta_l p_l + (1 - \Theta_l)p_g\right] b\boldsymbol{I}_3 \tag{3.62}$$

All of the above theories are discussed and compared within the framework of the thermodynamic constrained averaging theory Gray et al. (2009). Here the contribution of the interfacial terms is discussed as well. However, since the interfacial terms are usually neglected in practice, a simplified, effective stress formulation is also presented by the authors:

$$\boldsymbol{\sigma} = \boldsymbol{\sigma'} - \left[\chi_{l,s} p_{l,ss} + (1 - \chi_{l,s})p_{g,ss}\right] b\boldsymbol{I}_3 \tag{3.63}$$

with $\chi_{l,s}$ being the fraction of the solid surface being subjected to the liquid and $p_{l,ss}$ and $p_{g,ss}$ being the averages of the liquid and gaseous pressure averaged over the solid.

As described before, the change of void space available for permeation and moisture ingress is an essential aspect of most deterioration processes. Within the framework of poroelastic solids, the change in porosity can also be described. The Biot-Willes coefficient b is used to link the observed macroscopic volumetric strains to the volumetric change of void space and solid grains. In addition, the effect of the thermal expansion is also implemented in this formulation:

$$\frac{d\phi}{dt} = \frac{db\mathrm{tr}(\boldsymbol{\epsilon}_{el})}{dt} + \frac{b-\phi}{K_S}\frac{dP_S}{dt} + (b-\phi)\alpha\frac{dT}{dt} \tag{3.64}$$

This formulation can also be expressed with M the Biot's modulus or the moisture storativity $s_{storage}$:

$$M = \frac{K_S}{b-\phi} = \frac{1}{s_{storage}} \tag{3.65}$$

As the poroelastic theories can incorporate the liquid pressure during capillary suction, Eqs. 3.62-3.63 can also be used to incorporate hygric shrinkage when p_l <0 accounts for capillary effects in the partially saturated material (Coussy et al. 2004; Schrefler et al. 2010).

3.5 Deterioration mechanism in CBMs

As described at the beginning of this chapter, CBMs are subjected to multiple deterioration mechanisms, which generally can be classified into chemical processes that change the solid composition and physical-mechanical processes that impose loads or remove material without changing its chemical composition. Given that the chemical deterioration can also impose mechanical loads, e.g. by crystallization pressure, there is a smooth transition between both domains. In addition, the loss and change of material due to chemical deterioration changes the strength of the material and impacts the mechanical domain as well.

3.5.1 Chemical deterioration processes

Chemical deterioration processes are governed by changes within the composition of the solid phases of the cement-based material. As the solid phases of cement-based materials are usually not in equilibrium with the fluids in their environment, changes in composition are predestined in most cases. This is readily evident by the pore water's common pH value, which is usually greater than 12.5 for ordinary types of cement (Faucon et al. 1997). The high pH values are

caused by the solubility (see Sec. 3.3.1) of cementitious phases containing OH-Ions which dissolve within the pore water. Given that common pH Values of water in the environments are usually a lot lower, the potential for dissolution and, therefore, chemical deterioration of the CBMs is evident.

The interaction and all chemical deterioration types, dissolution, reaction and formation of new solids, with the change of mechanical properties and the stress are displayed in Fig. 3.8. The primary sources for chemical deterioration can be split into reactions that remove solids or parts of the solid, including the strength-defying calcium phases or reactions that form new solid phases. As phases are removed for the former process, porosity and permeability are increased while simultaneously reducing the strength and mass. When new solids are formed for the latter process, the precipitation of expansive solids can induce stresses causing cracking or similar effects.

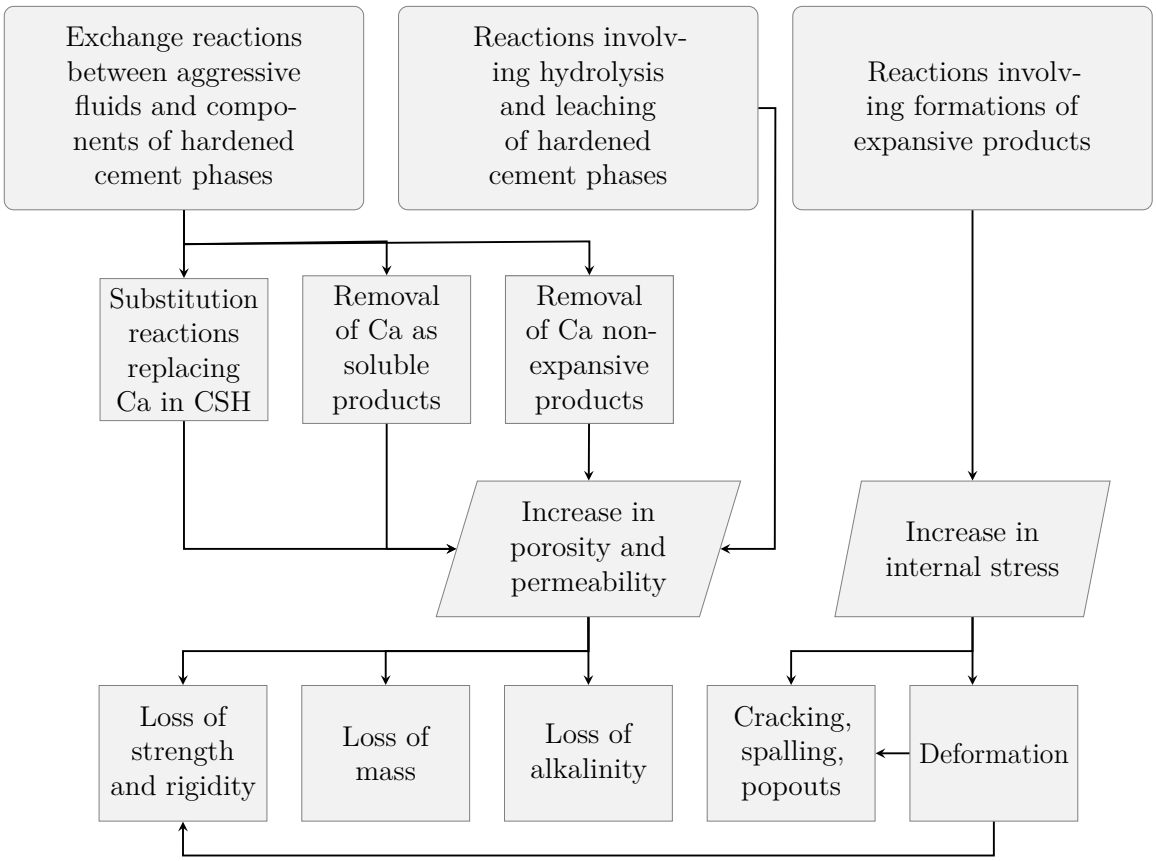

Fig. 3.8: Overview of chemical concrete deterioration processes and their interaction with the solid phases after Regourd (1981)

The rate of these processes is determined by the transport rates of the dissolved ions and phases as described before. The importance of transport rates on the chemical deterioration processes has been proven in multiple studies (Adenot 1992; Haga et al. 2005; Bourdette 1994) where the diffusion processes were found to govern the solid's overall dissolution/formation rates.

3.5.2 Chemical removal of solid phase

One of the most significant causes of deterioration of CBMs is the dissolution of solid phases. As calcium is contained in most of the dissolvable solid phases for CBMs, these dissolution processes are commonly termed calcium leaching. Given its high solubility, portlandite is usually dissolved until depletion first, before the CSH phases are dissolved (Heukamp et al. 2003). The succession of the dissolution has been more generalized by recent studies of Yang et al. (2018), which showed that the CSH phases remain stable as long as the pore solution is saturated with portlandite. Hence, only if an insufficient amount of portlandite is supplied CSH phases begin to dissolve. The dissolution of CSH phases is accompanied by a reduction in pH values and calcium content of the solution. In order to describe the course of this process, solid-equilibrium curves can be applied. These curves relate the solid's remaining Ca/Si ratios to the dissolved calcium in the pore solution, thus, displaying the course of the dissolution (Berner 1988).

The amount of solid phase that can be dissolved is increased when the material is subjected to acidic solutions. This is caused by the additional potential for the hydroxyl ions to dissolve. Multiple origins for acids in the environment of cement-based structures are possible, including abiotic sources such as industrial wastes or exhaust gases as well as biotic sources like bacteria and acidic rocks. These increased dissolution rates of CBMs in strong acids are used to accelerate leaching in lab experiments. Hence, when tests are conducted with added ammonium nitrate instead of distilled water, the rate of deterioration can be increased by 100 times (Wan et al. 2013).

Based on the hydroxide ions contained in the cement phases and their interrelation with the pH value, the leaching degree is often quantified using pH measurements. If portlandite and CSH phases are dissolved, the pH values remain within the strong alkaline regime. In contrast, if most of the calcium phases are removed, the material is considered fully leached and the pH value decreases below nine, which can be indicated with phenolphthalein (Jebli et al. 2016).

Thus, this indicator is often used to quantify the degree of leaching δ (Cheng et al. 2013):

$$\delta = \frac{V_{leached}}{V_{total}} = \frac{A_{leached}}{A_{total}} \tag{3.66}$$

by relating the material's leached volume (or area), as indicated by low pH values, to the total available volume (or area). The leaching degree of cement-based materials can then be directly linked to loss of macroscopic strength and stiffness, as shown later in Sec. 3.5.5.

3.5.3 Formation of expansive solid phase

When the chemical composition of the CBM is changed by the growth and addition of new solid phases, the macroscopic strength is not always increased. This is caused by the limited void space available for the newly formed solid phases. As the crystals of the precipitating solid form, the growth of the crystal applies pressure when its surfaces are in contact with the walls of the surrounding pores. Given the brittle nature of CBMs under tension, the applied pressure is able to form micro (or even macro) cracks and damage the structure significantly, as shown in Sellier et al. (2009), Thomas et al. (2008), and Godart et al. (2013a).

The initiation of crystallization can generally be described by a pore solution that is supersaturated regarding the solubility of a certain phase (e.g. $K_{s,current}>K_s$). The supersaturated solution then can induce the growth of an existing crystal. In order to quantify potential damage, the crystallization pressure can be evaluated. The crystallization pressure describes the mechanical pressure that is required at the crystal's surface in order to stop its growth. It can be quantified by Correns's equation (Correns 1949):

$$p_{cryst} = \frac{R_u T}{V_c} \ln\left(\frac{K_{s,current}}{K_s}\right) \tag{3.67}$$

with V_c being the molar volume of the growing crystal. As the growing crystal needs to be supplied with additional educts, a disjointing pressure between the pore and crystal is required, as a small liquid film between both phases is required to supply new reaction educts (Scherer 2004). In order to account for the spherical crystal-liquid interface in the pores, the above equation can be adjusted to account for the interfacial tension $\sigma_{s,c-l}$ by applying the Young-Laplace relation (Eq. 3.2) according to Scherer (2004):

$$\frac{2\sigma_{s,c-l}}{r_c} = \frac{R_u T}{V_c} \ln\left(\frac{K_{s,current}}{K_s}\right) \tag{3.68}$$

where r_c represents the radius of the crystal. Thus, given their larger interfacial contribution, smaller pores will be in equilibrium with a solution at a higher solubility product. This process then generally induces a shift of the crystals from smaller to larger pores. For cylindrical pores, the different curvatures induced by different sizes of pore radius and length also have to be taken into account, as the smallest radius will govern the pressure (usually the entry pore radius) (Scherer 2004).

In order to apply this relation, the above description then has to be adopted for the macroscopic response of the material by accounting for each void fraction and their interactions. Given the complexity of this task, this is not easy to achieve; thus, the pressure exerted on the solid phase is often related to changes in the pore space induced by the new solids (Bary et al. 2013; Multon et al. 2019; Qin et al. 2020), which then can be related to strains and stresses by using the framework of poromechanics (Eq. 3.64). Another simplified modeling approach is the direct application of a damage variable which reduces the material's stiffness to account for the damages induced by the microcracking (Cefis et al. 2017). Similar can be achieved if crack calculations are conducted on the microscale, which then are used to adjust the stiffness by upscaling (Iskhakov et al. 2019).

Many expansive reactions of this category exist for cement-based materials, which are induced by different mechanisms. Alkali-aggregate reactions (AAR) are initiated by the two alkali metals present in cement as sodium and potassium hydroxides. Two forms of AAR exist wherein the most cases, the alkali-silica reaction (ASR) is induced by alkali-sensitive silicon dioxide (SiO_2) in the aggregates, which produces an expansive alkali-silica gel. This reaction caused numerous repairs to structures, while the second form, the alkali-carbonate reaction (ACR), rarely causes damages (Godart et al. 2013b).

Another prominent deterioration mechanism involving expansive solid phases is sulfate attack. Sulfate attacks are divided into two different types in most literature. External sulfate attack arises from sulfates in the environment, e.g. in soils, seawater or wastewater treatment plants. Those sulfates are transported into the pore structure, where expansive products like gypsum and ettringite are formed when reacting with the hydration products of the cement (Esperanza et al. 2013). Here, the associated cation is also crucial as, e.g. magnesium ions from magnesium sulfates can crystallize with the dissolved portlandite by forming expansive brucite (Marchand et al. 2001). Delayed ettringite formation (DEF) is the second type of sulfate attack, which is caused by sulfides and sulfates contained in the material's solid phases. Here the increase of sulfates in pore solution, which can be originated by the dissolution of

aggregates, thermal changes or oxidation of sulfides, can initiate the formation of expansive ettringite without an additional supply of external sulfates.

3.5.4 Physicomechanical deterioration

Physicomechanical deterioration processes are not governed by the change of chemical composition but by mechanical loads. In this category, the most important deterioration process is freeze-thawing, where the density decrease during the phase change of water within the pore space can induce tensile stresses similar to expansive solids. Abrasive deterioration induced by shear forces on the surface of the material can be regarded as the second important deterioration mechanism.

Abrasive deterioration processes are governed by local (shear) stresses induced to the surface of the structure by tires and other mechanical loads, by flowing liquids and cavitation, as well as particles that are transported within the liquid flow. This includes the impact of sediments from beaches in coastal areas, bed-loads in rivers (Omoding et al. 2020), ice on rivers and reservoirs (Jacobsen et al. 2015) or wheels, tires or any general movement on concrete pavements (García et al. 2012). Given the relatively simple description of stress on the material's surface, the abrasive loss can be modeled by step-wise removing layers of material at the surface using an appropriate relation (García et al. 2012; Horszczaruk 2004).

Freeze-thawing is one severe type of deterioration originating from the volumetric expansion of liquid upon freezing (Hanjari et al. 2011). However, in contrast to the water on lakes and rivers, the freezing point of water in the pore space is reduced. This decrease is governed by the curvature of the ice crystal surface and its surface tension. The melting temperature T_m depression within the pore space can be derived after Penttala (1998):

$$\Delta T_m = T_m - T_{m,p} = T_m \frac{2\sigma_{s,i-l}}{E_f r_p} \tag{3.69}$$

with E_f donating the enthalpy of phase change $\sigma_{s,i-l}$ the surface tension between the ice and liquid phase and $T_{m,p}$ the melting temperature in the pore space. r_p represents the radius of the pore space but is usually reduced to account for a small liquid film between the crystal and the pore wall (Fagerlund 1973). Given the relation between the pore radius and the freezing point, it is evident that water in larger pores is frozen first.

The pressure of the ice crystals p_{ice} exerted on the solid can be obtained by the curvature of

the surface and the surface tension. The relation is given by the Gibbs-Duhem equation when second-order terms are neglected (Coussy et al. 2008; Coussy et al. 2009):

$$(1 - \frac{\rho_{ice}}{\rho_l})(p_l - p_{atm}) + p_{ice} - p_l = E_f(T_{m,p} - T_m) \tag{3.70}$$

where the first term, which includes the density of the ice ρ_{ice} and the atmospheric pressure p_{atm}, can be neglected in cases where $\rho_{ice}/\rho_l \approx 1$ or the liquid pressure is close to the atmospheric pressure. These criteria are fulfilled in many cases. The phase averaged pressure exerted on the pore walls upon freezing can then be derived by using the pores size distribution of the material (Fig. 2.9) while accounting for the amount of liquid-filled pores (Fig. 3.3). The averaged ice pressure is obtained by integrating over the liquid-filled pores that are subjected to freezing at a specific temperature by using Eq. 3.69 as described by Koniorczyk et al. (2015). This phase averaged pressures then can be applied in the framework of poroelastic solids as described in Sec. 3.4.2. In addition, the small entry pressure which governs the ice pressure during freezing results in lower freezing than melting temperature (hysteresis) within the pores. Hence, this behavior also has to be taken into account when accurately modeling freezing and thawing (Matala 1995). When the temperature of the ice is decreased even further, additional pressure arises due to the difference in thermal expansion coefficients α between the solid and ice crystals.

3.5.5 Effect of deterioration on the macroscopic material properties

The interaction between stress, transport, deterioration and macroscopic strength of the composite material is of major importance for the durability of the material and thus the structure. For the initiation and growth of (micro) cracks, the loss in strength is generally well documented in the literature, as crack propagation is usually modeled with an associated loss in strength. Hence, the crystallization pressure induced by the formation of new phases can directly be transferred to loss in material strength within the mechanical domain if cracking occurs. It is worth noting that the strength can also be increased when new phases are formed, which is very evident during the initial hydration of the material. However, the impact of the change of void structure induced by the cracks must also be represented in the material's transport and sorption properties.

In contrast to the formation of new solids, the strength loss induced by the removal of solid components must be considered by adjusting the observable material strength according to the remaining material composition. Since no direct force or pressure is induced by the removal

process, the cracking or failure can only be induced if the deterioration is accompanied by loads that act on the weakened material. Hence, the removal of material has to be represented within the macroscopic parameters. This includes the loss of stiffness (Young's modulus), tensile and compressive strength, density and porosity. These interactions are described in the following.

Loss of macroscopic strength

The most commonly applied strength properties of CBMs are Young's modulus and compressive strength, which are usually tested for characterizing the material's macroscopic properties. These properties are also closely linked to the pore structure and porosity of the material, which again is the basis for hydraulic transport processes. In addition, the tensile strength governs the cracks' growth and initiation, significantly changing the deterioration time scale. Hence, all four quantities are significant for describing deterioration itself, but their change during the process is also important. Therefore, the impact of the degree of leaching δ on these quantities is evaluated based on the data from multiple experiments published in the literature. The data set is displayed in a compiled way in Fig. 3.9.

For the strength parameters such as the compressive and tensile strength as well as Young's modulus, a linear reduction in strength with an increasing degree of leaching can be observed. This is generally expected as the leaching usually acts as a front shifting further into the material with ongoing deterioration. Hence, the tested samples are always composed of parts of the material that are fully leached (most of the strength governing solid phases removed) and parts that are still sound. The mechanical response is then composed of the contribution of both parts. According to the linear relationship in the experimental data presented in Fig. 3.9, it is evident that the combined response of both parts can be approximated by simply averaging both contributions. When the material is "fully leached", a residual value remains, representing the upper boundary for the loss of strength. According to the displayed data, this remaining strength is between 20 and 40 % of the initial value for all three parameters. However, it seems possible that linear averaging might not always be a good representation for localizing cracks.

While the strength-defying phases are dissolved and removed, the available void space increases when no new solid phases are formed. Similar to the other strength parameters, the porosity continuously increases with increasing dissolution, reflecting the material removal. However, it is evident that the removed volume is less, e.g. 20 % for cement paste than the 70 % loss in strength. This indicates that the dissolved solid phases are the phases that govern the strength, while other less soluble solid components such as the aggregates cannot achieve

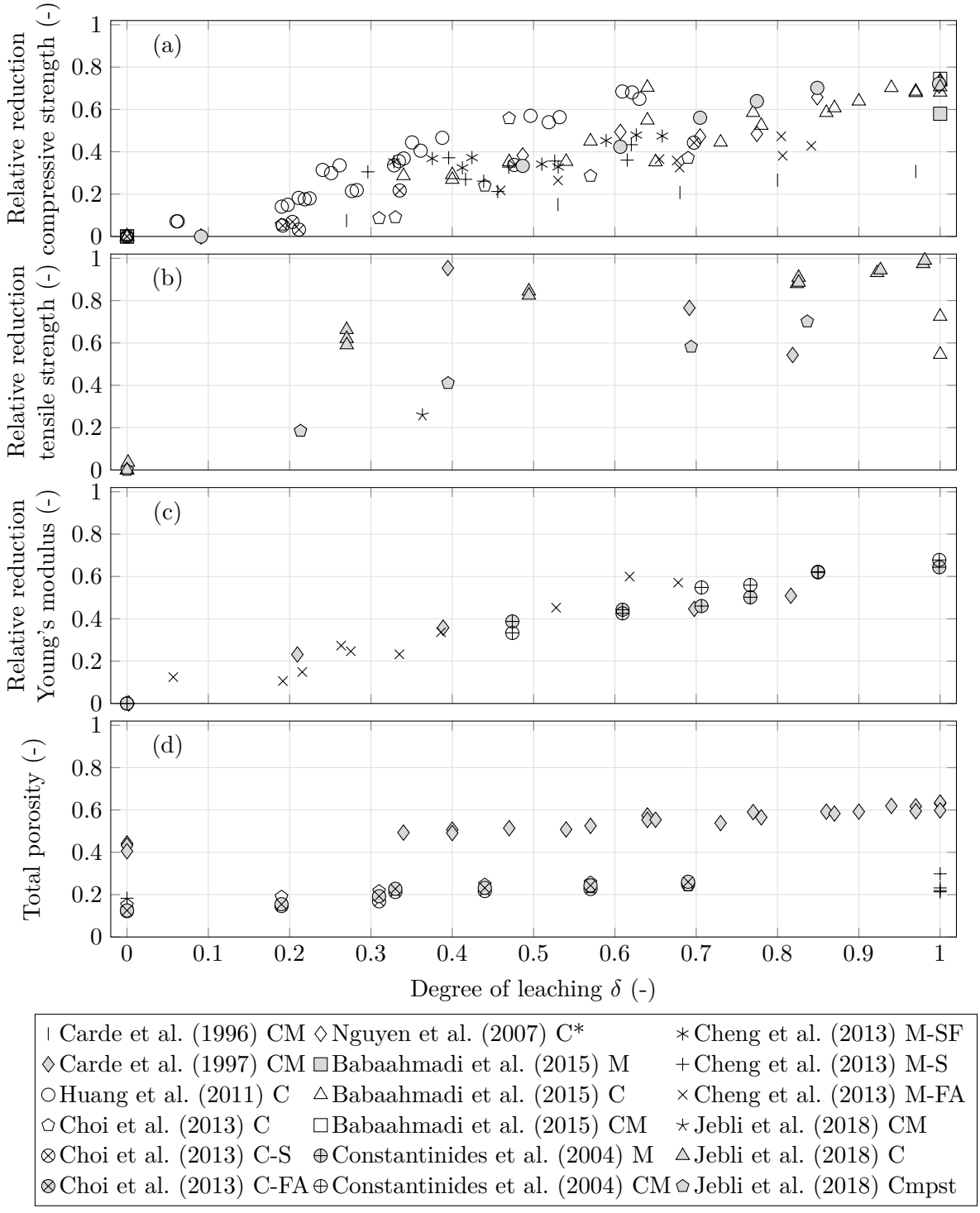

Fig. 3.9: Effect of the degree of leaching δ on the compressive strength (a), tensile strength (b), Young's modulus (c) and total porosity (d) for different cement (CM), concretes (C) and mortars (M) containing fly ash (FA), silica fume (SF) and slag (S)

the same strength by themselves. Again this loss of material and increase in porosity not only affect the average strength parameter but also allows the storage of more water in the void space while increasing the transport rates significantly (see Fig. 2.11).

Change of pore structure

The heterogeneity of the pore structure was already discussed in Sec. 2.1.5. As the pore structure cannot efficiently be computed on a structural scale, macroscopic quantities such as porosity and pore size distribution that capture essential microstructure effects are applied. While the porosity changes can be captured within the framework of poromechanics (Sec 3.4.2), the pore size distribution change also has to be taken into account. Similarly, the effect of chemical dissolution or precipitation also has to be applied to the pore size distribution.

For the latter, the change in the total porosity was already displayed in the previous section. The change of pore size distribution during leaching is well documented in literature which is displayed in Fig. 3.10. For both of the displayed studies, the amount of pores increases across all pore sizes, displaying that not only capillary pores are subject to leaching. In Ponloa et al. (2018) a shift of the pore size distribution towards larger pores is clearly visible. This shift makes it evident that not only new pores are formed, but the removal of solid phases enlarges existing pores.

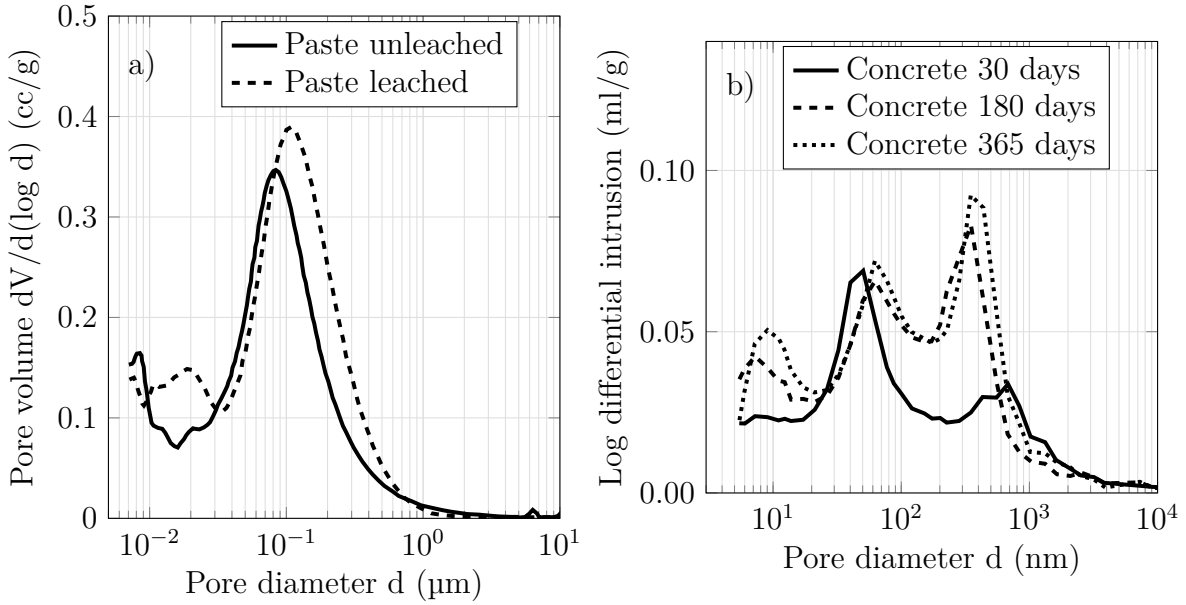

Fig. 3.10: Pore size distribution for unleached and leached cement paste (left: Ponloa et al. 2018) and leached concrete (right: Choi et al. 2013)

The effect of the mechanical strain on the pore size distribution is studied rarely (Rifai et al. 2018). In this work, the effect of the compressive strain on the pore size distribution is quantified during loading. The results are displayed in Fig. 3.11.

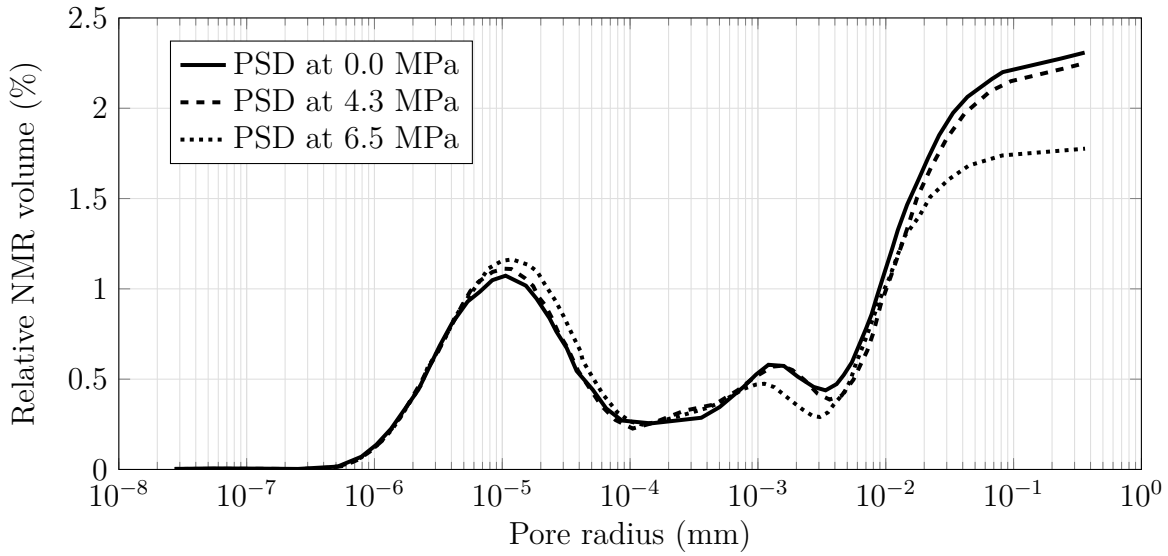

Fig. 3.11: Pore size distribution of porous concrete measured during compression at 0, 4.3 and 6.5 MPa using NMR (Rifai et al. 2018)

It is evident that larger pores are reduced due to compression. However, the amount of small voids is increased with increasing stress levels and the beginning of microcracking and the crushing of smaller pores. The combined behavior of micro cracking and compression of larger voids is also observed for the resistance to permeation during loading, as discussed in the following.

Loss of macroscopic resistance to permeation

Based on the changes in the void space, the resistance to the transport process is also changed. Especially the occurrence of (micro) cracks or general strain localization changes the flow rates significantly. As a result, these properties cannot always be accounted for with simple averaged void properties. This is illustrated in Fig. 3.12 where the hydraulic conductivity of concrete samples under compressive load is displayed.

As the sample is compressed, the void space is initially reduced, which should result in a lower hydraulic conductivity as the pore diameters decrease. However, this can only be validated in experiments for loading conditions up to approximately 30 % of the material's

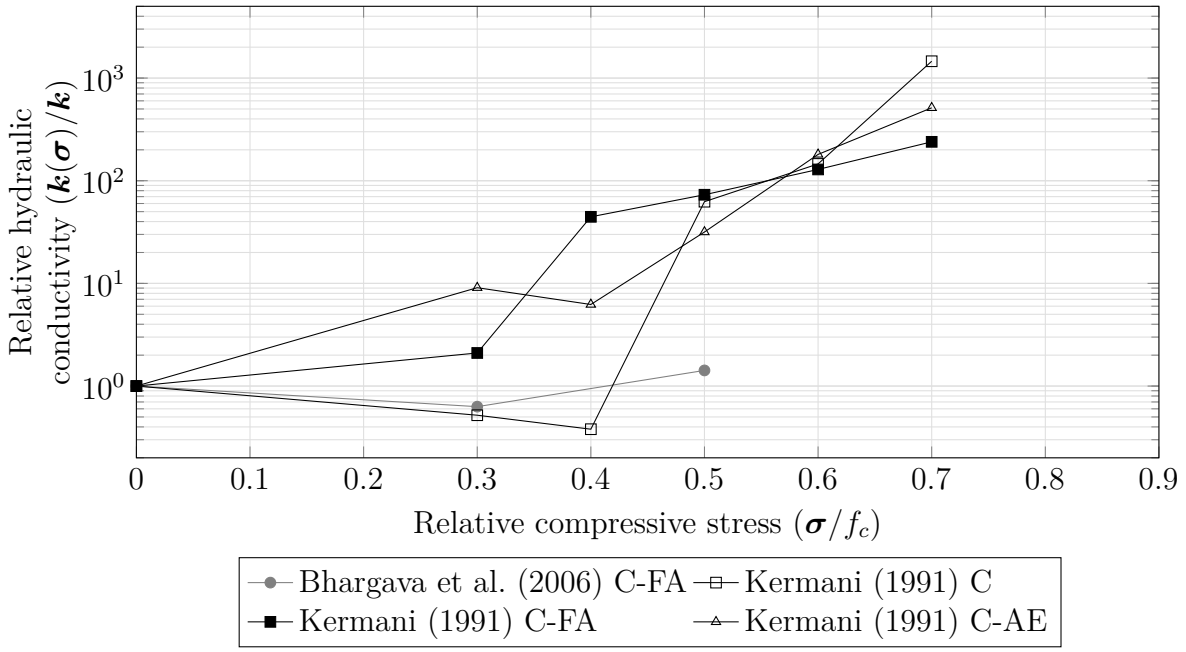

Fig. 3.12: Relation between relative change in hydraulic conductivity and the applied compressive stress

compressive strength. When strains localize and micro-cracks form, the hydraulic conductivity is increased as preferential flow paths are formed.

For concrete under tensile loading significant increase in hydraulic conductivity is observed when micro-cracking in the material occurs (Yuan et al. 2014). Once a crack in the material is formed, transport rates of the whole material section are primarily governed by these relatively large voids. In this case, the flow rates are often computed by using the Parallel Plate Model (PPM) based on the assumption of two smooth parallel plates that are separated by an aperture, w as it can be derived from the Navier-Stokes equation (Zimmerman et al. 1996):

$$\boldsymbol{k}_{s,c}(w) = \zeta_f \frac{g w^2}{12 \nu_k} \tag{3.71}$$

where $\boldsymbol{k}_{s,c}$ denotes the saturated hydraulic conductivity of the crack and ν_k the fluid kinematic viscosity. As cracks rarely form perfectly parallel smooth plates, roughness and geometrical differences can be considered by using an adjustment factor ζ_f that accounts for deviations.

For the selection of the adjustment factor, data from multiple experiments can be applied. A summary of experimental data sets is displayed in Fig. 3.13. Most of the original data is given as the hydraulic conductivity of the whole sample (averaging over the whole section).

Therefore, the data is converted to the hydraulic conductivity of the raw crack here to allow for a comparison with the PPM. However, the cracked area is crucial for this calculation. This data is rarely documented since only the crack aperture is measured. It is assumed that the crack covers the whole sample length with the measured average aperture for computing the raw crack's hydraulic conductivity.

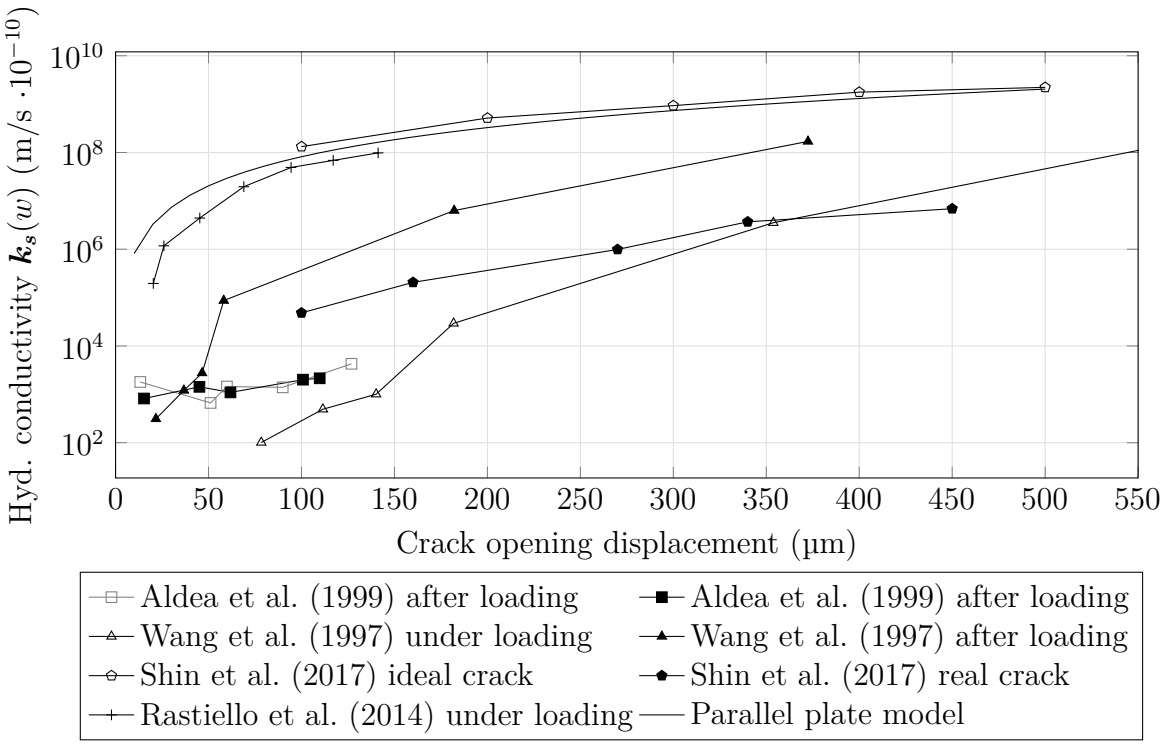

Fig. 3.13: Relation between crack opening displacement and hydraulic conductivity for cracked concretes

Given the lack of this data in the literature, a large scatter of the measured data can be observed in Fig.3.13 as most of the data sets were not documented in a way that allows a comprehensible comparison. However, the general form of the PPM (Eq. 3.71) can be verified with most of the data sets, even though more research is required to improve the assumption of the correction coefficient ζ_f.

The general applicability of the PPM for the hydraulic conductivity of concrete joints was also studied in Görtz et al. (2021c). It was found that the model also can be applied to joints by adjusting the hydraulic conductivity with similar correction coefficients as cracks. However, as the void area and aperture of the joint need to be evaluated, the heterogeneity of concrete joints still induces uncertainties.

4 Modeling approach for deterioration in cement-based structures

Based on the described processes, mechanisms, interactions and properties of the CBMs, a holistic modeling approach is developed. The approach is based on the general concept of the REV, which is enhanced by accounting for additional effects of discontinuities and void distributions. The concept is implemented into the numerical framework of foam-extend (Field Operation And Manipulation; Weller et al. 1998), which is based on the finite volume method (FVM). The framework is applied and extended to allow the modeling and interaction of the previously described deterioration mechanisms with the new approach. The framework has not only a flexible implementation of the FVM but also a multitude of temporal, gradient, divergence, Laplacian and interpolation schemes. Based on this baseline flexibility of the framework and the generalistic modeling approach, further implementation can also be easily done. The developed numerical code within the framework is labeled as STaC (Stress-Transport-and-Chemistry).

The solution approach accounts for the different transport and deterioration processes and allows the simulation of the continuous reduction of structural strength until failure. The structure and sequential procedure of the developed approach, as well as the applied solution techniques are described in the following section. At first, the detailed solutions of each individual modeling domain are described, followed by the general solution procedure accounting for the interactions of the domains. It is clear that depending on the environmental boundary conditions of a structure, different transport mechanisms are of greater importance or negligible. However, if the complexity of the deterioration process in cement-based materials is being modeled, a framework has to be able to account for the multitude of deterioration mechanisms, transport processes and their interactions.

4.1 Moisture solution procedure

The applied model description of the moisture domain is based on the conservation of moisture mass in the pore space. The local change in moisture content is modeled as the result of

all transport mechanisms described earlier. The general mass balance equation (MBE) for moisture in the CBM's pore space can be written as:

$$\frac{\partial(\rho_l\theta_l + \rho_v\theta_v)}{\partial t} = \nabla \cdot -\boldsymbol{v}_l\rho_l + \nabla \cdot -\boldsymbol{v}_v\rho_v - q_l\rho_l - q_v\rho_v \tag{4.1}$$

with $\boldsymbol{v}_l$ and $\boldsymbol{v}_v$ denoting the overall volumetric flux of the liquid and vapor phase and q_v being the volumetric source/sink term for both phases. Depending on the transport and sorption mechanisms that are being modeled, $\boldsymbol{v}_l$ and $\boldsymbol{v}_v$ have to be substituted by the contributions of advective, diffusive and capillary fluxes.

The above moisture balance can also be split into the general moisture balance for both phase states. The moisture balance for liquid water in the pore space reads as:

$$\frac{\partial\rho_l\theta_l}{\partial t} = \nabla \cdot \rho_l\boldsymbol{v}_l - \rho_l q_l = \nabla \cdot \boldsymbol{k}(h_l)(\nabla h_l + \boldsymbol{g}_n) - \rho_l q_l \tag{4.2}$$

Similarly, the mass balance for vapor can be written as:

$$\frac{\partial\rho_v\theta_v}{\partial t} = \nabla \cdot -\boldsymbol{v}_{d,v}\rho_v + \nabla \cdot -\boldsymbol{v}_{a,v}\rho_v - q_v\rho_v \tag{4.3}$$

Both of the above formulations account for exchange between liquid and gas phases (e.g. during evaporation) within the source and sink terms. In many applications, the densities of the liquid and vapor phase do not change significantly and can be taken as constant, which reduces the mass balance in Eqs 4.2-4.3 to volume balance equations. In this case, Eq. 4.2 is referred to as Richards equation (Richards 1931), representing a commonly applied form of a volume balance equation for moisture flow in porous media.

Based on the number of variables in the above equations, it is clear that additional relations have to be applied to reduce the number of unknowns. Moisture retention curves (MRC) can be applied to close the relation between matric potential and saturation if local equilibrium can be assumed. As a result, a specific maximum pore diameter can be assumed to be saturated at each saturation state. This assumption can be justified by the higher capillary potential in smaller pores which shifts the water from larger pores towards them. Moisture retention curves, therefore, inherently account for a pore size distribution and pore surfaces. Since pore size distributions can vary a lot for different materials, many general relations have been developed that can be fitted to the measured behavior in different applications (e.g. Brooks et al. 1964; Haverkamp et al. 1986; Van Genuchten 1980). The relation developed by Van Genuchten

(1980) is one of the best known and generally established relations and therefore is applied here:

$$\theta_l(h_l) = \left\{ \theta_{l,sat} + \theta_{l,sat}\kappa_l p_l \text{ for } h_l \geq 0\,;\, \theta_{lr} + \frac{\theta_{l,sat} - \theta_{l,r}}{\left[1 + (-h_l\alpha_{vg})^{n_{vg}}\right]^{1-\frac{1}{n_{vg}}}} \text{ for } h_l < 0 \right\} \tag{4.4}$$

with κ_l being the compressibility of the liquid and $\theta_{l,r}$ the residual water content of the medium. The parameters n_{vg} and α_{vg} in the equation can be fitted to measurements of the CBM, as illustrated in Fig. 4.1.

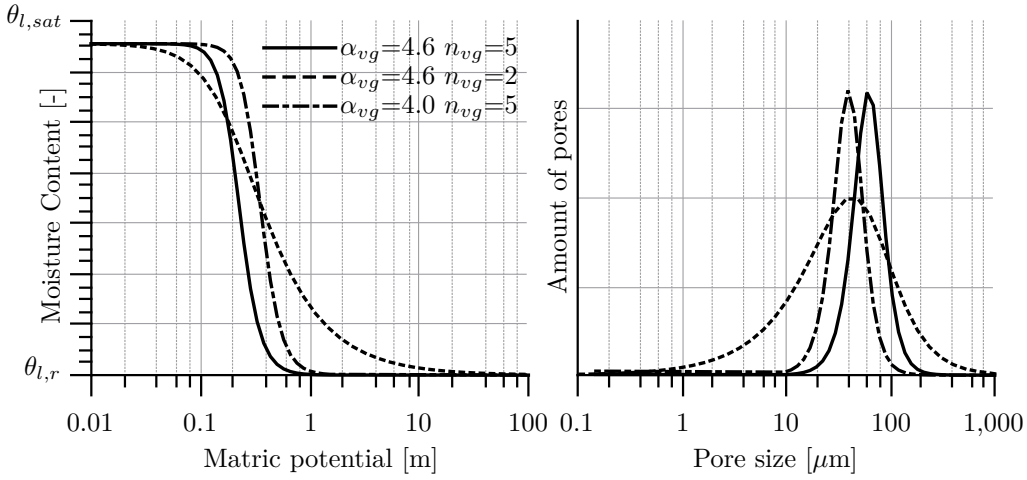

Fig. 4.1: Effect of the fitting parameter on Eq. 4.4 and the implied pore size distribution

Based on the description of moisture content and matric potential of the Van Genuchten model, Mualem's pore model (Mualem 1976) can be applied to obtain a functional relation between moisture content and relative hydraulic conductivity. The Mualem Van Genuchten (MVG) model is often applied for cementitious materials (Leech et al. 2008; Leech et al. 2006) and reads as:

$$\boldsymbol{k}(\theta_l) = \boldsymbol{k_s}\left(\frac{\theta_l - \theta_{l,r}}{\theta_{l,sat} - \theta_{l,r}}\right)^{0.5}\left\{1 - \left[1 - \left(\frac{\theta_l - \theta_{l,r}}{\theta_{l,sat} - \theta_{l,r}}\right)^{\frac{1}{1-1/n_{vg}}}\right]^{1-1/n_{vg}}\right\}^2 \tag{4.5}$$

where $\boldsymbol{k_s}$ is denoting the hydraulic conductivity of the saturated medium. With the application of a moisture retention curve, the primary solution variables can still be selected in multiple ways as the relation can be applied in all directions (e.g by using θ_l (h_l) or $h_l(\theta_l)$), as discussed for multiple applications in Bažant et al. (2018b). For structures that are not only subjected to moist air but also in direct contact with water, the use of the pressure head h_l or p_l can be advantageous as the suction can be described with negative pressure values and positive

values can be assigned for pressure. Given the application to hydraulic structures here, this formulation is applied.

The description above is applicable at REV scale of CBMs. In order to incorporate the distinct impact of discontinuities like cracks and joints, an additional formulation can be beneficial. Even though cracks and joints are of small thickness, their size and connectivity of their geometry impact the physics across a distinct plane decisively. These discontinuities can be implemented with "zero thickness" elements at interfaces between elements and within volumetric elements. Those elements can be implemented as a line, area or even as a network of line and area elements. When applied at the interfaces, the elements can be directly coupled to the surrounding volumetric elements or they are incorporated as a source term if they are located within elements (Roels et al. 2006). Internal zero thickness elements can be used to model complex discontinuities like fracture networks (Koudina et al. 1998; Paluszny et al. 2020; Li et al. 2016). While these elements generally represent the discontinuities at their actual location, the implementation of each element at a discrete location increases the effort. This is caused by the additional formulation required for these elements, the data required to track each location and the extra mesh description.

Another method for implementing joints and cracks is the application of multi-continuum approaches on the same mesh (Barenblatt et al. 1960; Warren et al. 1963). These formulations divide the continuum into multiple layers (in dual- or multi-continuum approaches) that are stacked in the same space. When applied to the modeling of joints and cracks in cement-based structures, the moisture content can then be divided into the fracture(s) and matrix content (Eq. 3.8). Hence, Eqs. 4.2-4.3 are applied to account for the flow velocities of each continuum. In order to allow an exchange between domains, the interaction between the regions has to be implemented as well. For the implementation of multi-continuum models, several equations have been developed in porous media (see Šimůnek et al. (2003) for an overview). As the efficiency of the implementation is high while the geometry of the joints and cracks is simple, the multi-continuum model is selected.

Within the category of dual continuum approaches, a dual permeability model is selected, where both regions, crack or joint (labeled as fracture f), are coupled with a homogeneous matrix (m). Both regions are then subjected to water transport. However, the hydraulic conductivity of the crack and joint region is often greater by magnitudes. The moisture exchange between both domains is implemented as displayed in Fig. 4.2.

Here the exchange flux Γ_l is induced by the difference in pressure head (e.g. difference in

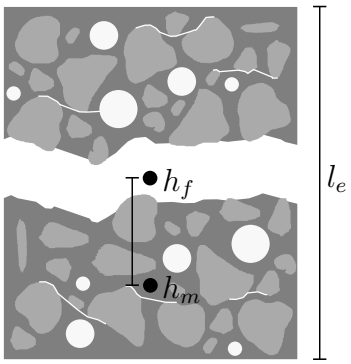

Fig. 4.2: Illustration of the applied coupling boundary between the fracture and matrix moisture pressure (Görtz et al. 2021a)

capillary suction), which is scaled with an appropriate exchange coefficient. This coefficient is selected to include the effect of the interface between the fracture and the matrix. Therefore, this coefficient is composed of the contributions of the surface area $A_{f,e}$ compared to the element volume V_e, the element length l_e, the relative saturation $\Theta_{l,f}(h_{l,f})$ and the hydraulic conductivity of the matrix perpendicular to the fracture $k_{m,f}(h_{l,f})$:

$$\Gamma_l = \zeta_s \Theta_{l,f}(h_{l,f}) \boldsymbol{k}_m(h_{l,f}) \frac{h_{l,f} - h_{l,m}}{0.25 l_e} \frac{2A_{f,e}}{V_e} = \omega_l \Theta_{l,f} \boldsymbol{k}(h_{l,f} - h_{l,m}) \tag{4.6}$$

The coefficient ζ_s can be adjusted to account for local changes in the matrix close to the interface, while ω_l is applied for a shorter description. This description allows modeling the system's behavior similar to a discrete fracture interface formulation. The baseline assumption for this transfer is a center location of the fracture or joint. This fracture then transfers the moisture to the matrix above and below the fracture at the same rate. Hence, the above description then represents two inner boundaries for the matrix domain with a hydraulic gradient of $\nabla h_{l,m} = (h_{l,f} - h_{l,m})/(0.25 l_e)$ at each interface.

For a dual continuum, the Richards equation with an exchange coefficient is derived as:

$$\frac{\partial \theta_{l,m}(h_{l,m})}{\partial t} = \nabla \cdot \boldsymbol{k}_m(h_{l,m}) \left[\nabla(h_{l,m}) + \boldsymbol{g}_n\right] - q_{l,m} + \Gamma_l \tag{4.7}$$

$$\frac{\partial \theta_{l,f}(h_{l,f})}{\partial t} = \nabla \cdot \boldsymbol{k}_f(h_{l,f}) \left[\nabla(h_{l,f}) + \boldsymbol{g}_n\right] - q_{l,f} - \Gamma_l \tag{4.8}$$

Two sets of material properties are also required for a dual permeability approach. Since properties like porosity and hydraulic conductivity are usually evaluated for the raw concrete or raw crack/joint, the values must be adjusted to the element size of the dual continuum solution. This is done by using a volumetric weighted average when assigning the hydraulic conductivity $\boldsymbol{k_s}_{,element}$ of an element at the location of a discontinuity:

$$\boldsymbol{k_s}_{,element} = \frac{V_{e,joint}}{V_e} \cdot \boldsymbol{k_s}_{,joint} + \frac{V_e - V_{e,joint}}{V_e} \cdot \boldsymbol{k_s}_{,matrix} \tag{4.9}$$

with $V_{e,joint} = w \cdot l$ denoting the volume of the actual joint and V_e being the total volume of the element. The above averaging can directly be applied to a single permeability solution. In contrast, for a dual permeability solution, the contributions of the $V_{e,joint}$ or the matrix have to be set to zero when calculating the parameter for the matrix or joint domain, respectively. Similarly, the available porosity (e.g. moisture content at saturation) of an element at the location of the joint can be determined

$$\theta_{l,element} = \frac{V_{e,joint}}{V_e} \cdot \theta_{l,joint} + \frac{V_e - V_{e,joint}}{V_e} \cdot \theta_{l,matrix} \tag{4.10}$$

here the raw porosity of the joint void area $\theta_{l,joint}$ is taken as unity.

4.1.1 Solution algorithm

Both non-linear equations Eqs. 4.7-4.8 are solved iteratively by using a modified Picard Iteration Scheme (Celia et al. 1990) until sufficient convergence is reached. This mixed scheme improves the convergence rate of the solution significantly since changes in saturation from the previous iteration i are added as artificial source terms, dampening potential oscillations between iterations. The applied scheme is given by:

$$\begin{aligned} C_m\left({h_l}^{k+1,i}\right)\frac{{h_l}^{k+1,i+1} - {h_l}^{k+1,i}}{\Delta t} = \\ \nabla \cdot \boldsymbol{k}({h_l})^{k+1,i})\left[\nabla {h_l}^{k+1,i+1} + \boldsymbol{g}_n\right] - \frac{{\theta_l}^{k+1,i} - {\theta_l}^{n}}{\Delta t} + {q_l}^{k+1} \pm {\Gamma_l}^{k+1,i} \end{aligned} \tag{4.11}$$

where $C_m\left(h_l\right)$ is the specific moisture capacity $= \frac{\partial \theta_l}{\partial h_l}$, k the time level and i the iteration level. The exchange term is updated after each iteration step, and the sign convention is used in agreement with Eq. 4.7 and Eq. 4.8. For the solution of the system, it can be beneficial to relax the solution between iterations with user-selected factors.

The convergence of the iterations can be evaluated with different convergence criteria within the developed framework. Hence, the relative or absolute change between two iterations (Eqs. 4.12-4.13) can be evaluated as less than specific convergence values ($\delta_{c,a}$ and $\delta_{c,r}$). If both criteria are combined, a mixed convergence criterion (Eqs. 4.14) is derived (Cooley 1983):

$$\left| {h_l}^{k+1,i+1} - {h_l}^{k+1,i} \right| \leq \delta_{c,a} \tag{4.12}$$

$$\left| {h_l}^{k+1,i+1} - {h_l}^{k+1,i} \right| \leq \delta_{c,r} \cdot \left| {h_l}^{k+1,i+1} \right| \tag{4.13}$$

$$\left| {h_l}^{k+1,i+1} - {h_l}^{k+1,i} \right| \leq \delta_{c,r} \cdot \left| {h_l}^{k+1,i+1} \right| + \delta_{c,a} \tag{4.14}$$

The above criteria are formulated for the convergence of the pressure head h_l. As the formulation is implemented flexibly, the convergence of any other field-type variables like saturation, hydraulic conductivity or exchange flux can also be evaluated similarly. This is done by exchanging the pressure head field with the respective field. Thus, similar criteria are also applied in the other solution domains.

For the temporal discretization, the initial timestep size is user-specified. Nevertheless, within the whole framework, the timestep is dynamically adjusted depending on the rates of archiving convergence. Hence, if convergence is reached within a few iterations, the timestep is slowly increased. In scenarios when the solution does not converge at all, the timestep is reduced. In order to detect the divergence of a solution, the convergence criterion (e.g. Eq. 4.14) is also evaluated. If the convergence value δ increases over multiple iterations, the current iterations are stopped and the timestep is reduced.

4.1.2 Solution sequence

The sequence of the described solution process is displayed in Fig. 4.3. Given the interaction with the other solution domains, it is evident that the results of these domains have to be incorporated into the moisture solution as well. This is displayed in Fig. 4.3, where the results of the mechanical solution domain are used to update the moisture properties iteratively within the same timestep. This can include properties such as hydraulic conductivities, which are updated according to cracking and straining. As the interaction with chemical and thermal

processes is usually weaker, updating them after finishing the whole timestep can be sufficient. This is reasonable when long time scales are needed for the mechanical and moisture solution to affect the chemical domain. For the thermal solution, the commonly low flow rates of moisture in CBMs generally induce a low impact of flow rates on the thermal solution. For stronger interactions such as the mechanical solution, the coupling to the moisture domain can be applied by updating the permeability and porosity according to the computed elastic and plastic strains (Sec. 4.6) within the solution sequence.

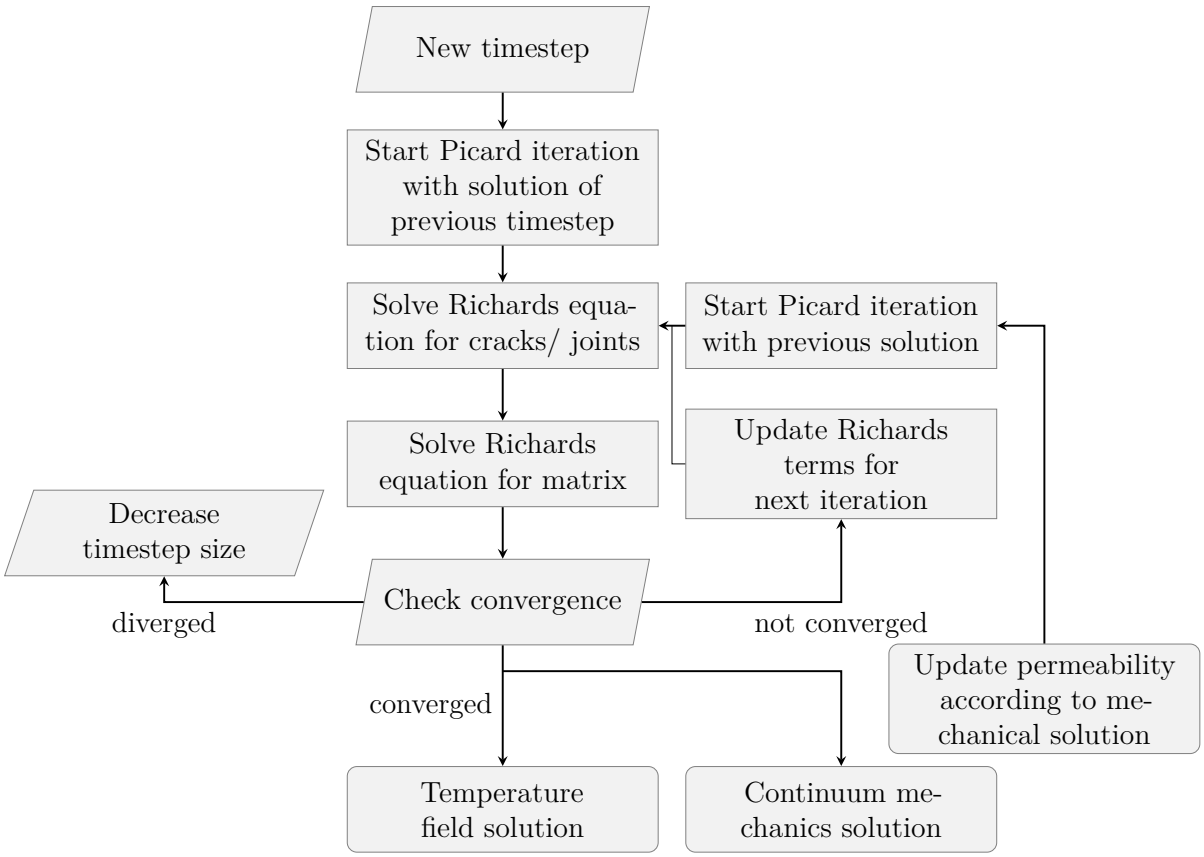

Fig. 4.3: Solution sequence of the double-permeability moisture solution

After adjusting all material properties to the current field values of all solution variables, the first iteration of the Picard scheme is conducted with the solution of the previous iteration. This procedure can increase convergence rates on small timesteps. All moisture domains are then solved segregated and checked for convergence by comparison to the previous iteration before the next iteration is conducted. If divergence is detected after multiple iterations, the timestep is reduced and repeated. Upon convergence, the solution is terminated and the moisture flow rates and computed saturations are passed to the temperature and mechanical

solution domain. If the hydraulic conductivity or porosity is changed within the mechanical or chemical solution, the moisture flow solution can be recalculated with the updated parameters.

4.2 Thermal energy balance

The radiative heat fluxes primarily affect the external faces of the structure, as discussed before. Therefore, the thermal energy balance in the structure can be described by the contribution of the advective heat transport in fluids and the conduction of heat. Both heat fluxes then can be related to the thermal energy state of the material based on the combined contributions to the thermal storage of the material. Based on the divergence of conductive and advective heat fluxes, the change in the stored thermal energy can be obtained:

$$\frac{\partial T}{\partial t} S_{total} = \nabla \cdot (-\boldsymbol{q}_a - \boldsymbol{q}_c) \tag{4.15}$$

$$\frac{\partial (1-\phi) C_s T + \theta_v C_v T + \theta_l C_l T}{\partial t} + L_v \frac{\partial \theta_v}{\partial t} = \nabla \cdot [-\boldsymbol{v}_l C_l T - \boldsymbol{v}_{a,v} C_v T - \boldsymbol{v}_{a,v} L_v + \lambda(\theta_l) \nabla T] \tag{4.16}$$

where the thermal conductivity is updated according to the moisture content of the material. The latent heat released by phase changes is also linked to the changes in moisture content. The above equation does not incorporate additional sources of vapor and liquid. If sources or sinks are present, those further thermal energy fluxes must be added.

When the heat flux across the exterior faces is computed, the external heat sources have to be considered. When the convective and advective contributions of the surrounding liquid are lumped together as convective transfer, the processes can be distinguished between the incoming and internal flow at the boundary. As the incoming heat flux at the boundary has to be accompanied by the same conductive-advective heat flux within the structure, the description of the material boundary reads as:

$$\boldsymbol{q}_c + \boldsymbol{q}_a = (q_{cnv} + q_{r,s} + q_{r,l}) \boldsymbol{n}_{\boldsymbol{bc}} \tag{4.17}$$

4.2.1 Solution algorithm

The moisture-dependent properties are updated at the beginning of the thermal solution process. If neither the thermal conductivity nor the thermal storage nor the boundary conditions are implemented as temperature-dependent, the equation system stays linear and can be

solved within one solution step. Nevertheless, if temperature-dependent material properties or boundary conditions (e.g. Eq. 4.17) are applied, the equation system must be solved multiple times while updating the temperature-dependent properties until convergence is reached. Similar to the moisture domain, convergence can be checked with relative, absolute or mixed convergence criteria (Eq. 4.12-4.14), which can be applied to the temperature field or any other relevant field variable in the thermal solution.

4.2.2 Solution sequence

The sequence of this thermal transport solution algorithm is displayed in Fig 4.4.

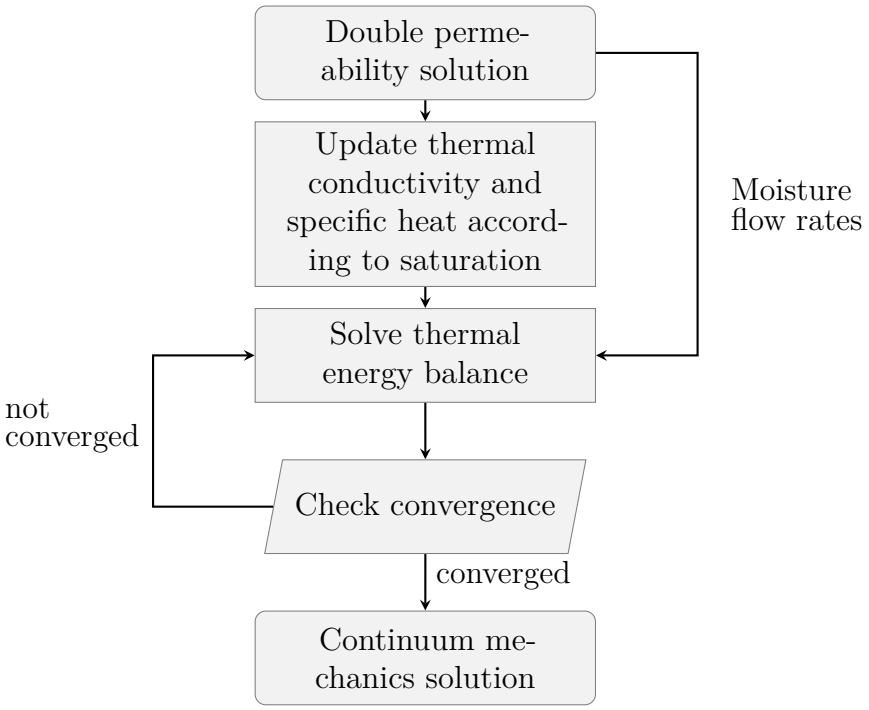

Fig. 4.4: Sequence of the thermal transport solution process

The thermal transport equation is solved based on the previously calculated moisture flow rates. In all other cases, the moisture solution is also applied to update the material's thermal conductivity and specific heat. For non-linear solutions, the balance equation is then iterated until little change in the solution is obtained. The computed moisture and temperature distributions are then passed to the continuum mechanics domain.

4.3 Mechanics solution

In the mechanical domain, the momentum balance in the CBM is used to link the arising internal stresses caused by temperature changes, moisture conditions, crystallization pressure and pore pressure to straining and cracking while accounting for the changes in material strength. Also, dynamic loads (e.g. earthquakes) can be considered if inertia and damping effects are taken into account. For computing the structural displacement, the momentum balance is assembled by assessing the momentum of the material and the sum of the divergence in total stresses while accounting for the applied body forces. If the effective stress definition is applied, the momentum balance for the CBM reads:

$$\frac{\partial^2 \rho_t \boldsymbol{u}}{\partial t^2} = \nabla \boldsymbol{\sigma} + \mathbf{b_f} \tag{4.18}$$

where ρ_t is the total density of the composite material and $\mathbf{b_f}$ the body force vector, including effects like gravity. Above equations can be expanded by applying the relations in Eq. 3.44 and Eq. 3.63 to derive:

$$\frac{\partial^2 \rho_t \boldsymbol{u}}{\partial t^2} = \nabla \left\{ \boldsymbol{C}(\boldsymbol{\epsilon}_{el}) - \left[\chi_{l,s} p_{l,ss} + (1 - \chi_{l,s}) p_{g,ss} \right] b \boldsymbol{I}_3 \right\} + \mathbf{b_f} \tag{4.19}$$

For CBMs, the fraction of the solid interface in contact with the liquid $\chi_{l,s}(\Theta_l)$ generally depends on the relative saturation as discussed in Gawin et al. (2006). Within the study the ratio of $b\chi_{l,s}/\Theta_l$ varies between 0.2 and 1.0 when changing the saturation for concretes. Based on the general uncertainty within the computed capillary pressure induced by the pore size distributions, the interface fractions $\chi_{l,s}$ are often replaced with the relative liquid saturation Θ_l in different applications (e.g. Lewis et al. 1998) without increasing the overall uncertainty significantly.

In order to solve the assembled momentum balance (Eq. 4.19), the equation is reformulated with displacement as the primary variable. This is achieved by substituting Eqs. 3.53 and 3.48 into the momentum balance:

$$\begin{aligned} \frac{\partial^2 \rho_t \boldsymbol{u}}{\partial t^2} &= \nabla \left[\mu_L \nabla \boldsymbol{u} + \mu_L (\nabla \boldsymbol{u})^T + \lambda_L \boldsymbol{I}_3 tr\left(\nabla \boldsymbol{u}\right) \right] \\ -\nabla \boldsymbol{C}(\boldsymbol{\epsilon}_{th} + \boldsymbol{\epsilon}_{sw} + \boldsymbol{\epsilon}_c + \boldsymbol{\epsilon}_{inel}) &- \nabla \left[\chi_{l,s} p_{l,ss} + (1 - \chi_{l,s}) p_{g,ss} \right] b \boldsymbol{I}_3 + \mathbf{b_f} \end{aligned} \tag{4.20}$$

This formulation only incorporates the effects of a single continuum moisture model. If the

dual permeability approach is used, the surface fraction $\chi_{l,s}$ has to be expanded to the amount of surface in contact with the liquid and gas coupled to the corresponding pressures in the fracture as well.

4.3.1 Cracking and viscoelasticity

While the hydraulic properties like the saturation and the pressure of liquid and gas phase as well as the thermal properties are updated according to the solution obtained in the respective domains, properties like the plastic strains or similar stress dependant properties like viscoelastic strains need to be updated within the solution iterations of the mechanical domain.

For the application of the verification, a simple elastic-plastic model is applied (Eq. 3.54). However, any yield criterion or formulation can be implemented within the combined framework. For the application, the yield criterion is selected as the Rankine criterion. The plastic strain increments are calculated in the principal stress space $\boldsymbol{\sigma}_{123}$ by solving the eigenvalue problem for the stress tensor $\boldsymbol{\sigma}_{xyz}$. The matrix of eigenvectors $\mathbf{M_{ev}}$ is then used to transform the stresses into the principal stress space:

$$\boldsymbol{\sigma}_{123} = \mathbf{M_{ev}} \boldsymbol{\sigma}_{xyz} \mathbf{M_{ev}}^{T} \tag{4.21}$$

The initiation of the plastic deformation is described with the yield criterion, which is evaluated against the effective plastic stress $\boldsymbol{\text{œ}}'_{\mathbf{p}}$ as proposed by Coussy (2010). In many cases, this plastic stress can be simplified by using the general effective stress $\boldsymbol{\sigma}'$. The damage state and its change with increasing stress is controlled by the internal variable κ_p, which is described with an exponential softening law based on the principle stress σ'_{p1}:

$$f_y(\sigma'_{p1},\kappa_p) = \sigma'_{p1} - f_t e^{-(\kappa_p)/\kappa_{u1})} \tag{4.22}$$

The variable $\kappa_{u1} = G_F/(f_t l)$ is applied to shorten the above description while accounting for the material properties fracture energy G_F and tensile strength f_t. Mesh size effects are counteracted by implementing the equivalent length parameter l according to the crack band theory after Bažant et al. (1983). This parameter generally depends on the element type, element shape, direction of the crack and integration schemes (Jirásek et al. 2012). Here, the equivalent length parameter is simplified and set according to the element length, similar to commercial codes. Within this basic implementation, the Rankine yield criterion is used as an associated flow rule. Based on Koiter's generalization, the increment of the plastic strain then

can be computed as:

$$d\epsilon_{p1} = d\lambda_p \frac{\partial g}{\partial \sigma'_{p1}} = d\lambda_p \frac{\partial f_y}{\partial \sigma'_{p1}} = d\lambda_p \tag{4.23}$$

The simple expression ($d\kappa_p$=$d\lambda_p$) can be recovered for a strain-softening hypothesis based on the principal maximum plastic strains according to Malyszko (2006). By making use of the Kuhn-Tucker loading/ unloading condition defined as:

$$f_y \leq 0, \quad d\kappa_p \geq 0, \quad d\kappa_p f_y = 0, \tag{4.24}$$

the identity of $\kappa_p = \ln(f_c/\sigma'_{p1})\kappa_{u1}$ gets evident. The plastic strain increment is then updated based on the computed total strain after each solution iteration of Eq. 4.20 by solving Eqs. 3.53, 3.55 and 4.22. Finally, the obtained principal plastic strains are then transformed back from the principal stress space to the initial coordinate orientation by using the inverse operation of Eq. 4.21.

4.3.2 Solution algorithm

The momentum balance is solved based on the works of Jasak et al. (2000) and Cardiff et al. (2018) in a segregated way for each direction. Based on this approach, the inter-component coupling is treated explicitly. The resulting sparsely populated matrix can then be solved efficiently by iterative solvers. This iterative process is well suited for implementing inelastic strains such as plastic strains, as they can be updated after each iteration step.

4.3.3 Solution sequence

The solution of the mechanical domain is based on solving Eq. 4.20 iteratively, as mentioned before. The full solution sequence is displayed in Fig. 4.5. Within the first step of the solution, the moisture-dependent properties like the pore pressure of the liquid and gaseous phase, the total density and phase fraction are updated. Similarly, the thermal strain is adjusted according to the current temperature field. If load ramping is applied, all loads, including loads from pore pressures, are ramped in user-specified steps. The momentum equation for the pore elasto-plastic composite material is then solved iteratively while updating the stress-dependent properties like the plastic strain after each iteration. The convergence of the solution can be checked with respect to the stresses or displacements after each iteration. After the solution has converged, the load is ramped again and the solution is repeated. Once the entire load is applied and the solution converges, the matrix's permeability and fracture's permeability

and porosity are updated according to the coupling description in Sec. 4.6. The updated permeability tensor is compared to the tensor applied to the moisture solution for convergence. If significant changes are observed, the moisture solution sequence is repeated with updated strain values. If no significant change in permeability is found, the solution data is processed towards the solute transport domain.

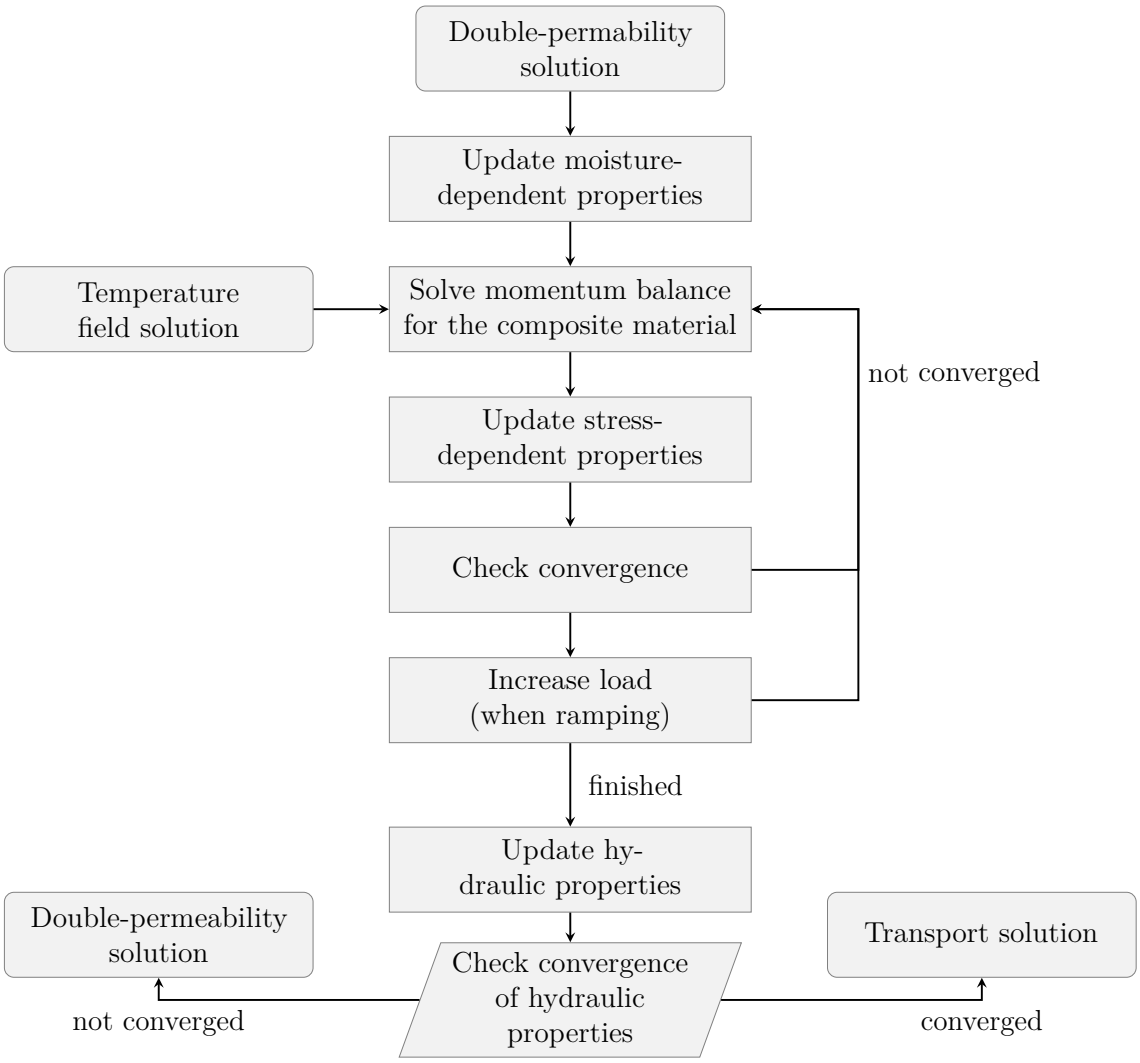

Fig. 4.5: Continuum mechanics solution

4.4 Solute transport solution

Based on the quantities described in Sec. 3.3.1, the mass balance of each ionic species can be assembled. The change of a dissolved mass of an ionic species $\delta c_s \theta_l$ is related to the change in mass of the ionic species in each solid phase $s_{p,s}$ as well as the overall divergence of the

transport:

$$\frac{\partial(c_s\theta_l + s_{p,s})}{\partial t} = \nabla \cdot (-\boldsymbol{v}_s - \boldsymbol{v}_{a,s}) + q_l c_{s,q} \tag{4.25}$$

Here, $c_{s,q}$ is the concentration of the ionic species in the liquid source. The expanded form of the above equations reads as (Samson et al. 2007b):

$$\frac{\partial(c_s\theta_l + s_{p,s})}{\partial t} = \nabla \cdot \left[D_s\theta_l \nabla(c_s) + D_s\theta_l c_s \nabla \ln(\gamma_s) + \frac{D_s\theta_l z_s F}{R_u T}\nabla\Psi + \frac{D_s\theta_l c_s \nabla \ln(\gamma_s)}{T}\nabla T \right] - \nabla \cdot c_s\theta_l \boldsymbol{v}_l + q_l c_{s,q} \tag{4.26}$$

where the interactions of the dissolution and precipitation of the solid phase components are taken into account by the change in solid density of a species $s_{p,s}$ based on the computation in the chemical solution domain.

When the moisture transport is calculated for fracture and matrix as dual permeability solution, the transport of solutes is also computed for both domains individually. Eq. 4.26 is then computed twice for matrix and fracture species. In addition, the equation has to be expanded for the species exchange flux Γ_s between both domains given as:

$$\Gamma_s = \Gamma_l c_s + D_s \omega_s(w,\delta,\Theta_{l,f},\Theta_{l,m})\theta_l \left[c_{s,f} - c_{s,m} + c_s(\ln\gamma_{s,f} - \ln\gamma_{s,m})\right] \tag{4.27}$$

where the liquid exchange flux Γ_l is applied in addition to the diffusive exchange. The diffusive transfer coefficient $\omega_s(w,\delta)$ is computed similarly to the moisture transfer coefficient by accounting for the joint and element geometry (Eq. 4.6). When data is available, the transfer coefficient can also be adopted according to the saturations, the degree of leaching δ and fracture aperture w as all affect the effective path length for diffusion.

Activity model

The transport solution sequence and the chemical solution require the implementation of an activity model for computing the activity coefficients for each species γ_s. The selected model shows a good agreement for ionic activities in cement-based materials (Samson et al. 1999a; Samson et al. 2007b; Glasser et al. 2008). The activity description is based on the ionic strength I of the solution:

$$\ln\gamma_s = -\frac{A_\gamma {z_s}^2\sqrt{I}}{1 + b_i B_\gamma \sqrt{I}} + \frac{(0.2 - 4.17\cdot 10^{-5} I) A_\gamma {z_s}^2 I}{\sqrt{1000}} \tag{4.28}$$

with b_i being species-dependent parameters. The temperature dependent coefficients A_γ and B_γ are given as:

$$A_\gamma = -\frac{\sqrt{2}F^2 e_0}{8\pi(\epsilon_m R_u T)^{3/2}} \tag{4.29}$$

$$B_\gamma = \sqrt{\frac{2F^2}{\epsilon_m R_u T}} \tag{4.30}$$

where e_0 is the electrical charge of one electron ($1.602{\cdot}10^{-19}$C).

4.4.1 Solution algorithm

The evaluation of both solutions can be conducted completely segregated, segregated with iterations between the domains or fully coupled. While the latter is the numerically most challenging, the segregated approach induces a numerical error which is generally scaled with the timestep size (Herzer et al. 1989). Hence, as timestep sizes are reduced, the numerical error tends to zero. In Walter et al. (1994) it was concluded that this segregated approach is more efficient, even if smaller timestep sizes have to be applied, given the numerical effort involved for coupling. Following these results, this segregated approach is selected here. In order to reduce the numerical diffusion, a user-specified maximum timestep criterion can be applied.

When the effect of the electrical charge of each species is to be included in the solution process, the Poisson equation 3.33 has to be solved simultaneously (Samson et al. 1999b). The fully coupled Poisson Nernst-Plank equations can also be used to account for the effect of externally applied electrical fields. In order to allow a flexible implementation of different models for the computation of the chemical activities, the contribution of the activities are updated within the outer iterations as the derivatives of different activity model might not always be known a priori.

4.4.2 Solution sequence

The full solution sequence of the described approach is displayed in Fig. 4.6. Based on the results of the transport rates of the moisture domain and the chemical equilibrium of the last timestep, the mass balance of each solute is solved. As the ionic strength is updated after each iteration, the convergence of the solution has to be assured by selecting one of the

previously described convergence criteria (Eqs. 4.12-4.14) for a species or quantity. Under certain conditions such as large advective flux rates, large timesteps, or small mesh sizes (high Courant numbers), the solution can diverge. For these cases, a divergence criterion is checked as well, which resets the times-step and decreases the timestep size upon divergence detection. If convergence is achieved, the chemical equilibrium solution process is started.

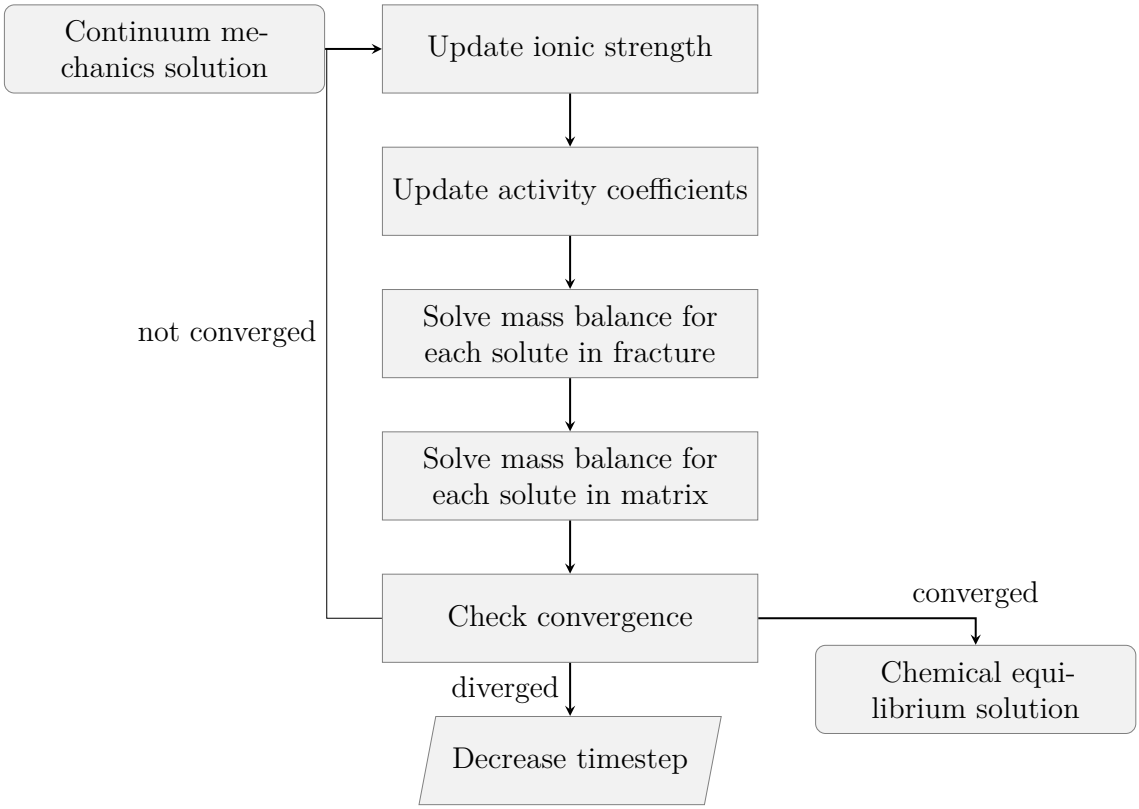

Fig. 4.6: Solution sequence of the transport domain

4.5 Chemical equilibrium calculations

The chemical solution solver is based on the assumption of the validity of the local chemical equilibrium in the CBM. Based on the non-linear nature of the law of mass action and the possibility of computing a nonphysical but mathematical correct (e.g. negative concentrations) solution, the solution process is selected as a combined solution technique. The procedure utilizes the Newton-Raphson algorithm and the simplex solver known for linear programming, resembling a sequence similar to the solution applied in Parkhurst et al. (1999).

In order to be applied in the Newton-Raphson algorithm, the baseline equations are for-

mulated as functions $f()$ that are being solved to be equal to zero. The equation system is assembled with the law of mass action equations for each solid phase, the applied aqueous reaction, the mass balance equation of each molecule/ion, as well as inequality constraints. The linear equations system of each Newton iteration is then solved with a simplex solver, which incorporates additional inequalities.

Law of mass action

The law of mass action applies at equilibrium between the solid phase and the solutes in the solution. Hence, at equilibrium the residuum for the law of mass action (Eq. 3.27) has to be zero and the equation can be rewritten for aqueous reaction as:

$$f(a_A,a_B,a_{AB}) = \frac{{a_A}^a {a_B}^b}{a_{AB}} - K_c(T) = 0 \tag{4.31}$$

For a solid phase (e.g. a_{AB}) the solution function is reduced according to (Eq. 3.28):

$$f(a_A, a_B) = {a_A}^a {a_B}^b - K_s(T) = 0 \tag{4.32}$$

Mole balance of solutes

The general mole balance of a species is formulated by summing the contribution of the concentration in the solution, the amount in the solid phases and other aqueous species composed of the respective ion. The total amount of moles contained per volume of species A $\rho_{mol,A}$ has to be maintained as the transport is calculated in a different solution step. Hence, each cell's molar density ρ_{mol} must be maintained within one chemical solution step. The initial molar density is computed as:

$$\rho_{mol,A} = \theta_l c_A + a \cdot \rho_{mol,AB} + q_{s,A} + ... \tag{4.33}$$

where $q_{s,A}$ accounts for additional sources or sinks of a species. Obviously, all additional molecules and solids containing the same species must also be added up. As the initial molar density has to be maintained during the chemical solution, the molar balance is also added to the equations system as the function:

$$f(c_A,\rho_{mol,AB}) = \theta_l c_A + a \cdot \rho_{mol,AB} + q_{s,A} - \rho_{mol,A} = 0 \tag{4.34}$$

Constraining equations

When an insufficient amount of solid phase is present to dissolve in the solution according to the LMA, the concentrations in the solution remain below saturation. This introduces two mathematical challenges to the solver as the LMA function (Eq. 4.32) cannot always be fulfilled and the solution for the solid phase density would continue to decrease to negative values, since this solution is valid from a mathematical perspective. Both problems can be resolved by applying the simplex solver, which can minimize the residuum in the LMA equations while keeping the molar balance equations as a strict equality equation. For optimizing the LMAs, the algorithm can also be selected to enforce values to be smaller or equal to saturation. In this way, the optimization is done based on the lower, physically more relatable range of values in the simplex method. In addition, the inequality constraints imposed for the simplex method restrict results with negative solid densities and concentrations. Two examples for simple inequality constraints read as follows:

$$\rho_{mol,AB} \geq 0 \; ; \; c_A \geq 0 \tag{4.35}$$

For the application of the simplex algorithm to the equations system, the improved algorithm proposed by Barrodale et al. (1973) is used.

4.5.1 Solution algorithm

The equation system contains the law of mass action equations, the balance equations and constraining equations for each relevant solid phase and ion and are solved for each cell in the grid. The user can specify the ions and solid phases, but the system is always solved with the described approach. A simple example of the arising equation system is displayed for the dissolution of portlandite. Here, only the ions Ca^{2+} OH^- and the pure phase $Ca(OH)_2$ are present:

$$\mathbf{F} = \begin{bmatrix} \theta_l c_{Ca^{2+}} + 1 \cdot \rho_{mol,Ca(OH)_2} - q_{s,Ca^{2+}} - \rho_{mol,Ca^{2+}} \\ \theta_l c_{OH^-} + 2 \cdot \rho_{mol,Ca(OH)_2} - q_{s,OH^-} - \rho_{mol,OH^-} \\ (a_{Ca^{2+}})^1 (a_{OH^-})^2 - K_{sCa(OH)_2} \\ \rho_{mol,Ca(OH)_2} \end{bmatrix} \begin{matrix} = \\ = \\ \approx \\ \geq \end{matrix} \begin{bmatrix} 0 \\ 0 \\ 0 \\ 0 \end{bmatrix} \tag{4.36}$$

The above equation system is generally non-linear and thus cannot be directly solved by the linear simplex solver. Therefore, the system is linearized by applying the Newton-Raphson method. By using this method, the values of the next iteration step $n+1$ of the state variables $c_{Ca^{2+}}, c_{OH^-}$ and $\rho_{mol,Ca(OH)_2}$ can be described with the Jacobian matrix $\mathbf{F}'$ of $\mathbf{F}$:

$$\begin{bmatrix} c_{Ca^{2+},n+1} \\ c_{OH^-,n+1} \\ \rho_{mol,Ca(OH)_2,n+1} \end{bmatrix} = \begin{bmatrix} c_{Ca^{2+},n} \\ c_{OH^-,n} \\ \rho_{mol,Ca(OH)_2,n} \end{bmatrix} - \frac{\mathbf{F}(c_{Ca^{2+},n}, c_{OH^-,n}, \rho_{mol,Ca(OH)_2,n})}{\mathbf{F}'(c_{Ca^{2+},n}, c_{OH^-,n}, \rho_{mol,Ca(OH)_2,n})} \tag{4.37}$$

The system can be rearranged by using the increments $\Delta x = x_{n+1} - x_n$ and $\mathbf{F}$ set to the residuals $\mathbf{R_n}$ of the last iteration:

$$\mathbf{F_n}' \cdot \begin{bmatrix} \Delta c_{Ca^{2+},n} \\ \Delta c_{OH^-,n} \\ \Delta \rho_{mol,Ca(OH)_2,n} \end{bmatrix} = -\mathbf{R_n} \tag{4.38}$$

The equation system is then solved for the increments ΔX and the obtained solution is then applied to obtain the next iteration step:

$$\begin{bmatrix} c_{Ca^{2+},n+1} \\ c_{OH^-,n+1} \\ \rho_{mol,Ca(OH)_2,n+1} \end{bmatrix} = \begin{bmatrix} c_{Ca^{2+},n} \\ c_{OH^-,n} \\ \rho_{mol,Ca(OH)_2,n} \end{bmatrix} + \begin{bmatrix} \Delta c_{Ca^{2+},n} \\ \Delta c_{OH^-,n} \\ \Delta \rho_{mol,Ca(OH)_2,n} \end{bmatrix} \tag{4.39}$$

Similar to the previously described solution sequences, the increments that are applied to the prime variables can be evaluated. This means the decreasing changes after each iteration can be monitored and used for detecting convergence. Hence, the increments are compared to a user-specified threshold. After reaching convergence, the computed solution is applied by updating the computed ionic concentrations and solid phase densities.

4.5.2 Solution sequence

The numerical solution sequence for the chemical domain is displayed in Fig. 4.7. The equation system is assembled based on the number of dissolved species transported in the previous step. Within the first step, the available solid phases which are existent as solid or are supersaturated in the aqueous phase are evaluated. If solids are not present, the equation system can be reduced by not accounting for these phases. Then the initial total amount of moles of each available species is computed. Based on the values, the simplex system is updated and solved for each cell. The solution increments are then applied and the activity coefficients are updated for the new concentration after each iteration.

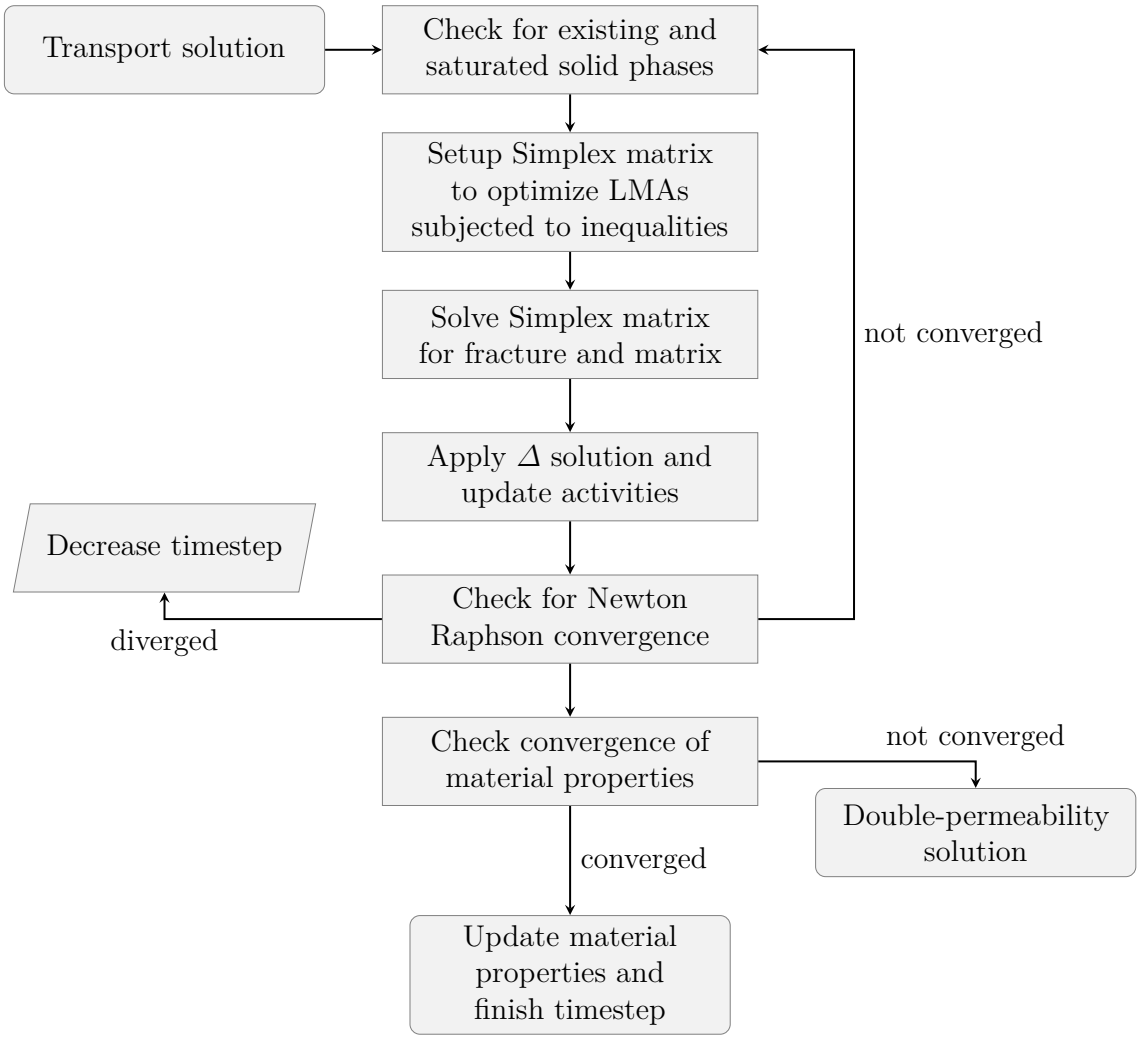

Fig. 4.7: Solution sequence for the chemical domain

The convergence of the Newton Raphson process is checked against a user-specified threshold for the solution increments. If the solution fails to converge, which can be the case for ionic compositions far from equilibrium, the timestep is decreased and the complete solution sequence is restarted. If convergence is detected, the material properties are updated and checked for convergence against the initial values of this timestep. Since the dissolution is generally a slow process, an update of the properties without additional convergence checks is sufficient in most cases. If the solution is converged, the material properties are updated as described in Sec. 4.6). The new parameters are then applied to the solution for the next timestep which is then computed with the same sequence.

4.6 Coupling between the solution domains

The interaction between the different solution domains can be modeled by updating the material properties according to the changes induced by each domain. The general description of this update process is displayed in Fig. 4.8.

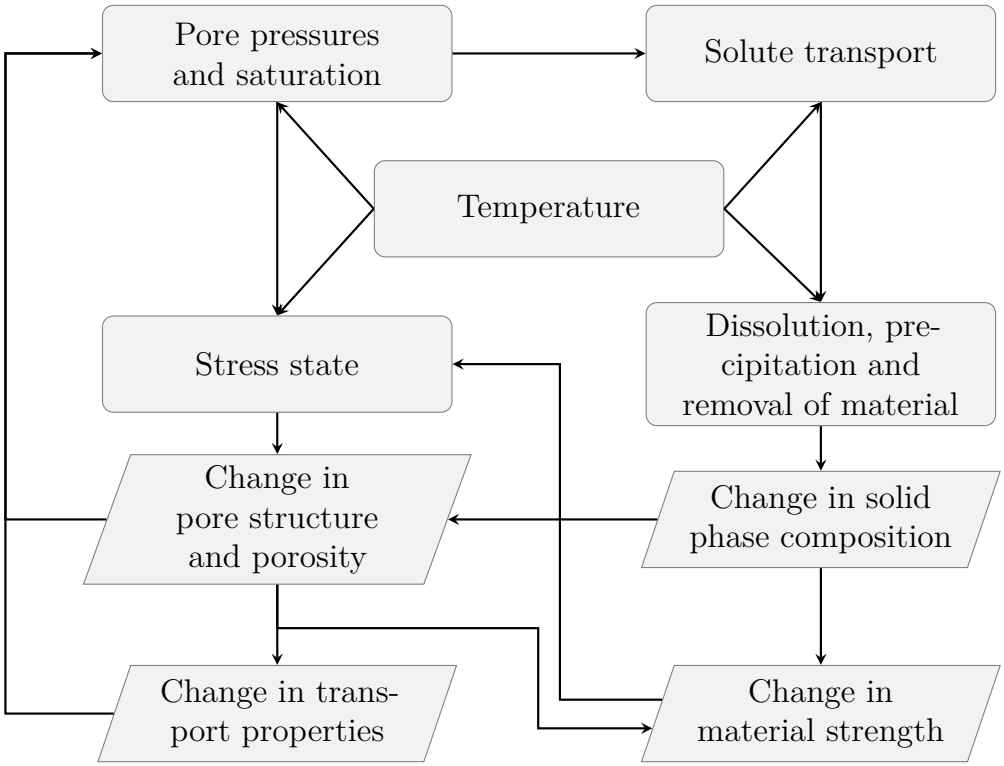

Fig. 4.8: Coupling sequence within the numerical solution

It can be seen that moisture, temperature and solute transport do not induce significant changes by themselves, but they induce changes in the material as their results affect the outcome of the mechanical and chemical domains. Hence, their effect on the material is inherently included when the stress state, dissolution, and precipitation are assessed. In contrast, the effect of the stress state on the pore space and the resulting change in moisture resistance needs to be explicitly addressed. Similarly, the effect of the change in chemical composition on the pore structure as well as the material strength needs to be taken into account. The applied modeling approach for the changes in pore structure and porosity, the change introduced to the material's permeation resistance, as well as the changes in material strength are described in the following.

4.6.1 Updating pore structure and porosity

Straining, cracking or localized strains, changes and removal of solid phases induce changes in the material's pore structure. As all three processes affect the pore structure slightly differently, different effects are implemented accordingly. Based on the observation discussed in Sec. 3.5.5, it can be concluded that all pores are subjected to straining at low loading stages. Nevertheless, new voids with different properties are formed with the growth of micro-cracks. For this reason, the implementation within this modeling approach splits the changes in the pore structure regarding elastic and inelastic strain components. Hence the formation of micro-cracks is included based on the growth of inelastic strain components.

Updating porosity based on elastic strain

The effect of the elastic strain on the porosity is implemented based on the poroelastic porosity changes $\Delta\phi$ as computed with Eq. 3.64. As no fracture is present at the elastic stage, the changes are applied to the moisture properties of the matrix domain. These changes in porosity then can be used to update the highest possible moisture content of the matrix, which is achieved upon saturation:

$$\theta_{l,sat,new} = \Delta\phi + \theta_{l,sat,ref} \tag{4.40}$$

with $\theta_{l,sat,new}$ and $\theta_{l,sat,ref}$ being the new (current) and the reference moisture content used for the initial pore size distribution. In order to apply this increase on the pore sizes distribution, the relative change Z_ϕ)in pore space, concerning the reference state ϕ_{ref} is calculated according to:

$$Z_\phi = \frac{\phi_{ref} + \Delta\phi}{\phi_{ref}} \tag{4.41}$$

For updating the pore size distribution, the elastic strain is assumed to strain all pores equally. If directional dependencies are neglected, the average ratio of change for the pore radii can be calculated as:

$$\frac{r_{new}}{r_{ref}} = \sqrt[3]{Z_\phi} \tag{4.42}$$

Given the linear relation between capillary suction and the pore radius (Eq. 3.2), any moisture retention curve based that is based on the reference state ($\mathrm{MRC}_{ref}(\Theta_l)$ can be scaled

as:

$$MRC_{new}^{-1}(\Theta_l) = MRC_{ref}^{-1}(\Theta_l) \cdot \frac{r_{ref}}{r_{new}} \tag{4.43}$$

accounting for the fact then an increase in pore radius reduces the capillary suction induced in the pores at the same relative saturation.

Not only is the available porosity changed, but the current dimensionless saturation Θ_l and the matric potential are affected by the changes in the pore space. Hence, both values have to be updated in order to account for the changes in pore dimensions.

Since the total volumetric liquid content θ_l stays unchanged if the available pore space is updated, the dimensionless saturation Θ_l can be updated first to account for the porosity changes according to:

$$\Theta_{l,new} = \frac{\theta_l - \theta_{l,r}}{\theta_{l,sat,new} + \theta_{l,r}} \tag{4.44}$$

The inverse of the updated water retention function then can be used to update the matric potential in agreement with the new dimensionless saturation.

$$h_{l,new} = MRC_{new}^{-1}(\Theta_{l,new}) \tag{4.45}$$

The above procedure is applied only for $\Theta_{l,new} < 1$, if negative $\Delta\phi$ are applied, the CBM cannot only get completely saturated, but the fluid can also be pressurized as predicted by poroelastic theory. When the compressibility of the water κ_l is taken into account, the new liquid pressure head h_{lnew} for the saturated case can be computed as:

$$h_{l,new} = \frac{\theta_l - \theta_{l,sat,new}}{\theta_l \kappa_l g \rho_l} \tag{4.46}$$

Updating porosity based on inelastic strain

The parameters of the additional pore structure induced by inelastic straining like cracking are modeled similarly to the elastic changes on the porosity described in the previous section. This means that the same subsequent steps are computed. However, not the elastic strain is evaluated in Eq. 3.64, but inelastic strains are applied. By making use of the volumetric plastic strains and the Biot coefficient of the fracture space b_f, the porosity of the fracture can be

calculated as:

$$\phi_f = b_f tr(\boldsymbol{\epsilon}_p) \tag{4.47}$$

When the average fracture width w_{avg} and crack/ joint orientation are known (see Eq. 4.51), a general formulation for the fracture porosity can also be derived. This formulation uses the area of the intersecting crack plane in the element ($A_{f,e}$) and the volume of the element V_e for computing the porosity of the fracture/joint domain ϕ_f:

$$\phi_f = \frac{A_{f,e} w}{V_e} \tag{4.48}$$

This splitting between elastic and inelastic strains allows for distinguishing the significantly different hydraulic properties of the matrix and fracture/crack void sizes.

Similar to the matrix domain, a pore size distribution of the fracture is added by the user for a specific reference porosity state. This allows to include effects like the formation of micro-cracks, as discussed in Sec 3.5.5, since small-sized (new) pores can be added to the material with this process.

Updating the porosity based on changes in the solid phase

The chemical changes in the solid phase affect the pore structure of the CBM as solid parts are removed or formed in the pore space. If a change in the molar density of each solid phase $\Delta\rho_{mol}$ is computed during the chemical solution, the porosity has to be updated. As concentrations can be computed for the fracture and matrix, the porosity is also to be updated for both domains specifically. This allows the modeling of the dissolution effect at the crack or a joint. Thus, the widening of the discontinuity can be explicitly computed. For this, both the fracture and matrix porosity can be updated by making use of V_m, the molar volume of the solid phases:

$$\Delta\phi = \sum_{n=1}^{nSP} V_{m,SP_n} \Delta\rho_{mol,SP_n} \tag{4.49}$$

where nSP is the number of solid phases present. As dissolution and precipitation can take place in all pore sizes, the change in porosity is distributed equally across all pore sizes. Hence, when the change in porosity is computed according to the changes of solid phase density, the update procedure for elastic porosity changes described in Sec 4.6.1 is applied here as well.

4.6.2 Updating the resistance to permeation

The changes induced to the pore size distribution of the material also affect the hydraulic conductivity. As cracks can form a connected section of larger voids, their impact on permeation is significantly larger than a more evenly distributed strain within the matrix. For this reason, elastic straining of the matrix is modeled in a different way than the fracture and joint domain.

4.6.3 Updating hydraulic conductivity of the matrix

As all localized strains are treated within the fracture domain, the effects of micro-cracking are excluded from the matrix domain. Based on the stiffness of CBMs, elastic strains and thus changes in hydraulic conductivity are generally not as significant as for joints and cracks. Even though this effect is not very significant, the Kozeny-Carman relation is applied to account for the changes in porosity on the saturated hydraulic conductivity (Cochepin et al. 2008):

$$\boldsymbol{k_s}_{,new} = \boldsymbol{k_s}_{,ref}(\frac{\phi_{,new}}{\phi_{,ref}})^3(\frac{1-\phi_{,ref}}{1-\phi_{,new}})^2 \tag{4.50}$$

Given the low data availability in the literature regarding measured hydraulic conductivities during straining, this application of this relation cannot be verified fully for this case. Nevertheless, the flexible implementation of the modeling approach allows the application of different formulas which can be based on the change of equivalent pore size or strain, such as the Katz-Thompson equations (Katz et al. 1986) or similar (e.g. Sakai 2019).

4.6.4 Updating hydraulic conductivity of the fracture

The fracture's hydraulic conductivity is computed using the parallel plate model (Eq. 3.71). This model has been verified by multiple experiments as discussed in Sec. 3.5.5. For the application of the model, a fracture aperture w is required. In order to estimate the average aperture, the principal plastic strains computed during the elastoplastic solution are evaluated. In the case of the first plastic principal strain, the related average aperture for the crack in the same direction w_1 is derived by using the crack band theory again to recover the fracture aperture. This assumption has been applied in different works (e.g. Sha et al. 2017; Rahal et al. 2017) and is applied here as:

$$w_1 = f(\epsilon_{p1})\epsilon_{p1} l_e \tag{4.51}$$

where l_e has to be adjusted according to the length of the element in fracture direction. In order to apply the hydraulic conductivity in the solution, the contribution in all principal directions has to be added and transformed back to initial coordinates similar to the plastic strains. In the above equation, the additional expression $f\epsilon_{p1})$ was added to describe the relation between the crack aperture and the total inelastic displacement. Given the lack of data, this function has been adopted as unity here, but more precise formulations could be applied in the future.

4.6.5 Updating material strength

The material strength is updated when the strength-defying solid phases are removed. This is the case for dissolution, abrasion or similar processes. Based on the observation of a linear decrease in strength with respect to the increase in the degree of leaching (see Fig. 3.1), the strength properties are updated similarly. The applied implementation is based on the total volume density of all strength-defying material phases V_{dsp}, which is defined as:

$$V_{dsp} = \sum_{n=1}^{nSSP} V_{m,SP_n} \rho_{mol,SP_n} \tag{4.52}$$

where $nSSP$ is the number of strength-defying solid phases in the material. With this relation, any strength parameter $X_{strength}$ (e.g. Youngs modulus or compressive strength) can be related to the ratio of removed solid phases as:

$$X_{strength}(V_{dsp}) = \frac{V_{dsp}}{V_{dsp,0}}(X_{strength,0} - X_{strength,res}) + X_{strength,res} \tag{4.53}$$

where the index "0" denotes the initial configuration and the index "res" the residual strength.

4.7 Global solution sequence

The combined global solution sequence based on the domain solutions as well as the interaction of all modeling domains is displayed in Fig. 4.9. After incrementing the timestep by the current timestep size, the temperature domain is solved at first based on the flow rates of the previous timestep. This is a reasonable choice in many cases since the temperature solution impacts all other solution domains but is less affected by the other solutions since conductive transport is usually the most decisive. However, if a strong two-way coupling effect between domains is present, an iterative or direct coupled solution between domains is required. In the following steps, the other domains are solved based on their impact on the following solutions as well

as their chance to diverge. If a domain tends to diverge more often, it is computed earlier in order to avoid unnecessary computations prior to a divergence.

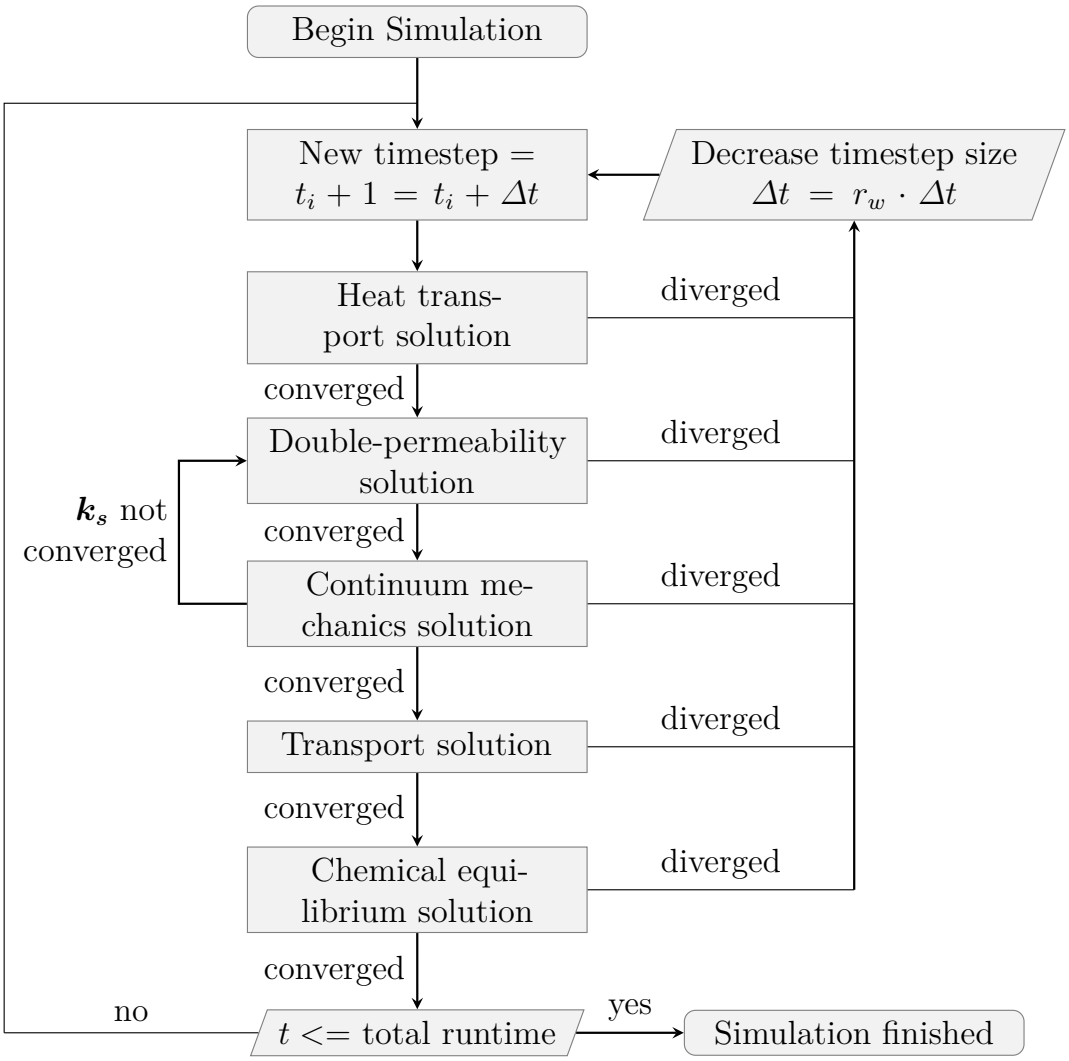

Fig. 4.9: Global solution algorithm for numerical framework

The moisture solution is solved next, as it has the biggest effect on the other solutions. In addition, convergence is not guaranteed as a result of the non-linear Richards equations for matrix and fracture domain. Based on the pore pressure distributions and the temperature field, the momentum equation of the composite solid is then solved in the mechanic solution. Given the strong interaction between cracks induced by the pore pressure and change in hydraulic conductivity, this solution can be coupled with the moisture domain. If this two-way coupling is applied, the hydraulic properties are compared between each iteration within one timestep and the solution is recomputed when the hydraulic properties between moisture and mechanical

solution differ too much. If convergence is found, the flow rates and the current saturation are passed into the transport domain, which computes the transport of solutes within the liquid phase. If the solution diverges, the timestep size is decreased and the solution is repeated. If convergence is achieved, the concentration of the species is passed to the chemical domain. In this last solution domain, the solid phase dissolution and precipitation are computed based on the law of mass action and the ionic concentration and available solid phase densities. If the equilibrium is found, the mechanical strength properties and the pore space parameters are updated before the next timestep is started.

5 Validation of the framework

The implementation of the transport processes in the STaC-framework is verified against experiments and analytical results from the literature. As no data set is available for a deterioration case with all different aspects and combined effects, the fully coupled solution procedure cannot be validated in one single example case. Thus, each domain is compared to experiments and analytical solutions separately. This way, it can be ensured that each solution is able to capture the physics for each domain. Based on these validation steps, the precision of the combined solution can be validated. However, the achieved accuracy of the results is limited by the applied coupling relations and the accuracy of the material data. For each parameter and assumption, the applied values and relations are uncertain to a certain degree and, thus, an accurate prediction of actual structures is only possible when precise parameters and coupling relations are selected.

5.1 Moisture transport

As the infiltration into the material is a crucial aspect of the deterioration of concrete structures, it is of utmost importance to evaluate the moisture transport solution by comparison with different data sets. The selected experimental data set from the literature has also been evaluated against other numerical models previously. Thus, the solution can be compared against these numerical results additionally. The single permeability model is validated first, while the results of the extended model's moisture ingress, including the dual permeability approach, are evaluated afterward. For the latter, the computed results are compared with the experimental data of moisture ingress into concrete joints and cracks.

5.1.1 Single permeability moisture ingress into a porous material

The single permeability model results are compared to column infiltration experiments of Skaggs et al. (1970). The experiments are conducted on a 62 cm long column initially filled with relatively dry sand. The column is then subjected to water ingress from the top surface of the column. The water level at the top is kept constant during the whole experiment. The initial pressure head of the column is selected according to the original literature as -150 cm.

This value can be related to an initial moisture saturation of 6.6 % for the sand. During the 90-minute duration of the experiment, the water infiltrates into the column's dry sand due to the pressure gradient and gravitational forces. As the bottom end of the column is not sealed, water can leave the column there. In the numerical implementation, this is represented by a free drainage boundary (see Annex B). However, as the moisture front does not reach the bottom of the column during the experiment, the boundary could also be effectively treated as a "no flow" boundary. The left and right sides of the column are sealed for the experiment. Thus, they are implemented as no flow boundary for the numerical model. The geometrical setup and the mesh applied for the validation are displayed in Fig. 5.1.

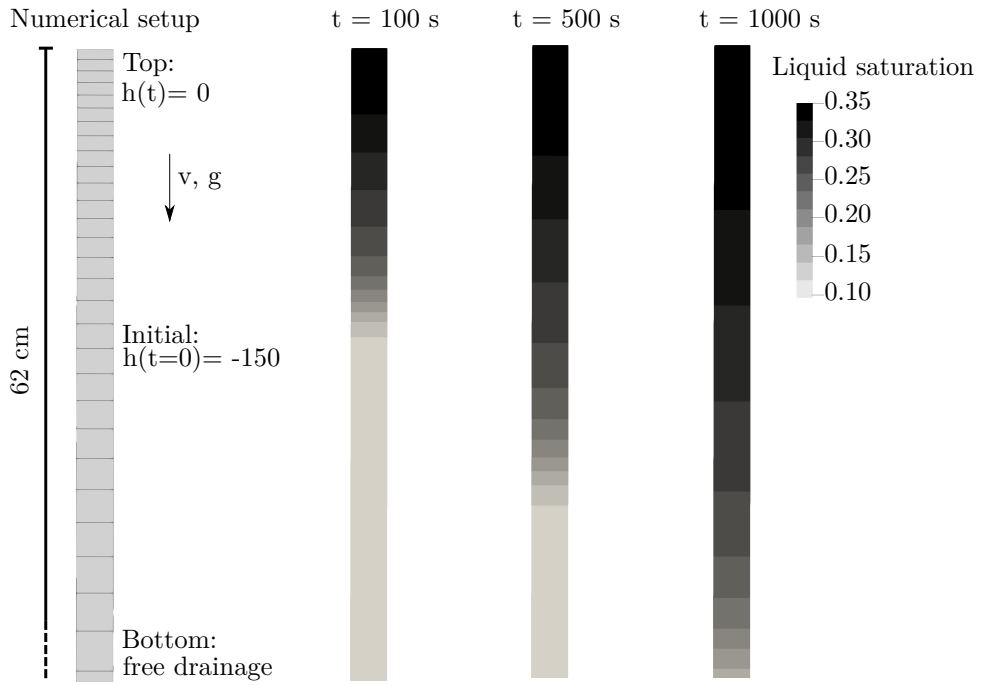

Fig. 5.1: Numerical setup and illustration of the results of the column infiltration validation example

The material's properties are selected according to the original investigations of Skaggs et al. (1970) and Šimůnek et al. (1994), and thus are similar to the published validation examples of different numerical codes (Šimůnek et al. 2008; Davis et al. 1983). The data points are extracted from the figures published in the original literature. The values between two data points are interpolated within the code. The gradient between two data points is evaluated for derivatives such as the specific moisture capacity C_m. The raw data of the moisture retention curve and relative conductivity presented by the original authors could be fitted with the Mualem-Van Genuchten Model (Eq. 4.4-4.5) to a certain degree. However, to closely resemble

the measured and modeled numerical data, the data set is implemented as data points rather than as a functional relation. The selected material relation used for the validation example is displayed in Fig. 5.2.

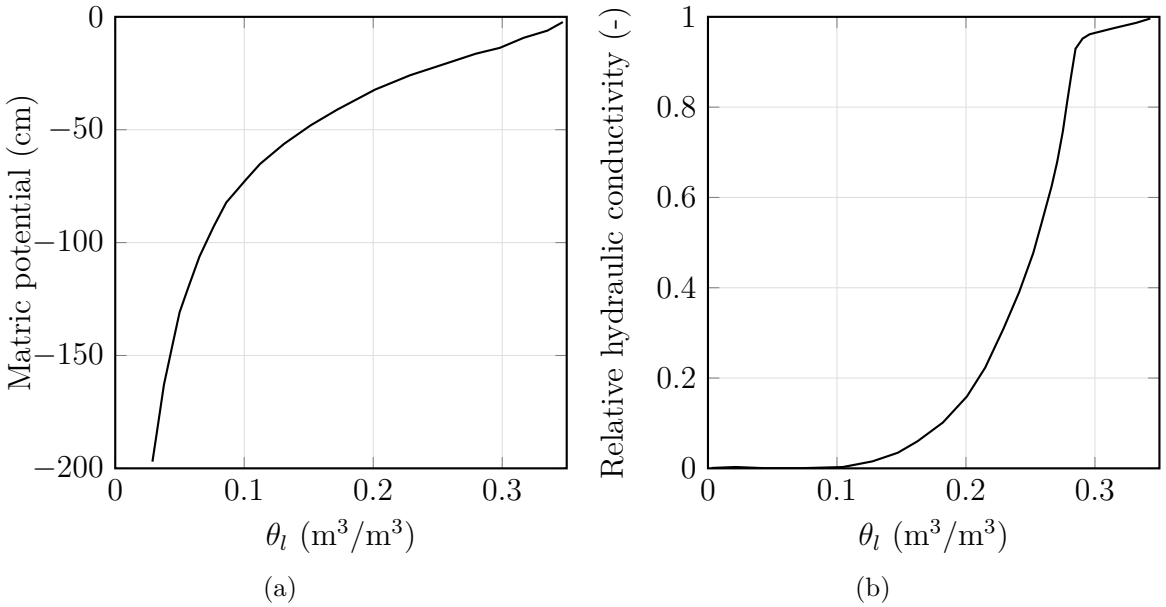

Fig. 5.2: Moisture retention curve (a) and relative hydraulic conductivity (b) of the material used for the column infiltration experiment (Skaggs et al. 1970)

The moisture transport is solved with a single permeability model for the column experiment. For comparison with the experimental and numerical data, the moisture flux across the top boundary is monitored. For a long-term evaluation, the cumulative inflow is compared as well. The results of both quantities are displayed in Fig. 5.3.

The computed results of the inflow curves show a good agreement with the numerical results published for the different solvers for both quantities. Generally, minor deviations are possible based on the different applied numerical solution methods. In addition, even greater deviations could be induced based on the precision of the implemented material properties. As both, the moisture retention curve and the relative hydraulic conductivity are only available as a graphical plot for the original experiment, errors can also be induced during the extraction of the parameters and the applied interpolation. Even though all these reasons for deviations exist, the numerical results agree well with each other while also resembling the experimental data. Thus, it can be concluded that the numerical solution of the single permeability moisture transport is quite accurate.

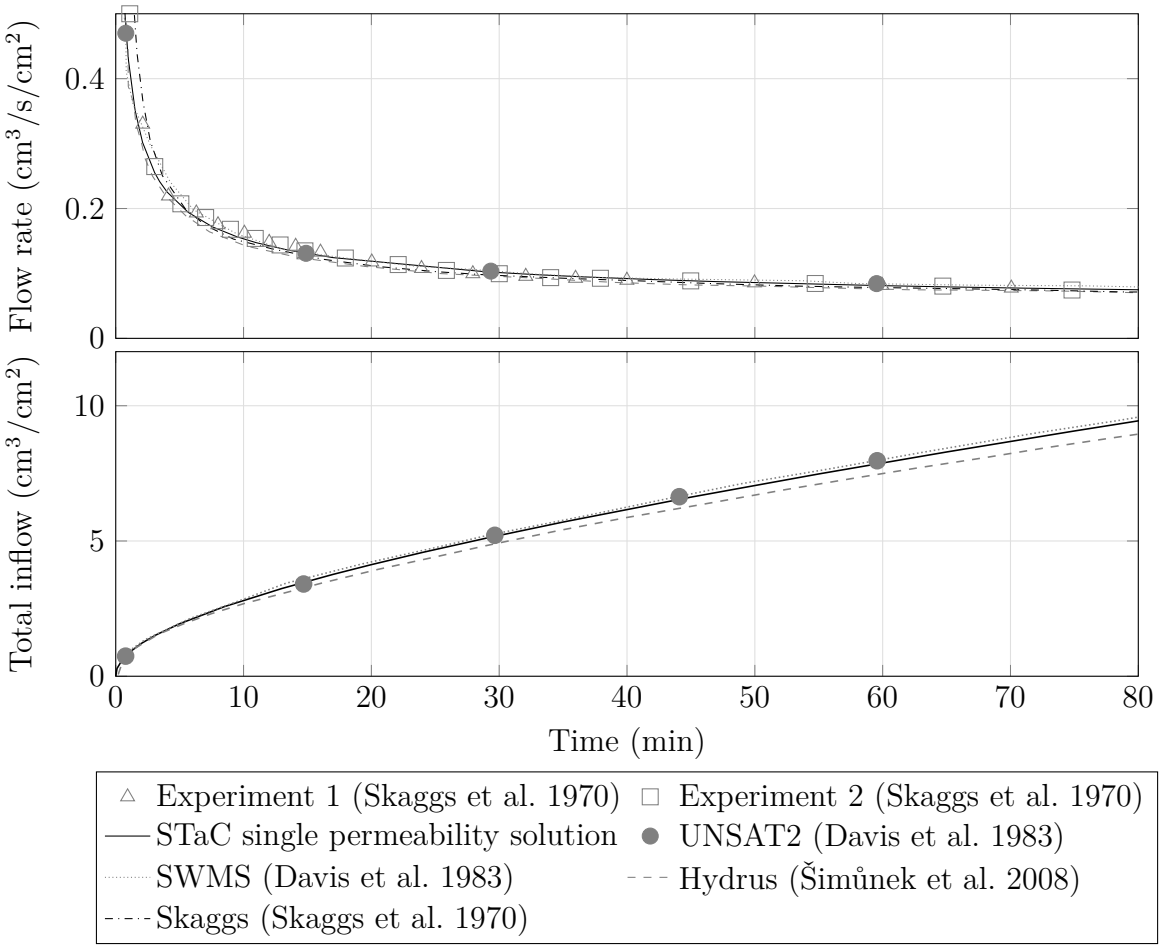

Fig. 5.3: Comparison of the results for the single permeability moisture transport computed with the presented numerical approach (STaC) with the original experimental data as well as similar numerical codes

5.1.2 Dual permeability moisture ingress into concrete joints

The dual permeability model is based on a combination of single permeability solutions, which individually had been validated in the previous section. For the dual permeability solution, the equation is solved two times on the same mesh. Nevertheless, the coupling term can reduce the convergence of the solution and thus also the required timesteps. As the main application of the dual permeability model is to model concrete cracks and joints, the applied solution is compared to experimental results for both cases.

While flow processes in concrete joints are already seldom measured and results are rarely published, transient results that could be used to evaluate numerical models cannot be found in the literature at all. Therefore, samples of construction joints were extracted from a gravity

dam to measure the transient moisture ingress. The core-drilled cylindrical samples were dried in a climate chamber and then subjected to moisture ingress at constant pressure from the top. The bottom side of the sample was open for drainage and the lateral sides were sealed with epoxy raisin. During the saturation process, the weight of the sample is recorded continuously. At the same time, the cumulative outflow of the bottom of the sample is collected and recorded. In order to evaluate the impact of the joints on moisture ingress, the obtained results are also compared to concrete samples without joints that were tested with the same procedure (Görtz et al. 2021b).

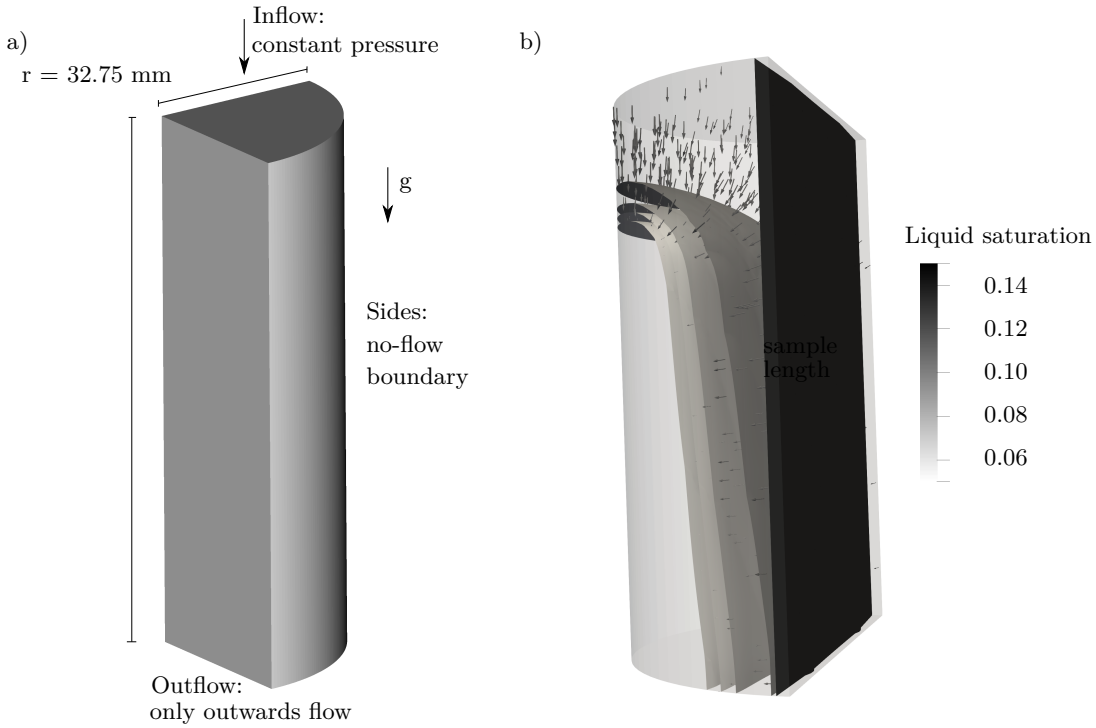

Fig. 5.4: Numerical setup (a) and illustration of the flow process (b) for the validation of the moisture ingress into joints (Görtz et al. 2021b)

The numerical framework implements the experimental setup by applying the boundary conditions and geometry displayed on the left in Fig. 5.4. The lateral cylinder surface is described as a “no flow” boundary as these sides are sealed by epoxy raisin. The bottom surface of the cylinder is modeled as a “free-drainage” boundary which allows only outward flow while remaining inaccessible for inwards flow (see Annex B). The top surface of the cylinder is selected as a constant head boundary set to the pressure head measured during each experiment. The resulting flow process is displayed on the right side of Fig. 5.4. For this setup, the matrix surrounding the joint is saturated by moisture from the cylinder top and

from the joint. The geometry of the cylinder is adopted equal to the measured geometry for each sample. Hence, the radius is kept similar at 32.72 mm for all samples, while the sample length is adjusted to the length of each sample. The porosity is adjusted according to the observed maximum water content values recorded during the measurement for each cylinder. The intrinsic hydraulic conductivity is set according to the measured flow rates after reaching saturation. The complete set of selected and measured properties is displayed in Tab. 5.1.

Tab. 5.1: Measured data for cylindrical concrete samples with expansion joints (V) and no joints (C) (Görtz et al. 2021b)

	Length	**Radius**	**K_s**	**Porosity**	**Pressure**	**Saturation time**
Unit	[mm]	[mm]	[m/s]	[%]	[bar]	[s]
V1	89.5	32.75	9.12e-06	15	4.2	2700
V2	91.5	32.75	1.44e-06	19.4	4.7	12000
V3	99	32.75	2.58e-05	17.1	3.3	4000
C1	95	32.75	6.38e-10	13.2	5.3	10670
C2	72.5	32.75	2.87e-09	11.1	5.3	2100
C3	66	32.75	1.32e-09	10.3	5.4	4080

For the dual permeability model, the value for the hydraulic conductivity of the matrix is generally taken as 2e-9 m/s but is changed for sample V2 to 0.5e-9 m/s as the matrix flow rate was significantly lower there. After selecting the hydraulic conductivity of the concrete matrix, the hydraulic conductivity of the elements associated with the joint is computed with the observed hydraulic conductivity of the whole sample and the area contribution of the joint elements using Eq. 4.9. The porosity associated with the joint was determined by using the average aperture of the joint measured by microscopy (Görtz et al. 2021c). When the porosity of the joint is known, the remaining void space obtained by subtracting the joint porosity from the measured total porosity is taken as matrix porosity. The values for α_{vg} and n_{vg} of the water retention curve (Eq. 4.4) are adjusted to 7e-3 and 1.38 according to literature (Hall et al. 2012).

The results of the conducted experiments and the computed results of the numerical framework are displayed in Fig. 5.5. It is evident that the beginning of the outflow of water at the cylinder bottom of the sample coincides with the time to reach saturation for the homogeneous concrete samples. For the concrete samples with joints, the outflow of water seepage starts almost immediately with the beginning of the experiment. This is caused by the infiltration rate into the joint, which is much faster than for the sound material since the hydraulic conductivity of the joint is greater by magnitudes. Nevertheless, the saturation of the surrounding material still takes some extra time as the conductivity is still lower in this region.

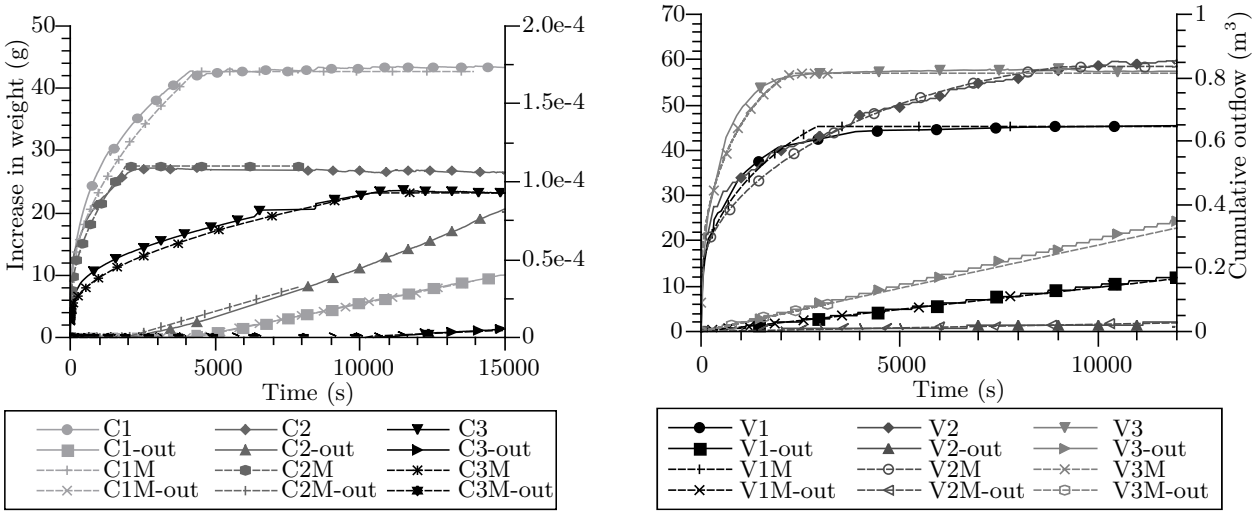

Fig. 5.5: Comparison of the numerical results (M) with the measured increase in weight (saturation) and outflow rates for homogeneous concrete samples (a) and samples with joints (b)(Görtz et al. 2021b)

Both effects, the increased seepage of the joint as well as the delayed saturation of the surrounding material, can be modeled with good precision with the proposed approach, as displayed by close agreement of the numerical results with the experiments in Fig. 5.5. Given the joints' simple geometrical setup (straight lines), the dual permeability approach is also found to be an efficient solution technique for concrete joints.

5.1.3 Dual permeability moisture ingress into concrete cracks

The dual permeability model can also be efficiently applied to describe moisture flow in the material's cracks, as will be displayed in the following section. In order to validate the solution for the moisture ingress into cracks, the results of the implemented model are compared to the experiments of Zhang et al. (2014) and Tsuchiya et al. (2014). Both experiments are conducted by connecting an initially dry, cracked concrete specimen to a tank containing water at a constant level. The moisture ingress from the tank into the specimen is then continuously measured by quantifying the moisture content using neutron radiography at different times. Within the studies of Tsuchiya et al. (2014), the crack is placed in the horizontal direction and filled with water from the connected tank using the pressure applied by the water level at the tank. In contrast, the water tank is placed below the sample for the investigations of Tsuchiya et al. (2014). This means that the moisture flow is only controlled by capillary suction, which

induces flow against the direction of gravity. For both experimental setups, the samples are sealed at the sides to prevent lateral flow. The experimental and numerical setup of both studies is displayed in Fig. 5.6.

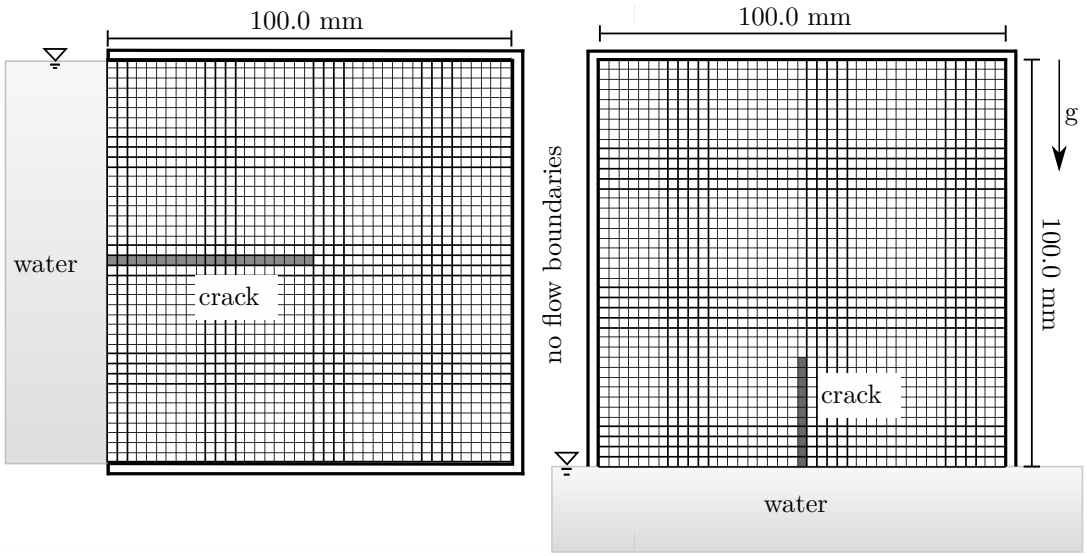

Fig. 5.6: Numerical setup for the validation of the framework with the experiments by Tsuchiya et al. (2014) (a) and Zhang et al. (2014) (b) as presented in Görtz et al. (2021a)

The material properties are selected according to the available data for both studies. The moisture content at saturation is taken from the maximum moisture contents measured during the experiments, while the initial moisture contents are selected according to moisture content at the beginning of each experiment. The data of the moisture retention curve is selected according to Hall et al. (2012) as no measurements were done in the original experiments. The hydraulic conductivity of the matrix and the moisture exchange coefficient are adjusted according to a previous calibration run. The hydraulic conductivity and porosity of the crack are selected using Eq. 3.71 and Eq. 4.48. All applied parameters are displayed in Tab. 5.2.

The results of the simulation are compared to the measured data for a cross-section perpendicular to the crack at different times. In the study of Zhang et al. (2014), different samples with different crack sizes are used. Thus, the results are each compared to the different computations with cracks with an aperture of 43 and 20 µm. The results are compared at 10, 20 and 60 minutes after the beginning of the moisture ingress. The numerical and experimental results are displayed in Fig. 5.7. In order to illustrate the effect of the dual permeability approach also a single permeability solution, where the joint is implemented by changing the material properties of the associated elements, is shown for comparison.

Tab. 5.2: Moisture transport properties for the validation examples in concrete cracks

	Zhang et al. (2014) C1		**Tsuchiya et al. (2014)**
Crack width [µm]	43	20	50
Crack length [mm]	22	14.5	50
Fracture porosity ϕ_f [-]	0.018	0.0082	0.021
Van Genuchten parameter α_{vgf}	4.03	1.88	4.68
Van Genuchten parameter n_{vgf}	5	5	5
Hydraulic conductivity fracture	2.70E-05	2.70E-06	4.20E-05
Matrix porosity ϕ_m [-]	0.073	0.073	0.073
Initial saturation θ_l [-]	0.001	0.001	0.023
Van Genuchten parameter α_{vgm}	0.007	0.007	0.007
Van Genuchten parameter n_{vgm}	1.38	1.38	1.38
Hydraulic conductivity matrix	5.00E-10	5.00E-10	5.00E-11
Transfer coefficient ζ_s	400	400	150

The results of the dual permeability model generally show a good agreement with the measured data. Evidently, the implemented model is also able to describe the moisture flow against gravity within cracks in an accurate manner. Nevertheless, it is clear that the heterogeneity of real samples induces some scatter and thus deviation in the measured data. The increased inflow and moisture content for a single permeability solution resulting from the effect of the element size is also evident. Thus, the advantage of the dual permeability model is apparent in this comparison.

The numerical results are compared with the experimental results by Tsuchiya et al. (2014) in Fig. 5.8. Again, the computed moisture content profile is compared to the distribution of moisture content measured by neutron radiography for a cross-section perpendicular to the crack. In contrast to the previous results, only one side at the crack is displayed in the original research. Thus, the center of the crack is displayed on the left side instead of in the center. By comparison, it can be seen that the general distribution of the moisture besides the crack can be captured sufficiently well. However, the original measurement seems to be captured with a larger spacial average, as the distinct peak moisture content in the crack is not captured in the same manner as displayed in the experiments of Zhang et al. (2014). Thus the difference between the results of the moisture flow is likely already induced by the original experimental data.

After evaluating the numerical results for the different experiments, it can be concluded that the applied dual permeability approach is suitable to replicate the inflow into cracked cement-based material for pressurized and capillary moisture ingress with high accuracy.

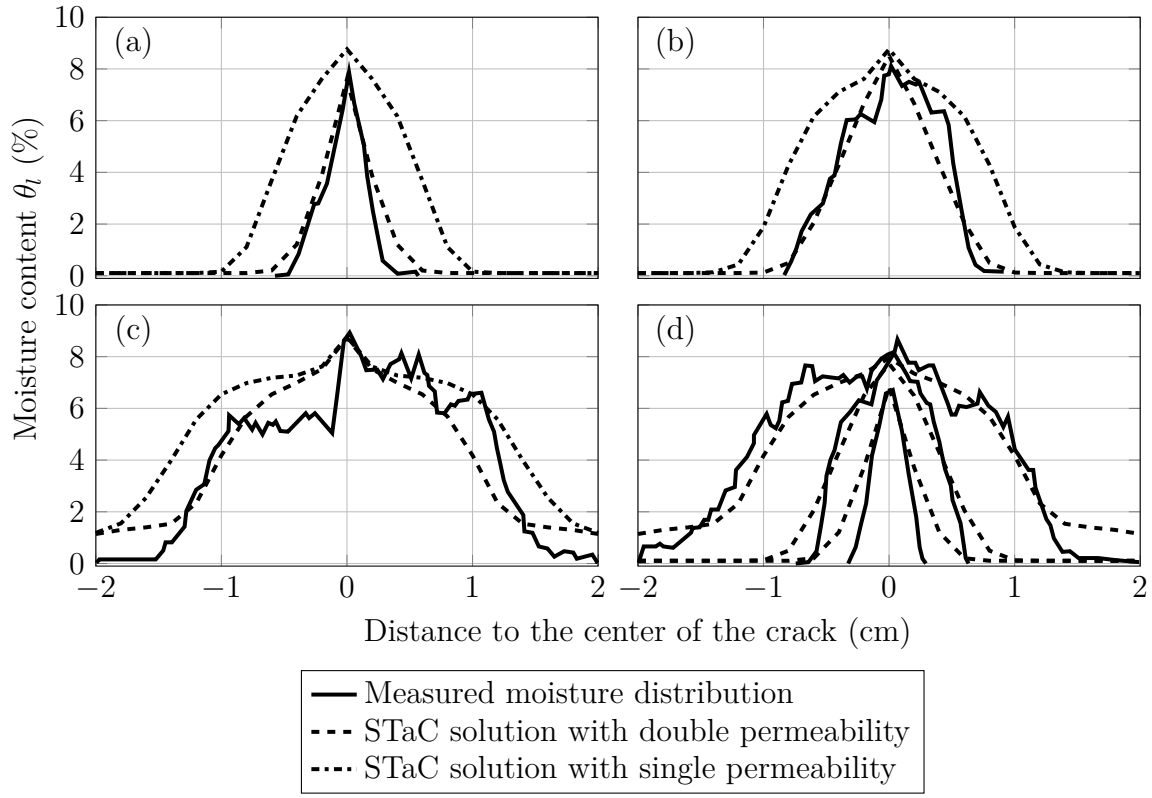

Fig. 5.7: Computed and measured (Zhang et al. 2014) profiles of moisture content perpendicular to the crack for two different samples with a crack aperture of 43 µm after 1 min (a), 10 min (b) and 1 h (c) and an aperture of 20 µm at the same times (d)

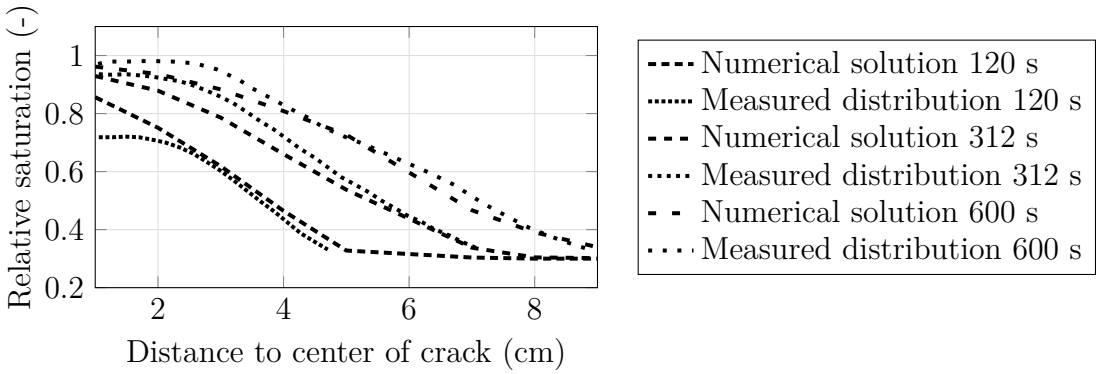

Fig. 5.8: Comparison of measured (Tsuchiya et al. 2014) and computed moisture saturation profiles perpendicular to the center of the crack at different times

Based on the good fit for numerical benchmark cases and the measured data for cement-based materials, it can be concluded that the selected representative macroscopic material models can represent the heterogeneous material sufficiently well.

5.2 Solute transport

The results of the solute transport equation in section 4.4 are evaluated against an analytical solution for a combined advective-diffusive transport case as presented in Javandel et al. (2013). The analytical solution is described for the half-plane (z>0, -∞>x<+∞) and a uniform constant flow in z-direction $\boldsymbol{v}_l$. The diffusion process is quantified with a diffusion coefficient in the transverse and longitudinal direction. The concentration is constant at the inflow boundary location at z=0. For the center region (-a<x<a), the inflow concentration remains at c_0. Away from the center (-a>x>a), the concentration is always set to zero. The geometrical setup and boundary conditions are displayed in Fig. 5.9 for the quarter-plane x>0.

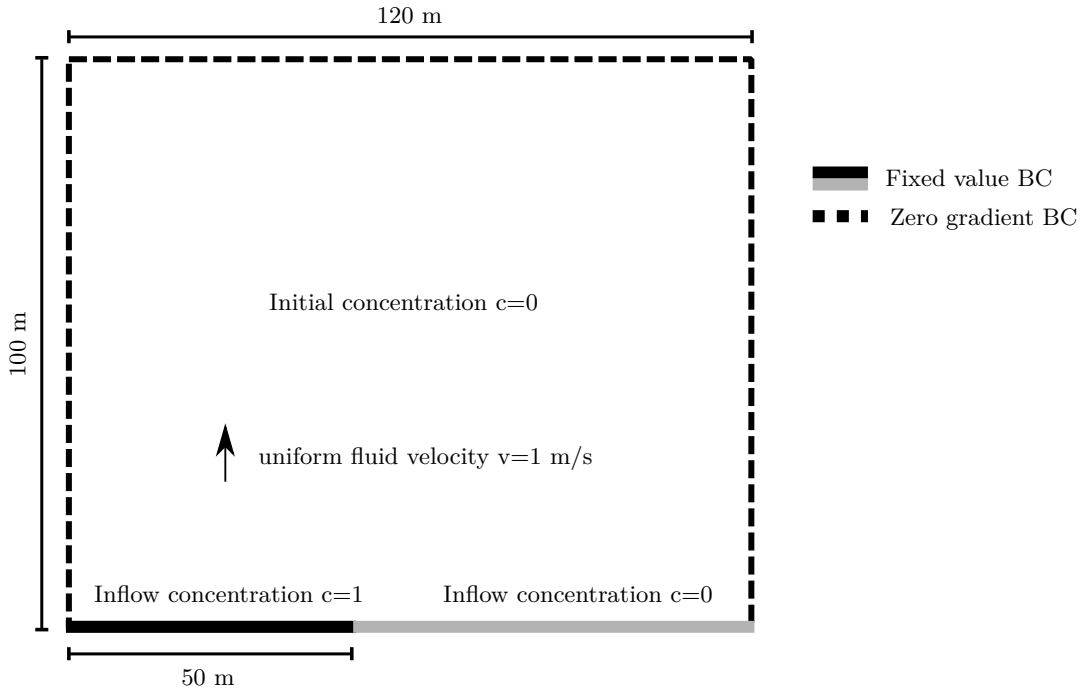

Fig. 5.9: Geometry and numerical setup for the advective diffusion validation example

The dimensions of the numerical model are selected to be sufficiently large to not affect the results within the simulated time scale. The material and transport properties of the analytical and numerical solution are selected in agreement with Šimůnek et al. (1994) with the center width a=50 m, the transverse and longitudinal diffusion coefficient D_s=1 m^2/s, the liquid flow velocity $\boldsymbol{v}_l$=1 m/s and the center concentration c_0=1 mol/l. The results are compared as different concentration isolines computed at 365 days after the start of the transport on the left side of Fig. 5.10. In addition, the ingress of the species is displayed as concentration isolines (c=0.1) at different time steps on the right side of the same figure.

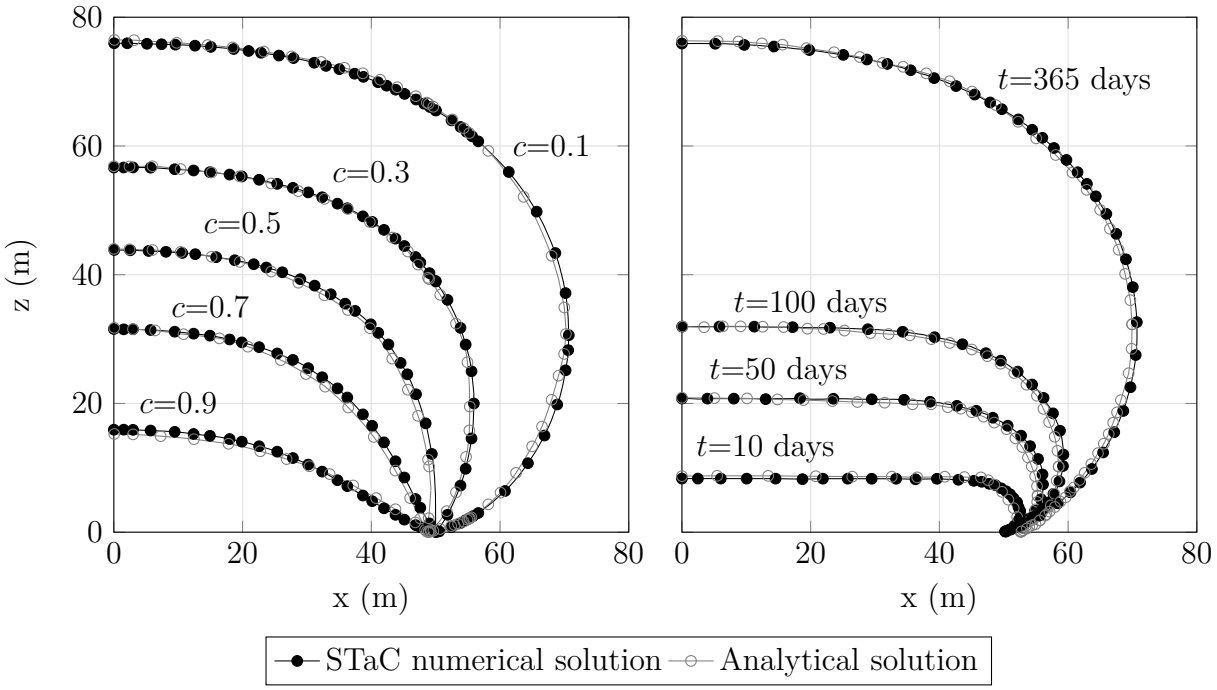

Fig. 5.10: Comparison of the numerical solution obtained by the presented approach and the analytical solution of (Javandel et al. 2013) for an advective-diffusion evaluation case

Both comparisons show a good agreement of the numerical results with the analytical solution. Therefore, the applied solution method can be validated as sufficiently accurate. This means that generally more limitations and restrictions are introduced by the precision of the selected material parameters and homogenization than by the numerical solution.

5.3 Heat transport

The differential equations applied for the heat transport solution have the same equation structure as the combined advective-diffusion equations. If the diffusion coefficient D_s of an ionic species is substituted with the thermal conductivity and the flow rates of the moisture phase by the heat transport rate, the similarity is evident. Hence, the heat transport solution can be validated with the same accuracy as the solute transport.

In order to show the applicability of the framework for heat transport in an actual structure, the numerical results are compared to a set of recorded concrete temperatures varied according to seasonal changes within the Schluchsee dam. The applied model is selected to describe the heat exchange at the dam's downstream face, accounting for long and short wave radiation, cooling induced by evaporation and the convective heat exchange with the ambient air. The

model is evaluated with the temperatures simulated and recorded at 20 and 80 cm beneath the dam's downstream surface. The model uses the recorded local climate data to derive the incoming and outgoing heat fluxes based on the detailed model description in Görtz et al. (2022). The results of the developed modeling approach are compared to the measured concrete temperature in Fig. 5.11 for the whole modeled period of 5 months.

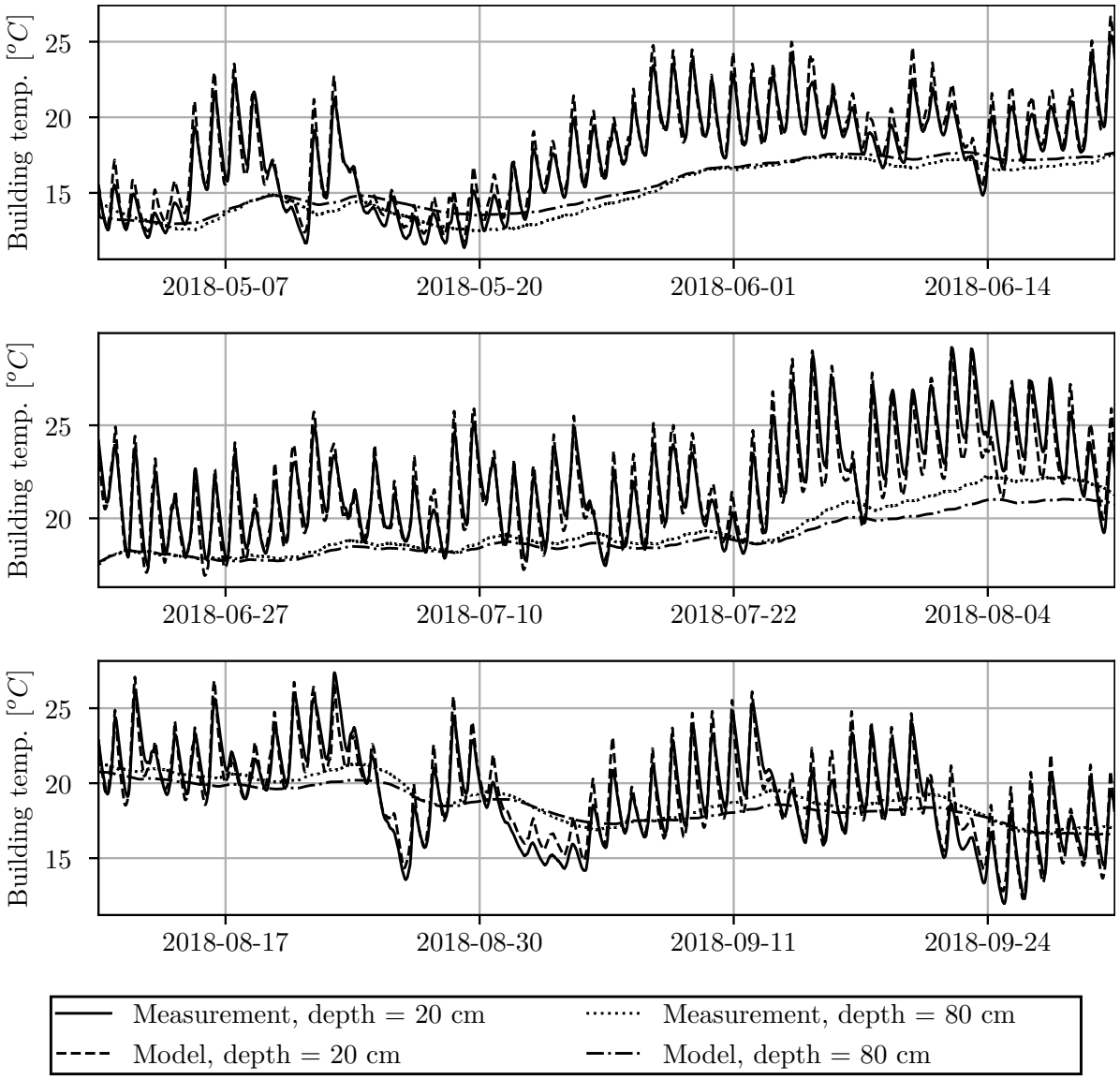

Fig. 5.11: Comparison of the results of the heat transport solution in STaC and the measured concrete temperatures at 20 and 80 cm below the Schluchsee dam's surface for 5 months modeling period (Görtz et al. 2022)

Based on the complexity of the meteorological data, e.g. changing scatter of direct and diffusive short wave radiation, transient change of longwave radiation based on particular body

temperatures, changes in cloudiness and all other constantly updating environmental factors on the actual structure, achieving high precision predictions is quite challenging. Therefore, the achieved accuracy for the prediction of the material temperatures based on changing climatic conditions over 5 month is quite good. Thus, the model cannot only solve the differential equation with sufficient precision but also predict complex cases of existing structures with good precision.

5.4 Mechanical solution

The results computed in the mechanical solution domain are compared to different results published in the literature. In this context, the Koyna gravity dam serves as a benchmark in numerous publications for validation of mechanical solutions in the case of massive structures (e.g. Gogoi et al. 2007; Cai et al. 2008; Hariri-Ardebili et al. 2016) and thus is selected here for comparison. The dam has a 103 m high cross-section, which is modeled as a 2D case. This means that the dam model is only composed of one element in the longitudinal direction while assuming a plain-strain formulation. The loads that are applied for this case are dead loads induced by gravity and the hydrostatic pressure of the water at the upstream face. The applied water level w_{se} is varied for the different cases. To allow for a comparison with published cases, the foundation rock of the structure is not modeled in agreement with the published literature. The dam displacement at the foundation joint is fixed in all directions. The applied loads and geometry are displayed on the left side in Fig. 5.12.

The structure's material properties are adjusted in agreement with the published literature (Bhattacharjee et al. 1995; Sha et al. 2017) as these values have been adopted in almost all subsequent studies. A summary of the material values is displayed in Tab. 5.3.

Tab. 5.3: Mechanical properties of the Koyna dam model

Parameter	**Value**	**Unit**
Youngs modulus	25	GPa
Poisson ratio	0.2	-
Solid density	2450	kg m^{-3}
Fracture energy	100	N/m
Tensile strength	1	MPa

The first evaluation of the results is done for the horizontal displacement at the dam crest with different upstream water levels for a pure elastic solution. This benchmark test has

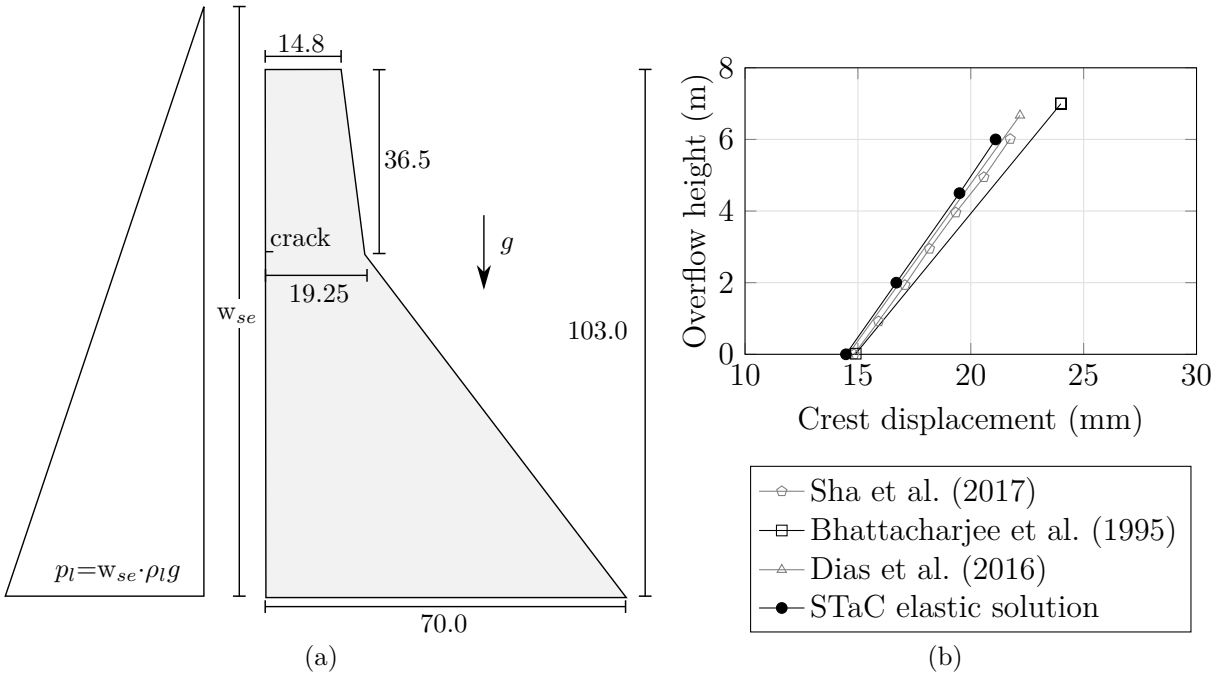

Fig. 5.12: Geometry (m) and loads applied to the selected cross-section of the Koyna dam (a) and horizontal crest displacement as computed with the developed framework compared to displacements published in the literature (b)

been selected as the computed crest displacement has been displayed in multiple published investigations. The upstream water level is denoted as "overflow height", computed as the height difference of the water level compared to the crest level of the structure. The computed results for the crest displacement of previous studies are compared to the numerical results with the developed framework on the right side of Fig. 5.12.

It is evident that the results of the previously published studies already have a certain scatter, which might be partly introduced by minor deviations in the geometry, load applications or numerical solutions applied. Nevertheless, within the scatter of the published results, the crest displacement computed with the developed approach shows a good agreement within the uncertainty of published data for the different water levels.
No stress distribution for the Koyna dam was published in the literature. Therefore, the results of the stress distribution computed with the adopted approach are compared to the results of the stress distribution obtained with the commercial, FEM-based code of ANSYS mechanical. The results are displayed for the horizontal and vertical stress for the cross-section of the Koyna dam in Fig. 5.13.

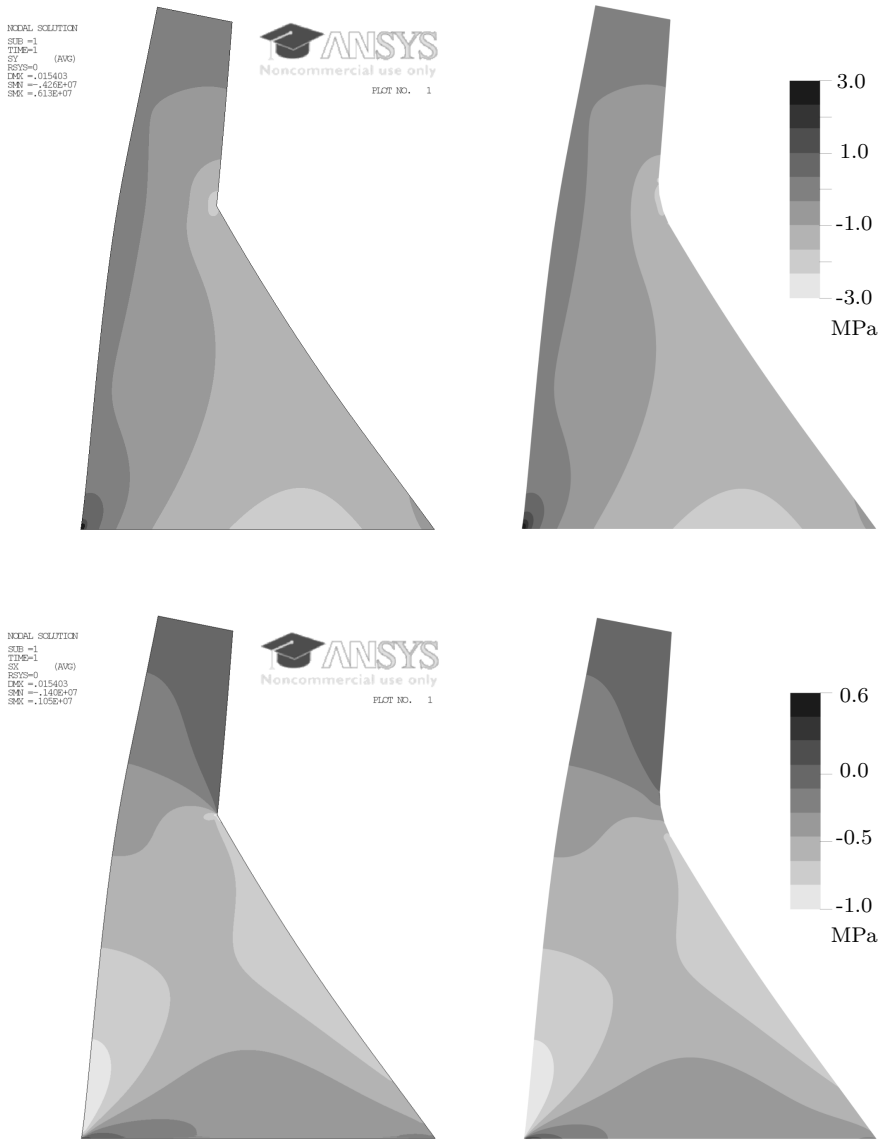

Fig. 5.13: Comparison of the vertical (top) and horizontal (bottom) stress distribution obtained with ANSYS mechanical (left) and the presented framework (right). The cross-sections are displaced with the computed displacement vectors magnified 1000 times.

It is apparent that both stress distributions show a good agreement over the entire cross-section, confirming the results of the previous evaluations of the crest displacement.

Within a second validation, the obtained inelastic solution is evaluated. This comparison is conducted by comparing the computed crack path to the crack paths published in previous studies. The crack path within this work is obtained by cells that are subjected to stresses exceeding the material's yield strength and thus are subjected to plastic strain in the solution.

The deformed structure during cracking and the inelastic cells are displayed on the left-hand side of Fig. 5.14. This crack path is then compared to the data of the previous studies on the right side of that figure.

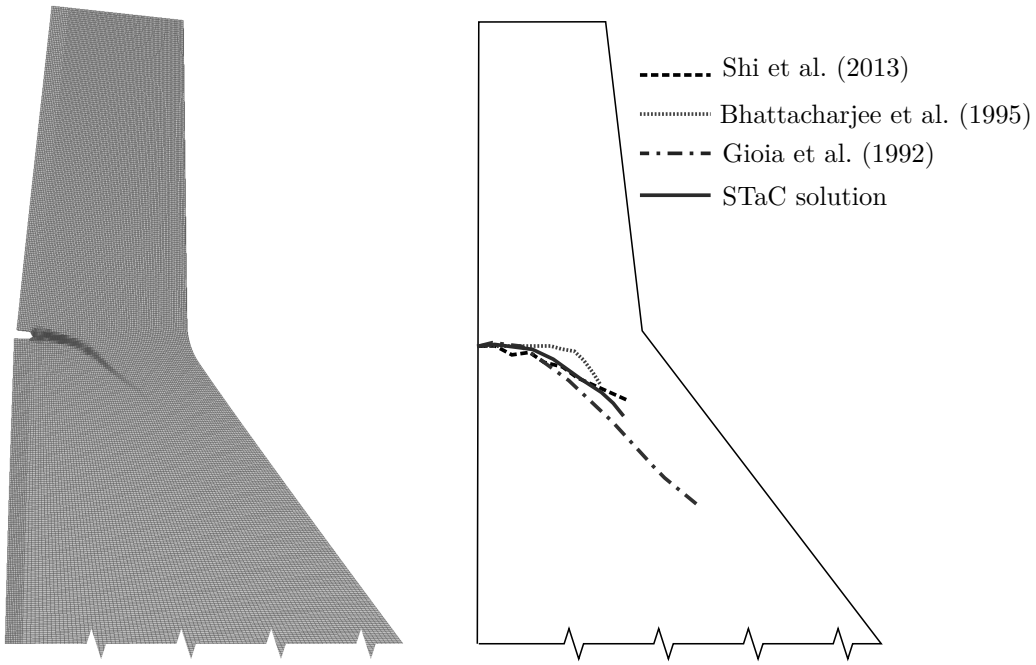

Fig. 5.14: Computed crack path and deformed model of the developed approach (left) and comparison of the computed crack path to published results for the same case (right)

The computed crack path corresponds well with the results from the previous studies. Nevertheless, the non-linear solution during the localization of strains requires a careful ramping of the load in order to avoid non-physical oscillations and results.

5.5 Chemical solution

The chemical solution domain is validated for test cases that are closely linked to the application reference case presented in the next chapter. However, as the chemical domain does not compute any transport but only solves the laws of mass action and the mass balance equations for each cell after each time step, no other error is induced by the spatial discretization. Nevertheless, as the chemical equilibrium is only assessed for each cell, the applied mesh sizes still influence the spatial resolution of the results.

Given the fact that no discretization error occurs, the precision of the solution can be directly assessed by the precision of the solution regarding the residuals of the LMAs and MBEs. As

both quantities are directly solved in the solution, the accuracy of the solution sequence is inherently controlled by the applied residuals for convergence. Thus, the accuracy is evaluated after each solution step based inherently.

In order to ensure a physically correct solution, the computed results are also compared to results obtained with the well-established chemical solver Phreeqc (Parkhurst et al. 1999) for five evaluation cases. Phreeqc has been validated within numerous research projects and remains one of the most commonly applied solver for (geo-) chemical projects (e.g. Marty et al. 2014; Šimůnek et al. 2016; Sanchez et al. 2020; Plusquellec et al. 2017). As the applied activity model of Samson et al. (1999a) (see Eq. 4.28) is not available in Phreeqc, this model could not be selected for a direct comparison. Therefore, the ionic activity coefficients computed in Phreeqc (Davis equation Davies 1962) differ slightly and thus affect the results to a small degree.

For the evaluation cases, the dissolution of the main cement phases CSH, portlandite (CH), ettringite (AFt) and monosulfate (AFm) is computed. The selected dissolvable cementitious solid phases as well as their dissolved ionic composition are displayed in Tab. 5.4.

Tab. 5.4: Solid phases and equilibrium relations according to Samson et al. (2007b)

Solid phase	**Equilibrium relation**	**-log(K_s)**
CH	$CaOH^2$	5.2
CSH	$CaOH^{2*}$	6.2
AFt	$Ca^6OH^4SO_4{}^3Al(OH)_4{}^2$	44.0
AFm	$Ca^4OH^4SO_4Al(OH)_4{}^2$	29.1
Gypsum	$CaSO_4$	4.6

*:Simplified model (Samson et al. 2007b)

In addition to the dissolution of solid phases, two aqueous reactions are modeled as well. Both reactions and their implemented equilibrium constants are displayed in Tab. 5.5.

Tab. 5.5: Modeled aqueous reactions and applied equilibrium constants

Aqueous reactions	**-log(K_c)**
$2H_2O \rightleftharpoons H_3O^+ + OH^-$	17.49
$Ca^{2+} + OH^- \rightleftharpoons CaOH^+$	1.21

For evaluation, these solid phases are dissolved in "pure" H_2O as well as in specific initial ionic composition termed "reservoir water". The "reservoir water" describes an ionic setup that represents the composition of a natural reservoir. This initial ionic composition of the reservoir

is selected according to the averages of the measured values displayed in Patil et al. (2013), representing the distribution of ionic species in a freshwater reservoir close to the location of the Koyna dam. The selected initial species compositions as well as the associated species coefficient for the activity model are displayed in Tab. 5.6.

Tab. 5.6: Initial ionic composition (Patil et al. 2013) and activity species coefficients (Samson et al. 1999a) for the chemical evaluation cases based on pure and reservoir water

Species	**Pure c_s (mmol/l)**	**Reservoir c_s (mmol/l)**	**Coefficient b_i (m)**
OH^-	10^{-4}	10^{-4}	$3{\cdot}10^{-10}$
Ca^{2+}	0	0.3	$1{\cdot}10^{-13}$
Na^+	0	0.4	$3{\cdot}10^{-10}$
K^+	0	0.01	$3.3{\cdot}10^{-10}$
SO_4^{2-}	0	0.004	$1{\cdot}10^{-10}$

Different dissolution periods are evaluated as the solid phase composition changes with the depletion of the solid phases during leaching. The dissolution periods are selected based on the complete removal of a solid phase, which changes the ionic composition of the water as the depleted solid phase cannot be dissolved anymore. As portlandite (CH) is depleted first, followed by CSH and AFm, the results are compared again after one of the solid phases has been completely removed. Consequently, five different setups are computed, which are summarized in Tab. 5.7.

Tab. 5.7: Available solid phases during the different leaching periods

Leaching period	**CH**	**CSH**	**AFm**	**AFt**
P1	✓	✓	✓	✓
P2		✓	✓	✓
P3			✓	✓
P4				✓

Each solution is computed as an equilibrium state as described earlier. Therefore, it is inherently assumed that “pure” and “reservoir” water is brought in contact with the solid cement phases long enough to achieve equilibrium. The computed activities of the ionic species are then compared between both simulation results. At the same time, the number of moles per solid phase that need to be dissolved or formed to achieve these ionic activities is also compared.

The results of both codes for the different dissolution periods are compared in Fig. 5.15. On the left side of the figure, the computed pH values are displayed for the different dissolution

periods for reservoir water (P1-P4). The dissolution periods are evaluated for the contact with the "reservoir water", which contains the initial ionic composition described in Tab. 5.6. In addition, the computed pH values for contact with pure water are displayed as well. The computed ionic activities of the different species are displayed on the right of Fig. 5.15 for both numerical solutions.

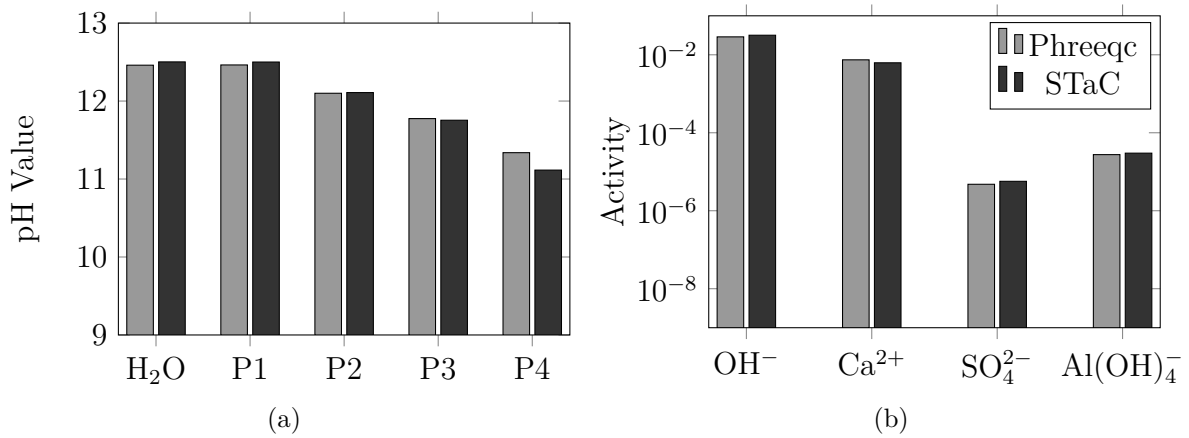

Fig. 5.15: Comparison of calculated pH values during the different periods of dissolution (a) and computed ionic activities for leaching periods P1 in contact with pure water (b)

It is evident that all computed results resemble the same characteristics as the solution results of the Phreeqc code, even when a different activity model is applied. In addition, the decrease in pH values with the reduction of the calcium content in the solid phase can be observed. As described before, this characteristic reduction of pH value is generally observed in cement-based materials during leaching, making it obvious why a low pH value is generally associated with a leached material. Hence, the developed framework is also able to replicate these characteristics.

The ionic activities, as well as the amount of solid phase dissolved or precipitated for achieving this equilibrium, are displayed on the right side of Fig. 5.16 for both solvers. The continuous removal of calcium phases during the successive leaching periods (P1-P4) and their effect on the results are displayed from top to bottom within the figure.

Again the results show a good agreement between for both solvers, while minor deviation can be explained by the different activity models applied. Based on the framework's flexibility, additional activity models could be implemented for further evaluation in the future. Nevertheless, the achieved accuracy for the chemical solution is sufficient to resemble the chemical changes in the cement-based material phases as uncertainties in the material's chemical composition are expected to be larger than the errors induced by the solution procedure.

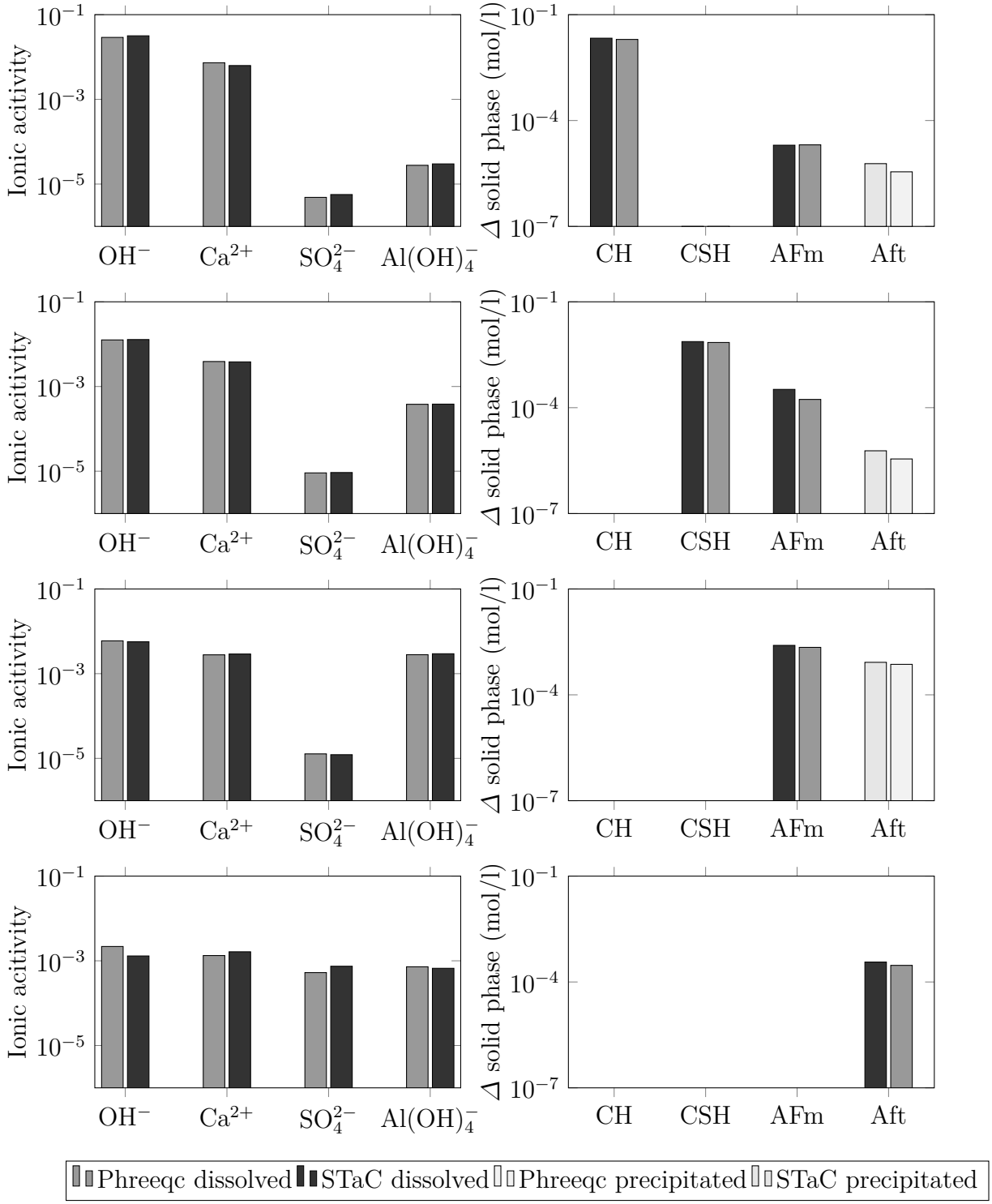

Fig. 5.16: Comparison of the calculated ionic activities (left) and dissolved and formed solid phases (right) using Phreeqc and the developed solver for the periods of dissolution (P1-P4 from top to bottom)

6 Modeling of deterioration of gravity dams

The developed approach is applied to model the deterioration of a gravity dam to evaluate the structure's service life. The selected dam is located in western India and is not affected by freeze-thawing actions based on the local climate. As a result, the main impacts on the dam are cracking and leaching of the cement phases. The selected dam is modeled for sets of different scenarios and setups to compare the effect of structural heterogeneities, concrete joints, cracking, various maintenance measures and the impact of varying modeling complexities. The studied dam case does not only serve as a demonstration but it is also the first combined model to compute the aging of a dam structure with such a fully coupled model. This selected case does not imply a limitation of the developed approach to applications to dam structures as the method can evaluate and compute a multitude of structural (deterioration) problems.

6.1 Modeling scenarios

The deterioration of the gravity dam is studied for a set of different scenarios. This allows the evaluation of the effect of varying modeling simplifications and complexities. Three sets of computational runs are compared, aiming to assess different effects. The first set of runs evaluates the long-term deterioration of the entire dam section without the impact of discontinuities like cracks and joints. Yet, the material properties vary across the structure to estimate the effect of heterogeneities on the deterioration rates. The modeled scenarios for the first set are selected as:

- The dam material is chosen to be homogeneous over the cross-section, excluding joints, cracks and changing concrete properties (homogeneous case)
- The variance of the material properties between the different concrete sections (blocks) is implemented in a case that will be further labeled as "block-wise" solution

Within the second set of comparisons, the general effect of joints and cracks on the deterioration rate is studied for the upper part of the Koyna dam. This part of the dam is selected as this section is subjected to the highest flow velocities and, thus, the highest deterioration rates.

As the interaction of the different transport mechanisms across the joint's and crack's interface influence the observed deterioration rates, a base setup is run, which is compared to varied modeling complexities. The varied parameters include the different exchange terms between matrix and joint, the effect of cracking, and the effect of varied hydraulic conductivities. A fully coupled setup is applied within the third set of modeling runs to evaluate the effects of two durability measures on deterioration rates. The results are compared for the effects of improved bonding of the joint interface as well as the application of an additional sealing layer on the upstream face. Thus, three different scenarios are compared:

- The dam modeled as before without any further durability measures
- An additional sealing layer improves the dam's upstream surface
- The dam's joints are enhanced by measures that increase their tightness and bond

Based on the comparison results, the impact of these countermeasures is discussed.

6.2 Model setup

The Koyna gravity dam is selected based on its role as a benchmark case in the scientific community for dynamic, static, and hydrocracking cases (Shi et al. 2020; Sha et al. 2017; Pal et al. 2013; Bernier et al. 2016; Wang et al. 2015). Thus, using the same structure as a benchmark for modeling deterioration seems reasonable.

6.2.1 Model geometry

The dam geometry is taken based on literature data and thus is identical to the previous setup displayed in Fig. 5.12. For the following computations, no initial cracking is considered. Again the foundation rock below the dam is not modeled similarly to cases in the literature. This simplification also affects the chemical solution as the rock material's chemical composition and the boundary interfaces' composition would add additional complexities. These effects are outside the scope of this study. The entire dam geometry is modeled first to evaluate the impact of block-wise heterogeneities, while only the upper 39 m section of the dam is modeled for the last cases. The dam geometry is meshed into primarily brick elements with an average element edge length of 0.25 m. As no data on the concrete construction techniques of the dam is accessible, the dam structure is assumed to be built with concrete sections of 4 m in height and roughly 12 m in length. However, based on the changes in available spaces on the

downstream side, the block length varies to avoid unrealistically small blocks. These block-wise properties are displayed for the initial distribution of concrete porosity on the right of Fig. 6.1.

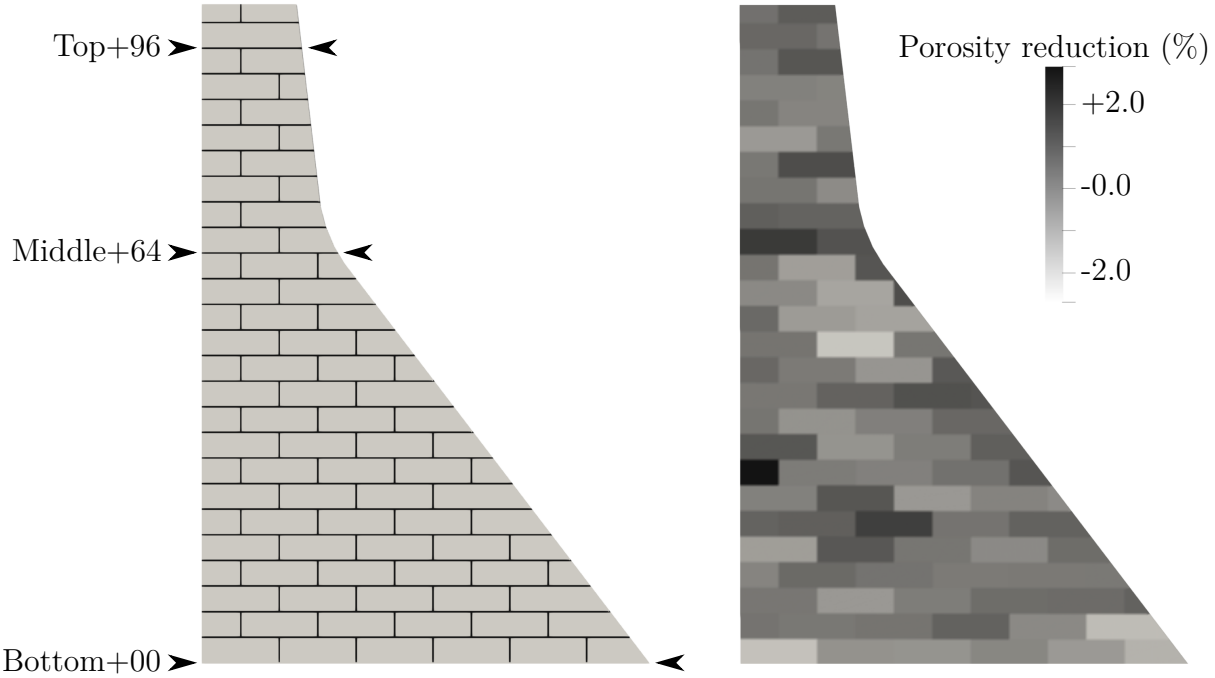

Fig. 6.1: Location of evaluation sections (m) of the modeled concrete joints (left) and initial changes in porosity as a result of the block-wise construction (right)

Most material properties described in the following are selected according to typical literature for concrete dams, as no specific data for the Koyna dam is published. As a result, the results are less representative of the actual Koyna dam but a more general solution for dams. The parameters selected and derived for the different solution domains, the applied boundary and initial conditions are displayed in the following.

Moisture transport

If no joints or cracks are modeled, the description of the moisture transport is based on the single permeability solution. When joints or cracks are present, the dual permeability solution is used. Independent of the applied model, the boundary conditions of the moisture domain are always applied identically for matrix and fracture as the external effects do not differ for both domains. The water level at the upstream side is 100 m which leaves 3 m of available freeboard to the dam crest. On the downstream side, a constant relative humidity of the air of 80 % is assumed, which approximately represents the annual average in western India. This assumption is implemented on the downstream side as “free drainage” boundary (see Annex B).

The initial water content is also in equilibrium with the local average humidity of 80 %.

This setup is simplified for the second set of comparisons to make the computed results more comparable. Therefore, all model runs are started from the same initial conditions calculated in a previous run. This pre-run is conducted using "outflow" boundary conditions at the downstream side and a dual permeability model without any exchange until a steady-state solution is found. Then, the model runs are started from this solution to remove the increasing saturation's impact until a steady-state is reached to allow a clear comparison of each parameter.

Again, the moisture retention curve is implemented based on the Van Genuchten isotherm (Eq. 4.4). The parameters of the moisture retention curve for the homogeneous concrete are selected as displayed previously in Tab. 5.1. The hydraulic conductivity of the matrix is chosen as 10^{-10} m/s. The parameters of the joints are selected based on data published in Pacelli et al. (1993). The study measured the hydraulic conductivity of cylindrical concrete samples with joints for the Itaipu dam. It is found that the conductivity of the samples increases up to 10^{-9} m/s for poor joint treatment. Based on this increase, the permeability contribution of the raw joint area is then calculated using Eq. 4.9. The permeability of the joint zone is then computed as $3{\cdot}10^{-5}$ m/s for a sample diameter of 20 cm. By using the PPM (Eq. 3.71) this result can be linked to an average joint aperture of 60 µm when ζ_f is set as 10. This value is then used for the initial joint porosity as well as the average capillary suction by using Eqs. 4.48 and 3.1. For cases with cracks and joints, the moisture transfer coefficient ω_l is set according to the joint geometry with ζ_s equal to 10. The adopted values are, therefore, similar to the factors that have been validated for the measured concrete joints (see Sec 5.1.2). If moisture exchange between matrix and joint is excluded, the transfer coefficient ω_l is set to zero.

6.2.2 Thermal transport

As described before, thermal transport can be an essential aspect of the deterioration of a concrete structure. Thermal cracking induces preferential paths for moisture flow and additional weak zones for further cracking, but temperature changes can also affect the chemical domain. The temperature effects on the chemical domain include changes in the ion activities, combined with temperature-dependent solubilities of the solid phases. Thus, it is possible that solid phases that dissolve during a warm day partially precipitate again during a cool night. In addition, similar long-term changes between winter and summer could arise. As all these temperature effects add additional levels of interaction to an already complex solution, these

effects are excluded from the computed cases. Nevertheless, these effects can be studied with the developed approach in further studies.

6.2.3 Solute transport

Effective diffusion coefficients for the material and species coefficients for the activity model are required for the solute transport solution. As the activity model of the validation example (see Sec. 5.5) is applied again, the same species coefficients are applied as well. The effective diffusion coefficients of the ionic species are selected in agreement with Samson et al. (2007b) and are displayed in Tab. 6.1.

Tab. 6.1: Effective diffusion coefficients of the ionic species (Samson et al. 2007b)

Ionic species	$\mathbf{D_e(10^{-11}m^2/s)}$
OH^-	40.6
Ca^{2+}	6.1
Na^+	10.3
K^+	15.1
SO_4^{2-}	8.2
$Al(OH)_4^-$	4.2

If a diffusive exchange flux between fracture and matrix domain is considered, the transfer coefficient ω_s needs to be adjusted. In the following cases, this coefficient is selected identically to the moisture transfer coefficient ω_l. The coefficient is set as constant here, but this assumption can be improved with experimental data in future works. In particular, a dependency on the leaching degree and fracture aperture is likely to yield more realistic results. Like the moisture transfer coefficient, the diffusive exchange coefficient is set to zero when the diffusive exchange is excluded. The initial ionic composition in the liquid phase is selected to be in equilibrium with the available cement phases. This equilibrium is calculated within a previous solution step and thus is identical to the values presented in the chemical validation example (see Fig. 5.16). The ionic composition of the lake water is assumed to be constant and is taken as fixed value boundary conditions for each species at the upstream side. A zero gradient boundary condition is applied at the dam's downstream side.

6.2.4 Chemical solution

The initial solid-phase composition as well as the modeled solid phases affect the chemical solution. For the initial composition, the chemical composition is adopted according to

the data published by Samson et al. (2007b). As the cement content of the described mixture (280 kg/m^3) is higher than common mixtures for dams (130-270 kg/m^3) (ICOLD 2008) the solid phase composition is scaled down to a cement content of 200 kg/^{3} for the modeled case.

Each phase requires molar volumes to link the molar changes to volumetric changes. Here the molar volumes published in Marty et al. (2014) are used to compute the volumetric phase content. The molar volumes and the adopted initial solid-phase composition of the dam concrete are displayed in Tab. 6.2.

Tab. 6.2: Initial solid-phase composition and molar volumes (Marty et al. 2014) of the dam concrete

Solid phase	**Initial (mol/m^3)**	**Molar volume (cm^3/mol)**
CH	824.8	33.1
CSH	575.1	84.7
AFt	35.6	311.2
AFm	5.3	710.3
Gypsum	0.0	73.8

The associated dissolution/precipitation and aqueous reactions for the ions and solid phases are selected identical to the validation examples (see Tab. 5.4). For double permeability solutions, the dissolution of a solid phase is either associated with removal from the joint or matrix. The contribution is selected depending on the domain where the phase is dissolved. Thus, a solid phase dissolved into the liquid in the joint will contribute to the joint's pore space. The dissolution then affects the joint's porosity and hydraulic conductivity. Nevertheless, it seems unlikely that joints can grow to infinite sizes as aggregates and other inert particles remain in the joint location. Therefore, the joint's aperture is limited to a specific value, and any further dissolution is contributed to the matrix. Here, the maximum aperture associated with the joint is selected to be 5 mm. As no data has been published on this topic, this number is set based on rough observation for the joints studied in Görtz et al. (2021c). Nevertheless, further research is needed to validate the selected value thoroughly.

Different material properties for each concrete block are required for the computation of the construction blocks. For this, the variance of the material properties between the concreting sections (blocks) needs to be selected. This variance is based on changes in initial cement content (solid phase content) for the computed case. Based on this change in available cement phases, the changes in material properties such as porosity or compressive strength can be derived for each block as described in Sec. 4.6.5. This simplifies the variance of mixture components, as the

impact of mixing and all other construction effects can also induce unrelated variations for the material. However, the multitude of combinations is not the subject of the computed cases but could be evaluated in further studies. In order to select a coefficient of variance for the phase contents, the observed coefficient of variance for concrete strength is studied. In experiments of Dayaratnam et al. (1976) an average coefficient of variance equal to 0.17 is found. When a residual strength of 25 % is assumed, the coefficient of variance for the initial solid-phase content is derived as 12.5 %. The measured values of the samples in Dayaratnam et al. (1976) are found to be a normal distribution in almost all cases. Therefore, a normal distribution is assumed for this study as well. The initial solid-phase contents then can be randomized for each block based on the variance and selected distribution. Only one set of material properties is studied for demonstration in the computed cases. Nevertheless, other impacts of the block heterogeneities could be studied with the described approach. The randomized block setup is displayed on the left of Fig. 6.1.

6.2.5 Mechanical solution

For the mechanical solution of the gravity dam, the mechanical properties and assumption of the Sec. 5.4 are applied again. This is done to keep results comparable to previous results within this work and published literature. As mechanical properties for the joint are missing, the joint's properties are assumed to reach 50 % of the material's monolithic strength. These values are within the range of the findings of Pacelli et al. (1993). Similar to the mechanical properties, all further modeling aspects are kept identical. This means the same elastic-plastic model and the same plain-strain formulation are selected. Nevertheless, elastic-plastic modeling is only implemented for cases that include the effects of cracks.

6.2.6 Time steps

The timestep size is adjusted during runtime based on the observed convergence rates. Initially, a small timestep is selected, increasing if fast convergence rates are achieved for all solution domains. If one solution domain diverges or converges slowly, the timestep size is reduced again. As the mechanical solution requires the most computation, this domain is only computed every 1000 days. This can be justified by the slow changes in solid-phase compositions and thus the stiffness of the dam. Based on these slow changes, the solution interval is still large enough to capture the continuous changes in the pore structure induced by the mechanical domain. All other domains are computed for every time step. The total runtime of the full model is set to 500,000 days and the reduced geometrical model of the dam top is computed for 55,000

days corresponding to 150 years. These durations are chosen to be sufficient to visualize the long-time aging processes of large structures.

6.2.7 Evaluation of the results

For the gravity dam case solution, 102 variables are computed for each cell of the mesh. It includes scalar variables like moisture saturation, pressure head, species concentrations and activities, solid-phase densities, and stress tensor and deformation vectors. In addition, the flux densities and directions can be computed for each cell. Different variables (e.g. concentrations) are also calculated for the fracture and joint solution when a dual permeability solution is selected. Some of these variable fields are displayed within the next section for assessment. Key variables are selected and compiled further as not all results can be displayed.

One of the key indicators for deterioration is the change of porosity (see Eq. 4.49), as it represents a cumulative measure of the change of solid-phase content. However, the value of a single cell is not the decisive indication as a greater section needs to deteriorate to cause failure. Therefore, the volume-averaged change in porosity $\Delta\phi_{Sec}$ across all elements E_s of sections is computed as:

$$\Delta\phi_{Sec} = \frac{1}{V_{Sec}} \sum_{e=0}^{E_s} V_e \cdot \Delta\phi_e \text{ with } V_{Sec} = \sum_{e=0}^{E_s} V_e \tag{6.1}$$

As the change in porosity can be associated with the matrix or the fracture space when a dual permeability solution is applied, the above formula is applied for both domains. The computed change in porosity then can be used to derive the degree of deterioration (or leaching) for the section δ_{Sec} by comparing the computed change to the maximum possible change ϕ_{Max} that occurs when all solid phases are dissolved:

$$\delta_{Sec} = \frac{\Delta\phi_{Sec}}{\Delta\phi_{Max}} \tag{6.2}$$

In order to simplify further descriptions, this degree of deterioration will be referred to as deterioration (%). The described evaluation process is applied for the sections that are marked on the left of Fig. 6.1. These sections include the lowest horizontal joint, labeled as “bottom”, the “middle joint” at the critical section and the “top joint” at the dam crest. To display the change in the densities of solid phases, the relative phase density (-) is also shown. This quantity is derived by relating the current phase density to the initial phase density of a phase.

6.3 Influence of construction blocks on the deterioration of a homogeneous structure

The deterioration of a structure without inhomogeneities is expected to occur relatively even across the structure. This is caused by relatively evenly distributed moisture flow rates across the system. Low deviations are obtained when hydraulic conductivities are fairly uniform, and thus flow rates are mainly governed by the thickness of each section as well as the applied pressures. However, within the first period of the deterioration, inflow rates are slightly increased, as the pressure gradient is greater while the moisture saturation is still rising. While the moisture content of a dam is initially increased, the direction of this process can also be reversed for structures in dry environments. Based on the modeled dam's size and the concrete's low hydraulic conductivity, it takes decades for the moisture flow to reach a steady-state. However, a full steady-state does never occur as the hydraulic conductivities continuously change during deterioration. This initial phase of increasing saturation of the gravity dam is displayed in Fig. 6.2 at different times. In all figures, the phreatic line (h_l=0) is also indicated by the white line.

When comparing the displayed saturations, it is evident that the structure is still not completely saturated after 25 years. At the thickest section at the dam heel, the saturation increases up to 50 years. Nevertheless, after that time, a pseudo-steady-state is reached. The position of the phreatic line indicates that large parts of the dam remain below saturation at steady-state. As the moisture transport in the unsaturated material is largely governed by surface forces, their contribution in addition to the applied upstream pressure is apparent. Small changes in the isolines can be observed due to the characteristics of the construction blocks. The isolines shift further into the dam body when blocks are more porous. In contrast, the isolines remain smooth when the dam is modeled as a homogeneous structure. As the slightly different flow rates contribute to these observations, similar effects are also observed when comparing the deterioration between blocks.

Based on the flow direction from the upstream (hydraulic pressure head) to the downstream (relative humidity of the air) side, the solid phases of the upstream faces are dissolved first as the incoming water from the reservoir has a lower ionic concentration. When solid phases are dissolved within the upstream section, the pore liquid is saturated concerning the solid phases. In consequence, no further dissolution occurs in the following sections. However, variations in diffusive flow rates can induce differences which then cause additional phase changes along the

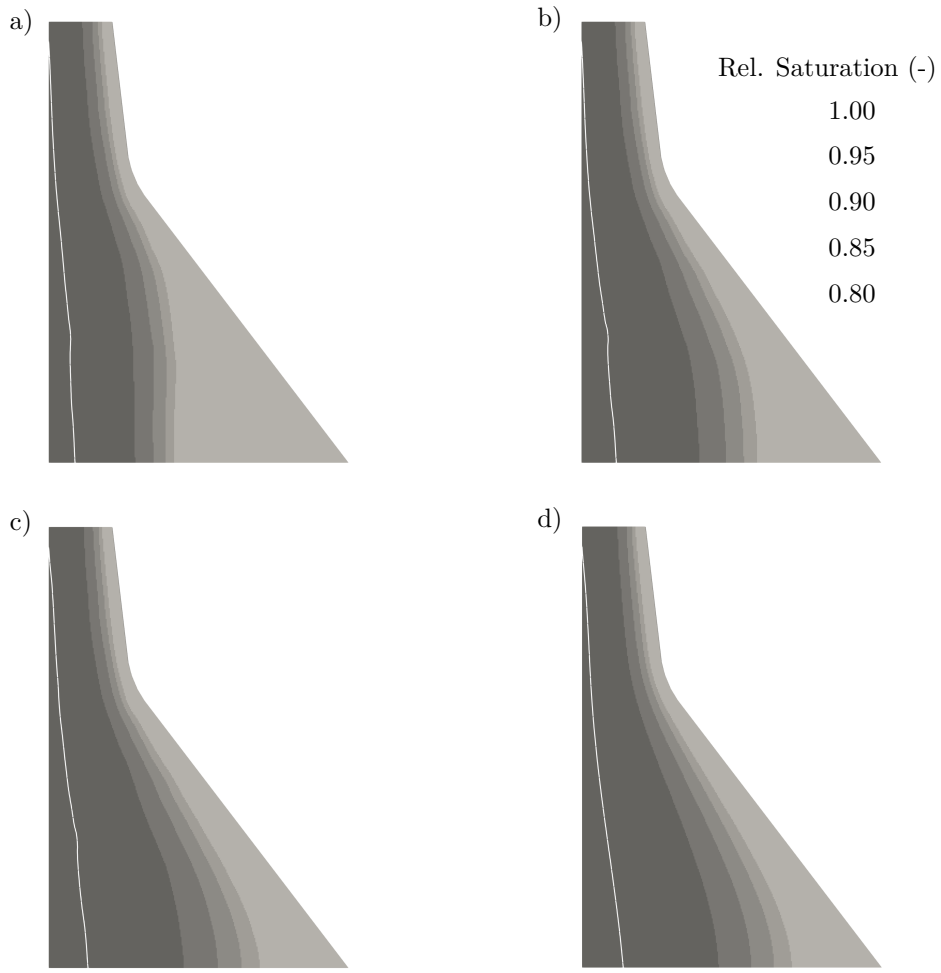

Fig. 6.2: Relative saturation and phreatic line (white) of the Koyna dam for the block-wise case after 25 (a), 50 (b) and 1000 (c) and the homogeneous case after 1000 years (d)

flow path. The computed changes in the solid phase densities are illustrated in Fig. 6.3 after 1350 years of deterioration.

Portlandite has the highest solubility and dissolves first. This is indicated by the furthest progression of its dissolved front. Parts of the ettringite are converted to monosulfate ahead of the portlandite dissolution front, which is similar to the results displayed by Samson et al. (2007b). Once the portlandite is locally depleted, the CSH phases are dissolved in the next step. This is also indicated in the same figure since the depth of removed CSH is the second largest. In the third phase, monosulfate is dissolved while some monosulfate is converted to ettringite at the same time. This conversion process is indicated by the sharp peak of increased ettringite behind sections that are depleted of monosulfate. However, once all monosulfate is removed, ettringite is also finally dissolved.

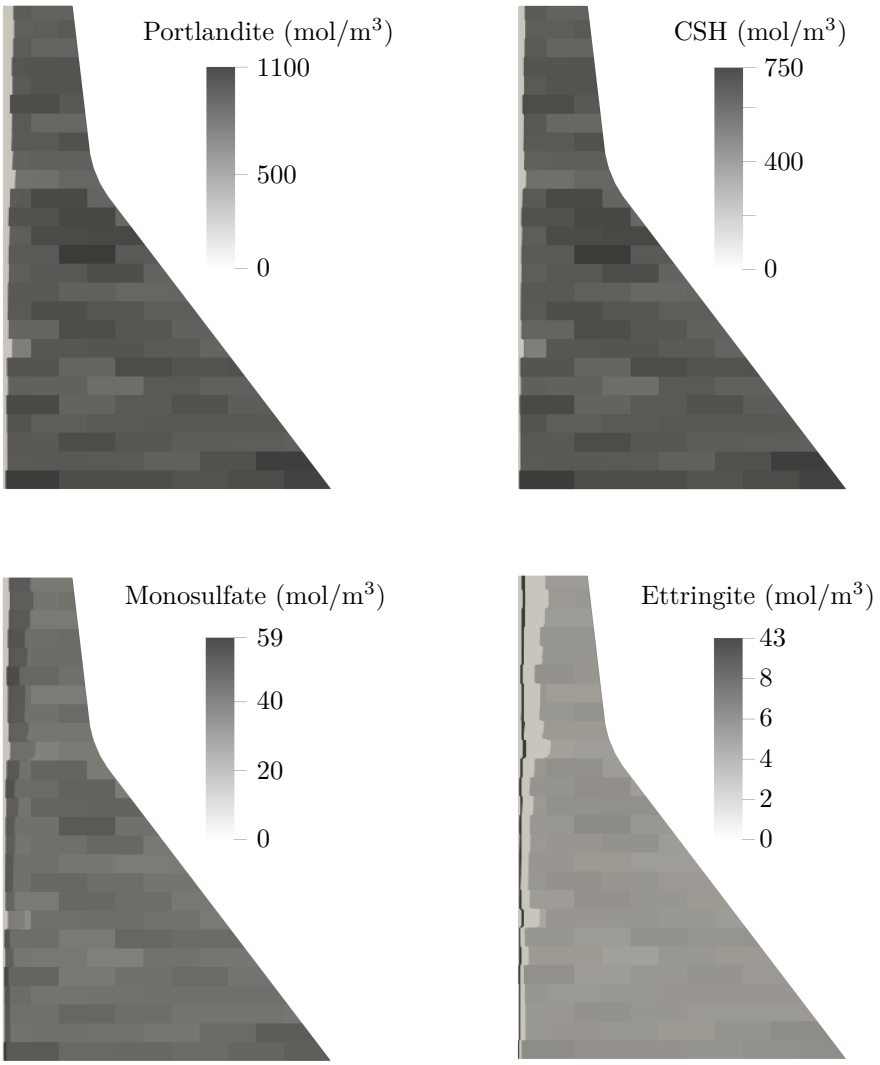

Fig. 6.3: Remaining phase densities (mol/m^3) of the modeled solid phases for the Koyna dam after 1350 years

The depletion of solid phases can also be observed when the ionic concentrations are compared. As long as calcium-rich phases are present, their dissolution increases the calcium concentration in the liquid phase. If no solid phases remain for dissolution, the calcium concentration prevails at the inflow level until the solute reaches a section where solid phases are available. The calcium concentrations within the dam body are compared at three different times in Fig. 6.4.

After 450 years, the reduction of the calcium concentration on the upstream side is only slightly visible for the most deteriorated sections of the upstream side. The change of concen-

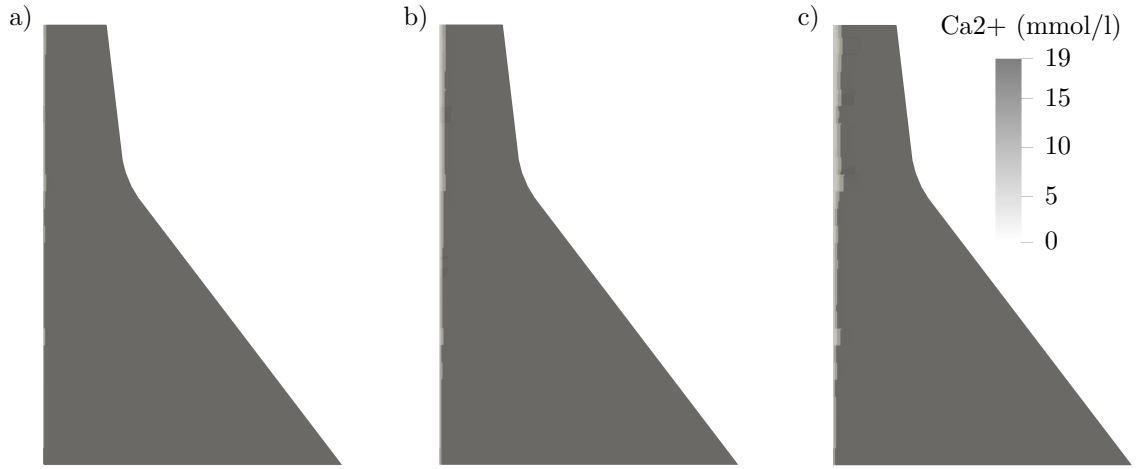

Fig. 6.4: Calcium concentration (mmol/l) in pore water for the block-wise case after 450 (a), 1000 (b) and 1350 years (c)

trations gets more evident after 1350 years, as the difference in their calcium concentrations can easily separate areas of portlandite depletion from areas of CSH phase depletion. Finally, the change in porosity after 1000 years of continuous leaching is displayed in Fig. 6.5. All changes in solid-phase densities are associated with a change in porosity, representing the combined effect of all phase changes.

The reduction of porosity is limited to the upstream sections of the dam, as previously shown by the dissolution of solid phases. Based on their increased flow rates, the largest deterioration is observed at the thinnest cross-sections. The porosity reduction is generally smooth across the structure's height for the homogeneous dam body. At the same time, the implementation of blocks increases or reduces the rate of deterioration in each block section. This is indicated by the slight differences in porosity reduction between blocks. In order to quantify these differences, the change in porosity is computed according to Eq. 6.1 for the middle and bottom sections shown in Fig. 6.1. The results of the changes as average section porosity are shown at the top of Fig. 6.6.

The middle and bottom sections initially have different porosities due to the variance between concrete blocks. While an additional 1.4 % porosity is added to the middle section, the bottom section has a decreased porosity by roughly the same amount. Throughout 1000 years, the average porosity of the middle section is increased by approximately 0.5 %. At the same time, the bottom section's porosity is only increased by a tenth of that value. Again, these values do not mean that these changes in porosity occur uniformly across the entire area but are

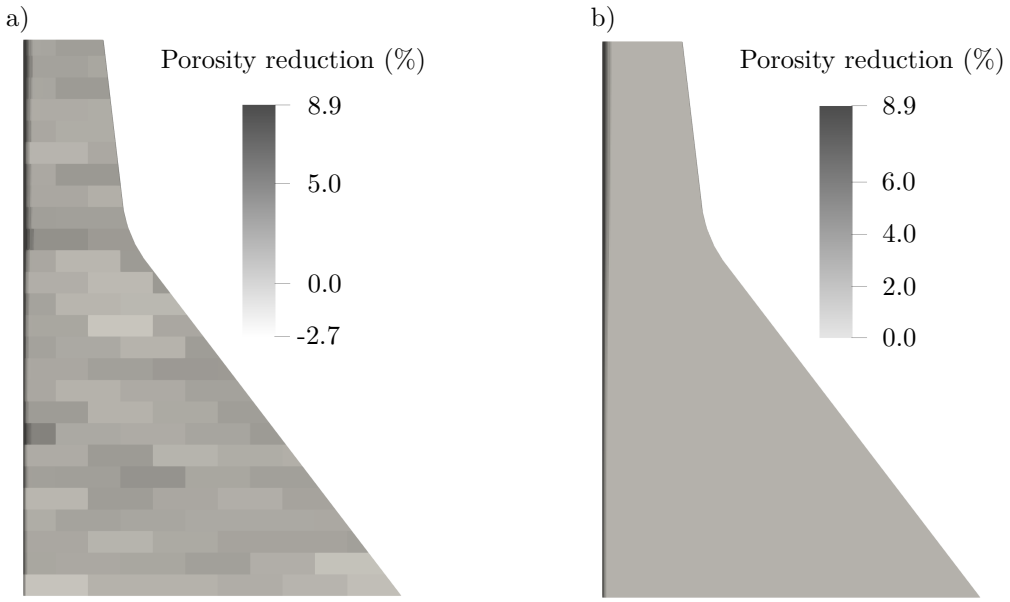

Fig. 6.5: Reduction in porosity (%) of the Koyna dam after 1000 years with (a) and without the effect of concrete blocks (b)

the averaged result of fully deteriorated sections on the upstream and unaffected sections on the downstream side. The difference in deterioration rate is induced by the reduction in hydraulic conductivity for the more dense material at the bottom and the increased hydraulic conductivity for the more porous material in the middle. However, the average porosity is mainly influenced by the initial distribution as the initial changes are still of greater impact after 1000 years. The initial porosity differences are removed at the bottom of Fig. 6.6 to make the block-wise and the homogeneous case better comparable. In addition to the middle and bottom sections, the average deterioration across the entire dam cross-section is also compared.

The results for the deterioration of the middle section are above 5 % for the block-wise and at 4 % for the homogeneous case. Evidently, this difference results from an increased hydraulic conductivity due to the high initial porosity. The inverse of this effect is visible in the bottom section. Here the reduction of initial porosity induces slower deterioration rates. When the average deterioration for the whole structure is compared, it is evident that both cases show almost identical results of 2 % deterioration. This is expected as the average porosity is almost identical for both cases. However, a difference could have been observed for cases where one specific section of the structure shows a significantly enhanced deterioration. In this case, the large deterioration of this section could increase the rates by such a margin that the differences would be visible in the average. For the presented results, this is not the case, and the local variance in material properties does not influence the deterioration in such a

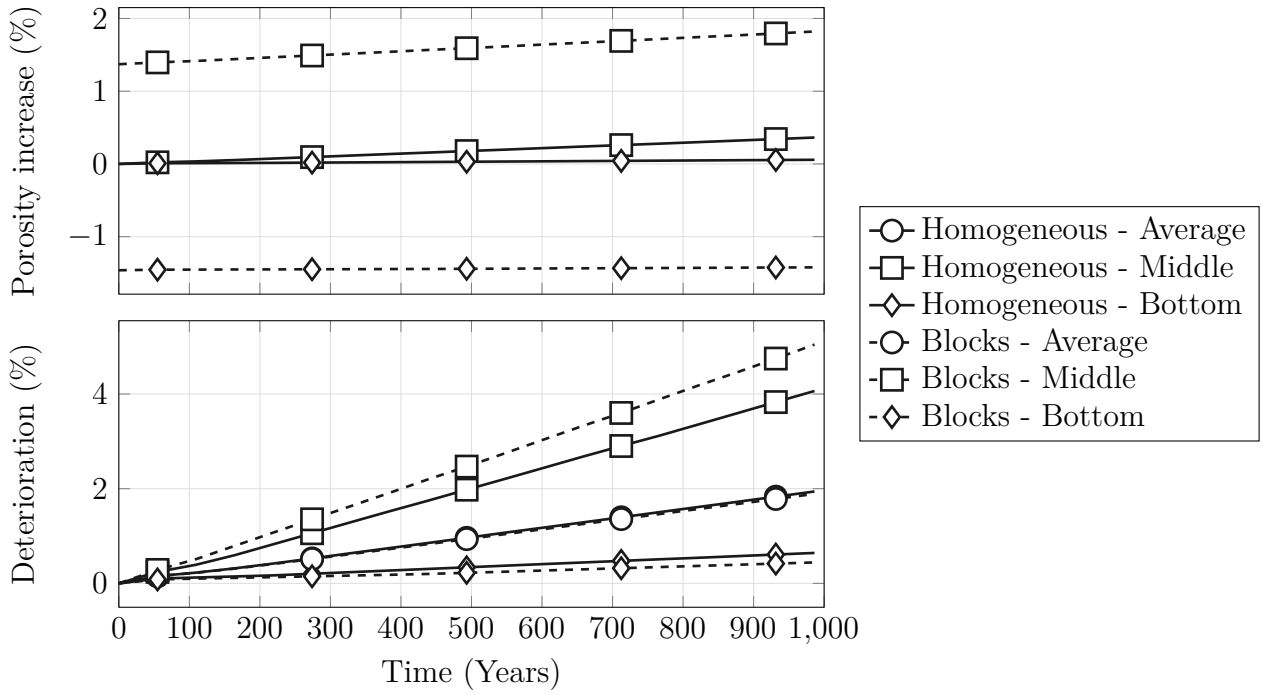

Fig. 6.6: Increase in porosity (top) and deterioration (bottom) for the selected sections for the block-wise and homogeneous case over 1000 years

significant way. Therefore, it can be concluded that the deterioration is influenced noticeably by the construction blocks for the computed case. Nevertheless, this impact is not large enough to essentially change the structure's deterioration within its service life.

6.4 Effect of joints and cracks on deterioration rates

Joints and cracks impact the deterioration in the vicinity of their interface. The magnitude of their impact depends on different aspects. The observed deterioration rates are influenced by the interaction between the change of hydraulic conductivities induced by the change in chemical composition, the effect of diffusive and advective exchange between matrix and joint and the further growth of cracks. As these impacts' interactions usually coincide, the single contributions are hard to separate within a fully coupled simulation. Hence, the effects have been decoupled here by computing a set of different model cases as displayed in Tab. 6.3.

The first case, the uncoupled case, represents a fully detached solution of matrix and joint where no exchange between both domains occurs. Even though this case does not reflect reality, it serves as a baseline for further comparison. For the second case, the effect of the change

Tab. 6.3: Modeled cases for evaluating the effect of joints and cracks on deterioration rates

Model Name	Updating Conductivity	Moisture Exchange	Diffusive Exchange	Cracking
Uncoupled				
modeling approachdating	✓			
Diffusive Coupling			✓	
Moisture Coupling	✓	✓		
Fully Coupled	✓	✓	✓	
Fully Coupled Cracking	✓	✓	✓	✓

in hydraulic conductivity based on the changes in pore space is implemented solely and can be compared to the uncoupled case. The diffusive and moisture coupling cases are computed to separate the effect of both coupling processes. For further comparison, both (diffusive and moisture coupling) are applied together in the fully coupled case. Finally, all the above effects and the impact of cracking are computed.

The results are compared visually for the observed deterioration across the structure. For visualizing the result parameter fields, only the lower part of the dam's top is shown (see Fig. 6.7a) to enhance the visibility of details. As in the previous section, the results are also presented as section averages for the mid and top joints. The results of the different cases are displayed with increasing complexity in the following.

6.4.1 Effect of uncoupled fractures

The uncoupled solution is a simple case to show a baseline result for further comparison. Joint and matrix do not exchange any moisture or ions and thus deteriorate independently. As a result, both domains are only influenced by their respective flow rates. Therefore, the sequence of the deterioration process is similar to the process described in the previous section. Based on the increased hydraulic conductivity of the joints, the flow rates within the joint are greater than the flow rates within the matrix. In addition, only 5 mm around the joint need to be removed until the joint's interface is considered to have fully deteriorated. The combination of the solid phase reduction and increased flow rates lead to weak zones around the joint significantly faster than for the matrix structure. This is displayed in the results of the joint deterioration of the uncoupled solution after 150 years in Fig. 6.7c.

Similar to the previous results of the Koyna dam, the matrix deteriorates almost uniformly across the dam height, as shown in Fig. 6.7b. The matrix flow directions are generally horizontal

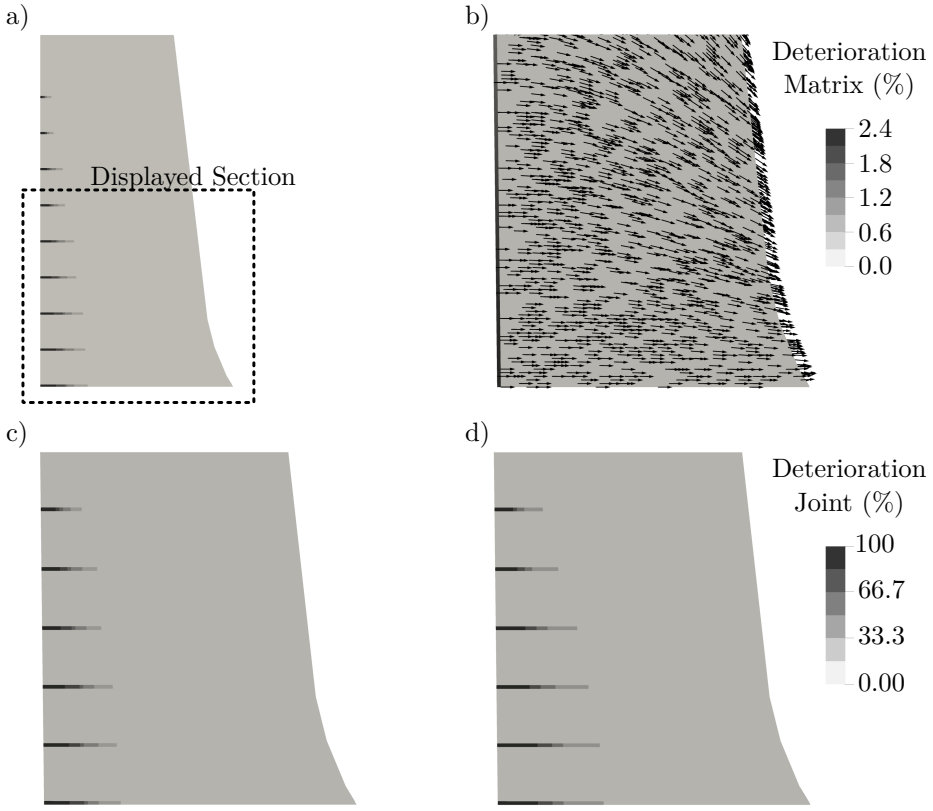

Fig. 6.7: Selected model section for evaluations (a), deterioration of the matrix (with matrix flow vectors, b), deterioration of joint for the uncoupled (c) and conductivity updating (d) case after 150 years.

between the upstream and downstream face and only show impacts of gravity near the phreatic line. In a direct comparison between joints and matrix, the increased deterioration of the joints is apparent. The highest deterioration is found for the lowest joint, subjected to higher water pressure at the upstream side. However, this increased pressure is slightly counteracted by the increase in thickness towards the bottom.

6.4.2 Impact of coupling deterioration with hydraulic conductivity

When the solid phases are removed from the matrix or joint interface, not only the porosity but also the hydraulic conductivity is increased, as described in Sec. 4.6. As a result, flow rates increase and thus the rates of deterioration. This effect is included for the case conductivity updating, while the rest of the model parameters remain identical to the uncoupled case. The increased rate is visible by the slightly deeper deterioration for the conductivity coupling case in Fig. 6.7 (d). In order to quantify this effect, the section averages are displayed for the top and middle joints in Fig. 6.8.

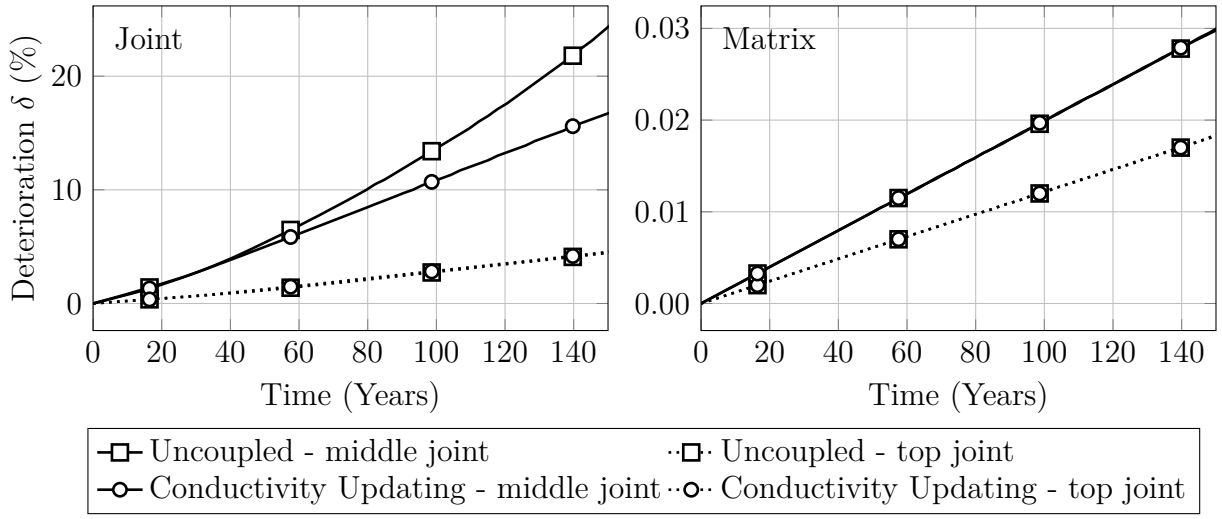

Fig. 6.8: Comparison of the impacts of updating the hydraulic conductivities on the deterioration of joint and matrix for the selected dam sections over 150 years

For the uncoupled case without conductivity updating, the deterioration of joint and matrix is linearly increased for the whole period. This is caused by the unchanged flow rates for the entire period of 150 years. Based on the difference in the applied hydraulic gradient, the deterioration of the middle joint is almost three times increased compared to the top joint for the same case. Nevertheless, the deterioration process remains linear. In contrast, flow rates are increased for the second case when the increase in hydraulic permeability for the deteriorated zones is considered. With the increasing share of deteriorated parts at the upstream side, flow rates continuously increase. Nevertheless, this change in flow rates is not very noticeable for small deterioration degrees, which is evident for the matrix and top joint results. However, changes in the middle joint are apparent after reaching deterioration degrees above 5 %. After that point, differences get increasingly evident with any further deterioration. Eventually, the deterioration obtained after 150 years is significantly increased by more than 45 % compared to the uncoupled case without conductivity updating.

6.4.3 Impact of joint-matrix exchange fluxes

The most complex interactions arise at the interface between the joint and matrix, as shown in the following. Here, ions can be transported in both directions due to advective transport and diffusive flow. Based on the ratio and direction of fluxes, this interaction can either slow down or speed up the deterioration of the joint or matrix. First, the effects of the fracture-matrix diffusion and then the impacts of advective exchange are discussed.

Joint-matrix diffusion occurs when concentration differences across the joint-matrix interface are present. At the beginning of the deterioration, all solid phases are available within the whole structure and thus can dissolve. Based on this, the initial concentrations of both domains are identical and no diffusion occurs. However, once a solid phase is depleted for certain parts of the structure, it cannot dissolve further. As a result, a different ionic composition is found in equilibrium with the remaining phases. Once a new ionic composition is found, concentration differences occur between leached and unleached sections. The same principles apply when a specific solid phase is no longer present in the vicinity of the joint but is still available for the matrix domain. The differences in concentrations in the liquid phase of the joint and the surrounding matrix then result in joint-matrix diffusion towards the joint. For the presented case, this process is initiated when portlandite at the joint interface is depleted for the first cells. Once all portlandite is removed, CSH phases start to dissolve, resulting in different concentrations. An example is the calcium concentration reduction when CSH phases begin to dissolve. When portlandite is still available in the surrounding matrix, the calcium concentration is still at the initial level there, resulting in a diffusive flux towards the joint. Based on this flux, the calcium concentration in the joint increases again, reducing the amount of dissolved CSH phases. If the joint-matrix diffusion is significant compared to the advective transport, it is even possible that new CSH phases are formed in the joint. Based on the ionic transport towards the joint, the matrix's deterioration rate is increased simultaneously. These different aspects of the joint-matrix diffusion are displayed in Fig. 6.9 for the diffusive coupling case.

Compared to the previous results, differences in joint deterioration are immediately visible in the results of the diffusive coupling case (Fig. 6.9a). The deterioration of the joint is still evident after 150 years. However, a zone of increased porosity is found between the fully leached zone close to the upstream side and the portlandite dissolution front (Fig. 6.9d). As explained before, this zone of increased porosity is caused by the reduced calcium concentration (Fig. 6.9c) in sections where portlandite is entirely removed at the joint interface but is still present in the surrounding matrix. The diffusion then leads to an increase in CSH (Fig. 6.9e) and ettringite (Fig. 6.9f) in the joint in regions where the portlandite is depleted. Nevertheless, these precipitated phases are eventually dissolved when the fully leached zone advances. When the deterioration of the surrounding matrix (Fig. 6.9b) is compared to the previous results, the effect of the joint-matrix diffusion is also apparent. Instead of a uniformly deteriorated structure, the matrix around the joints now shows increased deterioration due to the matrix-joint diffusion.

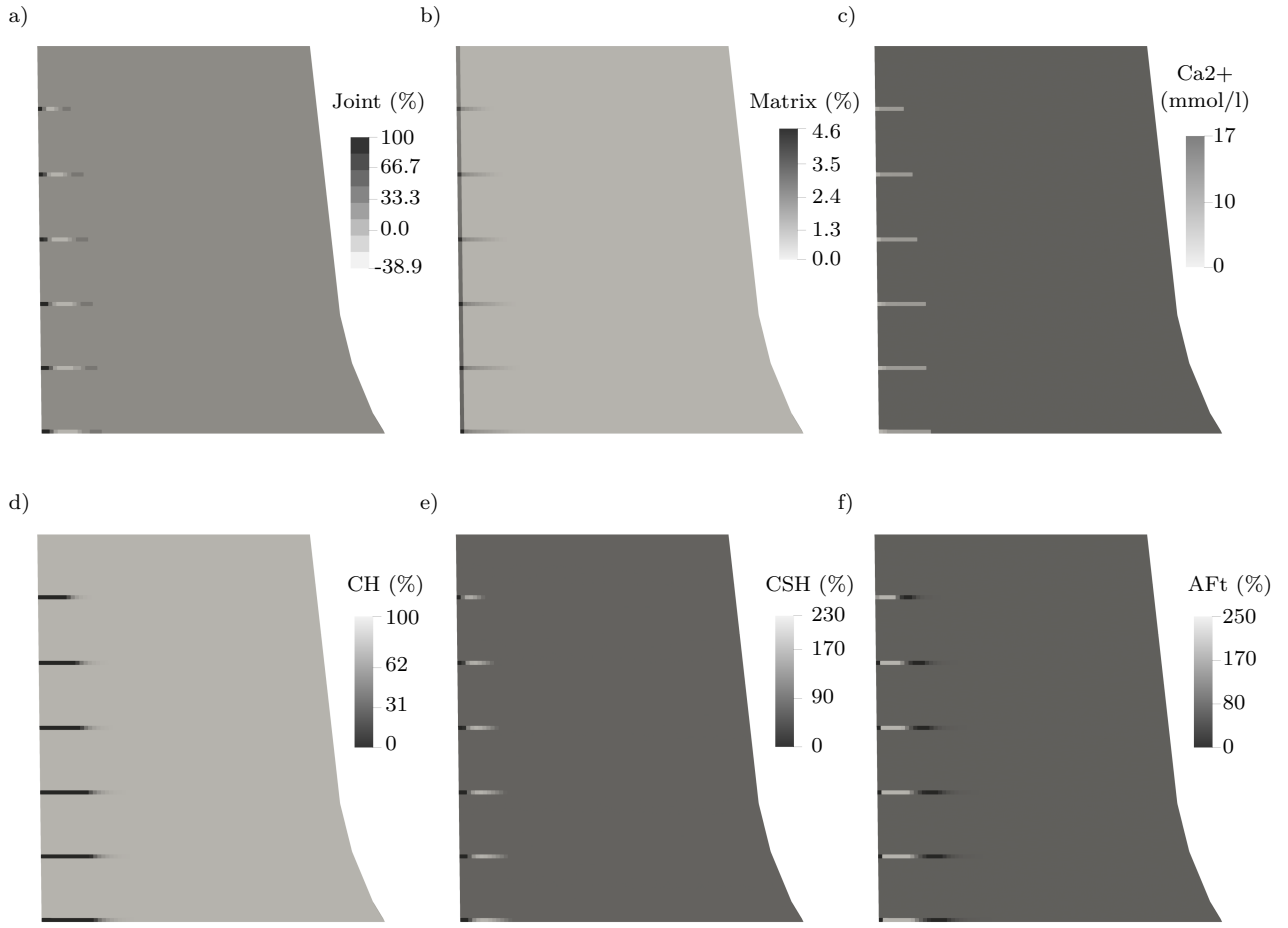

Fig. 6.9: Deterioration for diffusive coupling case for the joint (a) and matrix (b), joint calcium concentration (c) and relative phase densities at the joint interface for portlandite (d), CSH (e) and ettringite (f) after 150 years

It is worth noting that the strength of the effect of the joint-matrix diffusion largely depends on the ratio of the advective and diffusive fluxes. When advective flow rates are slow compared to diffusion rates, diffusive processes lead to an equilibrium between joint and matrix. For this case, a similar deterioration is observed in both domains. On the contrary, only the joint interface solids are dissolved if moisture flow rates are greater than diffusive fluxes. In this instance, the matrix is relatively unaffected compared to the joint. Thus, it seems reasonable to identify the type of process with dimensionless numbers like an adopted Peclet number in future works.

The effect of the advective transport of ions between matrix and fracture is determined by the moisture exchange rate between these domains. As this exchange is based on pressure differences, the advective exchange is closely linked to the deterioration process of the joint.

To clarify this process, the baseline principle of this interaction is shown in Fig. 6.10.

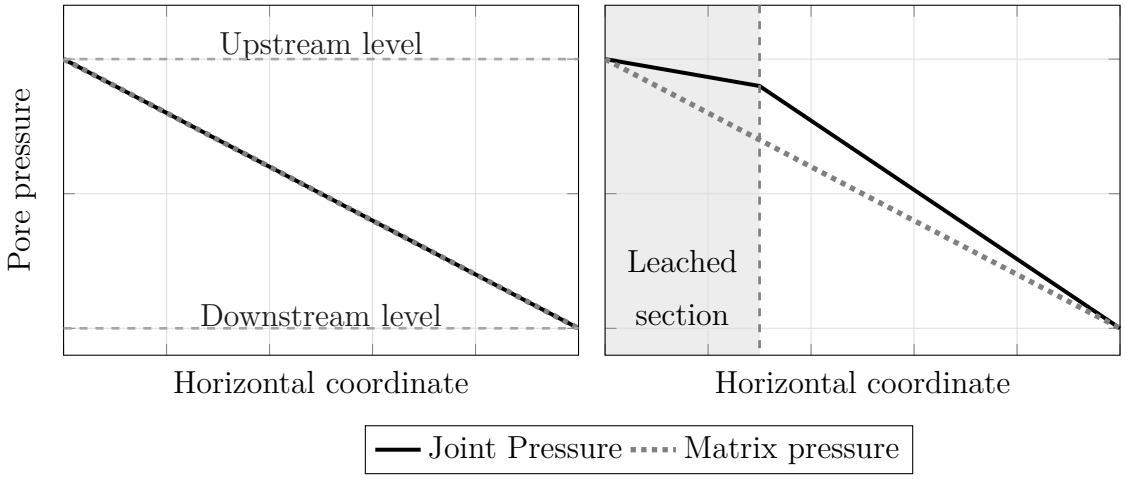

Fig. 6.10: Schematic illustration of the effect of joint-leaching on the pore pressure distribution of joint and matrix for an unleached joint (left) and leached joint (right)

When a structure with a homogeneous hydraulic conductivity is subjected to a difference in water pressure between upstream and downstream, a linear distribution between both levels is expected at a steady-state. As fracture and matrix space initially have homogeneous hydraulic conductivities, a linear pressure distribution is observed for both domains at a steady-state. This is displayed on the left of Fig. 6.10. As a result of these identical distributions, no exchange flow takes place as both systems are in equilibrium. For this case, the coupled solution is identical to the uncoupled case. However, the pressure distribution is shifted when the hydraulic conductivity changes for parts of the material. As the deterioration process of the joint usually progresses faster than that of the matrix, the resulting pressure distributions are not identical anymore, as indicated on the right side of Fig. 6.10. Once the pressure in the joint is greater than the pressure in the matrix, moisture from the joint is exchanged towards the matrix. This change of joint pressure also occurs for the computed case. The calculated pressure in the joint is displayed on top of Fig. 6.11 after 50 and 150 years.

The described shift of the joint pressure is already very apparent after 50 years, as the joints become visible as spots of increased pressure across the structure. This effect is even increased after continuous deterioration over 150 years. After that period, almost two-thirds of the lowest joint area is subjected to pressures between 36 and 30 meters of water column. Thus, the remaining 30 meters of pressure are reduced over only the last third of the section.

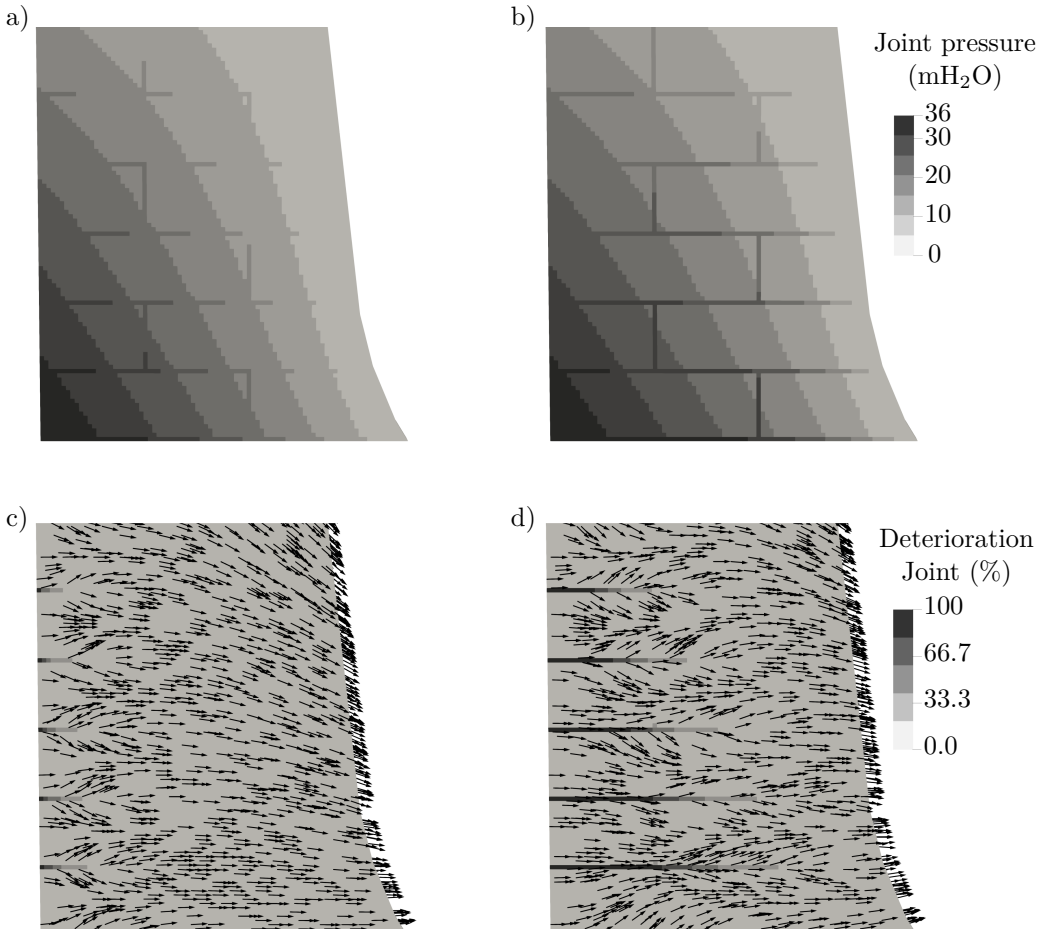

Fig. 6.11: Joint pressure distribution (top) and joint deterioration with matrix flow vectors (bottom) after 50 (left) and 150 years (right)

The resulting moisture flows from the joint into the matrix can be seen at the bottom of Fig. 6.11. This moisture ingress into the matrix is indicated by the vectors above and below the joint. The moisture ingress is apparent by the vector pointing towards the center of the block. As the amount of water distributed towards the matrix also increases the flow rates in the joint, this process inherently also increases the deterioration rate of the joint itself. Therefore, a more considerable deterioration can be observed in the joint compared to the previous cases.

However, in contrast to the earlier results, the deterioration of the lowest joint is not the largest in this case. This is explained by the fact that water leaves the joints upward and downward. Since the lowest joint only distributes water upwards, the flow rate increase is not as significant as for the other joints. The effect of both joint-matrix exchange processes is quantified for the middle- and top joint sections in Fig. 6.12.

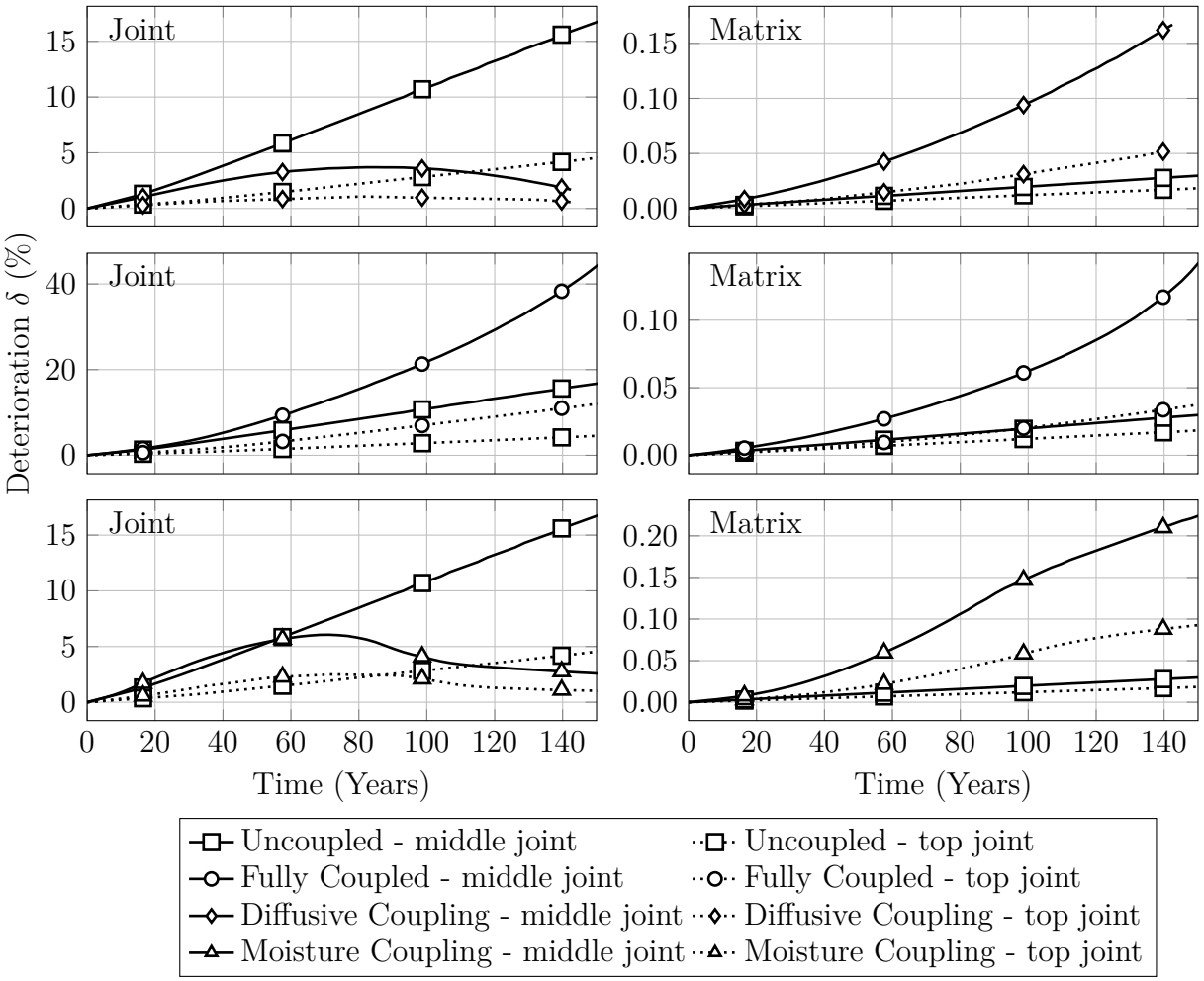

Fig. 6.12: Comparison of the impacts of diffusive (top), advective (middle) and the combined (bottom) exchange fluxes on the deterioration of joint and matrix for the selected dam sections over 150 years

The diagrams at the top of Fig. 6.12 compare the uncoupled case to the diffusive coupling case. The described effect of the joint-matrix diffusion is visible for the joint space by a continuous decrease in deterioration rate. This is caused by the increase of effective exchange length when the deteriorated zone shifts further into the structure. While this increased exchange slows down the deterioration of the joint, it increases the deterioration rates for the matrix, as displayed on the right-hand side for the matrix solution.

The diagrams in the middle of Fig. 6.12 display the increased deterioration rates obtained when the exchange moisture flow between joint and matrix is considered. Here, the moisture coupling solution is compared to the uncoupled case for joint and matrix space. The described increase in deterioration rate due to moisture transfer into the matrix is evident throughout

the 150 years. Nevertheless, the pressure gradient between joint and matrix has to develop within the first years. Once this process is started, it continuously increases its rate since the increase in flow rates also enhances the deterioration rates. Similarly, the increased moisture inflow into the matrix also increases the deterioration rates for the matrix itself. However, this increase is only obtained if the exchanged moisture is not already fully saturated concerning the solid phases. But since moisture is also transferred from fully deteriorated sections toward sound matrix materials, this exchange flux also increases matrix deterioration.

It is worth noting that not only deterioration can induce a difference in pressure distribution between joint and matrix. A similar exchange process is observed during the initial moisture ingress into the structure since pressure distribution has not achieved a steady-state yet. This effect is not observed in the presented case, as both solution domains are started from a steady-state. However, it can be expected that the initial moisture ingress into the structure also increases the joint's deterioration similarly.

At the bottom of Fig. 6.12, the combined effects of both exchange processes are visualized for the fully coupled case. Again, the deterioration of the joint is compared to the uncoupled scenario. At first, the effect of the advective exchange process slightly increases the deterioration rates. Nevertheless, with the continuous increase in the rate of the joint-matrix diffusion, the observed deterioration is reduced compared to the base case. As the joint's flow velocities slowly increase, this trend steadily declines as the ratios between diffusion and advection shift. Finally, as both processes increase deterioration rates for the matrix, the highest amount of matrix deterioration is observed for the fully coupled case.

6.4.4 Impact of cracking

Cracks increase the hydraulic conductivity of cement-based materials significantly, as displayed by the multitude of different experiments shown Fig. 3.13. The elastic-plastic crack model is included in the last set of comparisons to quantify the effect of cracking on deterioration. When the model is implemented into the modeled case, cracks are formed at the upstream side of the middle joint as tensile stresses are the highest here. As the deterioration degree also affects the material's tensile strength, the initial crack is even increased throughout the simulated period.

The computed crack at the upstream side of the middle joint is shown after 50 and 150 years of deterioration in Fig. 6.13.It can be seen that the crack covers a broad section of the middle

joint and is increased even further over the last 100 years. Given the significant increase in hydraulic conductivity for these cracked zones, their resistance against the fluid flow can be regarded as almost nonexistent compared to the sound material. This greatly increases the flow rates and thus impacts the deterioration significantly, as shown in Fig. 6.14.

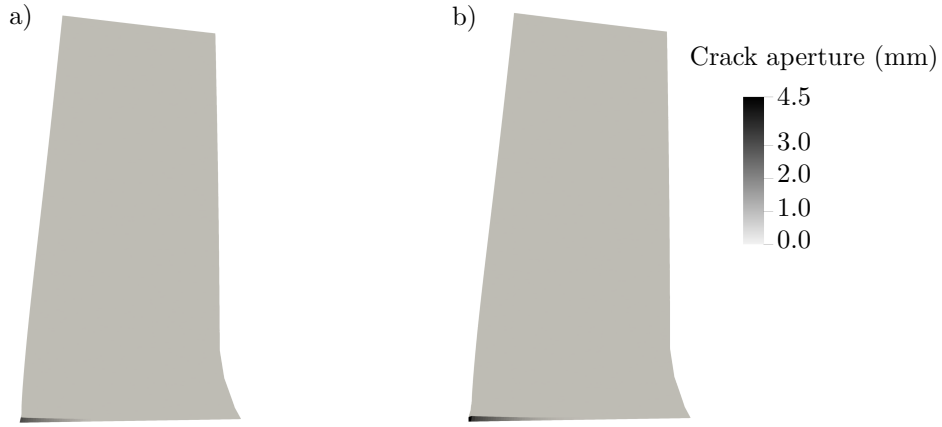

Fig. 6.13: Deformed structure (2000 times enhanced) and crack aperture computed for the fully coupled cracking case after 50 (a) and 150 years (b) of deterioration

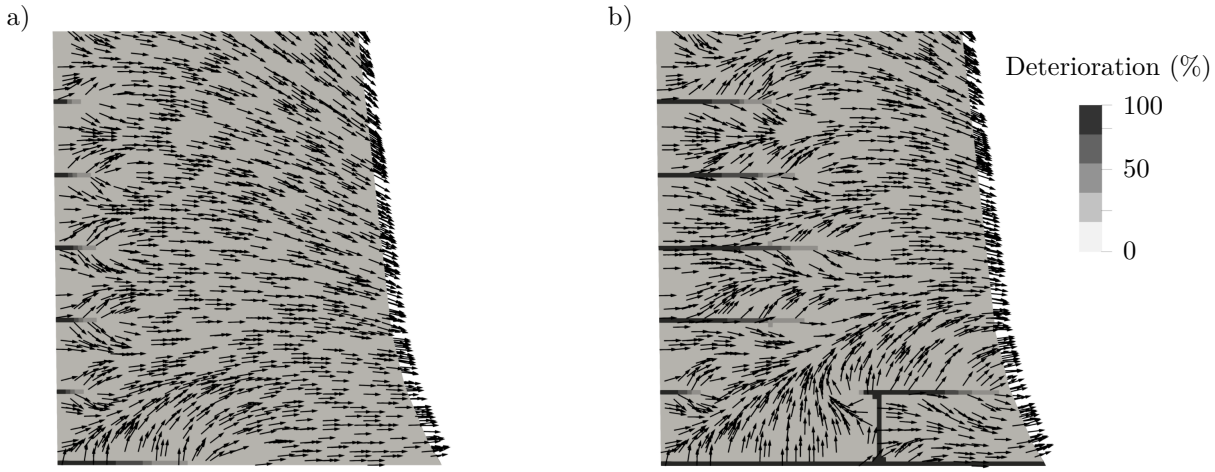

Fig. 6.14: Deterioration of the joint and moisture flow vectors in the matrix for the fully coupled cracking case after 50 (a) and 150 years (b)

For the fully coupled cracking case, the bottom joint entirely deteriorates after 150 years, as indicated on the right side of Fig. 6.14. In addition, even the connected vertical joint completely deteriorates, and further connected joints are affected. When the flow vectors after 50 years are compared with the results of the moisture coupling case (see Fig. 6.11), the changes in the flow field are very evident. For the cracking case, less moisture is introduced into the matrix by the second-lowest joint, as the increased moisture inflow of the cracked joint now governs the flow

field. This process can also be seen when comparing the deterioration after 150 years. Here, the second joint's deterioration is barely noticeable as the crack introduces all the water in the vicinity. Even more evident is that the vertical joint above the cracked joint now supplies more moisture into the second joint than the upstream side. For quantification, the effect of the fully coupled cracking solution is compared to the previous results by comparing the computed deterioration for the middle joint in Fig. 6.15.

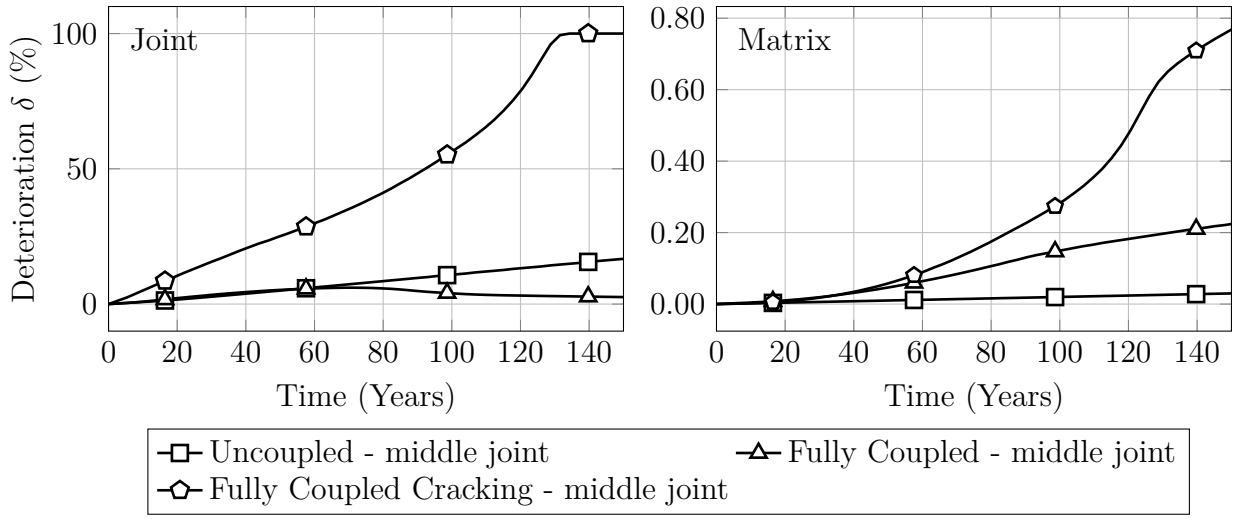

Fig. 6.15: Comparison of the impacts of cracking on the deterioration of joint and matrix for the middle joint over 150 years

The effect of cracking on the deterioration is immediately evident in this comparison. While the uncoupled case does not reach 20 % of deterioration after 150 years, the impact of the crack already results in a fully deteriorated joint interface after 130 years. Similar to the moisture exchange case, the additionally introduced moisture flow towards the matrix also increases the deterioration rates of the matrix the most significant.

Even though it is clear that the cracks have a crucial effect on the durability of a structure, their exact impact could not yet be quantified. While the computed solution cannot be generalized as the sizes of structures, cracks and joints generally vary too much; these first results already show the capabilities of the developed modeling approach for quantifying and comparing expected deterioration.

6.5 Impact of different durability measures on deterioration

The developed modeling approach is finally used to compare the effects of different measures for improving the durability of the dam. The comparison is made with the most realistic modeling setup to incorporate all relevant aspects. Therefore, the fully coupled cracking case from the previous section is selected as the initial setup for this comparison. Based on this case, two different measures to improve a structure's durability are compared.

One measure often used to improve a structure's durability is applying a sealing layer on its surface. This generally can be achieved with durable, watertight materials. One option for this is using a geomembrane with low hydraulic conductivity. Since this sealing layer reduces the flow velocities, the durability is expected to be increased. This measure has been applied to dams for decades and still is being applied in current projects (Scuero et al. 2017). A second durability measure is to improve the bonding of the joints. This can result from different actions such as better treatment of the joints during construction or improvement of the joints after construction (Silva 2019). The post-construction joint treatments can be achieved by injecting resins or cement suspensions. As a result, the interfaces of the joints are better connected, which enhances their mechanical properties while also reducing their hydraulic conductivity.

Both measures are implemented into the model by adjusting the local material properties. The first measure is applied by reducing the hydraulic conductivity of the first set of elements on the dam's upstream side. The reduction is made by assuming an additional 2 cm thick layer with a hydraulic conductivity of 10^{-15} m/s at the surface and updating the hydraulic conductivity according to the harmonic mean. The improvement of the joints is modeled by reducing the joint's hydraulic conductivity by one magnitude while also increasing the tensile strength of the joints up to 90 % of the homogeneous concrete. The results of the deterioration of the joints after 150 years are displayed in Fig. 6.16 for all three cases.

The base case's results in Fig. 6.16a serve for comparison and are identical to the results of the previous section. When the sealing layer is applied Fig. 6.16b, the observed deterioration of the middle joint is not decreased as could have been expected. In contrast, the joint's deterioration is further increased. This is caused by the cracking of this joint's upstream side, which counteracts the desired effect as the sealing layer is also destroyed at the crack. When the sealing layer is destroyed at the level of the middle joint but remains intact for the rest of the structure, the deterioration is greatly increased for the cracked section. This is caused by the increased moisture flow through the crack space, which distributes water to almost

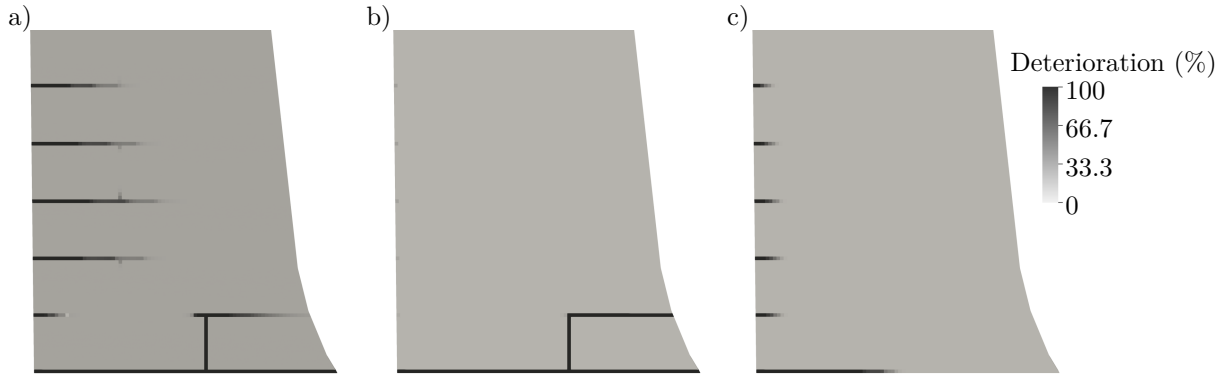

Fig. 6.16: Deterioration of the joints for the base case (a), the application of a sealing layer (b) and joint improvement measures (c) after 150 years

the entire dam body behind the sealing layer. Hence, the water that cannot be transported through the sealing anymore is now supplied by the crack. This increase in flow rates through the crack then again increases the rate of deterioration. The flow vectors illustrate the wide distribution of the moisture originating from the crack in Fig. 6.17b. Almost half of the top section is influenced by the inflow from the crack.

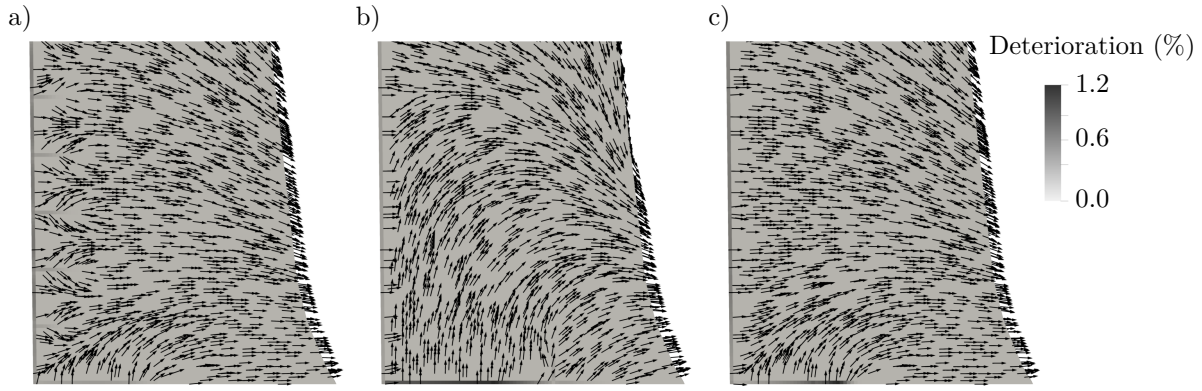

Fig. 6.17: Deterioration of the matrix and matrix flow vectors for the base case (a), the application of a sealing layer (b) and joint improvement measures (c) after 50 years

A similar effect is observed when the hydraulic conductivity of the joint interface is reduced Fig. 6.16c. Again the cracking of the upstream side of the middle joint counteracts the desired outcome for the first years. Similar to the observations for the surface sealing, the reduced flow through the uncracked joints increases the distribution of moisture from the cracked joint towards the surrounding matrix. This is also indicated by the increased upwards outflow of the middle joint in Fig. 6.17c.

However, once all the solid phases at the cracked part of the joint are removed, the deterioration process slows down since the reduced hydraulic conductivity of the remaining uncracked joint reduces the flow rates behind the crack tip. As a result of this, the deterioration of the joint is decreased significantly after 150 years (see Fig. 6.16c). The reduced hydraulic conductivity of the uncracked joint also becomes evident when comparing the matrix deterioration. Since significant parts of the moisture are exchanged towards the matrix before the beginning of the uncracked section, the deterioration of the matrix is enhanced at this location. This is displayed in Fig. 6.17c by the increased deterioration close to the crack tip. Again, all of the effects are quantified in Fig. 6.18 for the deterioration of the middle and top joint throughout 150 years.

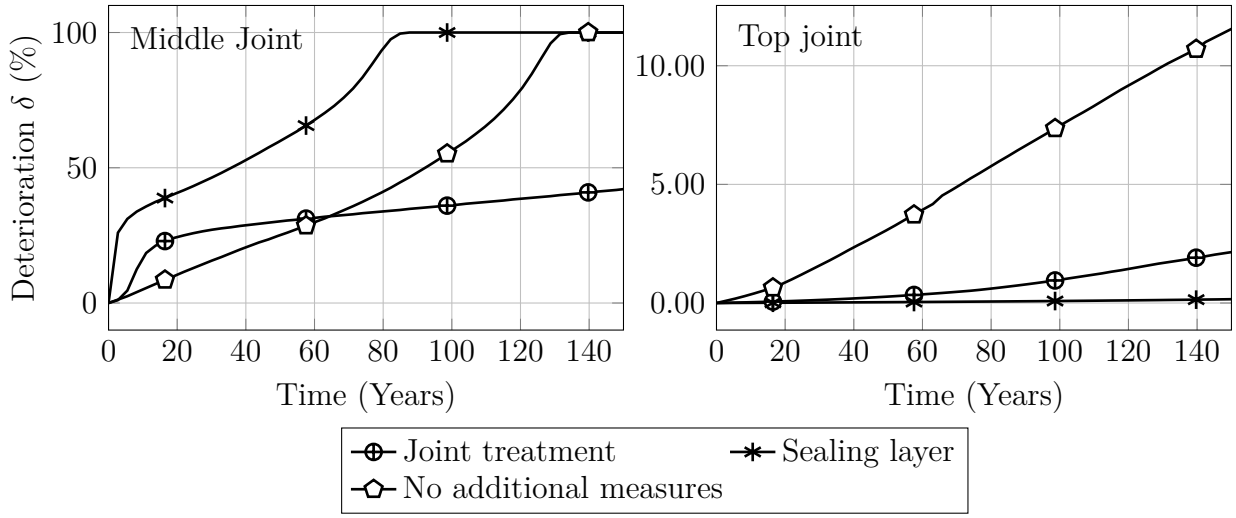

Fig. 6.18: Comparison of the impacts of different durability measures on the deterioration of middle and top joints over 150 years

The described effects are visible in the results of the middle joint on the left side of Fig. 6.18. For the sealed case, the deterioration increases rapidly up to 35 %, indicating that the cracked part of the joint deteriorates very quickly based on the significant exchange rates. But even after the initial phase, deterioration rates remain high since no further measures are taken to reduce the transport within the joints. Therefore, the joint is already fully deteriorated after 85 years which is even faster than the base case where 130 years are needed. Thus, in this specific case, applying a durability measure can even increase deterioration.

Even though this measure seems very ineffective initially, it is worth noting that several aspects can reduce the displayed negative effect. One aspect is the sealing layer's elastic properties, which might prevent the layer from being cracked at the same time as the concrete. Also, a drainage layer behind the sealing layer can be available to reduce the negative effect.

However, mechanical actions such as the modeled cracking are always a source of problems for surface sealing systems and can cause similar issues to the one described in the section. The results obtained for the second measure also indicate an increase in deterioration for the first years. Nevertheless, the increased flow rate through the crack is reduced once the cracked part of the joint has deteriorated, and the flow rate reducing effects get increasingly critical. As a result, this method eventually proves to be effective as not even 50 % deterioration is reached after 150 years.

When comparing all results, it becomes apparent that the initiation and growth of cracks are crucial in reducing both measures' effectiveness. This is also indicated by the results for the top joint on the right side of Fig. 6.18. The top joint remains uncracked, and thus the effect of the surface sealing remains intact. As a result, almost no deterioration is observed after 150 years. Similar observations are made for the improvement of the joints. Here the decreased hydraulic conductivity is also very evident by the reduced deterioration. In contrast to the results of the middle joint, the sealing solution is even more effective for the top joint. However, as the weakest section will likely induce failure and thus is decisive, the joint treatment solution remains the preferred option.

6.6 Discussion of the results

In the previous sections, different results indicate the capabilities of the developed modeling approach. Within a set of cases, it is shown that the applied method allows describing the physical processes that occur during deterioration. However, the detailed modeling of all processes does not directly result in quantitatively precise results. This is caused by the lack of reliable data for the detailed description of all coupling relations. In particular, the change in pore structure and leaching properties of joints are rarely studied. Therefore, the applied parameters have to rely on assumptions partially.

Notably, the computed diffusive and advective ion exchange rates between joints and matrix need to be validated with further experiments. Nevertheless, the predicted interaction of diffusive and advective ionic exchange fluxes is still valid. Studies on the impact of both processes based on threshold ratios can greatly influence the quality of quantitative results. In the presented application of the approach, both exchange coefficients are also constant. However, it seems reasonable that updating both factors based on properties like leaching degree and aperture can improve the precision of the modeled fluxes if data is available.

The amount of solid phase that needs to be removed to deteriorate the joint entirely is another subject that needs further studies. Since this factor directly impacts the deterioration rate of the joints, further experimental data can also increase the reliability of the results.

The modeling of the chemical domain is also subject to uncertainties. The applied modeling concept based on the law of mass action has proven to yield accurate results over a century. As local equilibrium is assumed (LEA) during the application, the flow velocities must remain low. Based on the large scatter of the published Damköhler numbers, the validity of the LEA cannot be assessed reliably. However, given the time needed for deterioration during the simulations, this validity of the assumption is very likely. In addition, the MAE concept is only fully valid for elementary reactions and thus induces a slight error for more complex reactions. Similarly, some applied modeling relations for the solid phases, such as the model for the CSH phase, are simplified. While all these factors induce a slight error in the calculations, it is unlikely that these limitations reduce the informative value of the results. This is supported by previous studies that evaluated similar concepts against experimental data for concretes (Samson et al. 2007b). In most application cases, it generally seems reasonable that the overall heterogeneity and variance in the material of an actual structure has a more significant effect on the result than these simplifications in modeling. Thus, the applied relation has sufficient precision within the natural uncertainty of the material. Nevertheless, when changes in cement composition are apparent, as for slag or fly ash cement, different phases need to be included in the initial phase composition.

In addition, many further mechanical effects can be included in future cases to yield even more realistic results. This includes modeling the impact of creep and applying more complex models to describe crack initiation and growth from the field of fracture mechanics. The additional models can then account for multi-axial effects and include descriptions for shear failure. In addition, the selected model only accounts for inelastic strains once the tensile strength is reached. However, accounting for micro-cracking before reaching the peak stress is likely to increase the precision of the results further. Here, the early inelastic strains need to be implemented into the stress solution, while the additional early fracture pore space must be added to the moisture solution. All the above effects can be added with minimal changes as the generalistic description of the modeling approach allows the application of all these different models.

When considering the most realistic modeling of deterioration, it is evident that specific effects were not included in the presented cases. Most of these missing effects could have been

implemented based on the modeling approach but were omitted to focus on predicting the baseline processes. One absent impact present for any actual structures is a dynamic boundary conditions. In the presented cases, all boundary conditions are assumed to be constant. When dynamic boundary conditions are considered, they can also include the effects of extreme events like flooding, earthquakes or periods of warm or cold temperatures. As these extreme events are likely to induce local cracking or other weakening effects like abrasion, they can have significant consequences for further deterioration. Similarly, dynamic water levels can also cause different effects on the moisture domain. Changing water levels can induce vertical and temporarily reversed flow, altering the deterioration characteristics. Also, the initial distribution of model parameters was only varied across concrete blocks. However, the initial distribution of the block's pore and mechanical parameters was omitted for simplicity. These parameters mainly differ based on the material's early stages of strength development, as moisture exchange of the surface, the release of hydration heat and the changes in stiffness during hardening differ based on the location within the block. For a more realistic distribution, the complete construction process and the material's hydration must be modeled for the cross-section. As the developed approach can be used to model these aspects, they can be implemented in later studies.

7 Summary and outlook

A holistic modeling approach for the simulation of the deterioration processes in cement-based materials is developed in the presented work. The new approach is based on a combined formulation of moisture, heat and solute transport with chemical equilibrium reactions, the description of pore structure changes, as well as deformation and cracking. The formulations for each domain are selected from available models for each physical domain based on their applicability to a combined modeling approach. Care is taken to implement the pore structure changes, as well as their impact on all modeling domains. Therefore, new relations for combining and coupling the models and their interactions are developed.

Within the presented modeling approach, solution domains are generally solved segregated, which are then coupled based on different interaction mechanisms. This includes the coupling of crack growth with changes in porosity, hydraulic conductivity, moisture saturation and pore pressure. These changes are then considered for the computation of moisture, vapor, heat and solute transport. Similarly, the modeled dissolution and precipitation of the solid phases are used to update the available pore space. This means when solid material is formed or removed, the effect of this process on the pore structure is taken into account. In the same way, the impacts of changes in solid densities are considered for the mechanical properties. The latter then affects the calculation of the structure's deformation and cracking and thus closes the interaction circle. As cracks and joints can form sharp interfaces in structures, a dual continuum formulation is applied for moisture and solute transport to avoid the need for fine discretization.

The described approach is implemented as a flexible, extendable framework based on the finite volume method in foamExtend. Each solution domain is validated against experimental or analytical data to ensure accurate results. The factors that govern the interaction between the domains are selected according to the available literature data as well as new experiments. The developed coupled modeling approach is then demonstrated for the deterioration of a gravity dam. For this application case, different aspects and effects of deterioration are then revealed and discussed.

Within the first set of computational runs, the general sequence of the deterioration of the dam is presented. The solid phases are slowly dissolved at the upstream side throughout the deterioration. Based on the size of the computed dam structure, only 5 % are removed at the critical section after 1000 years. The effect of the variance of material properties induced by the construction of the dam is found to increase deterioration rates but not by a critical amount.

In contrast, the effect of joints and cracks is found to change the deterioration process within another set of cases significantly. It is shown that moisture exchange between joint and matrix can increase the joint's deterioration beyond the level that the increased hydraulic conductivity of the joint would predict. At the same time, joint-matrix diffusion can spread the deterioration perpendicular to the joint, reducing the rate of deterioration for the joint itself. When the joint interface is subjected to cracking, the rate of deterioration is vastly increased, resulting in a fully deteriorated joint after 130 years for the presented case. In the last set of comparisons, the applicability of the modeling approach for the evaluation of different durability measures is demonstrated. It is found that the application of surface sealings can even increase the deterioration rate for the critical joint when cracking occurs. In contrast, an improvement of the joint's interface and bonding can reduce the rate of deterioration even when cracks are present.

The modeling approach was applied to a gravity dam and has been developed for application to hydraulic structures. However, the developed modeling approach remains universal and is not limited to specific scenarios. In contrast, the modeling approach can evaluate many additional effects and interactions in the deterioration of cement-based structures.

One research application is the utilization of the model to improve the understanding of temperature effects on deterioration. Here, the framework could be applied to model deterioration induced by freeze-thawing as well as the effect of thermal cracks on deterioration rates. In addition, the effect of daily temperature changes on dissolution and precipitation at exposed faces could yield new insights into the everyday dynamics. Another large field for further applications arises within the area of reinforced concrete. For this, phase changes around and at rebars need to be included in further developments. These developments could consist of the transport and interaction of chloride ions with reinforcements and the transport of carbon ions in the solute. Here, a dissolution of carbon dioxide contained in the air could be added to the boundary elements. The dissolved carbon ions can then result in carbonation of the cement phases and could also be used to study effects like the healing of cement-based materials.

The effects of the early phase of the material's strength gain were not modeled in the presented cases. The solution was initiated from a set of assumed material properties that were not varied across a concrete block. If early age effects are modeled during the construction, the impact of a more precise initial distribution could be evaluated for the deterioration. In further studies, the model can also be applied to evaluate the effect of more realistic dynamic boundary conditions and the occurrence of extreme events on the deterioration. These events, such as earthquakes or floods, can significantly affect deterioration by weakening the structure. The exchanges of dissolved species with different materials are additional effects at the boundaries. Here, the interaction with foundation rocks with a very different chemical composition than cement-based materials can be studied. As a result of this interaction, it can be expected that different solid phases are formed or dissolved. Significant changes are also expected if the cement type is varied and the chemical composition of the structure's material is changed. In this case, pozzolanic components could reduce the portlandite content while decreasing the pore space or expansive alkali aggregate reactions could be initiated and induce local cracking.

The demonstrated applicability of the modeling approach for evaluating designs also shows the relevance outside the research scope. Here, the model can assess different options and measures, which improves the knowledge when making design and restoration choices.

However, many applied coupling relations are based on a small set of available experiments. Therefore, the adopted parameters in the presented studies need to be further validated and improved in future experiments. By making the parameter choices more precise, the reliability of the results can be greatly improved. These results can then be used to evaluate the interaction of the discussed effects within one setup. These measurements should specifically cover the impact of leaching around joints and cracks as only little to no data is available here. Even though a combined setup for measuring all effects is complex and time-consuming, this direct validation can have a decisive impact on the reliability of the results.

Finally, it can be concluded that the developed approach can describe the relevant aspects during the deterioration of a structure. In particular, the inclusion of cracks and joints in the deterioration process has been excluded in most previous modeling approaches. However, further steps and measurements are necessary to allow a reliable prediction of the deterioration and thus potential weak zones in an actual structure. Even though many additional steps are still required in this research field, the developed modeling approach can contribute to improving deterioration modeling.

Appendix A

Composition of cement-based materials

A.1 Cement chemists notation

In order to shorten the long chemical formulas of the cement phases, a short form notation for the chemical components is oftentimes used in cement chemistry. This short form called CCN (Cement chemists notation) substitutes burnt lime (CaO) as C, silicon dioxide (SiO_2) as S, aluminum oxide (Al_2O_3) as A and iron(III) oxide (Fe_2O_3) as F. Water (H_2O) is shortened as H, sulfur trioxide (SO_3) as $\bar{S}$, carbon dioxide (CO_2) as $\bar{C}$ while magnesium oxide (MgO) is replaced with M.

A.2 Cement composition

The definition of cement in DIN EN 197-1 (2011) as a fine-grained inorganic hydraulic binder material is a general description for many different cement types. These cement types vary largely in their mineralogical compositions. However, cement based on Portland clinker are by far the most commonly used cement types. This is evident in the market share of CEM-IV/V in Germany. The share for this cement type, which is the least Portland clinker rich, combined with all other non-Portland hydraulics cement, is less than 1 % (Verein Deutscher Zementwerke (VDZ) 2020).

A.2.1 Portland cement composition

The base material for Portland cement, the Portland cement clinker, is manufactured by crushing and milling a specific mixture of raw materials, primarily oxides of calcium, silica, iron and alumina and then firing them in a cement kiln, where the hydraulic binder compound, the clinker phase, is formed. Based on the range and combination of different educts, a wide spread of clinker phase composition can be obtained as displayed in Tab. 2.1. In order to fulfill the criteria for Portland cement according to the European standard, the clinker phase has to

be composed of at least two-thirds of the calcium silicates. It is worth mentioning that outside of the DIN EN 197-1 (2011), several other definitions for cement exist which do not align with the European standard. The American Society for Testing and Materials (ASTM) defines an international standard ASTM C150 (2021) that specifies different types of Portland cement. In contrast to the European standard, this classification does not include blended cement, which are specified in C01 Committee (n.d.). In contrast to the European standard, it is sufficient for cement to contain only 30 % gypsum or Portland clinker to be classified as Portland cement according to ASTM.

Within the European definition, different cement types can be distinguished based on a few basic ingredients. If cement is primarily composed of Portland cement clinker (>95 %), it is classified as a CEM-I type. By adding supplementary cementing materials (SCMs) to the Portland clinker, different types of blended cement can be produced. The addition of SCMs allows for the modification of different properties and characteristics of the hardened cement paste. The most important SCMs are listed in the following.

A.2.2 Supplementary cementitious materials

Supplementary cementitious materials (SCMs) are a set of different supplements that can be added to the raw clinker during manufacturing or mixing to enhance or change the cement's properties. This includes a set of positive effects on the material's durability, such as the reduction of hydration heat and permeation of moisture, as well as their resistance to chemical attacks.

In addition to these positive effects, the usage of cheap industrial byproducts can also reduce energy usage and production costs. Depending on the SCMs and the amount that is added to the cement, the DIN EN 197-1 (2011) distinguishes cement as different CEM classes. The most common SCMs, according to the European code, are associated with a specific character (e.g. blast furnace slag as S) which is added to the cement type description depending on its additives. Given their significance for durability, the most important SCMs are described in the following.

Pozzolans (P, Q)

The SCMs classified as pozzolans are based on materials that contain silicic acid or alumo silica and undergo a 'pozzolanic' reaction:

$$3CH + 2S \rightarrow C_3 - S_2 - H_3 \tag{A.1}$$

This means that pozzolans do not act as a hydraulic binder by themselves, but they react with water when calcium hydroxide (portlandite CH) is present by forming calciumsilicate and calciumaluminate compounds. It is worth mentioning that Eq. A.1 can be complemented by similar pozzolanic reactions where portlandite is consumed to form aluminate and ferrit phases (Papadakis et al. 1992). Pozzolanic reactions are beneficial for the cement paste since the calciumhydroxide that is formed during the hydration process is replaced with the more stable calcium silicate hydrate phases (CSH). This formation of the additional calciumsilicate hydrates within the pore space also reduces the amount of pore space available in the material. This, in consequence, increases the resistance to permeation for the material.

According to their origin, pozzolans can be distinguished between natural pozzolan (P), which originate from volcanic or sedimentary rocks with pozzolanic chemicals or industrial pozzolans (Q), primarily either being activated clays, shales or air-cooled slags from lead, copper, zinc and other products from the ferroalloys industry (DIN EN 197-1 2011). Even though fly ash and silica fume also contain pozzolanic compounds, they are considered separate SCMs within this European standard.

Fly Ash (V, W)

If coal is burned within power plants, the exhaust gases leaving the combustion chamber contain fly ash, which is filtered by using electrostatic filters. Given its origin, fly ash is primarily composed of coal mineral compounds (such as clay, feldspar, quartz and shale), which are released when most of the unstable coal compounds are burned off. The result is fine-grained dust primarily made of spherical particles, which, depending on its components, can either be pozzolanic or hydraulic in nature. Depending on its chemical composition, fly ash can either be defined as siliceous fly (V) ash if siliceous and alumina components are primarily contained. The fly ash reacts mainly pozzolanic in this case. In addition to reducing the portlandite content of the hardened material, fly ash also decreases the release of hydration heat significantly (Klemczak et al. 2016), which is beneficial in many cases. If the fly ash contains more than 10 % of reactive calcium oxid, it is considered as calcareous fly ash (W) within the European standard. Given the hydraulic nature of calcium oxid, this type of fly ash also has hydraulic properties.

Silica fume (D)

Silica fume, microsilica or condensed silica fume is a byproduct of the manufacturing of silicon and ferrosilicon alloys. Similar to fly ash, silica fume is composed of airborne particles, which

result from the reduction of quartz with coal, iron or other ores in electric arc furnaces at very high temperatures. The results are fine spherical amorphous particles primarily composed of silicon dioxide. As discussed earlier, the additional silicon dioxide allows the cement to undergo additional pozzolanic reactions during its hardening while reducing the amount of portlandite formed. The addition of silica fume can increase the cumulative heat of hydration as well as the strength of the paste (Kadri et al. 2009).

Slag (H)

Ground granulated blast-furnace slag (GGBS) or slag, is another byproduct used as a cement additive. Slag melt develops in molten conditions as a non-metallic substance when iron ore is reduced by using coal in a blast furnace. When slag melt with appropriate composition is cooled, a latent hydraulic cementitious material can be obtained. It primarily consists of silicates and aluminosilicates of calcium and other bases (RILEM Committee 73-SBC 1988). Slag is formed at temperatures of about 1500°C and needs to be cooled rapidly by quenching it in water as air-cooled slag develops different properties. The final material is a glassy sand-like granulated material.

Given the different iron ores manufactured, the composition of the GGBS can vary in broad ranges. However, most of the compositions do not have cementitious properties but need an appropriate activator in order to hydrate when subjected to water. Sulfates, sodium silicate or calcium hydroxide can act as an activator and can be (partially) supplied by the Portland cement itself when used in blended cement (Kolani et al. 2012). In addition, slag cement can also have some pozzolanic properties as well. Similar to fly ash, the hydration heat released can be reduced significantly (Klemczak et al. 2016).

Burnt shale (T)

Burnt shale is a SCM with hydraulic and pozzolanic properties. The hydraulic properties are caused by the contained shale clinker phases, primarily Belite, Monocalcium aluminate with parts of free lime, while parts of silicon dioxide mainly govern the pozzolanic properties. Burnt shale, similar to Portland cement, is produced with special ovens, where shale and oil shale are the primary educts. Given its hydraulic properties, burnt shale is required to reach a compressive strength of 25 MPa after 28 days by itself (DIN EN 197-1 2011).

Limestone (L, LL)

For limestone cement, the limestone is added during the milling of cement, which produces a fine mixture. The limestone primarily acts as a fine inert aggregate which enhances the workability and reduces the water demand and permeability of the paste.

A.2.3 Chemical admixtures

In addition to SCMs, chemical admixtures can be used to change the properties of the material further. Chemical admixtures can be added to the cement during mixture or production. These admixtures are applied to control the workability and applicability of the mixture under certain conditions, to overcome emergencies upon mixing and for economic reasons. A short introduction to chemical admixtures that have an impact on durability is given in the following.

Air-entraining admixtures

Air-entraining admixtures deliberately induced additional air voids into the material. This improves the durability regarding freeze-thaw cycles, as well as expansive reactions in sulfate and alkali-reactive environments. Given their immense benefits, they are applied in many constructions.

Water-reducing admixtures

Water-reducing admixtures increase the workability of the mixtures, which allows the usage of lower water content mixtures that could not have been used in this application otherwise. This allows for achieving a higher strength material and better durability. When used as a superplasticizer, the water content is kept constant during its application which then increases the workability of the mixture.

Set retarding/ accelerating admixtures

Set retarding/ accelerating admixtures change the rate of hardening of the material. This can be beneficial if, depending on the application, a fast rate might be required to speed up production. If different concrete sections are placed in larger time intervals, their connection can be improved if the hydration of the previous block is slowed down.

Bonding admixtures

Similarly, bonding admixtures can be used to increase the connectivity of old and fresh concrete blocks. As the joint in between sections can form a weak link regarding deterioration, the service life can be improved by using bonding admixtures.

Shrinkage-reducing admixtures

Shrinkage-reducing admixtures are introduced into the mixture to decrease the shrinkage strain occurring upon drying of the material. As the cracks caused by shrinkage affect the durability, these admixtures can also be used to increase the longevity of the material.

Alkali-aggregate reactivity inhibitors

The usage of lithium nitrate, lithium carbonate, lithium hydroxide, lithium aluminum silicate and barium salts as an additive can significantly reduce the effect of the expansive alkali-silica reaction (ASR) in the hardened material. Given this is a significant deterioration mechanism in many structures, this admixture can increase the service life.

Permeability reducing admixtures

Permeability reducing admixtures reduced the moisture transport and uptake in the material by using water repellent or pore space blocking additives. Given the importance of moisture transport on durability, their impact on durability is evident.

A.3 Impacts of the construction on the durability

The actual construction of a cement-based structure can change the achieved material properties for certain sections or the whole structure. These changes are not only introduced by different sources of human error but are also affected by weather conditions, construction schedules and heterogeneities in materials. Thus, construction processes always induce changes in the material. However, the quantity of these effects is affected by different factors. These construction factors that affect durability are discussed in the following.

A.3.1 Manufacturing cement-based materials for construction

The construction of each structure can be conducted in multiple ways. Based on the structure's dimensions, the available construction sites and local materials, an adequate construction method is selected. As the cement-based material is always batched and mixed first, the process is the first source of deviation between planned and achieved properties.

Batching and Mixing

Batching and Mixing describes the process of weighing in the raw materials and then mixing them together until a homogeneous result is obtained. Generally, batching should be conducted by material mass fractions, usually within an accuracy of +-1 %, while only liquid additives can be measured by volume (ASTM C94 2021). However, given the ease of volumetric batching, it is still conducted in places where quality control is not yet common practice resulting in lower material strength and thus durability (Olusola et al. 2012). The mixing of concrete can either be conducted within stationary mixers or mobile mixers while delivering the material to the construction site. In order to achieve a good quality of the hardened materials, the variance of the mixer's output needs to be assessed continuously and ensured to remain low (ASTM C94 2021). Generally, the batching and mixing process can either be conducted on-site (site-mixed) or within a specific (concrete) plant (ready-mix). From a durability point of view, the manufacturing of the material within a specific plant tends to result in higher reproducibility of the material properties, which is desirable, despite the usually higher costs.

Placing and Compaction

After the material is mixed, it needs to be extracted from the mixer and placed within its formwork for hardening. This can be done by "direct tip", when the mixture is leaving the mixer directly into the formwork, by intermediate mobile transportation vehicles, by pumps, by cranes or combinations of the above (Lu et al. 2004). Depending on the placing technique

required, different mixture components have to be selected in order to achieve the desired work- and pump-ability, which again influences the final chemical and pore composition of the material. As the placing of the mixture induces air and propels de-mixing of the mixture, resulting in entrapped air, stone pockets or honeycombs, additional compacting measures have to be taken. This measure can include hand rodding, using self-compacting mixtures, shock tables and external- and internal vibrations. Depending on the compaction method, the achieved compressive strength can vary widely (Juradin et al. 2013). Hence, it is evident that insufficient compaction can leave major flaws that again impact the durability of the structure.

Curing

During the hardening of the hydraulic components of the cement, the supplied water is consumed. However, the surface of the freshly placed material is subjected to environmental conditions. Thus, an exchange between the environment and the material takes place. Given the fact that air is rarely saturated with moisture by itself, the surface of the material is continuously dried, reducing the water available for hydration. Hence, if the surface of the material is kept continuously moist, the highest final strength can be achieved (Price 1951). In addition, the surface temperature can influence the rate of hydration and the final strength as increased temperatures tend to reduce the achieved strength (Kim et al. 1998). As a result, the freshly placed material can be cured by methods of supplying additional water or by reducing the loss of water from the surface. In terms of durability, curing conditions are one of the most significant factors affecting the achieved material properties (Santamaria et al. 2019; Idowu et al. 2017).

A.3.2 Step-wise construction

For many reasons, cement-based structures usually cannot be placed as one monolithic block. Amongst the reasons for this are the logistics of preparing and pouring large quantities of material into formwork at once, the geometry of the structure requiring solid parts to be finished before others as well as the potential pressure induced on the formwork. In addition, the heat generated during the hydration of the cement need to be released without a major increase in temperature in order to avoid thermal cracks during hardening. However, not only thermal strains but also strains induced by shrinkage and creep needs to be released safely. Moreover, the usage of prefabricated parts on the construction site can be a financially beneficial option.

Construction joints

Construction joints arise inevitably when a new section of fresh material is poured next or on top of a more mature and already hardened section of material. Depending on the degree of hydration of the first section, the surface conditions, curing methods, potential reinforcements, material properties and stress state, the bond strength between both sections differs from those of the homogeneous section. As a result, these surfaces between the different sections form a layer of weakness in the structure, as evident in many experimental studies (e.g. Clark et al. 1985, Hwang et al. 2016). Nevertheless, the effect can be reduced by using bonding agents (e.g. epoxy raisins) as shown in Santos et al. (2012). In addition, the shear strength can be increased by adjusting the geometry of the surface with shear keys (Bureau of Reclamation 1976). Besides joints arising inevitably from construction blocks, joints can also be induced by design. This can be beneficial if thermal, shrinkage or creep strains are expected and uncontrolled cracking is to be avoided. In this case, the deformation that is allowed to take place within contraction or expansion joints releases these induced strains in a predictable way. Nonetheless, as these joints also allow an increased ingress of fluids, an additional layer of sealing might be required in order to increase the durability (Tons 1965).

Precast parts

Another form of piece-wise construction arises when cement-based materials are cast in form within a factory and then are transported and assembled on the construction site. The main advantage is the cost reduction in countries where labor is expensive and the increased speed of construction. Given the part-wise assembly, this process leaves even more pronounced joints within the structure, as every part is already hardened upon placing. In order to achieve stability, these joints have to be designed in order to ensure load transfer and reduce interface friction. (Elliott 2017) These joints between the parts offer a potential path of weakness. However, given the usually higher quality achieved within the factory, each part by itself offers increased durability (Abbas 2014), which sometimes can offset the negative factor of the joint.

Masonry

Given the nature of masonry, it is clear that it generally can be considered as a small-scale piece-wise assembly, as bricks or stones are each placed in layers on top of a bond-providing mortar bed. Given the increased amount of discontinuities and joints within a masonry structure, it is clear that these interfaces impact not only the structural strength but also fluid transport rates. Hence, these interfaces are usually the first section to deteriorate (Cultrone

et al. 2007). However, masonry structures can still last for centuries, as the loss of bond strength does not get as significant as masonry structures are usually designed in a way to prevent tensile stresses at these interfaces. Hence, this effect can be outweighed when durable stones (natural rocks), which make up most of the material, are used. Nevertheless, if ceramic bricks are used, the potentially contained salts cannot only be dissolved but also form expansive and damaging products elsewhere in the composite system (Kropyvnytska et al. 2017).

Roller compacted concrete

Roller compacted concrete (RCC) can be considered a material as well as a construction method (Bureau of Reclamation 2017). As the material used is low-slump concrete, this allows the usage of regular earth-moving machinery for the placement of the concrete, which is then done in layers. The usage of earth-moving machinery and construction methods allows for cheap construction of structures with simple shapes like weirs and dams. Since the material is placed in layers, joints arise between each layer, making the bonding of these (lift) joints a plane of weakness (Bureau of Reclamation 2017). Similarly, these zones do affect not only the structural performance but also the durability

A.3.3 Additional durability measures

Not only does the mixture and placement of material affect the durability, but there is also a multitude of not directly material-related measures that can be done before, during and post-construction to increase the structure's durability.

Surface Sealing

In order to reduce the ingress of fluids and thus the deterioration rates, the exposed surface of a structure can be sealed with additional measures. In order to reduce permeability, impervious substrates are applied on the surface either by dipping, brushing or spraying. The coatings can be based on polymers, silanes, and siloxane-based additives (Muhammad et al. 2015). Similarly, a sealing layer can be achieved by applying the additives during mixing within the top layer of the cementitious material. A third method of surface sealing is the inclusion of a waterproof membrane during construction (Konečný et al. 2016)

Drainage

Another strategy to protect certain parts of the structure from ingress of liquids is the usage of drainage pipes/layers. If certain parts of the structure are subjected to water at higher

pressures, for example, in subsurface structures such as tunnels or hydraulic structures like dams, drainage pipes can be used to reduce the pore pressure in the material. As the drainage is subjected to atmospheric pressure, the pore pressure is reduced at this point (Chen et al. 2016, Stematiu et al. 2011). However, drainage pipes can also increase the hydraulic gradient as the flow path is shortened. This, on the one hand, increases the flow rate through the overlying material and thus increases the deterioration of this portion of the material. On the other hand, the flow through the underlying material is reduced, which is beneficial for the durability of this section.

Grouting

Grouting can be used to apply additional sealing to the rock foundation of a structure or cracked material. For grouting, a liquid sealing material such as cement or bentonite suspension is injected into the fractures/cracks and then left to harden in place. This technique is oftentimes applied to the foundation of hydraulic structures in order to prevent high flow rates through the sub-surface (Lin et al. 2016; Heidarzadeh et al. 2011).

Quality checks and monitoring

Most of the mentioned durability factors during construction are selected during the planning phase of the structure. Nevertheless, it has to be ensured that the desired material quality as well as durability features are actually achieved and built during construction. According to DIN EN 13670 (2011), the degree of documentation and quality checks is selected according to three classes depending on the impact of the structure. The classes can be selected for the structure or for structural parts. Generally, it has to be ensured and documented that all works are done according to the current codes and specifications.

Appendix B

Boundary conditions

Boundary conditions are applied during the solution at the boundaries of the mesh. A brief description of the base types of boundary conditions is given in this section.

Dirichlet boundary conditions

The Dirichlet boundary condition directly specifies the boundary values for the solution variable at the location of the boundary $\boldsymbol{x_{bc}}$. A Dirichlet boundary condition for the pressure head h_l reads as

$$h_l(\boldsymbol{x_{bc}},t) = h_{l,applied}(\boldsymbol{x_{bc}},t) \tag{B.1}$$

Thus, this boundary type can be applied at constant water levels (pressure heads) for the moisture solution, fixed inflow concentrations during the ionic transport or zero displacement conditions during the mechanical solution.

Neumann boundary conditions

The second base type of boundary condition is the Neumann boundary condition:

$$\frac{\partial h_l(\boldsymbol{x_{bc}},t)}{\partial \boldsymbol{n_{bc}}} = \nabla h_{l,applied}(\boldsymbol{x_{bc}},t) \cdot \boldsymbol{n_{bc}} \tag{B.2}$$

where the gradient of a solution variable (e.g. ∇h_l) is fixed in direction of the boundary face normal vector. If a no flow boundary conditions is applied, the gradient can be simply set to zero in most cases. However, in the case of moisture flow with gravity, the contribution of gravity has to be taken into account ($\partial h_l/\partial z = -1$)) if zero flow should be computed. The Neumann boundary condition is also used to apply a specific flow rate $\boldsymbol{v}_{l,applied}$ across the boundary in thermal, ionic and moisture transport solutions. For this, the applied gradient has to be scaled with the resistance coefficient (e.g. hydraulic or thermal conductivity) of the

material. For moisture transport, the flow rate can be expressed as the gradient of:

$$(\nabla h_l \cdot \boldsymbol{n_{bc}}) = \frac{\boldsymbol{v}_{l,applied}}{\boldsymbol{k} \cdot \boldsymbol{n_{bc}}} \tag{B.3}$$

by making use of the hydraulic conductivity in the boundary face normal direction. In addition to the base boundary conditions, a multitude of combined and derived boundary conditions can be formulated.

Mixed boundary conditions

The mixed boundary conditions are derived by a linear blend between the Neumann and the Dirichlet boundary conditions. Hence, the contribution of both boundary conditions to the solution is computed by using weights. The boundary condition is applied for thermal boundary conditions, which can either act as a fixed flow based on radiation or fixed a value for large heat transfer coefficients.

Direction mixed boundary condition

Similarly, boundary conditions can also be different if the gradient is also evaluated in different directions. This means that a fixed value can be applied in the boundary face normal direction, while a zero gradient condition is applied in all other directions. This boundary condition is applied in mechanical solutions if the movement of a boundary is only restricted in one direction.

Value-dependent boundary conditions

In addition, the boundary condition type can also be switched depending on the computed values. A threshold value for the boundary is used to switch the boundary type during simulation. This solution is applied for the combined moisture transport solution when a free drainage solution boundary is applied. As free drainage is assumed, the pressure head at the boundary is limited to a maximum of zero as moisture cannot be stored. If the boundary is not fully saturated, moisture transfer is described by using a moisture transfer coefficient based h_{mois} on the gradient of relative moisture content (Bednar et al. 2020; Künzel 1995). The free drainage boundary is implemented as:

$$BC(h_l(\boldsymbol{x_{bc}})) = \begin{cases} h_l(\boldsymbol{x_{bc}}) = 0 & \textbf{for } h_{l,comp}(\boldsymbol{x_{bc}}) > 0 \\ \nabla h_l(\boldsymbol{x_{bc}}) = \frac{(\varphi_{r,bc} - \varphi_{r,air}) \cdot h_{mois}}{\boldsymbol{k} \cdot \boldsymbol{n_{bc}}} & \textbf{else} \end{cases} \tag{B.4}$$

In a similar way, an "outflow" boundary condition can be defined. This boundary type only enables outward flow at the boundary surface as inward flow is restricted. This is implemented by applying a no flow condition, as a zero-pressure assumption would induce non physical inward flow for low initial saturation. For outward flow directions, the boundary face pressure is switched to zero pressure. As a result, this boundary condition can be applied when capillary effects at the boundary are negligible as in case of free drainage conditions. The "outflow" boundary condition is defined as:

$$BC(h_l(\boldsymbol{x_{bc}})) = \begin{cases} h_l(\boldsymbol{x_{bc}}) = 0 & \textbf{for } h_{l,comp}(\boldsymbol{x_{bc}}) > 0 \\ \nabla h_l(\boldsymbol{x_{bc}}) = 0 & \textbf{else} \end{cases} \tag{B.5}$$

Appendix C

Further application examples

Not all results that were computed during the evaluation and application of the framework are displayed within the result section of this work. However, as the additional cases also have relevance for the presented topics, they are displayed in the following. These cases include the effect of drainage pipes on the moisture flow rates through a gravity dam as well as the crest displacement of the Koyna dam during annual temperature changes.

C.1 Drainage pipes in a gravity dam

Drainage layers are a common measure to prevent seepage in certain sections of a foundation or structure. These layers consist of pipes, slits or geomeshes, which are connected to some outlet where the drained water can be released while monitoring the discharge.

For gravity dams, drainage layers are often installed within the foundation ahead of the dam to reduce the uplift pressure below the structure. In addition, drainage systems are also installed within the dam body to reduce the moisture flow within the structure behind this section. While the structure behind this layer is more protected, the concrete between the upstream water and the drainage layer is subjected to increased flow rates. This is caused by the reduced flow length between the water and the drainage layer, while the water pressure remains the same. As a result of the increased flow rates, the deterioration rates of the first concrete layer are enhanced.

To evaluate the effect of drainage layers on the flow rates, the developed approach is used to compute the impact of drainage on moisture flow rates for a fictitious gravity dam. The geometry of the studied gravity dam is displayed in Fig. C.1.

Here the foundation rock below the dam is modeled as well. This size of the foundation rock is selected large enough not to impact the results of the studied dam. 20 cm thick drainage

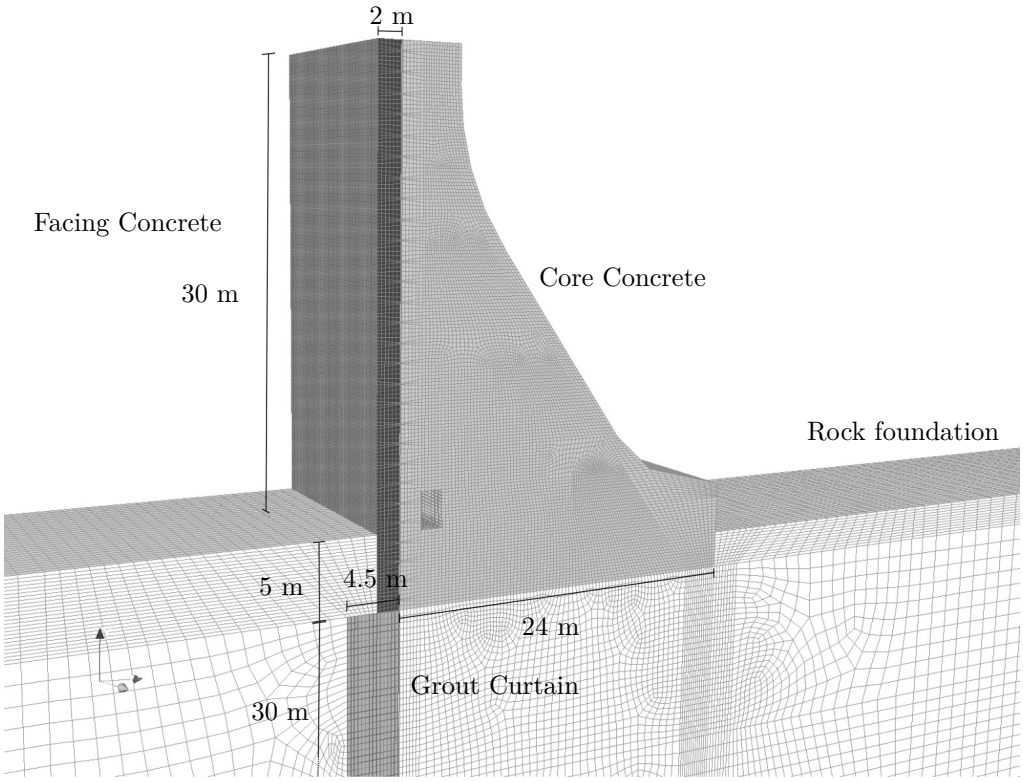

Fig. C.1: Geometry and dam sections of the gravity dam with drainage system

pipes traverse the dam structure at a 2 m distance behind the upstream face. One pipe is placed every 2 meters from the dam crest to the foundation level. The inspection gallery used for monitoring the dam also acts as an additional drain. In addition, two inspection shafts with 2 m of width are present on both sides of the dam block. The foundation below the dam has been injected to be less conductive up to 30 m below the dam. This section is labeled as grout curtain. The upstream water level is selected to be 2.5 m below the dam crest. The drainage pipes, inspection shaft, inspection gallery and downstream section are considered "outflow" boundary types. The parameters of the Van Genuchten water retention curve (Eq. 4.4) are simplified to be constant for all sections as $\alpha_{vg} = 0.1$ m^{-1}, $n_{vg} = 1.5$, $\theta_{l,sat} = 0.1$, $\theta_{l,r} = 0.0$

In order to evaluate the effect of the drainage system on the flow rates, their effectiveness is varied by changing their hydraulic conductivities in different cases. Such reduction in effectiveness can be caused by clogging induced by multiple factors. The applied hydraulic conductivity for each section and computed case (A1-A3) is displayed in Tab. C.1.

The results of the different computational cases are displayed in Fig. C.2 for the flow rates for different sections as well as the phreatic lines at a steady state.

Tab. C.1: Hydraulic conductivities (m/s) for the different computed scenarios

Case	Core concrete	Facing concrete	Foundation	Grout curtain	Drainage
A1	$1 \cdot 10^{-9}$	$1 \cdot 10^{-10}$	$1 \cdot 10^{-6}$	$1 \cdot 10^{-7}$	$1 \cdot 10^{-9}$
A2	$1 \cdot 10^{-9}$	$1 \cdot 10^{-10}$	$1 \cdot 10^{-6}$	$1 \cdot 10^{-7}$	$1 \cdot 10^{-10}$
A3	$1 \cdot 10^{-9}$	$1 \cdot 10^{-10}$	$1 \cdot 10^{-6}$	$1 \cdot 10^{-7}$	$1 \cdot 10^{-11}$

The effect of the drainage system is very evident in the comparison of the results. When comparing the phreatic lines, the shift of the phreatic line towards the upstream side is visible. This indicates that the material behind the drainage system receives less moisture. However, the flow rates for the first section are significantly increased by more than 20 times in some cases. This increase then also yields a faster deterioration of the first section. In all cases, water is also drained to the inspection shafts and the inspection gallery. Thus, these measures also increase deterioration. Their effect is even more apparent when the drainage system is clogged as moisture flow is diverted to those still available sections.

C.2 Thermal deformation of the Koyna dam

Constant changes in environmental temperatures affect a structure's displacements throughout the year. While the occurrence of thermal cracks is of importance, the observed global deformations of a structure are also regularly monitored. This is done to identify smaller damages before major problems occur. In order to identify an irregular deformation, the expected deformation needs to be known. Thus, it makes sense to compute the expected deformation of a structure for comparison.

In the following application example, the displacement of the Koyna dam is computed based on the annual temperature changes. The dam geometry is adopted as the cracked geometry previously displayed in Fig. 5.12. The water level in the reservoir is set to 100 m again, and the material's density is kept identical to the previous cases. The thermal properties of the material are selected according to basic literature values. The thermal expansion coefficient α is applied as 10^{-5} (1/K), the thermal conductivity λ as 1.5 W/(m·K) and the dry specific heat capacity as 800 J/(kg·K).

For the boundary conditions, the annual and daily change of the ambient temperature is only assumed for this application case. Therefore, the following boundary conditions are applied. A double cyclic behavior is imposed on the downstream side, which is exposed to ambient

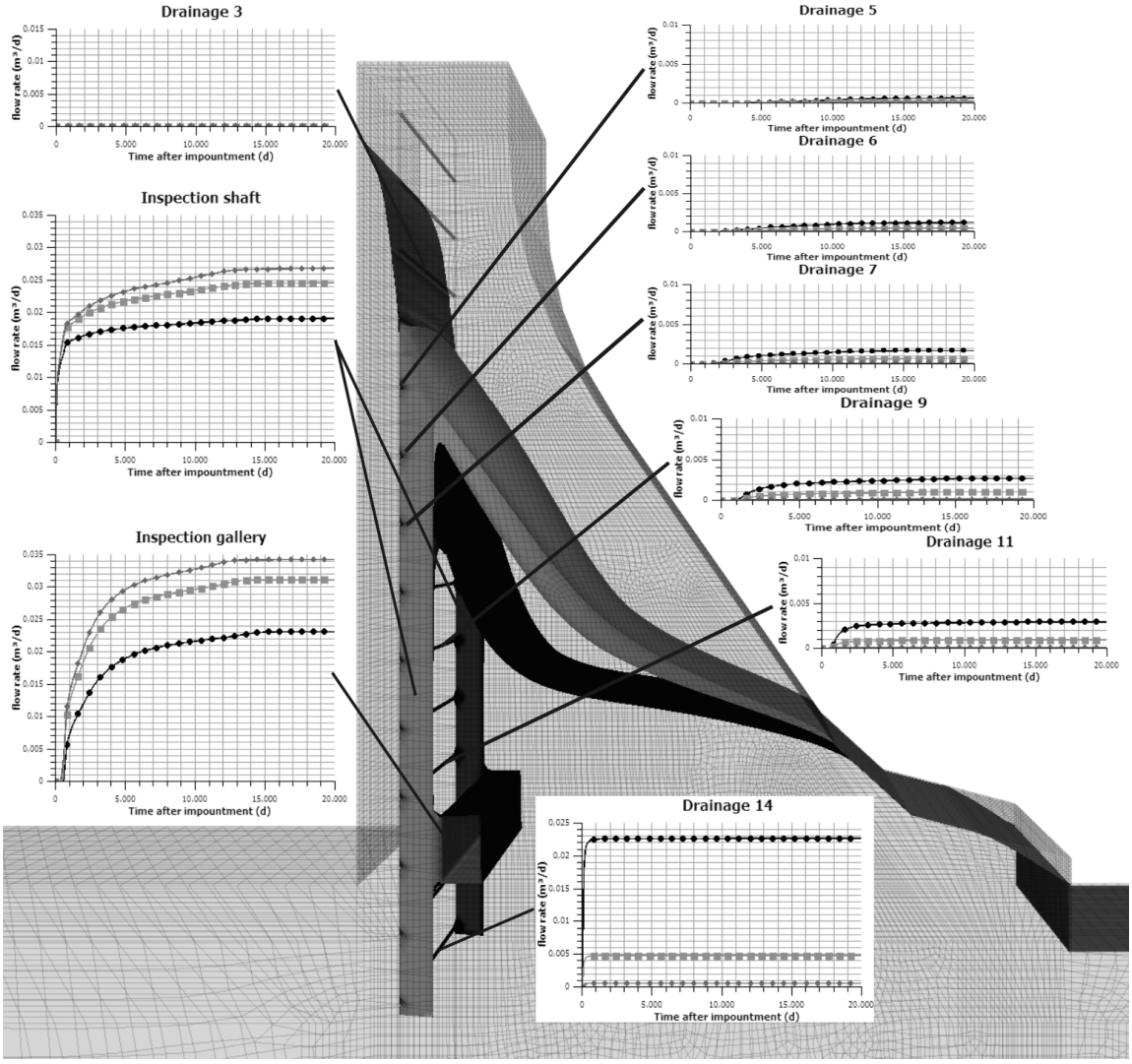

Fig. C.2: Steady state phreatic lines and computed flow rates at different sections for case A1 (black-circles), A2 (light gray-squares) and A3 (gray-diamonds)

air. This means a sinusoidal change with an amplitude of 10 °C is applied to model the daily changes, while the annual changes between 38 and 17 °C are used as a second long term sinusoidal function.

Additional assumptions have to be selected for the temperature distribution on the upstream side. Above the water surface of 100 m, the changing ambient temperature is applied as described above. For locations below the water level, a mixing layer is used, where the water temperature changes linear towards a constant temperature of 20 °C, which is assumed at lower levels below 70 m. This is a significant simplification of the actual water temperature but is applied as no data is available.

A long-term simulation computes the initial temperature distribution before the beginning of the case. Therefore, 30 years of annual temperature changes are computed before the actual modeling. After these 30 years, the new initial temperature distribution no longer influences the previous initial temperature assumption. Consequently, the further simulations are not influenced by the initial conditions. Therefore, the presented results are computed for the following year, when a steady annual cycle is already present. For the reference temperature T_{ref}, the yearly average for each cell is calculated. Again this is a simplification as the computation of the actual reference temperature does depend on many factors, as discussed in Stolz (2019).

The results of the simulation are displayed in Fig. C.3.

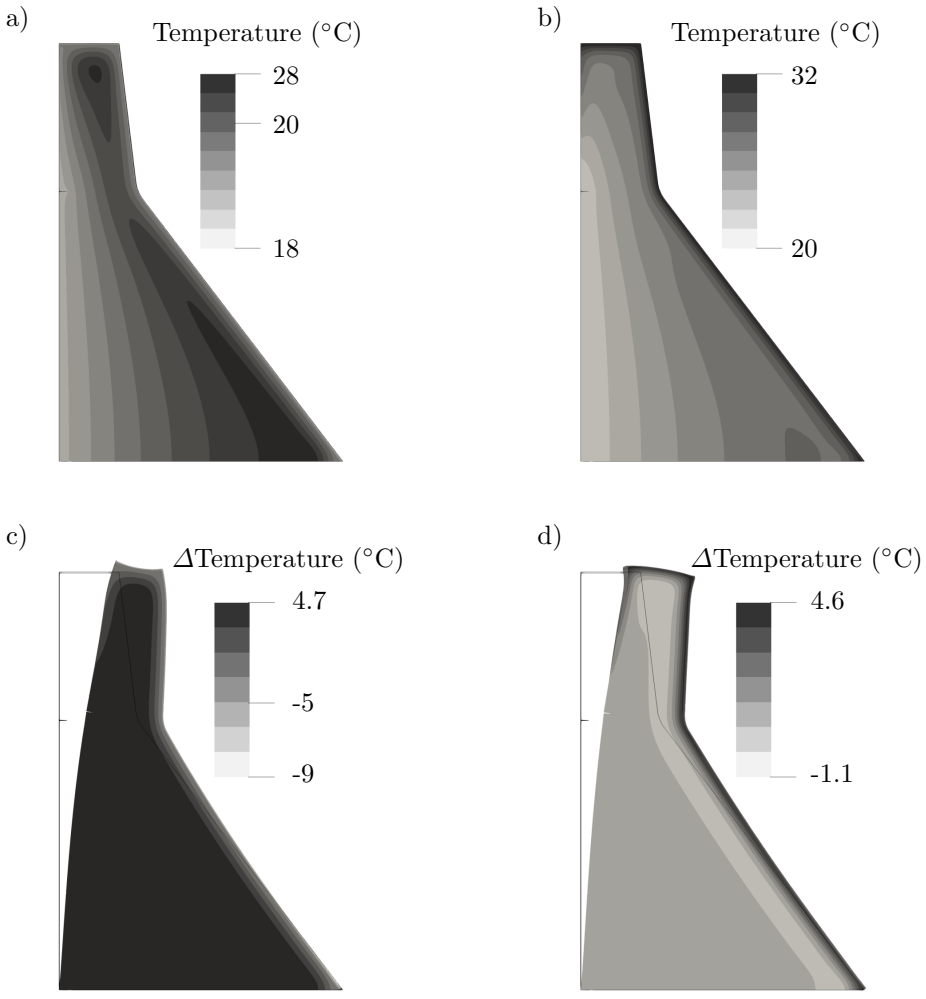

Fig. C.3: Computed dam temperature (top) and effective thermal loads and displaced structure (200 times enhanced, bottom) for the 30th (a,c) and 150th day (b,d) of the year.

Based on the constant water temperatures below 70 meters, the most apparent temperature changes occur on the downstream side. Generally, the most evident changes are visible at the dam's crest since the structure is less thick here and thus a larger fraction is subjected to temperature change. In contrast, large parts of the bottom section remain unaffected since the annual temperature variance only occurs in the first meters. This is well visible when comparing the temperature loads (ΔTemperature = T-T_{ref}) at the bottom of the figure. For the 30th day of the year, the current trend of decreasing temperatures is visible since higher temperatures are still stored in the central region, while surface temperatures are already reduced. As a result, the surface is contracting and shrinking the size of the dam crest. The opposite process occurs during summer (150th day) when increasing temperature expands the dam crest.

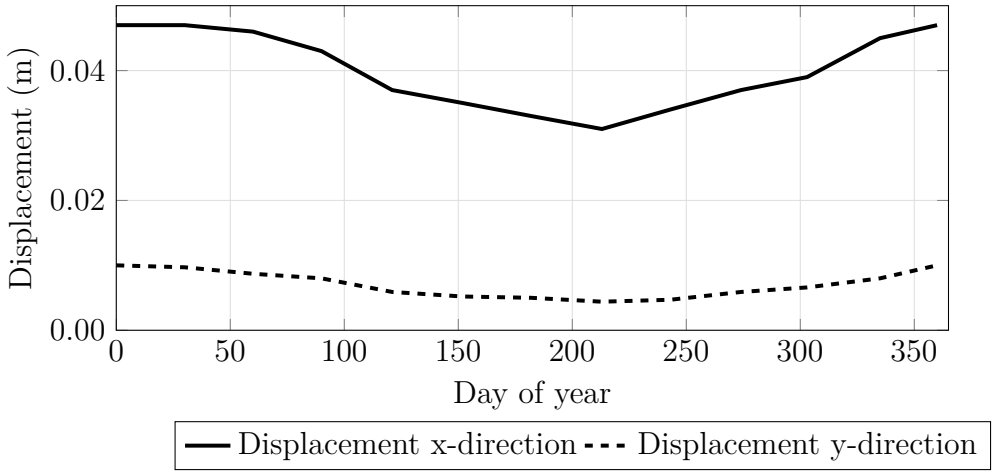

Fig. C.4: Displacement of the upstream side of the dam crest for the computed year

Finally, the displacement of the upstream side of the dam crest is displayed throughout the year in Fig. C.4. Here, the effect of the sinusoidal applied temperature is transferred to a slightly shifted (as a result of the thermal storage) almost sinusoidal response in both displacement directions. It is evident that the x-displacement of the dam crest is the highest during winter. This is mainly caused by the contraction of the downstream side, which moves the crest further backward. In contrast, the expansion of the downstream side during summer induces a movement of the dam crest towards the water. The changes in the y-direction are affected by the contraction of the dam crest, as visible in Fig. C.4. Here, the contraction of the shifts both ends upwards, while the reverse of the effect occurs during expansion during summer.

Bibliography

ACI 318. *Building code requirements for structural concrete and commentary*. Standard. Farmington Hills, MI: American Concrete Institute, 2019.

ASTM C150. *Standard Specification for Portland Cement*. Standard. West Conshohocken, PA: ASTM International, 2021.

ASTM C94. *Standard Specification for Ready-Mixed Concrete*. Standard. West Conshohocken, PA: ASTM International, 2021.

Abbas, S. "Structural and Durability Performance of Precast Segmental Tunnel Linings". PhD thesis. The University of Western Ontario, 2014.

Adenot, F. "Durabilite du beton: caracterisation et modelisation des processus physiques et chimiques de degradation du ciment". PhD thesis. S.l., 1992.

Adolphs, J., M. J. Setzer, and P. Heine. "Changes in Pore Structure and Mercury Contact Angle of Hardened Cement Paste Depending on Relative Humidity". In: *Materials and Structures* 35.8 (Sept. 2002), pp. 477–486. ISSN: 1871-6873. DOI: 10.1007/BF02483135.

Akiyama, M. and D. M. Frangopol. "Long-Term Seismic Performance of RC Structures in an Aggressive Environment: Emphasis on Bridge Piers". In: *Structure and Infrastructure Engineering* 10.7 (July 2014), pp. 865–879. ISSN: 1573-2479, 1744-8980. DOI: 10.1080/15732479.2012.761246.

Aldea, C.-M., S. P. Shah, and A. Karr. "Permeability of Cracked Concrete". In: *Materials and Structures* 32.5 (June 1999), pp. 370–376. ISSN: 1359-5997, 1871-6873. DOI: 10.1007/BF02479629.

Alexander, M. G. "Durability and Service Life Prediction for Concrete Structures – Developments and Challenges". In: *MATEC Web of Conferences* 149 (2018). Ed. by A. Diouri et al., p. 01006. ISSN: 2261-236X. DOI: 10.1051/matecconf/201814901006.

Alexander, M. G., Y. Ballim, and K. Stanish. "A Framework for Use of Durability Indexes in Performance-Based Design and Specifications for Reinforced Concrete Structures". In: *Materials and Structures* 41.5 (June 2008), pp. 921–936. ISSN: 1359-5997, 1871-6873. DOI: 10.1617/s11527-007-9295-0.

Alexander, M. G. and H. Beushausen. “Durability, Service Life Prediction, and Modelling for Reinforced Concrete Structures – Review and Critique”. In: *Cement and Concrete Research* 122 (Aug. 2019), pp. 17–29. ISSN: 00088846. DOI: 10.1016/j.cemconres.2019.04.018.

Arel, H. S., E. Aydin, and S. D. Kore. “Ageing Management and Life Extension of Concrete in Nuclear Power Plants”. In: *Powder Technology* 321 (Nov. 2017), pp. 390–408. ISSN: 00325910. DOI: 10.1016/j.powtec.2017.08.053.

Babaahmadi, A., L. Tang, Z. Abbas, and P. Mårtensson. “Physical and Mechanical Properties of Cementitious Specimens Exposed to an Electrochemically Derived Accelerated Leaching of Calcium”. In: *International Journal of Concrete Structures and Materials* 9.3 (Sept. 2015), pp. 295–306. ISSN: 1976-0485, 2234-1315. DOI: 10.1007/s40069-015-0108-5.

Badmann, R., N. Stockhausen, and M. J. Setzer. “The Statistical Thickness and the Chemical Potential of Adsorbed Water Films”. In: *Journal of Colloid and Interface Science* 82.2 (Aug. 1981), pp. 534–542. ISSN: 00219797. DOI: 10.1016/0021-9797(81)90395-7.

Barenblatt, G. I., I. P. Zheltov, and I. N. Kochina. “Basic Concepts in the Theory of Seepage of Homogeneous Liquids in Fissured Rocks [Strata]”. In: *Journal of Applied Mathematics and Mechanics* 24.5 (Jan. 1960), pp. 1286–1303. ISSN: 00218928. DOI: 10.1016/0021-8928(60)90107-6.

Barnes, B. D., S. Diamond, and W. L. Dolch. “The Contact Zone between Portland Cement Paste and Glass “Aggregate” Surfaces”. In: *Cement and Concrete Research* 8.2 (Mar. 1978), pp. 233–243. ISSN: 00088846. DOI: 10.1016/0008-8846(78)90012-1.

Baroghel-Bouny, V. “Water Vapour Sorption Experiments on Hardened Cementitious Materials”. In: *Cement and Concrete Research* 37.3 (Mar. 2007), pp. 414–437. ISSN: 00088846. DOI: 10.1016/j.cemconres.2006.11.019.

Baroghel-Bouny, V., M. Mainguy, T. Lassabatere, and O. Coussy. “Characterization and Identification of Equilibrium and Transfer Moisture Properties for Ordinary and High-Performance Cementitious Materials”. In: *Cement and Concrete Research* 29.8 (Aug. 1999), pp. 1225–1238. ISSN: 00088846. DOI: 10.1016/S0008-8846(99)00102-7.

Baroghel-Bouny, V., T. Q. Nguyen, and P. Dangla. “Assessment and prediction of RC structure service life by means of durability indicators and physical/chemical models”. In: *Cement and Concrete Composites* 31.8 (2009). Sustainability of Civil Engineering Structures - Durability of Concrete, pp. 522–534. ISSN: 0958-9465. DOI: https://doi.org/10.1016/j.cemconcomp.2009.01.009. URL: https://www.sciencedirect.com/science/article/pii/S0958946509000195.

Barpi, F. and S. Valente. “The Cohesive Frictional Crack Model Applied to the Analysis of the Dam-Foundation Joint”. In: *Engineering Fracture Mechanics* 77.11 (July 2010), pp. 2182–2191. ISSN: 00137944. DOI: 10.1016/j.engfracmech.2010.02.030.

Barrodale, I. and F. DK. Roberts. “An Improved Algorithm for Discrete L_1 Linear Approximation”. In: *SIAM Journal on Numerical Analysis* 10.5 (1973), pp. 839–848.

Bary, B., N. Leterrier, E. Deville, and P. Le Bescop. “Coupled Mechanical and Chemo-Transport Model for the Simulation of Cementitious Materials Subjected to External Sulfate Attack”. In: *Cement-Based Materials for Nuclear Waste Storage*. Ed. by Florence Bart, Céline Cau-di-Coumes, Fabien Frizon, and Sylvie Lorente. New York, NY: Springer New York, 2013, pp. 85–92. ISBN: 978-1-4614-3444-3 978-1-4614-3445-0. DOI: 10.1007/978-1-4614-3445-0_8.

Basheer, L., J. Kropp, and D. J. Cleland. “Assessment of the Durability of Concrete from Its Permeation Properties: A Review”. In: *Construction and Building Materials* 15.2-3 (Mar. 2001), pp. 93–103. ISSN: 09500618. DOI: 10.1016/S0950-0618(00)00058-1.

Bažant, Z. P. and M. Jirásek. “Fundamentals of Linear Viscoelasticity”. In: *Creep and Hygrothermal Effects in Concrete Structures*. Ed. by Z. P. Bažant and M. Jirásek. Solid Mechanics and Its Applications. Dordrecht: Springer Netherlands, 2018, pp. 9–28. ISBN: 978-94-024-1138-6. DOI: 10.1007/978-94-024-1138-6_2.

Bažant, Z. P. and M. Jirásek. “Moisture Transport in Concrete”. In: *Creep and Hygrothermal Effects in Concrete Structures*. Vol. 225. Dordrecht: Springer Netherlands, 2018, pp. 271–408. ISBN: 978-94-024-1136-2 978-94-024-1138-6. DOI: 10.1007/978-94-024-1138-6_8.

Bažant, Z. P. and B. H. Oh. “Crack Band Theory for Fracture of Concrete”. In: *Matériaux et Constructions* 16.3 (May 1983), pp. 155–177. ISSN: 0025-5432, 1871-6873. DOI: 10.1007/BF02486267.

Bažant, Z. P. and E. Osman. “Double Power Law for Basic Creep of Concrete”. In: *Matériaux et Constructions* 9.1 (Jan. 1976), pp. 3–11. ISSN: 0025-5432, 1871-6873. DOI: 10.1007/BF02478522.

Bažant, Z. P. and S. Prasannan. “Solidification Theory for Concrete Creep. I: Formulation”. In: *Journal of Engineering Mechanics* 115.8 (Aug. 1989), pp. 1691–1703. ISSN: 0733-9399, 1943-7889. DOI: 10.1061/(ASCE)0733-9399(1989)115:8(1691).

Bear, J. and M. Y. Corapcioglu, eds. *Advances in Transport Phenomena in Porous Media*. Dordrecht: Springer Netherlands, 1987. ISBN: 978-94-010-8121-4 978-94-009-3625-6. DOI: 10.1007/978-94-009-3625-6.

Becker, R. “Fundamentals of Performance-Based Building Design”. In: *Building Simulation* 1.4 (Dec. 2008), pp. 356–371. ISSN: 1996-3599, 1996-8744. DOI: 10.1007/s12273-008-8527-8.

Bednar, T. and I. Dreyer. “Determination of Moisture Surface Transfer Coefficients under Transient Conditions”. In: *Research in Building Physics*. Ed. by J. Carmeliet, H. Hens, and G. Vermeir. First. CRC Press, Dec. 2020, pp. 233–236. ISBN: 978-1-00-307885-2. DOI: 10.1201/9781003078852-33.

Bensted, J. and P. Barnes. *Structure and Performance of Cements*. London; New York: Spon Press, 2002. ISBN: 978-0-203-47778-6.

Berner, U. R. "Modelling the Incongruent Dissolution of Hydrated Cement Minerals". In: *Radiochimica Acta* 44/45.pt.2 (1988), pp. 387–393. ISSN: ISSN 0033-8230.

Bernier, C., J. E. Padgett, J. Proulx, and P. Paultre. "Seismic Fragility of Concrete Gravity Dams with Spatial Variation of Angle of Friction: Case Study". In: *Journal of Structural Engineering* 142.5 (May 2016), p. 05015002. ISSN: 0733-9445, 1943-541X. DOI: 10.1061/(ASCE)ST.1943-541X.0001441.

Bettzieche, V., R. Deutch, and C. Heitfuss. "100 Years of Experience in Ageing of Masonry Dams and Life-Time-Based Rehabilitation". In: *2nd International Conference on Lifetime Oriented Design Concept—ICOLD*. 2004.

Beushausen, H., R. Torrent, and M. G. Alexander. "Performance-Based Approaches for Concrete Durability: State of the Art and Future Research Needs". In: *Cement and Concrete Research* 119 (May 2019), pp. 11–20. ISSN: 00088846. DOI: 10.1016/j.cemconres.2019.01.003.

Bhargava, A. and N. Banthia. "Measurement of concrete permeability under stress". In: *Experimental Techniques* 30.5 (Sept. 2006), pp. 28–31. ISSN: 0732-8818, 1747-1567. DOI: 10.1111/j.1747-1567.2006.00082.x.

Bhattacharjee, S. S. and P. Léger. "Fracture Response of Gravity Dams Due to Rise of Reservoir Elevation". In: *Journal of Structural Engineering* 121.9 (1995), pp. 1298–1305.

Bhattacharya, B., D. Li, and M. Chajes. "Bridge Rating Using In-Service Data in the Presence of Strength Deterioration and Correlation in Load Processes". In: *Structure and Infrastructure Engineering* 4.3 (June 2008), pp. 237–249. ISSN: 1573-2479, 1744-8980. DOI: 10.1080/15732470600753584.

Bhatty, J. I. and P. D. Tennis. *U.S. and Canadian Cement Characteristics: 2004*. Tech. rep. PCA R& D Serial No. 2879. Portland Cement Association, 2008, p. 67.

Biot, M. A. "Theory of Propagation of Elastic Waves in a Fluid-Saturated Porous Solid. I. Low-Frequency Range". In: *The Journal of the Acoustical Society of America* 28.2 (Mar. 1956), pp. 168–178. ISSN: 0001-4966. DOI: 10.1121/1.1908239.

Bishop, A. W. "The Principle of Effective Stress". In: 39 (1959), pp. 859–863.

Bjegović, D. et al. "Test Methods for Concrete Durability Indicators". In: *Performance-Based Specifications and Control of Concrete Durability: State-of-the-Art Report RILEM TC 230-PSC*. Ed. by Hans Beushausen and Luis Fernandez Luco. RILEM State-of-the-Art Reports. Dordrecht: Springer Netherlands, 2016, pp. 51–105. ISBN: 978-94-017-7309-6. DOI: 10.1007/978-94-017-7309-6_4.

Bockris, J. O'M. and Amulya K. N. Reddy. *Modern Electrochemistry*. Boston, MA: Springer US, 1970. ISBN: 978-1-4615-7469-9 978-1-4615-7467-5. DOI: 10.1007/978-1-4615-7467-5.

Bourdette, B. “Durabilité Du Mortier : Prise En Compte Des Auréoles de Transition Dans La Caractérisation et La Modélisation Des Processus Physiques et Chimiques d’altération”. These de Doctorat. Toulouse, INSA, Jan. 1994.

Braun, M. and J. Fernández-Sáez. “A New 2D Discrete Model Applied to Dynamic Crack Propagation in Brittle Materials”. In: *International Journal of Solids and Structures* 51.21-22 (Oct. 2014), pp. 3787–3797. ISSN: 00207683. DOI: 10.1016/j.ijsolstr.2014.07.014.

Braverman, J. I. et al. “Degradation Assessment of Structures and Passive Components at Nuclear Power Plants”. In: *Nuclear Engineering and Design* 228.1-3 (Mar. 2004), pp. 283–304. ISSN: 00295493. DOI: 10.1016/j.nucengdes.2003.06.012.

Brooks, R. H. and A. T. Corey. *Hydraulic Properties of Porous Media*. Colorado State University, 1964.

Bruce, D. A. and P. D. Porcellinis. “Sealing Cracks in Concrete Dams to Provide Structural Stability”. In: *Hydro Review; (United States)* 10:4 (July 1991). ISSN: 0884-0385.

Brunauer, S., P. H. Emmett, and E. Teller. “Adsorption of Gases in Multimolecular Layers”. In: *Journal of the American Chemical Society* 60.2 (Feb. 1938), pp. 309–319. ISSN: 0002-7863, 1520-5126. DOI: 10.1021/ja01269a023.

Bullard, J. W. et al. “Mechanisms of Cement Hydration”. In: *Cement and Concrete Research* 41.12 (Dec. 2011), pp. 1208–1223. ISSN: 00088846. DOI: 10.1016/j.cemconres.2010.09.011.

Bureau of Reclamation. *Concrete Manual: A Manual for the Control of Concrete Construction.* xxxvi, 627 p. Denver: U.S. Department of the Interior, Bureau of Reclamation, 1975. ISBN: 978-0894990267.

Bureau of Reclamation. *Design of Gravity Dams: Design Manual for Concrete Gravity Dams.* Design of Gravity Dams: Design Manual for Concrete Gravity Dams. U.S. Department of the Interior, Bureau of Reclamation, 1976. URL: https://books.google.de/books?id=PL1GxgEACAAJ.

Bureau of Reclamation. *Roller-compacted concrete: design and construction considerations for hydraulic structures - Second Edition*. U.S. Department of the Interior, Bureau of Reclamation, 2017. URL: https://books.google.de/books?id=WuZRAAAAMAAJ.

Burieke, F. and H. K. Hilsdorf. “Verfahren Zur Bestimmung Der Potentiellen Dauerhaftigkeit von Beton.” In: *Beton- und Stahlbetonbau* 88.11 (Nov. 1993), pp. 306–308. ISSN: 00059900. DOI: 10.1002/best.199300470.

C01 Committee. *Specification for Blended Hydraulic Cements*. Tech. rep. ASTM International. DOI: 10.1520/C0595_C0595M-20.

Cai, Q., J. M. Robberts, and B. W. J. Van Rensburg. “Finite Element Fracture Modelling of Concrete Gravity Dams: Technical Paper”. In: *Journal of the South African Institution of Civil Engineering* 50.1 (2008), pp. 13–24.

Carde, C. and R. François. “Aging Damage Model of Concrete Behavior during the Leaching Process”. In: *Materials and Structures* 30.8 (Oct. 1997), pp. 465–472. ISSN: 1871-6873. DOI: 10.1007/BF02524774.

Carde, C., R. François, and J.-M. Torrenti. “Leaching of Both Calcium Hydroxide and C-S-H from Cement Paste: Modeling the Mechanical Behavior”. In: *Cement and Concrete Research* 26.8 (Aug. 1996), pp. 1257–1268. ISSN: 00088846. DOI: 10.1016/0008-8846(96)00095-6.

Cardiff, P. et al. “An Open-Source Finite Volume Toolbox for Solid Mechanics and Fluid-Solid Interaction Simulations”. In: *arXiv:1808.10736 [physics]* (Sept. 2018). arXiv: 1808.10736 [physics].

Carreira, D. J. and K-H. Chu. “Stress-Strain Relationship for Plain Concrete in Compression”. In: *ACI Journal* 82.6 (1985). ISSN: 0002-8061. DOI: 10.14359/10390.

Cefis, N. and C. Comi. “Chemo-Mechanical Modelling of the External Sulfate Attack in Concrete”. In: *Cement and Concrete Research* 93 (Mar. 2017), pp. 57–70. ISSN: 00088846. DOI: 10.1016/j.cemconres.2016.12.003.

Celia, M. A., E. T. Bouloutas, and R. L. Zarba. “A General Mass-Conservative Numerical Solution for the Unsaturated Flow Equation”. In: *Water Resources Research* 26.7 (July 1990), pp. 1483–1496. ISSN: 00431397. DOI: 10.1029/WR026i007p01483.

Chen, H. H. and R. K. L. Su. “Tension Softening Curves of Plain Concrete”. In: *Construction and Building Materials* 44 (July 2013), pp. 440–451. ISSN: 09500618. DOI: 10.1016/j.conbuildmat.2013.03.040.

Chen, Y.-F. et al. “Evaluation of Groundwater Leakage into a Drainage Tunnel in Jinping-I Arch Dam Foundation in Southwestern China: A Case Study”. In: *Rock Mechanics and Rock Engineering* 49.3 (Mar. 2016), pp. 961–979. ISSN: 0723-2632, 1434-453X. DOI: 10.1007/s00603-015-0786-y.

Cheng, A., S.-J. Chao, and W.-T. Lin. “Effects of Leaching Behavior of Calcium Ions on Compression and Durability of Cement-Based Materials with Mineral Admixtures”. In: *Materials* 6.5 (May 2013), pp. 1851–1872. ISSN: 1996-1944. DOI: 10.3390/ma6051851.

Choi, Y. S. and E. I. Yang. “Effect of Calcium Leaching on the Pore Structure, Strength, and Chloride Penetration Resistance in Concrete Specimens”. In: *Nuclear Engineering and Design* 259 (June 2013), pp. 126–136. ISSN: 0029-5493. DOI: 10.1016/j.nucengdes.2013.02.049.

Chong-Shi, G., S. Huai-Zhi, and Z. Hong. “Study on Coupling Model of Seepage-Field and Stress-Field for Rolled Control Concrete Dam”. In: *Applied Mathematics and Mechanics* 26.3 (2005), pp. 355–363.

Clark, L. A. and B. S. Gill. “Shear Strength of Smooth Unreinforced Construction Joints”. In: *Magazine of Concrete Research* 37.131 (June 1985), pp. 95–100. ISSN: 0024-9831, 1751-763X. DOI: 10.1680/macr.1985.37.131.95.

Cochepin, B. et al. “Approaches to Modelling Coupled Flow and Reaction in a 2D Cementation Experiment”. In: *Advances in Water Resources* 31.12 (Dec. 2008), pp. 1540–1551. ISSN: 03091708. DOI: 10.1016/j.advwatres.2008.05.007.

Constantinides, G. and F.-J. Ulm. “The effect of two types of C-S-H on the elasticity of cement-based materials: Results from nanoindentation and micromechanical modeling”. In: *Cement and Concrete Research* 34.1 (Jan. 2004). ISSN: 0008-8846.

Cooley, R. L. “Some New Procedures for Numerical Solution of Variably Saturated Flow Problems”. In: *Water Resources Research* 19.5 (Oct. 1983), pp. 1271–1285. ISSN: 1944-7973. DOI: 10.1029/WR019i005p01271.

Correns, Carl W. “Growth and Dissolution of Crystals under Linear Pressure”. In: *Discussions of the Faraday Society* 5.0 (Jan. 1949), pp. 267–271. ISSN: 0366-9033. DOI: 10.1039/DF9490500267.

Coussy, O. *Mechanics and Physics of Porous Solids*. Chichester, West Sussex, U.K: Wiley, 2010. ISBN: 978-0-470-72135-3.

Coussy, O and P Dangla. “The Equivalent Pore Pressure and the Swelling and Shrinkage of Cement-Based Materials”. In: *Materials and Structures* 37 (2004), p. 6.

Coussy, O. and P. J. M. Monteiro. “Poroelastic Model for Concrete Exposed to Freezing Temperatures”. In: *Cement and Concrete Research* 38.1 (Jan. 2008), pp. 40–48. ISSN: 00088846. DOI: 10.1016/j.cemconres.2007.06.006.

Coussy, O. and P. J. M. Monteiro. “Errata to “Poroelastic Model for Concrete Exposed to Freezing Temperatures” [Cement and Concrete Research 38 (2008) 40–48]”. In: *Cement and Concrete Research* 39.4 (Apr. 2009), pp. 371–372. ISSN: 00088846. DOI: 10.1016/j.cemconres.2009.01.009.

Cultrone, G., E. Sebastián, and M. Ortega Huertas. “Durability of Masonry Systems: A Laboratory Study”. In: *Construction and Building Materials* 21.1 (Jan. 2007), pp. 40–51. ISSN: 09500618. DOI: 10.1016/j.conbuildmat.2005.07.008.

Cusatis, G., M. Alnaggar, P. Gardoni, M. D’Ambrosia, and J. Qu. “Aging and Deterioration of Concrete Structures: Learning from the Past, Assessing the Present, and Predicting the Future; Science or Magic?” In: *CONCREEP 10*. Vienna, Austria: American Society of Civil Engineers, Sept. 2015, pp. 24–33. ISBN: 978-0-7844-7934-6. DOI: 10.1061/9780784479346.004.

Cusson, D., F. de Larrard, C. Boulay, and P. Paultre. “Strain Localization in Confined High-Strength Concrete Columns”. In: *Journal of Structural Engineering* 122.9 (Sept. 1996), pp. 1055–1061. ISSN: 0733-9445, 1943-541X. DOI: 10.1061/(ASCE)0733-9445(1996)122:9(1055).

DIN EN 12620. *Aggregates for concrete*. Standard. Brussels: European Committee for Standardization, 2008.

DIN EN 13670. *Execution of concrete structures*. Standard. Brussels: European Committee for Standardization, 2011.

DIN EN 197-1. *Cement - Part 1: Composition, specifications and conformity criteria for common cements*. Standard. Brussels: European Committee for Standardization, 2011.

DIN EN 1992. *Eurocode 2: Design of concrete structures*. Standard. Brussels: European Committee for Standardization, 2011.

DIN EN 206. *Concrete - Specification, performance, production and conformity*. Standard. Brussels: European Committee for Standardization, 2021.

Darcy, H. *Les Fontaines Publiques de La Ville de Dijon*. Paris: Dalmont, 1856.

Davies, C. W. *Ion Association*. London: Butterworths, 1962.

Davis, L. A. and S. P. Neuman. *Documentation and User's Guide: UNSAT2 - Variably Saturated Flow Model (Including 4 Example Problems). Final Report*. Tech. rep. NUREG/CR-3390; WWL/TM-1791-1. Water, Waste and Land, Inc., Fort Collins, CO (USA), Dec. 1983.

Day, Ken W. "Perspective on Prescriptions". In: *Concrete International* 27.7 (July 2005). ISSN: 0162-4075.

Dayaratnam, P. and R. Ranganathan. "Statistical Analysis of Strength of Concrete". In: *Building and Environment* 11.2 (Jan. 1976), pp. 145–152. ISSN: 03601323. DOI: 10.1016/0360-1323(76)90029-9.

De Rooij, M. R., J. M Bijen, and G Frens. "Introduction of Syneresis in Cement Paste". In: *RILEM Second International Conference on the Interfacial Transition Zone in Cementitious Composites*. RILEM Proceedings. Haifa, Isarel: E & FN Spon, 1998, pp. 59–66. ISBN: 978-0-419-24310-6.

Debye, P. and E. Hückel. "Zur Theorie Der Elektrolyte". In: *Physikalische Zeitschrift*. 24.9 (1923). Ed. by Hirzel Verlag, pp. 185–206.

Dhir, R. K., P. C. Hewlett, E. A. Byars, and J. P. Bai. "Estimating the durability of concrete in structures". In: *CONCRETE* 28.6 (1994). ISSN: 0010-5317.

Diamond, S. and J. Huang. "Interfacial Transition Zone: Reality or Myth?" In: *RILEM Second International Conference on the Interfacial Transition Zone in Cementitious Composites*. RILEM Proceedings. Haifa, Isarel: E & FN Spon, 1998, pp. 59–66. ISBN: 978-0-419-24310-6.

Dias, I.F., J. Oliver, J.V. Lemos, and O. Lloberas-Valls. "Modeling Tensile Crack Propagation in Concrete Gravity Dams via Crack-Path-Field and Strain Injection Techniques". In: *Engineering Fracture Mechanics* 154 (Mar. 2016), pp. 288–310. ISSN: 00137944. DOI: 10.1016/j.engfracmech.2015.12.028.

Dolen, T.P., G.A. Scott, K.F. von Fay, and B. Hamilton. *Effects of Concrete Deterioration on Safety of Dams*. U.S. Department of Interior, Bureau of Reclamation, 2003. URL: https://books.google.de/books?id=4Td3rgEACAAJ.

Du, M., X. Jin, H. Ye, N. Jin, and Y. Tian. "A Coupled Hygro-Thermal Model of Early-Age Concrete Based on Micro-Pore Structure Evolution". In: *Construction and Building Materials* 111 (May 2016), pp. 689–698. ISSN: 09500618. DOI: 10.1016/j.conbuildmat.2015.10.187.

Dubois, S. "Modelling the Hygrothermal Behaviour of Crop-Based Construction Materials". PhD thesis. 2014.

Eliáš, J., M. Vořechovský, J. Skoček, and Z. P. Bažant. "Stochastic Discrete Meso-Scale Simulations of Concrete Fracture: Comparison to Experimental Data". In: *Engineering Fracture Mechanics* 135 (Feb. 2015), pp. 1–16. ISSN: 00137944. DOI: 10.1016/j.engfracmech.2015.01.004.

Elliott, K. S. *Precast Concrete Structures*. Boca Raton: Taylor & Francis, CRC Press, 2017. ISBN: 978-1-4987-2399-2.

Esperanza, M., Thomas Matschei, and F. P. Glasser. "2. Sulfate Attack of Concrete". In: *Performance of Cement-Based Materials in Aggressive Aqueous Environments*. Springer Netherlands, 2013.

Fabien, A., M. Choinska, S. Bonnet, and A. Khelidj. "Experimental Study of Aggregates Size Effect on Strain, Damage and Permeability of Concrete". In: *Key Engineering Materials* 729 (Feb. 2017), pp. 115–121. ISSN: 1662-9795. DOI: 10.4028/www.scientific.net/KEM.729.115.

Fagerlund, G. "Determination of Pore-Size Distribution from Freezing-Point Depression". In: *Materials and Construction* 6.3 (May 1973), pp. 215–225. ISSN: 0025-5432, 1871-6873. DOI: 10.1007/BF02479036.

Farage, M. C. R., J. L. D. Alves, and E. M. R. Fairbairn. "Macroscopic Model of Concrete Subjected to Alkali–Aggregate Reaction". In: *Cement and Concrete Research* (2004), p. 11.

Faucon, P., F. Adenot, M. Jorda, and R. Cabrillac. "Behaviour of crystallised phases of Portland cement upon water attack". In: *Materials and Structures* 30.8 (1997), pp. 480–485. DOI: 10.1007/BF02524776. URL: https://doi.org/10.1007/BF02524776.

Fehling, E. et al., eds. *Entwicklung, Dauerhaftigkeit und Berechnung ultrahochfester Betone (UHPC): Forschungsbericht DFG FE 497/1-1*. Schriftenreihe Baustoffe und Massivbau 1. Kassel: Kassel Univ. Press, 2005. ISBN: 978-3-89958-108-9.

Figg, J. W. "Methods of Measuring the Air and Water Permeability of Concrete". In: *Magazine of Concrete Research* 25.85 (Dec. 1973), pp. 213–219. ISSN: 0024-9831, 1751-763X. DOI: 10.1680/macr.1973.25.85.213.

Fisher, L. R., R. A. Gamble, and J. Middlehurst. "The Kelvin Equation and the Capillary Condensation of Water". In: *Nature* 290.5807 (Apr. 1981), pp. 575–576. ISSN: 0028-0836, 1476-4687. DOI: 10.1038/290575a0.

Gaitero, J. J., J. S. Dolado, C. Neuen, F. Heber, and E. a. B. Koenders. "3D Computational Simulation of Calcium Leaching in Cement Matrices". In: *Materiales De Construccion* 64.316 (2014). ISSN: 0465-2746. DOI: 10.3989/mc.2014.08813.

García, A., D. Castro-Fresno, J. A. Polanco, and C. Thomas. "Abrasive Wear Evolution in Concrete Pavements". In: *Road Materials and Pavement Design* 13.3 (Sept. 2012), pp. 534–548. ISSN: 1468-0629, 2164-7402. DOI: 10.1080/14680629.2012.694094.

Gasch, T., R. Malm, and A. Ansell. "A Coupled Hygro-Thermo-Mechanical Model for Concrete Subjected to Variable Environmental Conditions". In: *International Journal of Solids and Structures* 91 (Aug. 2016), pp. 143–156. ISSN: 0020-7683. DOI: 10.1016/j.ijsolstr.2016.03.004.

Gawin, Dariusz, Francesco Pesavento, and Bernhard A. Schrefler. "Hygro-Thermo-Chemo-Mechanical Modelling of Concrete at Early Ages and beyond. Part II: Shrinkage and Creep of Concrete". In: *International Journal for Numerical Methods in Engineering* 67.3 (July 2006), pp. 332–363. ISSN: 0029-5981, 1097-0207. DOI: 10.1002/nme.1636.

Gioia, Gustavo, Zdenek P. Bazant, and Bert B. Pohl. "Is No-Tension Dam Design Always Safe? -A Numerical Study". In: 3(1) (1992), pp. 23–34.

Gjørv, O. E. "Durability of Concrete Structures". In: *Arabian Journal for Science and Engineering* 36.2 (Mar. 2011), pp. 151–172. ISSN: 1319-8025, 2191-4281. DOI: 10.1007/s13369-010-0033-5.

Glasser, F. P., J. Marchand, and E. Samson. "Durability of Concrete — Degradation Phenomena Involving Detrimental Chemical Reactions". In: *Cement and Concrete Research*. Special Issue — The 12th International Congress on the Chemistry of Cement. Montreal, Canada, July 8-13 2007 38.2 (Feb. 2008), pp. 226–246. ISSN: 0008-8846. DOI: 10.1016/j.cemconres.2007.09.015.

Godart, B. and L. Divet. "Lessons learned from structures damaged by delayed ettringite formation and the French prevention strategy". In: *Fifth international conference on Forensic Engineering, Institution of Civil Engineers*. France, Apr. 2013, 12p. URL: https://hal.archives-ouvertes.fr/hal-00945667.

Godart, B., M. de Rooij, and J. G. M. Wood, eds. *Guide to Diagnosis and Appraisal of AAR Damage to Concrete in Structures: Part 1 Diagnosis (AAR 6.1)*. RILEM State-of-the-Art Reports. Springer Netherlands, 2013. ISBN: 978-94-007-6566-5. DOI: 10.1007/978-94-007-6567-2.

Gogoi, I. and D. Maity. “Influence of Sediment Layers on Dynamic Behavior of Aged Concrete Dams”. In: *Journal of Engineering Mechanics* 133.4 (Apr. 2007), pp. 400–413. ISSN: 07339399. DOI: 10.1061/(ASCE)0733-9399(2007)133:4(400).

Gong, F., D. Zhang, E. Sicat, and T. Ueda. “Empirical Estimation of Pore Size Distribution in Cement, Mortar, and Concrete”. In: *Journal of Materials in Civil Engineering* 26.7 (July 2014), p. 04014023. ISSN: 0899-1561, 1943-5533. DOI: 10.1061/(ASCE)MT.1943-5533.0000945.

Görtz, J., J. Jürgensen, D. Stolz, S. Wieprecht, and K. Terheiden. “Impact of modelling different heat exchange processes”. In: *Applied Energy* (2022). submitted.

Görtz, J., S. Wieprecht, and K. Terheiden. “Coupled Model for Crack-Moisture Interaction in Brittle Porous Materials”. In: *International Journal of Solids and Structures* (2021), p. 14.

Görtz, J., S. Wieprecht, and K. Terheiden. “Dual Permeability Modelling of Concrete Joints”. In: *Construction and Building Materials* 302 (Oct. 2021), p. 124090. ISSN: 09500618. DOI: 10.1016/j.conbuildmat.2021.124090.

Görtz, J., A. Zafar, S. Wieprecht, and K. Terheiden. “Aperture and Permeability of Aged Concrete Joints”. In: *Construction and Building Materials* 307 (Nov. 2021), p. 124783. ISSN: 0950-0618. DOI: 10.1016/j.conbuildmat.2021.124783.

Gräf, H. and J. Bonzet. “Über den Einfluß der Porosität des erhärteten Betons auf seine Gebrauchseigenschaften”. In: 8 (1990), pp. 127–155.

Grathwohl, P. and B. Susset. “Comparison of Percolation to Batch and Sequential Leaching Tests: Theory and Data”. In: *Waste Management* 29.10 (Oct. 2009), pp. 2681–2688. ISSN: 0956-053X. DOI: 10.1016/j.wasman.2009.05.016.

Gray, W. G. and C. T. Miller. “A Generalization of Averaging Theorems for Porous Medium Analysis”. In: *Advances in Water Resources* 62 (Dec. 2013), pp. 227–237. ISSN: 03091708. DOI: 10.1016/j.advwatres.2013.06.006.

Gray, W. G., B. A. Schrefler, and F. Pesavento. “The Solid Phase Stress Tensor in Porous Media Mechanics and the Hill–Mandel Condition”. In: *Journal of the Mechanics and Physics of Solids* 57.3 (Mar. 2009), pp. 539–554. ISSN: 00225096. DOI: 10.1016/j.jmps.2008.11.005.

Grimal, E., A. Sellier, S. Multon, Y. Le Pape, and E. Bourdarot. “Concrete Modelling for Expertise of Structures Affected by Alkali Aggregate Reaction”. In: *Cement and Concrete Research* (2010), p. 6.

Guthrie, G. D. and J. W. Carey. “A Thermodynamic and Kinetic Model for Paste-Aggregate Interactions and the Alkali-Silica Reaction”. In: *Cement and Concrete Research* (2015), p. 14.

Hadley, D. W., W. L. Dolch, and S. Diamond. “On the Occurrence of Hollow-Shell Hydration Grains in Hydrated Cement Paste”. In: *Cement and Concrete Research* 30.1 (Jan. 2000), pp. 1–6. ISSN: 00088846. DOI: 10.1016/S0008-8846(99)00207-0.

Haecker, C.-J. et al. “Modeling the Linear Elastic Properties of Portland Cement Paste”. In: *Cement and Concrete Research* 35.10 (Oct. 2005), pp. 1948–1960. ISSN: 00088846. DOI: 10.1016/j.cemconres.2005.05.001.

Haga, K., S. Sutou, M. Hironaga, S. Tanaka, and S. Nagasaki. “Effects of Porosity on Leaching of Ca from Hardened Ordinary Portland Cement Paste”. In: *Cement and Concrete Research* 35.9 (Sept. 2005), pp. 1764–1775. ISSN: 00088846. DOI: 10.1016/j.cemconres.2004.06.034.

Hall, C. and W. D. Hoff. *Water Transport in Brick, Stone, and Concrete*. 2nd ed. London ; New York: Spon Press, 2012. ISBN: 978-0-415-56467-0.

Hanjari, K. Z., P. Utgenannt, and K. Lundgren. “Experimental Study of the Material and Bond Properties of Frost-Damaged Concrete”. In: *Cement and Concrete Research* 41.3 (Mar. 2011), pp. 244–254. ISSN: 0008-8846. DOI: 10.1016/j.cemconres.2010.11.007.

Hariri-Ardebili, M. A., S. M. Seyed-Kolbadi, and M. R. Kianoush. “FEM-based Parametric Analysis of a Typical Gravity Dam Considering Input Excitation Mechanism”. In: *Soil Dynamics and Earthquake Engineering* 84 (May 2016), pp. 22–43. ISSN: 02677261. DOI: 10.1016/j.soildyn.2016.01.013.

Hassanizadeh, S. M. and W. G. Gray. “High Velocity Flow in Porous Media”. In: *Transport in Porous Media* 2.6 (Dec. 1987). ISSN: 0169-3913, 1573-1634. DOI: 10.1007/BF00192152.

Haverkamp, R. and J. Y. Parlange. “Predicting the water-retention curve from particle-size distribution. 1. Sandy soils without organic matter”. In: *Soil Science* 142.6 (1986), pp. 325–339.

Heidarzadeh, M., F. Eslamian, and A. Mirghasemi. “Application of Grouting Technique for Stabilization of Coarse Materials - Karkheh Storage Dam Expenence, Iran”. In: *Dams and Reservoirs under Changing Challenges*. June 2011.

Herzer, J. and W. Kinzelbach. “Coupling of Transport and Chemical Processes in Numerical Transport Models”. In: *Geoderma* 44.2-3 (Aug. 1989), pp. 115–127. ISSN: 00167061. DOI: 10.1016/0016-7061(89)90022-0.

Heukamp, F. H., F.-J. Ulm, and J. T. Germaine. “Poroplastic Properties of Calcium-Leached Cement-Based Materials”. In: *Cement and Concrete Research* 33.8 (Aug. 2003), pp. 1155–1173. ISSN: 00088846. DOI: 10.1016/S0008-8846(03)00024-3.

Hilsdorf, H. K. *Dauerhaftigkeit von Betonen Schlussbericht Zum Forschungsauftrag FTB 30020/3114 Der Forschungsgemeinschaft Transportbeton e.V. (FTB) Sowie IfBt IV-1-5-427/85 Des Instituts Für Bautechnik, Berlin*. (Gestraffte Fassung). Schriftenreihe Des Bun-

desverbandes Der Deutschen Transportbetonindustrie e.V. Duisburg. Beton-Verl., 1997. ISBN: 978-3-7640-0359-3.

Hooton, R. D. and J. A. Bickley. "Design for Durability: The Key to Improving Concrete Sustainability". In: *Construction and Building Materials* 67 (Sept. 2014), pp. 422–430. ISSN: 09500618. DOI: 10.1016/j.conbuildmat.2013.12.016.

Horszczaruk, E. "The Model of Abrasive Wear of Concrete in Hydraulic Structures". In: *Wear* 256.7-8 (Apr. 2004), pp. 787–796. ISSN: 00431648. DOI: 10.1016/S0043-1648(03)00525-8.

Huang, B. and C. Qian. "Experiment Study of Chemo-Mechanical Coupling Behavior of Leached Concrete". In: *Construction and Building Materials* 25.5 (May 2011), pp. 2649–2654. ISSN: 0950-0618. DOI: 10.1016/j.conbuildmat.2010.12.014.

Huang, Y., H. Shao, E. Wieland, O. Kolditz, and G. Kosakowski. "A New Approach to Coupled Two-Phase Reactive Transport Simulation for Long-Term Degradation of Concrete". In: *Construction and Building Materials* 190 (Nov. 2018), pp. 805–829. ISSN: 09500618. DOI: 10.1016/j.conbuildmat.2018.09.114.

Hwang, S.-T. and K. Kammermeyer. "Surface Diffusion in Microporous Media". In: *The Canadian Journal of Chemical Engineering* (1966), p. 8.

Hwang, Y. H. et al. "Effect of Concrete Types and Construction Joints on Concrete Shear Friction Characteristics". In: *Key Engineering Materials* 723 (Dec. 2016), pp. 700–705. ISSN: 1662-9795. DOI: 10.4028/www.scientific.net/KEM.723.700.

ICOLD, ed. *The Physical Properties of Hardened Conventional Concrete in Dams (Pre-Print).* 2008.

Idowu, O. and L. Black. "The Effect of Improper Curing on Properties That May Affect Concrete Durability". In: *Magazine of Concrete Research* (2017), p. 15.

Isgor, O. B. and W. J. Weiss. "A Nearly Self-Sufficient Framework for Modelling Reactive-Transport Processes in Concrete". In: *Materials and Structures* 52.1 (Feb. 2019). ISSN: 1359-5997, 1871-6873. DOI: 10.1617/s11527-018-1305-x.

Iskhakov, T., J. J. Timothy, and G. Meschke. "Expansion and Deterioration of Concrete Due to ASR: Micromechanical Modeling and Analysis". In: *Cement and Concrete Research* 115 (Jan. 2019), pp. 507–518. ISSN: 00088846. DOI: 10.1016/j.cemconres.2018.08.001.

Jacobsen, S., G. W. Scherer, and E. M. Schulson. "Concrete–Ice Abrasion Mechanics". In: *Cement and Concrete Research* 73 (July 2015), pp. 79–95. ISSN: 00088846. DOI: 10.1016/j.cemconres.2015.01.001.

Jasak, H. and H. G. Weller. "Application of the Finite Volume Method and Unstructured Meshes to Linear Elasticity". In: *International Journal for Numerical Nethods in Engineering* 48.2 (2000), pp. 267–287.

Javandel, I., C. Doughty, and C.-F. Tsang. *Groundwater Transport: Handbook of Mathematical Models*. Washington (D.C.), 2013.

Javanmardi, Farrokh, Pierre Léger, and René Tinawi. "Seismic Structural Stability of Concrete Gravity Dams Considering Transient Uplift Pressures in Cracks". In: *Engineering Structures* 27.4 (Mar. 2005), pp. 616–628. ISSN: 01410296. DOI: 10.1016/j.engstruct.2004.12.005.

Jebli, M., F. Jamin, E. Garcia-Diaz, M. El Omari, and M. S. El Youssoufi. "Influence of Leaching on the Local Mechanical Properties of an Aggregate-Cement Paste Composite". In: *Cement and Concrete Composites* 73 (Oct. 2016), pp. 241–250. ISSN: 0958-9465. DOI: 10.1016/j.cemconcomp.2016.05.001.

Jebli, M. et al. "Leaching Effect on Mechanical Properties of Cement-Aggregate Interface". In: *Cement & Concrete Composites* 87 (Mar. 2018), pp. 10–19. ISSN: 0958-9465. DOI: 10.1016/j.cemconcomp.2017.11.018.

Jendele, L., V. Šmilauer, and J. Červenka. "Multiscale Hydro-Thermo-Mechanical Model for Early-Age and Mature Concrete Structures". In: *Advances in Engineering Software* 72 (June 2014), pp. 134–146. ISSN: 09659978. DOI: 10.1016/j.advengsoft.2013.05.002.

Jennings, H. M. "Refinements to Colloid Model of C-S-H in Cement: CM-II". In: *Cement and Concrete Research* 38.3 (Mar. 2008), pp. 275–289. ISSN: 00088846. DOI: 10.1016/j.cemconres.2007.10.006.

Jennings, H. M. and P. L. Pratt. "An Experimental Argument for the Existence of a Protective Membrane Surrounding Portland Cement during the Induction Period". In: *Cement and Concrete Research* 9.4 (July 1979), pp. 501–506. ISSN: 00088846. DOI: 10.1016/0008-8846(79)90048-6.

Jennings, H. M. et al. "Characterization and Modeling of Pores and Surfaces in Cement Paste: Correlations to Processing and Properties". In: *Journal of Advanced Concrete Technology* 6 (2008), p. 25.

Jennings, S. G. "The Mean Free Path in Air". In: *Journal of Aerosol Science* 19.2 (Apr. 1988), pp. 159–166. ISSN: 00218502. DOI: 10.1016/0021-8502(88)90219-4.

Jiang, Z., Y. Xi, X. Gu, Q. Huang, and W. Zhang. "Modelling of Water Vapour Sorption Hysteresis of Cement-Based Materials Based on Pore Size Distribution". In: *Cement and Concrete Research* 115 (Jan. 2019), pp. 8–19. ISSN: 00088846. DOI: 10.1016/j.cemconres.2018.09.015.

Jirásek, M. and M. Bauer. "Numerical Aspects of the Crack Band Approach". In: *Computers & Structures* 110–111 (Nov. 2012), pp. 60–78. ISSN: 00457949. DOI: 10.1016/j.compstruc.2012.06.006.

Juilland, P., L. Nicoleau, R. S. Arvidson, and E. Gallucci. “Advances in Dissolution Understanding and Their Implications for Cement Hydration”. In: *RILEM Technical Letters* 2 (Dec. 2017), pp. 90–98. ISSN: 2518-0231. DOI: 10.21809/rilemtechlett.2017.47.

Julnipitawong, P. “Moisture Transport in Concrete Experiment Investigations and Simulation Programs”. PhD thesis. Hamburg: Inst. für Baustoffe, Bauphysik und Bauchemie, Technische Univ. Hamburg-Harburg, 2011.

Juradin, S., G. Baloević, and A. Harapin. “Impact of Vibrations on the Final Characteristics of Normal and Self-Compacting Concrete”. In: *Materials Research* 17.1 (Dec. 2013), pp. 178–185. ISSN: 1980-5373, 1516-1439. DOI: 10.1590/S1516-14392013005000201.

Kadri, E-H. and R. Duval. “Hydration Heat Kinetics of Concrete with Silica Fume”. In: *Construction and Building Materials* 23.11 (Nov. 2009), pp. 3388–3392. ISSN: 09500618. DOI: 10.1016/j.conbuildmat.2009.06.008.

Katz, A. J. and A. H. Thompson. “Quantitative Prediction of Permeability in Porous Rock”. In: *Physical Review B* 34.11 (Dec. 1986), pp. 8179–8181. ISSN: 0163-1829. DOI: 10.1103/PhysRevB.34.8179.

Kenny, A. and A. Katz. “Characterization of the Interfacial Transition Zone around Steel Rebar by Means of the Mean Shift Method”. In: *Materials and Structures* 45.5 (May 2012), pp. 639–652. ISSN: 1359-5997, 1871-6873. DOI: 10.1617/s11527-011-9786-x.

Kermani, A. “Permeability of Stressed Concrete: Steady-state Method of Measuring Permeability of Hardened Concrete Studies in Relation to the Change in Structure of Concrete under Various Short-term Stress Levels”. In: *Building Research & Information* 19.6 (Nov. 1991), pp. 360–366. ISSN: 0961-3218, 1466-4321. DOI: 10.1080/09613219108727156.

Kim, H.-K., Y. Lettry, D.-W. Ryu, and W.-K. Song. “Mock-up Experiments on Permeability Measurement of Concrete and Construction Joints for Air Tightness Assessment”. In: *Materials and Structures* 47.1 (Jan. 2014), pp. 127–140. ISSN: 1871-6873. DOI: 10.1617/s11527-013-0050-4.

Kim, J.-K, Y.-H Moon, and S.-H Eo. “Compressive Strength Development of Concrete with Different Curing Time and Temperature”. In: *Cement and Concrete Research* 28.12 (Dec. 1998), pp. 1761–1773. ISSN: 00088846. DOI: 10.1016/S0008-8846(98)00164-1.

Kim, T., J. Olek, and H. Jeong. “Alkali–Silica Reaction: Kinetics of Chemistry of Pore Solution and Calcium Hydroxide Content in Cementitious System”. In: *Cement and Concrete Research* 71 (May 2015), pp. 36–45. ISSN: 00088846. DOI: 10.1016/j.cemconres.2015.01.017.

Klemczak, B. and M. Batog. “Heat of Hydration of Low-Clinker Cements: Part I. Semi-adiabatic and Isothermal Tests at Different Temperature”. In: *Journal of Thermal Analysis and Calorimetry* 123.2 (Feb. 2016), pp. 1351–1360. ISSN: 1388-6150, 1588-2926. DOI: 10.1007/s10973-015-4782-y.

Klinkenberg, L. J. "The Permeability Of Porous Media To Liquids And Gases". In: *Drilling and Production Practice*. OnePetro, Jan. 1941.

Kolani, B. et al. "Hydration of Slag-Blended Cements". In: *Cement and Concrete Composites* 34.9 (Oct. 2012), pp. 1009–1018. ISSN: 09589465. DOI: 10.1016/j.cemconcomp.2012.05.007.

Konečný, P. and P. Lehner. "Durability Assessment of Concrete Bridge Deck Considering Waterproof Membrane and Epoxy-Coated Reinforcement". In: *Perspectives in Science* 7 (Mar. 2016), pp. 222–227. ISSN: 22130209. DOI: 10.1016/j.pisc.2015.11.036.

Koniorczyk, M., D. Gawin, and B. A. Schrefler. "Modeling Evolution of Frost Damage in Fully Saturated Porous Materials Exposed to Variable Hygro-Thermal Conditions". In: *Computer Methods in Applied Mechanics and Engineering* 297 (Dec. 2015), pp. 38–61. ISSN: 00457825. DOI: 10.1016/j.cma.2015.08.015.

Kosmatka, S. H. and M. L. Wilson. *Design and Control of Concrete Mixtures: The Guide to Applications, Methods, and Materials*. 15th ed. Engineering Bulletin 1. Skokie, Ill: Portland Cement Association, 2011. ISBN: 978-0-89312-272-0.

Koudina, N., R. Gonzalez Garcia, J.-F. Thovert, and P. M. Adler. "Permeability of Three-Dimensional Fracture Networks". In: *Physical Review E* 57.4 (Apr. 1998), pp. 4466–4479. ISSN: 1063-651X, 1095-3787. DOI: 10.1103/PhysRevE.57.4466.

Kropyvnytska, T., R. Semeniv, and H. Ivashchyshyn. "Increase of Brick Masonry Durability for External Walls of Buildings and Structures". In: *MATEC Web of Conferences* 116 (2017). Ed. by G. Vatulia, A. Plugin, and O. Darenskyi, p. 01007. ISSN: 2261-236X. DOI: 10.1051/matecconf/201711601007.

Künzel, H. M. *Simultaneous Heat and Moisture Transport in Building Components: One- and Two-Dimensional Calculation Using Simple Parameters*. Stuttgart: IRB Verlag, 1995. ISBN: 978-3-8167-4103-9.

Kurdowski, W. *Cement and Concrete Chemistry*. Dordrecht: Springer Netherlands, 2014. ISBN: 978-94-007-7944-0 978-94-007-7945-7. DOI: 10.1007/978-94-007-7945-7.

Lai, D. and R. Liang. "Coupled Creep and Seepage Model for Hybrid Media". In: *Journal of Engineering Mechanics* 134.3 (2008), pp. 217–223.

Lamichhane, K. "The effect of aggregate porosity on the chloride penetrability of high performance concretes". PhD thesis. University of Wisconsin, 2005, p. 228.

Leech, C., D. Lockington, and D. Hooton. "Estimation of Water Retention Curve from Mercury Intrusion Porosimetry and van Genuchten Model". In: *ACI Structural Journal* 103.2 (2006). ISSN: 0889-3241. DOI: 10.14359/15187.

Leech, C. et al. "Validation of Mualem's conductivity model and prediction of saturated permeability from sorptivity". In: *ACI Materials Journal* 105 (Jan. 2008). ISSN: 0889-325X. DOI: 10.14359/19206.

Lewis, R. W. and B. A. Schrefler. “Finite element simulation of the subsidence of gas reservoirs undergoing a waterdrive”. In: *Finite Elements in Fluids* (Dec. 1982), pp. 179–199.

Lewis, R. W., B. A. Schrefler, and R. W. Lewis. *The Finite Element Method in the Static and Dynamic Deformation and Consolidation of Porous Media*. 2nd ed. Chichester ; New York: John Wiley, 1998. ISBN: 978-0-471-92809-6.

Li, X., Q. Xu, and S. Chen. “An Experimental and Numerical Study on Water Permeability of Concrete”. In: *Construction and Building Materials* 105 (Feb. 2016), pp. 503–510. ISSN: 09500618. DOI: 10.1016/j.conbuildmat.2015.12.184.

Lin, P., X. Zhu, Q. Li, H. Liu, and Y. Yu. “Study on Optimal Grouting Timing for Controlling Uplift Deformation of a Super High Arch Dam”. In: *Rock Mechanics and Rock Engineering* 49.1 (Jan. 2016), pp. 115–142. ISSN: 0723-2632, 1434-453X. DOI: 10.1007/s00603-015-0732-z.

Locher, F. W., W. Richartz, and S. Sprung. “Erstarren von Zement. T. 1. Reaktion Und Gefuegeentwicklung”. In: *ZKG international* (1976), pp. 435–442.

Lu, M. and M. Anson. “Establish Concrete Placing Rates Using Quality Control Records from Hong Kong Building Construction Projects”. In: *Journal of Construction Engineering and Management* 130.2 (Apr. 2004), pp. 216–224. ISSN: 0733-9364, 1943-7862. DOI: 10.1061/(ASCE)0733-9364(2004)130:2(216).

MacQuarrie, K. T.B. and K. U. Mayer. “Reactive Transport Modeling in Fractured Rock: A State-of-the-Science Review”. In: *Earth-Science Reviews* 72.3-4 (Oct. 2005), pp. 189–227. ISSN: 00128252. DOI: 10.1016/j.earscirev.2005.07.003.

Mainguy, M. and O. Coussy. “Propagation Fronts during Calcium Leaching and Chloride Penetration”. In: *Journal of Engineering Mechanics* 126.3 (2000), pp. 250–257. ISSN: 0733-9399, 1943-7889. DOI: 10.1061/(ASCE)0733-9399(2000)126:3(250).

Malyszko, L. “The Rankine-Type Criterion Aimed at Describing Masonry Orthotropy”. In: *Structural Analysis of Historical Constructions*. 2006, p. 10.

Marchand, J., I. Odler, and J. P. Skalny. *Sulfate Attack on Concrete*. Zeroth. CRC Press, Oct. 2001. ISBN: 978-0-203-30162-3. DOI: 10.4324/9780203301623.

Marty, N. C. M. et al. “Simulation of Cement/Clay Interactions: Feedback on the Increasing Complexity of Modelling Strategies”. In: *Transport in Porous Media* 104.2 (Sept. 2014), pp. 385–405. ISSN: 0169-3913, 1573-1634. DOI: 10.1007/s11242-014-0340-5.

Matala, S. “Effects of Carbonation on the Pore Structure of Granulated Blast Furnace Slag Concrete”. PhD thesis. Espoo: Helsinki University of Technology, 1995. ISBN: 9789512225866.

Mayer, G., F. Jacobs, and F. H. Wittmann. “Experimental Determination and Numerical Simulation of the Permeability of Cementitious Materials”. In: *Nuclear Engineering and*

Design 138.2 (Dec. 1992), pp. 171–177. ISSN: 00295493. DOI: 10.1016/0029-5493(92)90293-5.

Meddah, M. S., S. Zitouni, and S. Belâabes. "Effect of Content and Particle Size Distribution of Coarse Aggregate on the Compressive Strength of Concrete". In: *Construction and Building Materials* 24.4 (Apr. 2010), pp. 505–512. ISSN: 09500618. DOI: 10.1016/j.conbuildmat.2009.10.009.

Mirsadeghi, M., D. Cóstola, B. Blocken, and J. L. M. Hensen. "Review of External Convective Heat Transfer Coefficient Models in Building Energy Simulation Programs: Implementation and Uncertainty". In: *Applied Thermal Engineering* 56.1-2 (2013), pp. 134–151. ISSN: 13594311. DOI: 10.1016/j.applthermaleng.2013.03.003.

Mu, D., Z.-S. Liu, C. Huang, and N. Djilali. "Determination of the Effective Diffusion Coefficient in Porous Media Including Knudsen Effects". In: *Microfluidics and Nanofluidics* 4.3 (Mar. 2008), pp. 257–260. ISSN: 1613-4982, 1613-4990. DOI: 10.1007/s10404-007-0182-3.

Mualem, Y. "A New Model for Predicting the Hydraulic Conductivity of Unsaturated Porous Media". In: *Water Resources Research* 12.3 (June 1976), pp. 513–522. ISSN: 1944-7973. DOI: 10.1029/WR012i003p00513.

Muhammad, N. Z., A. Keyvanfar, M. Z. Abd. Majid, A. Shafaghat, and J. Mirza. "Waterproof Performance of Concrete: A Critical Review on Implemented Approaches". In: *Construction and Building Materials* 101 (Dec. 2015), pp. 80–90. ISSN: 09500618. DOI: 10.1016/j.conbuildmat.2015.10.048.

Multon, S. and A. Sellier. "Expansion Modelling Based on Cracking Induced by the Formation of New Phases in Concrete". In: *International Journal of Solids and Structures* 160 (Mar. 2019), pp. 293–306. ISSN: 00207683. DOI: 10.1016/j.ijsolstr.2018.11.001.

Navarro, V. et al. "Characterization of the Water Flow through Concrete Based on Parameter Estimation from Infiltration Tests". In: *Cement and Concrete Research* 36.9 (Sept. 2006), pp. 1575–1582. ISSN: 00088846. DOI: 10.1016/j.cemconres.2005.11.015.

Nechnech, W., F. Meftah, and J.M. Reynouard. "An Elasto-Plastic Damage Model for Plain Concrete Subjected to High Temperatures". In: *Engineering Structures* 24.5 (May 2002), pp. 597–611. ISSN: 01410296. DOI: 10.1016/S0141-0296(01)00125-0.

Nemati, K. M., P. J. M. Monteiro, and K. L. Scrivener. "Analysis of Compressive Stress-Induced Cracks in Concrete". In: *Materials Journal* 95.5 (Sept. 1998), pp. 617–630. ISSN: 0889-325X. DOI: 10.14359/404.

Neville, A. M. and J. J. Brooks. *Concrete Technology*. 2. ed. Harlow: Prentice Hall, 2010. ISBN: 978-0-273-73219-8.

Nguyen-Tuan, Long, M. A. Etzold, C. Rößler, and H.-M. Ludwig. "Growth and porosity of C-S-H phases using the sheet growth model". In: *Cement and Concrete Research* 129 (2020),

p. 105960. ISSN: 0008-8846. DOI: https://doi.org/10.1016/j.cemconres.2019.105960. URL: https://www.sciencedirect.com/science/article/pii/S0008884619306428.

Nguyen, V. H., H. Colina, J. M. Torrenti, C. Boulay, and B. Nedjar. "Chemo-Mechanical Coupling Behaviour of Leached Concrete Part I: Experimental Results". In: *Nuclear Engineering and Design* (2007), p. 7.

Obi, L. E. "Evaluation of the Effects of Coarse Aggregate Sizes on Concrete Quality". In: *European Journal of Engineering Research and Science* 2.10 (Oct. 2017), p. 1. ISSN: 2506-8016. DOI: 10.24018/ejers.2017.2.10.470.

Olusola, K. O., A. J. Babafemi, A. A. Umoh, and B. J. Olawuyi. "Effect of Batching Methods on the Fresh and Hardened Properties of Concrete". In: *IJRRAS 13 (3)* (2012), p. 7.

Omoding, N., L. S. Cunningham, and G. F. Lane-Serff. "Review of Concrete Resistance to Abrasion by Waterborne Solids". In: *ACI Materials Journal* 117.3 (May 2020). ISSN: 0889325X, 0889325X. DOI: 10.14359/51724592.

Pacelli, W. A., F. R. Andriolo, and G. S. Sarkaria. "Treatment and Performance of Construction Joints in Concrete Dams". In: *International water power & dam construction* 45 (1993), pp. 26–31.

Pal, S. and D. K. Paul. "Influence of Dam and Foundation Discountinuities Using Discountinuum Approach—A Case Study". In: *Seventh International Conference on Case histories in Geotechnical Engineering*. USA, 2013.

Paluszny, A. and S. K. Matthäi. "Numerical Modeling of Discrete Multi-Crack Growth Applied to Pattern Formation in Geological Brittle Media". In: *International Journal of Solids and Structures* (2009), p. 15.

Paluszny, A., R. N. Thomas, M. C. Saceanu, and R. W. Zimmerman. "Hydro-Mechanical Interaction Effects and Channelling in Three-Dimensional Fracture Networks Undergoing Growth and Nucleation". In: *Journal of Rock Mechanics and Geotechnical Engineering* 12.4 (Aug. 2020), pp. 707–719. ISSN: 16747755. DOI: 10.1016/j.jrmge.2020.04.004.

Papadakis, V. G., M. N. Fardis, and C. G. Vayenas. "Hydration and Carbonation of Pozzolanic Cements". In: *ACI Materials Journal* 89.2 (Jan. 1992). DOI: 10.14359/2185.

Parkhurst, D. L. and C.A.J. Appelo. *User's guide to PHREEQC (Version 2): A computer program for speciation, batch-reaction, one-dimensional transport, and inverse geochemical calculations*. Tech. rep. Denver: U.S. DEPARTMENT OF THE INTERIOR, 1999.

Parrott, L. J. "Water Absorption in Cover Concrete". In: *Materials and Structures* 25.5 (June 1992), pp. 284–292. ISSN: 0025-5432, 1871-6873. DOI: 10.1007/BF02472669.

Patil, S. and R. Mahavidyalaya. "Limnological Status of Maligre Freshwater Reservoir of Ajara Tahsil, Kolhapur District (MS), India". In: *International Journal of Science, Environment and Technology* 2.6 (2013).

Penttala, V. “Freezing-Induced Strains and Pressures in Wet Porous Materials and Especially in Concrete Mortars”. In: *Advanced Cement Based Materials* 7.1 (Jan. 1998), pp. 8–19. ISSN: 10657355. DOI: 10.1016/S1065-7355(97)00011-4.

Pinson, M. B. et al. “Hysteresis from Multiscale Porosity: Modeling Water Sorption and Shrinkage in Cement Paste”. In: *Physical Review Applied* 3.6 (June 2015). ISSN: 2331-7019. DOI: 10.1103/PhysRevApplied.3.064009.

Plusquellec, G. et al. “Determination of the pH and the Free Alkali Metal Content in the Pore Solution of Concrete: Review and Experimental Comparison”. In: *Cement and Concrete Research* 96 (June 2017), pp. 13–26. ISSN: 00088846. DOI: 10.1016/j.cemconres.2017.03.002.

Polder, R. B., M. R. de Rooij, and TNO Bouw en Ondergrond. “Durability of Marine Concrete Structures - Field Investigations and Modelling”. In: *Heron* 50.3 (2005), p. 133.

Ponloa, W. and S. Sajjavanich. “Effects of Calcium Leaching from High Volume Fly Ash Cement Paste and Mortar”. In: *Materials Today: Proceedings* 5.3 (2018), pp. 9453–9460. ISSN: 22147853. DOI: 10.1016/j.matpr.2017.10.124.

Powers, T. C. “Structure and Physical Properties of Hardened Portland Cement Paste”. In: *Journal of the American Ceramic Society* 41.1 (Jan. 1958), pp. 1–6. ISSN: 0002-7820, 1551-2916. DOI: 10.1111/j.1151-2916.1958.tb13494.x.

Price, W. H. “Factors Influencing Concrete Strength”. In: *Journal Proceedings* 47.2 (Feb. 1951), pp. 417–432. ISSN: 0002-8061. DOI: 10.14359/12003.

Qi, H., Y.-G. Li, and X.-L. Lü. “Practical Elasto-Plastic Damage Model for Dynamic Loading and Nonlinear Analysis of Koyna Concrete Dam”. In: *Journal of Central South University* 20.9 (Sept. 2013), pp. 2586–2592. ISSN: 2095-2899, 2227-5223. DOI: 10.1007/s11771-013-1772-8.

Qin, S., D. Zou, T. Liu, and A. Jivkov. “A Chemo-Transport-Damage Model for Concrete under External Sulfate Attack”. In: *Cement and Concrete Research* 132 (June 2020), p. 106048. ISSN: 00088846. DOI: 10.1016/j.cemconres.2020.106048.

RILEM Committee 73-SBC. “Final Report Siliceous By-Products for Use in Concrete”. In: *Materials and Structures* 21.1 (Jan. 1988), pp. 69–80. ISSN: 1871-6873. DOI: 10.1007/BF02472530.

RILEM. “RILEM TC 116-PCD: Permeability of Concrete as a Criterion of Its Durability. Concrete Durability - An Approach towards Performance Testing.” In: *Materials and Structures* 32.217 (1999), pp. 163–173. ISSN: 1359-5997.

Rahal, S., A. Sellier, and G. Casaux-Ginestet. “Finite Element Modelling of Permeability in Brittle Materials Cracked in Tension”. In: *International Journal of Solids and Structures* 113–114 (May 2017), pp. 85–99. ISSN: 0020-7683. DOI: 10.1016/j.ijsolstr.2016.12.023.

Rastiello, G., C. Boulay, S. Dal Pont, J. L. Tailhan, and P. Rossi. “Real-Time Water Permeability Evolution of a Localized Crack in Concrete under Loading”. In: *Cement and Concrete Research* 56 (Feb. 2014), pp. 20–28. ISSN: 00088846. DOI: 10.1016/j.cemconres.2013.09.010.

Regourd, M. “Resistance of concrete to chemical attack”. In: *Materials & Structures* 14.80 (1981).

Richards, L. A. “Capillary Conduction of Liquids through Porous Mediums”. In: *Physics* 1.5 (1931), pp. 318–333. ISSN: 01486349. DOI: 10.1063/1.1745010.

Richardson, I. G. “The Calcium Silicate Hydrates”. In: *Cement and Concrete Research* 38.2 (Feb. 2008), pp. 137–158. ISSN: 00088846. DOI: 10.1016/j.cemconres.2007.11.005.

Rifai, H., A. Staude, D. Meinel, B. Illerhaus, and G. Bruno. “In-Situ Pore Size Investigations of Loaded Porous Concrete with Non-Destructive Methods”. In: *Cement and Concrete Research* 111 (Sept. 2018), pp. 72–80. ISSN: 00088846. DOI: 10.1016/j.cemconres.2018.06.008.

Roels, S., P. Moonen, K. De Proft, and J. Carmeliet. “A Coupled Discrete-Continuum Approach to Simulate Moisture Effects on Damage Processes in Porous Materials”. In: *Computer Methods in Applied Mechanics and Engineering* 195.52 (Nov. 2006), pp. 7139–7153. ISSN: 00457825. DOI: 10.1016/j.cma.2005.05.051.

Sakai, Y. “Relationship between Water Permeability and Pore Structure of Cementitious Materials”. In: *Magazine of Concrete Research* (July 2019), pp. 1–31. ISSN: 0024-9831, 1751-763X. DOI: 10.1680/jmacr.19.00135.

Samson, E., G. Lemaire, J. Marchand, and J. J. Beaudoin. “Modeling Chemical Activity Effects in Strong Ionic Solutions”. In: *Computational Materials Science* 15.3 (Aug. 1999), pp. 285–294. ISSN: 0927-0256. DOI: 10.1016/S0927-0256(99)00017-8.

Samson, E. and J. Marchand. “Numerical Solution of the Extended Nernst–Planck Model”. In: *Journal of colloid and interface science* 215.1 (1999), pp. 1–8.

Samson, E. and J. Marchand. “Modeling the Transport of Ions in Unsaturated Cement-Based Materials”. In: *Computers & Structures* 85.23-24 (Dec. 2007), pp. 1740–1756. ISSN: 00457949. DOI: 10.1016/j.compstruc.2007.04.008.

Samson, E. and J. Marchand. “Modeling the Transport of Ions in Unsaturated Cement-Based Materials”. In: *Computers & Structures* 85.23-24 (Dec. 2007), pp. 1740–1756. ISSN: 00457949. DOI: 10.1016/j.compstruc.2007.04.008.

Sanchez, T., P. Henocq, O. Millet, and A. Aït-Mokhtar. “Coupling PhreeqC with Electro-Diffusion Tests for an Accurate Determination of the Diffusion Properties on Cementitious Materials”. In: *Journal of Electroanalytical Chemistry* 858 (Feb. 2020), p. 113791. ISSN: 15726657. DOI: 10.1016/j.jelechem.2019.113791.

Sangoju, B., R. Gopal, and B. Bhajantri. “A Review on Performance-based Specifications toward Concrete Durability”. In: *Structural Concrete* 22.5 (Oct. 2021), pp. 2526–2538. ISSN: 1464-4177, 1751-7648. DOI: 10.1002/suco.201900542.

Santamaria, J. L., V. Valentin, and G. Huerta. “Quantifying the Effect of Construction Site Factors on Concrete Compressive Strength Using Designed Experiments”. In: *International Journal of Experimental Design and Process Optimisation* 6.1 (2019), p. 26. ISSN: 2040-2252, 2040-2260. DOI: 10.1504/IJEDPO.2019.097466.

Santillán, D., J. C. Mosquera, and L. Cueto-Felgueroso. “Phase-Field Model for Brittle Fracture. Validation with Experimental Results and Extension to Dam Engineering Problems”. In: *Engineering Fracture Mechanics* 178 (June 2017), pp. 109–125. ISSN: 00137944. DOI: 10.1016/j.engfracmech.2017.04.020.

Santos, D. S., P. M.D. Santos, and D. Dias-da-Costa. “Effect of Surface Preparation and Bonding Agent on the Concrete-to-Concrete Interface Strength”. In: *Construction and Building Materials* 37 (Dec. 2012), pp. 102–110. ISSN: 09500618. DOI: 10.1016/j.conbuildmat.2012.07.028.

Scherer, G. W. “Stress from Crystallization of Salt”. In: *Cement and Concrete Research* 34.9 (Sept. 2004), pp. 1613–1624. ISSN: 00088846. DOI: 10.1016/j.cemconres.2003.12.034.

Schonlin, K. and H. K. Hilsdorf. “Evaluation of the Effectiveness of Curing of Concrete Structures”. In: *ACI Symposium Publication* 100 (Jan. 1987). DOI: 10.14359/3541.

Schrefler, B. A. et al. “A General Framework for Modeling Long-Term Behavior of Earth and Concrete Dams”. In: *Frontiers of Architecture and Civil Engineering in China* 5.1 (Aug. 2010), pp. 41–52. ISSN: 1673-7407, 1673-7512. DOI: 10.1007/s11709-010-0070-x.

Scrivener, K. L., A. K. Crumbie, and P. Laugesen. “The Interfacial Transition Zone (ITZ) Between Cement Paste and Aggregate in Concrete”. In: *Interface Science* 12.4 (Oct. 2004), pp. 411–421. ISSN: 0927-7056. DOI: 10.1023/B:INTS.0000042339.92990.4c.

Scrivener, K., A. Ouzia, Patrick Juilland, and A. Kunhi Mohamed. “Advances in Understanding Cement Hydration Mechanisms”. In: *Cement and Concrete Research* 124 (Oct. 2019), p. 105823. ISSN: 00088846. DOI: 10.1016/j.cemconres.2019.105823.

Scuero, A. and G. Vaschetti. “Geomembrane Sealing Systems for Dams: ICOLD Bulletin 135”. In: *Innovative Infrastructure Solutions* 2.1 (Dec. 2017), p. 29. ISSN: 2364-4176, 2364-4184. DOI: 10.1007/s41062-017-0089-0.

Sellier, Alain, Eric Bourdarot, StÃ©phane Multon, Martin Cyr, and Etienne Grimal. “Combination of structural monitoring and laboratory tests for assessment of Alkali-Aggregate Reaction swelling: application to gate structure dam”. In: *ACI Materials Journal* 106 (May 2009), pp. 281–290. DOI: 10.14359/56553.

Sha, S. and G. Zhang. “Modeling of Hydraulic Fracture of Concrete Gravity Dams by Stress-Seepage-Damage Coupling Model”. In: *Mathematical Problems in Engineering* 2017 (2017), pp. 1–15. ISSN: 1024-123X, 1563-5147. DOI: 10.1155/2017/8523213.

Shi, B.-W., M.-C. Li, L.-G. Song, M.-X. Zhang, and Y. Shen. “Deformation Coordination Analysis of CC-RCC Combined Dam Structures under Dynamic Loads”. In: *Water Science and Engineering* 13.2 (June 2020), pp. 162–170. ISSN: 16742370. DOI: 10.1016/j.wse.2020.07.001.

Shi, M., H. Zhong, E. T. Ooi, C. Zhang, and C. Song. “Modelling of Crack Propagation of Gravity Dams by Scaled Boundary Polygons and Cohesive Crack Model”. In: *International Journal of Fracture* 183.1 (Sept. 2013), pp. 29–48. ISSN: 0376-9429, 1573-2673. DOI: 10.1007/s10704-013-9873-9.

Shin, K. J., W. Bae, S.-W. Choi, M. W. Son, and K. M. Lee. “Parameters Influencing Water Permeability Coefficient of Cracked Concrete Specimens”. In: *Construction and Building Materials* 151 (Oct. 2017), pp. 907–915. ISSN: 09500618. DOI: 10.1016/j.conbuildmat.2017.06.093.

Silva, J. R. M. C. Da. “Use of Cement Based Grouts in the Rehabilitation of Concrete Dams: A Review”. In: *5th International Conference on Smart Monitoring, Assessment and Rehabilitation of Civil Structures*. Potsdam, Germany, 2019.

Šimůnek, J., M. Sejna, H. Saito, M. Sakai, and M. T. van Genuchten. *The HYDRUS-1D Software Package for Simulating the One-Dimensional Movement of Water, Heat, and Multiple Solutes in Variably-Saturated Media*. Tech. rep. Riverside, California, USA: Department of Environmental Sciences, University of California Riverside, 2008.

Šimůnek, J., T. Vogel, and M. T. van-Genuchten. *The SWMS_2D Code for Simulating Water Flow and Solute Transport in Two-Dimensional Variably Saturated Media*. Tech. rep. 132. Riverside, California, USA: Salinity Laboratory, USDA,ARS, 1994.

Šimůnek, J., N. J. Jarvis, M. T. van Genuchten, and A. Gärdenäs. “Review and Comparison of Models for Describing Non-Equilibrium and Preferential Flow and Transport in the Vadose Zone”. In: *Journal of Hydrology* 272.1-4 (Mar. 2003), pp. 14–35. ISSN: 00221694. DOI: 10.1016/S0022-1694(02)00252-4.

Šimůnek, J., M. T.. van Genuchten, and M. Šejna. “Recent Developments and Applications of the HYDRUS Computer Software Packages”. In: *Vadose Zone Journal* 15.7 (July 2016), vzj2016.04.0033. ISSN: 15391663. DOI: 10.2136/vzj2016.04.0033.

Skaggs, R. W., E. J. Monke, and L. F. Huggins. *An Approximate Method For Determining The Hydraulic Conductivity Of Unsaturated Soils*. Tech. rep. Indiana Water Resources Research Center, 1970.

Skarżyński, Ł. and J. Tejchman. “Experimental Investigations of Fracture Process in Concrete by Means of X-ray Micro-computed Tomography: X-ray Micro-computed Tomography”. In: *Strain* 52.1 (Feb. 2016), pp. 26–45. ISSN: 00392103. DOI: 10.1111/str.12168.

Skempton, A. W. “Effective Stress in Soils, Concrete and Rocks”. In: *Selected papers on soil mechanics*. 1961, pp. 106–118. DOI: 10.1680/sposm.02050.0014. URL: https://www.icevirtuallibrary.com/doi/abs/10.1680/sposm.02050.0014.

Spyrakos, C. C. “Bridging Performance Based Seismic Design with Restricted Interventions on Cultural Heritage Structures”. In: *Engineering Structures* 160 (Apr. 2018), pp. 34–43. ISSN: 01410296. DOI: 10.1016/j.engstruct.2018.01.022.

Stematiu, D., R. Sarghiuta, and A. Constantinescu. “Long Term Behavior of the Concrete Dams Drainage System and Ageing Phenomena”. In: *Dams and Reservoirs under Changing Challenges*. June 2011.

Stolz, D. *Die Nullspannungstemperatur in Gewichtsstaumauern unter Berücksichtigung der Festigkeitsentwicklung des Betons*. Stuttgart : Eigenverlag des Instituts für Wasser- und Umweltsystemmodellierung der Universität Stuttgart, 2019. ISBN: 978-3-942036-75-7. DOI: 10.18419/opus-10945.

Sun, G., Y. Zhang, W. Sun, Z. Liu, and C. Wang. “Multi-Scale Prediction of the Effective Chloride Diffusion Coefficient of Concrete”. In: *Construction and Building Materials* 25.10 (Oct. 2011), pp. 3820–3831. ISSN: 09500618. DOI: 10.1016/j.conbuildmat.2011.03.041.

Sun, X., Q. Dai, and K. Ng. “Computational Investigation of Pore Permeability and Connectivity from Transmission X-ray Microscope Images of a Cement Paste Specimen”. In: *Construction and Building Materials* 68 (Oct. 2014), pp. 240–251. ISSN: 09500618. DOI: 10.1016/j.conbuildmat.2014.06.049.

Tang, S. W., Y. Yao, C. Andrade, and Z. J. Li. “Recent Durability Studies on Concrete Structure”. In: *Cement and Concrete Research* 78 (Dec. 2015), pp. 143–154. ISSN: 00088846. DOI: 10.1016/j.cemconres.2015.05.021.

Tasong, W. A., C. J. Lynsdale, and J. C. Cripps. “Aggregate-Cement Paste Interface. Ii: Influence of Aggregate Physical Properties”. In: *Cement and Concrete Research* 28.10 (Oct. 1998), pp. 1453–1465. ISSN: 00088846. DOI: 10.1016/S0008-8846(98)00126-4.

Tauzowski, P. “Topology Optimization of Elasto-Plastic Structures under Reliability Constraints: A First Order Approach”. In: *Computers and Structures* (2021), p. 15.

Tennis, P. D. and H. M. Jennings. “A Model for Two Types of Calcium Silicate Hydrate in the Microstructure of Portland Cement Pastes”. In: *Cement and Concrete Research* 30.6 (June 2000), pp. 855–863. ISSN: 00088846. DOI: 10.1016/S0008-8846(00)00257-X.

Terzaghi, K. *Erdbaumechanik auf bodenphysikalischer Grundlage*. Leipzig: F. Deuticke, 1925.

Thomas, M., K. Folliard, T. Drimalas, and T. Ramlochan. “Diagnosing Delayed Ettringite Formation in Concrete Structures”. In: *Cement and Concrete Research* 38.6 (June 2008), pp. 841–847. ISSN: 00088846. DOI: 10.1016/j.cemconres.2008.01.003.

Tons, E. “Factors in Joint Seal Design”. In: *Highway Research Record* 80 (1965).

Torero, J. L. “Fire Safety of Historical Buildings: Principles and Methodological Approach”. In: *International Journal of Architectural Heritage* 13.7 (Oct. 2019), pp. 926–940. ISSN: 1558-3058, 1558-3066. DOI: 10.1080/15583058.2019.1612484.

Tsuchiya, N., M. Kanematsu, and T. Noguchi. “Quick Water Movement around Concrete Cracks under Unsaturated Conditions”. In: *Construction and Building Materials* 67 (Sept. 2014), pp. 95–99. ISSN: 09500618. DOI: 10.1016/j.conbuildmat.2013.11.082.

Tuller, M. and D. Or. “Water retention and characteristic curve”. In: *Encyclopedia of Soils in the Environment*. Elsevier, 2005, pp. 278–289. ISBN: 978-0-12-348530-4. DOI: 10.1016/B0-12-348530-4/00376-3.

Ulm, F.-J., J.-M. Torrenti, and F. Adenot. “Chemoporoplasticity of Calcium Leaching in Concrete”. In: *Journal of Engineering Mechanics* 125.10 (Oct. 1999), pp. 1200–1211. ISSN: 0733-9399. DOI: 10.1061/(ASCE)0733-9399(1999)125:10(1200).

Val, D. V. and M. G. Stewart. “Reliability Assessment of Ageing Reinforced Concrete Structures—Current Situation and Future Challenges”. In: *Structural Engineering International* 19.2 (May 2009), pp. 211–219. ISSN: 1016-8664, 1683-0350. DOI: 10.2749/101686609788220114.

Van Genuchten, M. T. “A Closed-Form Equation for Predicting the Hydraulic Conductivity of Unsaturated Soils”. In: *Soil Science Society of America Journal* 44.5 (1980), pp. 892–898.

Vandamme, M. and F.-J. Ulm. “Nanogranular Origin of Concrete Creep”. In: *Proceedings of the National Academy of Sciences* 106.26 (June 2009), pp. 10552–10557. ISSN: 0027-8424, 1091-6490. DOI: 10.1073/pnas.0901033106.

Vandamme, M. and F.-J. Ulm. “Nanoindentation Investigation of Creep Properties of Calcium Silicate Hydrates”. In: *Cement and Concrete Research* 52 (Oct. 2013), pp. 38–52. ISSN: 00088846. DOI: 10.1016/j.cemconres.2013.05.006.

Verein Deutscher Zementwerke (VDZ), ed. *Zementindustrie Im Überblick 2020/2021*. 2020.

Walraven, J. C. “Design for Service Life: How Should It Be Implemented in Future Codes. In: International Conference on Concrete Repair, Rehabilitation and Retrofitting”. In: *Proceedings ICCRRR 2008*. 2008, pp. 3–10.

Walter, A. L., E. O. Frind, D. W. Blowes, C. J. Ptacek, and J. W. Molson. “Modeling of Multicomponent Reactive Transport in Groundwater: 1. Model Development and Evaluation”. In: *Water Resources Research* 30.11 (Nov. 1994), pp. 3137–3148. ISSN: 00431397. DOI: 10.1029/94WR00955.

Wan, K., Y. Li, and W. Sun. "Experimental and Modelling Research of the Accelerated Calcium Leaching of Cement Paste in Ammonium Nitrate Solution". In: *Construction and Building Materials* 40 (Mar. 2013), pp. 832–846. ISSN: 09500618. DOI: 10.1016/j.conbuildmat.2012.11.066.

Wang, G. et al. "XFEM Based Seismic Potential Failure Mode Analysis of Concrete Gravity Dam–Water–Foundation Systems through Incremental Dynamic Analysis". In: *Engineering Structures* 98 (Sept. 2015), pp. 81–94. ISSN: 01410296. DOI: 10.1016/j.engstruct.2015.04.023.

Wang, J., A. P. Jivkov, Q. M. Li, and D. L. Engelberg. "Experimental and Numerical Investigation of Mortar and ITZ Parameters in Meso-Scale Models of Concrete". In: *Theoretical and Applied Fracture Mechanics* 109 (Oct. 2020), p. 102722. ISSN: 01678442. DOI: 10.1016/j.tafmec.2020.102722.

Wang, K., D. C. Jansen, S. P. Shah, and A. F. Karr. "Permeability Study of Cracked Concrete". In: *Cement and Concrete Research* 27.3 (Mar. 1997), pp. 381–393. ISSN: 00088846. DOI: 10.1016/S0008-8846(97)00031-8.

Warren, J. E. and P. J. Root. "The Behavior of Naturally Fractured Reservoirs". In: *Society of Petroleum Engineers Journal* 3.03 (Sept. 1963), pp. 245–255. ISSN: 0197-7520. DOI: 10.2118/426-PA.

Wei, Z., C. Xiaolin, Z. Chuangbing, and L. Xinghong. "Failure Analysis of High-Concrete Gravity Dam Based on Strength Reserve Factor Method". In: *Computers and Geotechnics* 35.4 (July 2008), pp. 627–636. ISSN: 0266352X. DOI: 10.1016/j.compgeo.2007.10.005.

Weller, H. G., G. Tabor, H. Jasak, and C. Fureby. "A Tensorial Approach to Computational Continuum Mechanics Using Object-Oriented Techniques". In: *Computers in Physics* 12.6 (1998), pp. 620–631.

Whitaker, S. "Flow in Porous Media I: A Theoretical Derivation of Darcy's Law". In: *Transport in porous media* 1.1 (1986), pp. 3–25.

Winslow, D. N., M. D. Cohen, D. P. Bentz, K. A. Snyder, and E. J. Garboczi. "Percolation and Pore Structure in Mortars and Concrete". In: *Cement and Concrete Research* 24.1 (1994), pp. 25–37. ISSN: 00088846. DOI: 10.1016/0008-8846(94)90079-5.

Yang, C. C., S. W. Cho, and L. C. Wang. "The Relationship between Pore Structure and Chloride Diffusivity from Ponding Test in Cement-Based Materials". In: *Materials Chemistry and Physics* 100.2-3 (Dec. 2006), pp. 203–210. ISSN: 02540584. DOI: 10.1016/j.matchemphys.2005.12.032.

Yang, H., Y. Che, and F. Leng. "Calcium Leaching Behavior of Cementitious Materials in Hydrochloric Acid Solution". In: *Scientific Reports* 8.1 (June 2018), p. 8806. ISSN: 2045-2322. DOI: 10.1038/s41598-018-27255-x.

Yu, Y., Y. X. Zhang, and A. Khennane. “Numerical Modelling of Degradation of Cement-Based Materials under Leaching and External Sulfate Attack”. In: *Computers & Structures* 158 (Oct. 2015), pp. 1–14. ISSN: 00457949. DOI: 10.1016/j.compstruc.2015.05.030.

Yuan, Y. and Y. Chi. “Water Permeability of Concrete under Uniaxial Tension”. In: *Structural Concrete* 15.2 (June 2014), pp. 191–201. ISSN: 14644177. DOI: 10.1002/suco.201300059.

Zhang, M. “Pore-Scale Modelling of Relative Permeability of Cementitious Materials Using X-ray Computed Microtomography Images”. In: *Cement and Concrete Research* 95 (May 2017), pp. 18–29. ISSN: 00088846. DOI: 10.1016/j.cemconres.2017.02.005.

Zhang, P., F. H. Wittmann, and M. Haist. “Water Penetration into Micro-cracks in Reinforced Concrete”. In: *Restoration of Buildings and Monuments, An International Journal - Bauinstandsetzen und Baudenkmalpflege* 20.2 (2014), pp. 85–94. ISSN: 1864-7251. DOI: 10.12900/RBM14.20.2-0008.

Zhang, R., P. H. Yin X.and Winterfeld, and Y.-S. Wu. “A Fully Coupled Thermal-Hydrological-Mechanical-Chemical Model for CO2 Geological Sequestration”. In: *Journal of Natural Gas Science and Engineering* 28 (Jan. 2016), pp. 280–304. ISSN: 18755100. DOI: 10.1016/j.jngse.2015.11.037.

Zhao, E., C. Wu, S. Wang, J. Hu, and W. Wang. “Seepage Dissolution Effect Prediction on Aging Deformation of Concrete Dams by Coupled Chemo-Mechanical Model”. In: *Construction and Building Materials* 237 (Mar. 2020), p. 117603. ISSN: 09500618. DOI: 10.1016/j.conbuildmat.2019.117603.

Zhou, W., T. Qi, X. Liu, C. Feng, and S. Yang. “A Hygro-Thermo-Chemical Analysis of Concrete at an Early Age and beyond under Dry-Wet Conditions Based on a Fixed Model”. In: *International Journal of Heat and Mass Transfer* 115 (Dec. 2017), pp. 488–499. ISSN: 00179310. DOI: 10.1016/j.ijheatmasstransfer.2017.08.014.

Zimmerman, R. W. and G. S. Bodvarsson. “Hydraulic conductivity of rock fractures”. In: *Transport in Porous Media* 23 (1996), pp. 1–30.

dos Santos, W. N. “Effect of Moisture and Porosity on the Thermal Properties of a Conventional Refractory Concrete”. In: *Journal of the European Ceramic Society* 23.5 (Apr. 2003), pp. 745–755. ISSN: 09552219. DOI: 10.1016/S0955-2219(02)00158-9.

Institut für Wasser- und Umweltsystemmodellierung
Universität Stuttgart

Pfaffenwaldring 61
70569 Stuttgart (Vaihingen)
Telefon (0711) 685 - 60156
Telefax (0711) 685 - 51073
E-Mail: iws@iws.uni-stuttgart.de
http://www.iws.uni-stuttgart.de

Direktoren
Prof. Dr.-Ing. Rainer Helmig
Prof. Dr.-Ing. Wolfgang Nowak
Prof. Dr.-Ing. Silke Wieprecht

Emeriti
Prof. Dr.-Ing. habil. Dr.-Ing. E.h. Jürgen Giesecke
Prof. Dr.h.c. Dr.-Ing. E.h. Helmut Kobus, PhD

Lehrstuhl für Wasserbau und Wassermengenwirtschaft
Leiterin: Prof. Dr.-Ing. Silke Wieprecht
Stellv.: Dr.-Ing. Kristina Terheiden
Versuchsanstalt für Wasserbau
Leiter: Stefan Haun, PhD

Lehrstuhl für Hydromechanik und Hydrosystemmodellierung
Leiter: Prof. Dr.-Ing. Rainer Helmig
Stellv.: apl. Prof. Dr.-Ing. Holger Class

Lehrstuhl für Stochastische Simulation und Sicherheitsforschung für Hydrosysteme
Leiter: Prof. Dr.-Ing. Wolfgang Nowak
Stellv.: apl. Prof. Dr.-Ing. Sergey Oladyshkin
Hydrogeophysik der Vadosen Zone
(mit Forschungszentrum Jülich)
Leiter: Prof. Dr. J.A. Sander Huisman

***VEGAS,* Versuchseinrichtung zur Grundwasser- und Altlastensanierung**
Leiter: Dr.-Ing. Simon Kleinknecht
PD Dr.-Ing. Claus Haslauer

Verzeichnis der Mitteilungshefte

7 *Sonderheft anläßlich des 65. Geburtstages von Prof. Arthur Röhnisch mit Beiträgen von* Benk, Dieter; Breitling, J.; Gurr, Siegfried; Haberhauer, Robert; Honekamp, Hermann; Kuz, Klaus Dieter; Marotz, Günter; Mayer-Vorfelder, Hans-Jörg; Miller, Rudolf; Plate, Erich J.; Radomski, Helge; Schwarz, Helmut; Vollmer, Ernst; Wildenhahn, Eberhard; 1967

8 Jumikis, Alfred: *Beitrag zur experimentellen Untersuchung des Wassernachschubs in einem gefrierenden Boden und die Beurteilung der Ergebnisse*, 1968

9 Marotz, Günter: *Technische Grundlagen einer Wasserspeicherung im natürlichen Untergrund*, 1968

10 Radomski, Helge: *Untersuchungen über den Einfluß der Querschnittsform wellenförmiger Spundwände auf die statischen und rammtechnischen Eigenschaften*, 1968

11 Schwarz, Helmut: *Die Grenztragfähigkeit des Baugrundes bei Einwirkung vertikal gezogener Ankerplatten als zweidimensionales Bruchproblem*, 1969

12 Erbel, Klaus: *Ein Beitrag zur Untersuchung der Metamorphose von Mittelgebirgsschneedecken unter besonderer Berücksichtigung eines Verfahrens zur Bestimmung der thermischen Schneequalität*, 1969

13 Westhaus, Karl-Heinz: *Der Strukturwandel in der Binnenschiffahrt und sein Einfluß auf den Ausbau der Binnenschiffskanäle*, 1969

14 Mayer-Vorfelder, Hans-Jörg: *Ein Beitrag zur Berechnung des Erdwiderstandes unter Ansatz der logarithmischen Spirale als Gleitflächenfunktion*, 1970

15 Schulz, Manfred: *Berechnung des räumlichen Erddruckes auf die Wandung kreiszylindrischer Körper*, 1970

16 Mobasseri, Manoutschehr: *Die Rippenstützmauer. Konstruktion und Grenzen ihrer Standsicherheit*, 1970

17 Benk, Dieter: *Ein Beitrag zum Betrieb und zur Bemessung von Hochwasserrückhaltebecken*, 1970

18 Gàl, Attila: *Bestimmung der mitschwingenden Wassermasse bei überströmten Fischbauchklappen mit kreiszylindrischem Staublech*, 1971, *vergriffen*

19 Kuz, Klaus Dieter: *Ein Beitrag zur Frage des Einsetzens von Kavitationserscheinungen in einer Düsenströmung bei Berücksichtigung der im Wasser gelösten Gase*, 1971, *vergriffen*

20 Schaak, Hartmut: *Verteilleitungen von Wasserkraftanlagen*, 1971

21 *Sonderheft zur Eröffnung der neuen Versuchsanstalt des Instituts für Wasserbau der Universität Stuttgart mit Beiträgen von* Brombach, Hansjörg; Dirksen, Wolfram; Gàl, Attila; Gerlach, Reinhard; Giesecke, Jürgen; Holthoff, Franz-Josef; Kuz, Klaus Dieter; Marotz, Günter; Minor, Hans-Erwin; Petrikat, Kurt; Röhnisch, Arthur; Rueff, Helge; Schwarz, Helmut; Vollmer, Ernst; Wildenhahn, Eberhard; 1972

22 Wang, Chung-su: *Ein Beitrag zur Berechnung der Schwingungen an Kegelstrahlschiebern*, 1972

23 Mayer-Vorfelder, Hans-Jörg: *Erdwiderstandsbeiwerte nach dem Ohde-Variationsverfahren*, 1972

24 Minor, Hans-Erwin: *Beitrag zur Bestimmung der Schwingungsanfachungsfunktionen überströmter Stauklappen*, 1972, *vergriffen*

25 Brombach, Hansjörg: *Untersuchung strömungsmechanischer Elemente (Fluidik) und die Möglichkeit der Anwendung von Wirbelkammerelementen im Wasserbau*, 1972, *vergriffen*

26 Wildenhahn, Eberhard: *Beitrag zur Berechnung von Horizontalfilterbrunnen*, 1972

27 Steinlein, Helmut: *Die Eliminierung der Schwebstoffe aus Flußwasser zum Zweck der unterirdischen Wasserspeicherung, gezeigt am Beispiel der Iller*, 1972

28 Holthoff, Franz Josef: *Die Überwindung großer Hubhöhen in der Binnenschiffahrt durch Schwimmerhebewerke*, 1973

29 Röder, Karl: *Einwirkungen aus Baugrundbewegungen auf trog- und kastenförmige Konstruktionen des Wasser- und Tunnelbaues*, 1973

30 Kretschmer, Heinz: *Die Bemessung von Bogenstaumauern in Abhängigkeit von der Talform*, 1973

31 Honekamp, Hermann: *Beitrag zur Berechnung der Montage von Unterwasserpipelines*, 1973

32 Giesecke, Jürgen: *Die Wirbelkammertriode als neuartiges Steuerorgan im Wasserbau*, und Brombach, Hansjörg: *Entwicklung, Bauformen, Wirkungsweise und Steuereigenschaften von Wirbelkammerverstärkern*, 1974

33 Rueff, Helge: *Untersuchung der schwingungserregenden Kräfte an zwei hintereinander angeordneten Tiefschützen unter besonderer Berücksichtigung von Kavitation*, 1974

34 Röhnisch, Arthur: *Einpreßversuche mit Zementmörtel für Spannbeton - Vergleich der Ergebnisse von Modellversuchen mit Ausführungen in Hüllwellrohren*, 1975

35 *Sonderheft anläßlich des 65. Geburtstages von Prof. Dr.-Ing. Kurt Petrikat mit Beiträgen von*: Brombach, Hansjörg; Erbel, Klaus; Flinspach, Dieter; Fischer jr., Richard; Gàl, Attila; Gerlach, Reinhard; Giesecke, Jürgen; Haberhauer, Robert; Hafner Edzard; Hausenblas, Bernhard; Horlacher, Hans-Burkhard; Hutarew, Andreas; Knoll, Manfred; Krummet, Ralph; Marotz, Günter; Merkle, Theodor; Miller, Christoph; Minor, Hans-Erwin; Neumayer, Hans; Rao, Syamala; Rath, Paul; Rueff, Helge; Ruppert, Jürgen; Schwarz, Wolfgang; Topal-Gökceli, Mehmet; Vollmer, Ernst; Wang, Chung-su; Weber, Hans-Georg; 1975

36 Berger, Jochum: *Beitrag zur Berechnung des Spannungszustandes in rotationssymmetrisch belasteten Kugelschalen veränderlicher Wandstärke unter Gas- und Flüssigkeitsdruck durch Integration schwach singulärer Differentialgleichungen*, 1975

37 Dirksen, Wolfram: *Berechnung instationärer Abflußvorgänge in gestauten Gerinnen mittels Differenzenverfahren und die Anwendung auf Hochwasserrückhaltebecken*, 1976

38 Horlacher, Hans-Burkhard: *Berechnung instationärer Temperatur- und Wärmespannungsfelder in langen mehrschichtigen Hohlzylindern*, 1976

39 Hafner, Edzard: *Untersuchung der hydrodynamischen Kräfte auf Baukörper im Tiefwasserbereich des Meeres*, 1977, ISBN 3-921694-39-6

40 Ruppert, Jürgen: *Über den Axialwirbelkammerverstärker für den Einsatz im Wasserbau*, 1977, ISBN 3-921694-40-X

41 Hutarew, Andreas: *Beitrag zur Beeinflußbarkeit des Sauerstoffgehalts in Fließgewässern an Abstürzen und Wehren*, 1977, ISBN 3-921694-41-8, vergriffen

42 Miller, Christoph: *Ein Beitrag zur Bestimmung der schwingungserregenden Kräfte an unterströmten Wehren*, 1977, ISBN 3-921694-42-6

43 Schwarz, Wolfgang: *Druckstoßberechnung unter Berücksichtigung der Radial- und Längsverschiebungen der Rohrwandung*, 1978, ISBN 3-921694-43-4

44 Kinzelbach, Wolfgang: *Numerische Untersuchungen über den optimalen Einsatz variabler Kühlsysteme einer Kraftwerkskette am Beispiel Oberrhein*, 1978, ISBN 3-921694-44-2

45 Barczewski, Baldur: *Neue Meßmethoden für Wasser-Luftgemische und deren Anwendung auf zweiphasige Auftriebsstrahlen*, 1979, ISBN 3-921694-45-0

46 Neumayer, Hans: *Untersuchung der Strömungsvorgänge in radialen Wirbelkammerverstärkern*, 1979, ISBN 3-921694-46-9

47 Elalfy, Youssef-Elhassan: *Untersuchung der Strömungsvorgänge in Wirbelkammerdioden und -drosseln*, 1979, ISBN 3-921694-47-7

48 Brombach, Hansjörg: *Automatisierung der Bewirtschaftung von Wasserspeichern*, 1981, ISBN 3-921694-48-5

49 Geldner, Peter: *Deterministische und stochastische Methoden zur Bestimmung der Selbstdichtung von Gewässern*, 1981, ISBN 3-921694-49-3, vergriffen

50 Mehlhorn, Hans: *Temperaturveränderungen im Grundwasser durch Brauchwassereinleitungen*, 1982, ISBN 3-921694-50-7, *vergriffen*

51 Hafner, Edzard: *Rohrleitungen und Behälter im Meer*, 1983, ISBN 3-921694-51-5

52 Rinnert, Bernd: *Hydrodynamische Dispersion in porösen Medien: Einfluß von Dichteunterschieden auf die Vertikalvermischung in horizontaler Strömung*, 1983, ISBN 3-921694-52-3, *vergriffen*

53 Lindner, Wulf: *Steuerung von Grundwasserentnahmen unter Einhaltung ökologischer Kriterien*, 1983, ISBN 3-921694-53-1, *vergriffen*

54 Herr, Michael; Herzer, Jörg; Kinzelbach, Wolfgang; Kobus, Helmut; Rinnert, Bernd: *Methoden zur rechnerischen Erfassung und hydraulischen Sanierung von Grundwasserkontaminationen*, 1983, ISBN 3-921694-54-X

55 Schmitt, Paul: *Wege zur Automatisierung der Niederschlagsermittlung*, 1984, ISBN 3-921694-55-8, *vergriffen*

56 Müller, Peter: *Transport und selektive Sedimentation von Schwebstoffen bei gestautem Abfluß*, 1985, ISBN 3-921694-56-6

57 El-Qawasmeh, Fuad: *Möglichkeiten und Grenzen der Tropfbewässerung unter besonderer Berücksichtigung der Verstopfungsanfälligkeit der Tropfelemente*, 1985, ISBN 3-921694-57-4, *vergriffen*

58 Kirchenbaur, Klaus: *Mikroprozessorgesteuerte Erfassung instationärer Druckfelder am Beispiel seegangsbelasteter Baukörper*, 1985, ISBN 3-921694-58-2

59 Kobus, Helmut (Hrsg.): *Modellierung des großräumigen Wärme- und Schadstofftransports im Grundwasser*, Tätigkeitsbericht 1984/85 (DFG-Forschergruppe an den Universitäten Hohenheim, Karlsruhe und Stuttgart), 1985, ISBN 3-921694-59-0, *vergriffen*

60 Spitz, Karlheinz: *Dispersion in porösen Medien: Einfluß von Inhomogenitäten und Dichteunterschieden*, 1985, ISBN 3-921694-60-4, *vergriffen*

61 Kobus, Helmut: *An Introduction to Air-Water Flows in Hydraulics*, 1985, ISBN 3-921694-61-2

62 Kaleris, Vassilios: *Erfassung des Austausches von Oberflächen- und Grundwasser in horizontalebenen Grundwassermodellen*, 1986, ISBN 3-921694-62-0

63 Herr, Michael: *Grundlagen der hydraulischen Sanierung verunreinigter Porengrundwasserleiter*, 1987, ISBN 3-921694-63-9

64 Marx, Walter: *Berechnung von Temperatur und Spannung in Massenbeton infolge Hydratation*, 1987, ISBN 3-921694-64-7

65 Koschitzky, Hans-Peter: *Dimensionierungskonzept für Sohlbelüfter in Schußrinnen zur Vermeidung von Kavitationsschäden*, 1987, ISBN 3-921694-65-5

66 Kobus, Helmut (Hrsg.): *Modellierung des großräumigen Wärme- und Schadstofftransports im Grundwasser*, Tätigkeitsbericht 1986/87 (DFG-Forschergruppe an den Universitäten Hohenheim, Karlsruhe und Stuttgart) 1987, ISBN 3-921694-66-3

67 Söll, Thomas: *Berechnungsverfahren zur Abschätzung anthropogener Temperaturanomalien im Grundwasser*, 1988, ISBN 3-921694-67-1

68 Dittrich, Andreas; Westrich, Bernd: *Bodenseeufererosion, Bestandsaufnahme und Bewertung*, 1988, ISBN 3-921694-68-X, *vergriffen*

69 Huwe, Bernd; van der Ploeg, Rienk R.: *Modelle zur Simulation des Stickstoffhaushaltes von Standorten mit unterschiedlicher landwirtschaftlicher Nutzung*, 1988, ISBN 3-921694-69-8, *vergriffen*

70 Stephan, Karl: *Integration elliptischer Funktionen*, 1988, ISBN 3-921694-70-1

71 Kobus, Helmut; Zilliox, Lothaire (Hrsg.): *Nitratbelastung des Grundwassers, Auswirkungen der Landwirtschaft auf die Grundwasser- und Rohwasserbeschaffenheit und Maßnahmen zum Schutz des Grundwassers*. Vorträge des deutsch-französischen Kolloquiums am 6. Oktober 1988, Universitäten Stuttgart und Louis Pasteur Strasbourg (Vorträge in deutsch oder französisch, Kurzfassungen zweisprachig), 1988, ISBN 3-921694-71-X

72 Soyeaux, Renald: *Unterströmung von Stauanlagen auf klüftigem Untergrund unter Berücksichtigung laminarer und turbulenter Fließzustände*,1991, ISBN 3-921694-72-8

73 Kohane, Roberto: *Berechnungsmethoden für Hochwasserabfluß in Fließgewässern mit überströmten Vorländern*, 1991, ISBN 3-921694-73-6

74 Hassinger, Reinhard: *Beitrag zur Hydraulik und Bemessung von Blocksteinrampen in flexibler Bauweise*, 1991, ISBN 3-921694-74-4, *vergriffen*

75 Schäfer, Gerhard: *Einfluß von Schichtenstrukturen und lokalen Einlagerungen auf die Längsdispersion in Porengrundwasserleitern*, 1991, ISBN 3-921694-75-2

76 Giesecke, Jürgen: *Vorträge, Wasserwirtschaft in stark besiedelten Regionen; Umweltforschung mit Schwerpunkt Wasserwirtschaft*, 1991, ISBN 3-921694-76-0

77 Huwe, Bernd: *Deterministische und stochastische Ansätze zur Modellierung des Stickstoffhaushalts landwirtschaftlich genutzter Flächen auf unterschiedlichem Skalenniveau*, 1992, ISBN 3-921694-77-9, *vergriffen*

78 Rommel, Michael: *Verwendung von Kluftdaten zur realitätsnahen Generierung von Kluftnetzen mit anschließender laminar-turbulenter Strömungsberechnung*, 1993, ISBN 3-92 1694-78-7

79 Marschall, Paul: *Die Ermittlung lokaler Stofffrachten im Grundwasser mit Hilfe von Einbohrloch-Meßverfahren*, 1993, ISBN 3-921694-79-5, *vergriffen*

80 Ptak, Thomas: *Stofftransport in heterogenen Porenaquiferen: Felduntersuchungen und stochastische Modellierung*, 1993, ISBN 3-921694-80-9, *vergriffen*

81 Haakh, Frieder: *Transientes Strömungsverhalten in Wirbelkammern,* 1993, ISBN 3-921694-81-7

82 Kobus, Helmut; Cirpka, Olaf; Barczewski, Baldur; Koschitzky, Hans-Peter: *Versuchseinrichtung zur Grundwasser- und Altlastensanierung VEGAS, Konzeption und Programmrahmen*, 1993, ISBN 3-921694-82-5

83 Zang, Weidong: *Optimaler Echtzeit-Betrieb eines Speichers mit aktueller Abflußregenerierung*, 1994, ISBN 3-921694-83-3, *vergriffen*

84 Franke, Hans-Jörg: *Stochastische Modellierung eines flächenhaften Stoffeintrages und Transports in Grundwasser am Beispiel der Pflanzenschutzmittelproblematik*, 1995, ISBN 3-921694-84-1

85 Lang, Ulrich: *Simulation regionaler Strömungs- und Transportvorgänge in Karstaquiferen mit Hilfe des Doppelkontinuum-Ansatzes: Methodenentwicklung und Parameteridenti-fikation*, 1995, ISBN 3-921694-85-X, *vergriffen*

86 Helmig, Rainer: *Einführung in die Numerischen Methoden der Hydromechanik*, 1996, ISBN 3-921694-86-8, *vergriffen*

87 Cirpka, Olaf: *CONTRACT: A Numerical Tool for Contaminant Transport and Chemical Transformations - Theory and Program Documentation -*, 1996, ISBN 3-921694-87-6

88 Haberlandt, Uwe: *Stochastische Synthese und Regionalisierung des Niederschlages für Schmutzfrachtberechnungen*, 1996, ISBN 3-921694-88-4

89 Croisé, Jean: *Extraktion von flüchtigen Chemikalien aus natürlichen Lockergesteinen mittels erzwungener Luftströmung*, 1996, ISBN 3-921694-89-2, *vergriffen*

90 Jorde, Klaus: *Ökologisch begründete, dynamische Mindestwasserregelungen bei Ausleitungskraftwerken*, 1997, ISBN 3-921694-90-6, *vergriffen*

91 Helmig, Rainer: *Gekoppelte Strömungs- und Transportprozesse im Untergrund - Ein Beitrag zur Hydrosystemmodellierung-*, 1998, ISBN 3-921694-91-4, *vergriffen*

92 Emmert, Martin: *Numerische Modellierung nichtisothermer Gas-Wasser Systeme in porösen Medien,* 1997, ISBN 3-921694-92-2

93 Kern, Ulrich: *Transport von Schweb- und Schadstoffen in staugeregelten Fließgewässern am Beispiel des Neckars*, 1997, ISBN 3-921694-93-0, *vergriffen*

94 Förster, Georg: *Druckstoßdämpfung durch große Luftblasen in Hochpunkten von Rohrleitungen 1997*, ISBN 3-921694-94-9

95 Cirpka, Olaf: *Numerische Methoden zur Simulation des reaktiven Mehrkomponententransports im Grundwasser*, 1997, ISBN 3-921694-95-7, *vergriffen*

96 Färber, Arne: *Wärmetransport in der ungesättigten Bodenzone: Entwicklung einer thermischen In-situ-Sanierungstechnologie*, 1997, ISBN 3-921694-96-5

97 Betz, Christoph: *Wasserdampfdestillation von Schadstoffen im porösen Medium: Entwicklung einer thermischen In-situ-Sanierungstechnologie*, 1998, SBN 3-921694-97-3

98 Xu, Yichun: *Numerical Modeling of Suspended Sediment Transport in Rivers*, 1998, ISBN 3-921694-98-1, *vergriffen*

99 Wüst, Wolfgang: *Geochemische Untersuchungen zur Sanierung CKW-kontaminierter Aquifere mit Fe(0)-Reaktionswänden,* 2000, ISBN 3-933761-02-2

100 Sheta, Hussam: *Simulation von Mehrphasenvorgängen in porösen Medien unter Einbeziehung von Hysterese-Effekten*, 2000, ISBN 3-933761-03-4

101 Ayros, Edwin: *Regionalisierung extremer Abflüsse auf der Grundlage statistischer Verfahren*, 2000, ISBN 3-933761-04-2, *vergriffen*

102 Huber, Ralf: *Compositional Multiphase Flow and Transport in Heterogeneous Porous Media*, 2000, ISBN 3-933761-05-0

103 Braun, Christopherus: *Ein Upscaling-Verfahren für Mehrphasenströmungen in porösen Medien*, 2000, ISBN 3-933761-06-9

104 Hofmann, Bernd: *Entwicklung eines rechnergestützten Managementsystems zur Beurteilung von Grundwasserschadensfällen*, 2000, ISBN 3-933761-07-7

105 Class, Holger: *Theorie und numerische Modellierung nichtisothermer Mehrphasenprozesse in NAPL-kontaminierten porösen Medien,* 2001, ISBN 3-933761-08-5

106 Schmidt, Reinhard: *Wasserdampf- und Heißluftinjektion zur thermischen Sanierung kontaminierter Standorte*, 2001, ISBN 3-933761-09-3

107 Josef, Reinhold: *Schadstoffextraktion mit hydraulischen Sanierungsverfahren unter Anwendung von grenzflächenaktiven Stoffen*, 2001, ISBN 3-933761-10-7

108 Schneider, Matthias: *Habitat- und Abflussmodellierung für Fließgewässer mit unscharfen Berechnungsansätzen*, 2001, ISBN 3-933761-11-5

109 Rathgeb, Andreas: *Hydrodynamische Bemessungsgrundlagen für Lockerdeckwerke an überströmbaren Erddämmen*, 2001, ISBN 3-933761-12-3

110 Lang, Stefan: *Parallele numerische Simulation instätionärer Probleme mit adaptiven Methoden auf unstrukturierten Gittern*, 2001, ISBN 3-933761-13-1

111 Appt, Jochen; Stumpp Simone: *Die Bodensee-Messkampagne 2001, IWS/CWR Lake Constance Measurement Program 2001*, 2002, ISBN 3-933761-14-X

112 Heimerl, Stephan: *Systematische Beurteilung von Wasserkraftprojekten,* 2002, ISBN 3-933761-15-8, *vergriffen*

113 Iqbal, Amin: *On the Management and Salinity Control of Drip Irrigation,* 2002, ISBN 3-933761-16-6

114 Silberhorn-Hemminger, Annette: *Modellierung von Kluftaquifersystemen: Geostatistische Analyse und deterministisch-stochastische Kluftgenerierung,* 2002, ISBN 3-933761-17-4

115 Winkler, Angela: *Prozesse des Wärme- und Stofftransports bei der In-situ-Sanierung mit festen Wärmequellen,* 2003, ISBN 3-933761-18-2

116 Marx, Walter: *Wasserkraft, Bewässerung, Umwelt - Planungs- und Bewertungsschwerpunkte der Wasserbewirtschaftung,* 2003, ISBN 3-933761-19-0

117 Hinkelmann, Reinhard: *Efficient Numerical Methods and Information-Processing Techniques in Environment Water,* 2003, ISBN 3-933761-20-4

118 Samaniego-Eguiguren, Luis Eduardo: *Hydrological Consequences of Land Use / Land Cover and Climatic Changes in Mesoscale Catchments*, 2003, ISBN 3-933761-21-2

119 Neunhäuserer, Lina: *Diskretisierungsansätze zur Modellierung von Strömungs- und Transportprozessen in geklüftet-porösen Medien*, 2003, ISBN 3-933761-22-0

120 Paul, Maren: *Simulation of Two-Phase Flow in Heterogeneous Poros Media with Adaptive Methods*, 2003, ISBN 3-933761-23-9

121 Ehret, Uwe: *Rainfall and Flood Nowcasting in Small Catchments using Weather Radar*, 2003, ISBN 3-933761-24-7

122 Haag, Ingo: *Der Sauerstoffhaushalt staugeregelter Flüsse am Beispiel des Neckars - Analysen, Experimente, Simulationen -,* 2003, ISBN 3-933761-25-5

123 Appt, Jochen: *Analysis of Basin-Scale Internal Waves in Upper Lake Constance,* 2003, ISBN 3-933761-26-3

124 Hrsg.: Schrenk, Volker; Batereau, Katrin; Barczewski, Baldur; Weber, Karolin und Koschitzky, Hans-Peter: *Symposium Ressource Fläche und VEGAS - Statuskolloquium 2003, 30. September und 1. Oktober 2003,* 2003, ISBN 3-933761-27-1

125 Omar Khalil Ouda: *Optimisation of Agricultural Water Use: A Decision Support System for the Gaza Strip,* 2003, ISBN 3-933761-28-0

126 Batereau, Katrin: *Sensorbasierte Bodenluftmessung zur Vor-Ort-Erkundung von Schadensherden im Untergrund*, 2004, ISBN 3-933761-29-8

127 Witt, Oliver: *Erosionsstabilität von Gewässersedimenten mit Auswirkung auf den Stofftransport bei Hochwasser am Beispiel ausgewählter Stauhaltungen des Oberrheins*, 2004, ISBN 3-933761-30-1

128 Jakobs, Hartmut: *Simulation nicht-isothermer Gas-Wasser-Prozesse in komplexen Kluft-Matrix-Systemen*, 2004, ISBN 3-933761-31-X

129 Li, Chen-Chien: *Deterministisch-stochastisches Berechnungskonzept zur Beurteilung der Auswirkungen erosiver Hochwasserereignisse in Flussstauhaltungen,* 2004, ISBN 3-933761-32-8

130 Reichenberger, Volker; Helmig, Rainer; Jakobs, Hartmut; Bastian, Peter; Niessner, Jennifer: *Complex Gas-Water Processes in Discrete Fracture-Matrix Systems: Up-scaling, Mass-Conservative Discretization and Efficient Multilevel Solution,* 2004, ISBN 3-933761-33-6

131 Hrsg.: Barczewski, Baldur; Koschitzky, Hans-Peter; Weber, Karolin; Wege, Ralf: *VEGAS - Statuskolloquium 2004,* Tagungsband zur Veranstaltung am 05. Oktober 2004 an der Universität Stuttgart, Campus Stuttgart-Vaihingen, 2004, ISBN 3-933761-34-4

132 Asie, Kemal Jabir: *Finite Volume Models for Multiphase Multicomponent Flow through Porous Media*. 2005, ISBN 3-933761-35-2

133 Jacoub, George: *Development of a 2-D Numerical Module for Particulate Contaminant Transport in Flood Retention Reservoirs and Impounded Rivers,* 2004, ISBN 3-933761-36-0

134 Nowak, Wolfgang: *Geostatistical Methods for the Identification of Flow and Transport Parameters in the Subsurface,* 2005, ISBN 3-933761-37-9

135 Süß, Mia: *Analysis of the influence of structures and boundaries on flow and transport processes in fractured porous media*, 2005, ISBN 3-933761-38-7

136 Jose, Surabhin Chackiath: *Experimental Investigations on Longitudinal Dispersive Mixing in Heterogeneous Aquifers,* 2005, ISBN: 3-933761-39-5

137 Filiz, Fulya: *Linking Large-Scale Meteorological Conditions to Floods in Mesoscale Catchments,* 2005, ISBN 3-933761-40-9

138 Qin, Minghao: *Wirklichkeitsnahe und recheneffiziente Ermittlung von Temperatur und Spannungen bei großen RCC-Staumauern*, 2005, ISBN 3-933761-41-7

139 Kobayashi, Kenichiro: *Optimization Methods for Multiphase Systems in the Subsurface - Application to Methane Migration in Coal Mining Areas*, 2005, ISBN 3-933761-42-5

140 Rahman, Md. Arifur: *Experimental Investigations on Transverse Dispersive Mixing in Heterogeneous Porous Media,* 2005, ISBN 3-933761-43-3

141 Schrenk, Volker: *Ökobilanzen zur Bewertung von Altlastensanierungsmaßnahmen,* 2005, ISBN 3-933761-44-1

142 Hundecha, Hirpa Yeshewatesfa: *Regionalization of Parameters of a Conceptual Rainfall-Runoff Model*, 2005, ISBN: 3-933761-45-X

143 Wege, Ralf: *Untersuchungs- und Überwachungsmethoden für die Beurteilung natürlicher Selbstreinigungsprozesse im Grundwasser,* 2005, ISBN 3-933761-46-8

144 Breiting, Thomas: *Techniken und Methoden der Hydroinformatik - Modellierung von komplexen Hydrosystemen im Untergrund*, 2006, ISBN 3-933761-47-6

145 Hrsg.: Braun, Jürgen; Koschitzky, Hans-Peter; Müller, Martin: *Ressource Untergrund: 10 Jahre VEGAS: Forschung und Technologieentwicklung zum Schutz von Grundwasser und Boden,* Tagungsband zur Veranstaltung am 28. und 29. September 2005 an der Universität Stuttgart, Campus Stuttgart-Vaihingen, 2005, ISBN 3-933761-48-4

146 Rojanschi, Vlad: *Abflusskonzentration in mesoskaligen Einzugsgebieten unter Berücksichtigung des Sickerraumes,* 2006, ISBN 3-933761-49-2

147 Winkler, Nina Simone: *Optimierung der Steuerung von Hochwasserrückhaltebeckensystemen,* 2006, ISBN 3-933761-50-6

148 Wolf, Jens: *Räumlich differenzierte Modellierung der Grundwasserströmung alluvialer Aquifere für mesoskalige Einzugsgebiete*, 2006, ISBN: 3-933761-51-4

149 Kohler, Beate: *Externe Effekte der Laufwasserkraftnutzung*, 2006, ISBN 3-933761-52-2

150 Hrsg.: Braun, Jürgen; Koschitzky, Hans-Peter; Stuhrmann, Matthias: *VEGAS-Statuskolloquium 2006,* Tagungsband zur Veranstaltung am 28. September 2006 an der Universität Stuttgart, Campus Stuttgart-Vaihingen, 2006, ISBN 3-933761-53-0

151 Niessner, Jennifer: *Multi-Scale Modeling of Multi-Phase - Multi-Component Processes in Heterogeneous Porous Media*, 2006, ISBN 3-933761-54-9

152 Fischer, Markus: *Beanspruchung eingeerdeter Rohrleitungen infolge Austrocknung bindiger Böden,* 2006, ISBN 3-933761-55-7

153 Schneck, Alexander: *Optimierung der Grundwasserbewirtschaftung unter Berücksichtigung der Belange der Wasserversorgung, der Landwirtschaft und des Naturschutzes*, 2006, ISBN 3-933761-56-5

154 Das, Tapash: *The Impact of Spatial Variability of Precipitation on the Predictive Uncertainty of Hydrological Models,* 2006, ISBN 3-33761-57-3

155 Bielinski, Andreas: *Numerical Simulation of CO_2 sequestration in geological formations*, 2007, ISBN 3-933761-58-1

156 Mödinger, Jens: *Entwicklung eines Bewertungs- und Entscheidungsunterstützungssystems für eine nachhaltige regionale Grundwasserbewirtschaftung*, 2006, ISBN 3-933761-60-3

157 Manthey, Sabine: *Two-phase flow processes with dynamic effects in porous media - parameter estimation and simulation,* 2007, ISBN 3-933761-61-1

158 Pozos Estrada, Oscar: *Investigation on the Effects of Entrained Air in Pipelines,* 2007, ISBN 3-933761-62-X

159 Ochs, Steffen Oliver: *Steam injection into saturated porous media – process analysis including experimental and numerical investigations*, 2007, ISBN 3-933761-63-8

160 Marx, Andreas: *Einsatz gekoppelter Modelle und Wetterradar zur Abschätzung von Niederschlagsintensitäten und zur Abflussvorhersage, 2007,* ISBN 3-933761-64-6

161 Hartmann, Gabriele Maria: *Investigation of Evapotranspiration Concepts in Hydrological Modelling for Climate Change Impact Assessment*, 2007, ISBN 3-933761-65-4

162 Kebede Gurmessa, Tesfaye: *Numerical Investigation on Flow and Transport Characteristics to Improve Long-Term Simulation of Reservoir Sedimentation*, 2007, ISBN 3-933761-66-2

163 Trifković, Aleksandar: *Multi-objective and Risk-based Modelling Methodology for Planning, Design and Operation of Water Supply Systems*, 2007, ISBN 3-933761-67-0

164 Götzinger, Jens: *Distributed Conceptual Hydrological Modelling - Simulation of Climate, Land Use Change Impact and Uncertainty Analysis*, 2007, ISBN 3-933761-68-9

165 Hrsg.: Braun, Jürgen; Koschitzky, Hans-Peter; Stuhrmann, Matthias: *VEGAS – Kolloquium 2007,* Tagungsband zur Veranstaltung am 26. September 2007 an der Universität Stuttgart, Campus Stuttgart-Vaihingen, 2007, ISBN 3-933761-69-7

166 Freeman, Beau: *Modernization Criteria Assessment for Water Resources Planning; Klamath Irrigation Project, U.S.*, 2008, ISBN 3-933761-70-0

167 Dreher, Thomas: *Selektive Sedimentation von Feinstschwebstoffen in Wechselwirkung mit wandnahen turbulenten Strömungsbedingungen*, 2008, ISBN 3-933761-71-9

168 Yang, Wei: *Discrete-Continuous Downscaling Model for Generating Daily Precipitation Time Series*, 2008, ISBN 3-933761-72-7

169 Kopecki, Ianina: *Calculational Approach to FST-Hemispheres for Multiparametrical Benthos Habitat Modelling,* 2008*,* ISBN 3-933761-73-5

170 Brommundt, Jürgen: *Stochastische Generierung räumlich zusammenhängender Niederschlagszeitreihen*, 2008, ISBN 3-933761-74-3

171 Papafotiou, *Alexandros: Numerical Investigations of the Role of Hysteresis in Heterogeneous Two-Phase Flow Systems*, 2008, ISBN 3-933761-75-1

172 He, Yi: *Application of a Non-Parametric Classification Scheme to Catchment Hydrology*, 2008, ISBN 978-3-933761-76-7

173 Wagner, Sven: *Water Balance in a Poorly Gauged Basin in West Africa Using Atmospheric Modelling and Remote Sensing Information*, 2008, ISBN 978-3-933761-77-4

174 Hrsg.: Braun, Jürgen; Koschitzky, Hans-Peter; Stuhrmann, Matthias; Schrenk, Volker: *VEGAS-Kolloquium 2008 Ressource Fläche III*, Tagungsband zur Veranstaltung am 01. Oktober 2008 an der Universität Stuttgart, Campus Stuttgart-Vaihingen, 2008, ISBN 978-3-933761-78-1

175 Patil, Sachin: *Regionalization of an Event Based Nash Cascade Model for Flood Predictions in Ungauged Basins*, 2008, ISBN 978-3-933761-79-8

176 Assteerawatt, Anongnart: *Flow and Transport Modelling of Fractured Aquifers based on a Geostatistical Approach,* 2008, ISBN 978-3-933761-80-4

177 Karnahl, Joachim Alexander: *2D numerische Modellierung von multifraktionalem Schwebstoff- und Schadstofftransport in Flüssen*, 2008, ISBN 978-3-933761-81-1

178 Hiester, Uwe: *Technologieentwicklung zur In-situ-Sanierung der ungesättigten Bodenzone mit festen Wärmequellen,* 2009, ISBN 978-3-933761-82-8

179 Laux, Patrick: *Statistical Modeling of Precipitation for Agricultural Planning in the Volta Basin of West Africa,* 2009, ISBN 978-3-933761-83-5

180 Ehsan, Saqib: *Evaluation of Life Safety Risks Related to Severe Flooding,* 2009, ISBN 978-3-933761-84-2

181 Prohaska, Sandra: *Development and Application of a 1D Multi-Strip Fine Sediment Transport Model for Regulated Rivers,* 2009, ISBN 978-3-933761-85-9

182 Kopp, Andreas: *Evaluation of CO_2 Injection Processes in Geological Formations for Site Screening,* 2009, ISBN 978-3-933761-86-6

183 Ebigbo, Anozie: *Modelling of biofilm growth and its influence on CO_2 and water (two-phase) flow in porous media,* 2009, ISBN 978-3-933761-87-3

184 Freiboth, Sandra: *A phenomenological model for the numerical simulation of multiphase multicomponent processes considering structural alterations of porous media*, 2009, ISBN 978-3-933761-88-0

185 Zöllner, Frank: *Implementierung und Anwendung netzfreier Methoden im Konstruktiven Wasserbau und in der Hydromechanik*, 2009, ISBN 978-3-933761-89-7

186 Vasin, Milos: *Influence of the soil structure and property contrast on flow and transport in the unsaturated zone*, 2010, ISBN 978-3-933761-90-3

187 Li, Jing: *Application of Copulas as a New Geostatistical Tool*, 2010, ISBN 978-3-933761-91-0

188 AghaKouchak, Amir: *Simulation of Remotely Sensed Rainfall Fields Using Copulas*, 2010, ISBN 978-3-933761-92-7

189 Thapa, Pawan Kumar: *Physically-based spatially distributed rainfall runoff modelling for soil erosion estimation*, 2010, ISBN 978-3-933761-93-4

190 Wurms, Sven: *Numerische Modellierung der Sedimentationsprozesse in Retentionsanlagen zur Steuerung von Stoffströmen bei extremen Hochwasserabflussereignissen*, 2011, ISBN 978-3-933761-94-1

191 Merkel, Uwe: *Unsicherheitsanalyse hydraulischer Einwirkungen auf Hochwasserschutzdeiche und Steigerung der Leistungsfähigkeit durch adaptive Strömungsmodellierung*, 2011, ISBN 978-3-933761-95-8

192 Fritz, Jochen: *A Decoupled Model for Compositional Non-Isothermal Multiphase Flow in Porous Media and Multiphysics Approaches for Two-Phase Flow*, 2010, ISBN 978-3-933761-96-5

193 Weber, Karolin (Hrsg.): *12. Treffen junger WissenschaftlerInnen an Wasserbauinstituten*, 2010, ISBN 978-3-933761-97-2

194 Bliefernicht, Jan-Geert: *Probability Forecasts of Daily Areal Precipitation for Small River Basins,* 2011, ISBN 978-3-933761-98-9

195 Hrsg.: Koschitzky, Hans-Peter; Braun, Jürgen: *VEGAS-Kolloquium 2010 In-situ-Sanierung - Stand und Entwicklung Nano und ISCO -,* Tagungsband zur Veranstaltung am 07. Oktober 2010 an der Universität Stuttgart, Campus Stuttgart-Vaihingen*,* 2010*,* ISBN 978-3-933761-99-6

196 Gafurov, Abror: *Water Balance Modeling Using Remote Sensing Information - Focus on Central Asia,* 2010, ISBN 978-3-942036-00-9

197 Mackenberg, Sylvia: *Die Quellstärke in der Sickerwasserprognose: Möglichkeiten und Grenzen von Labor- und Freilanduntersuchungen,* 2010, ISBN 978-3-942036-01-6

198 Singh, Shailesh Kumar: *Robust Parameter Estimation in Gauged and Ungauged Basins,* 2010, ISBN 978-3-942036-02-3

199 Doğan, Mehmet Onur: *Coupling of porous media flow with pipe flow,* 2011, ISBN 978-3-942036-03-0

200 Liu, Min: *Study of Topographic Effects on Hydrological Patterns and the Implication on Hydrological Modeling and Data Interpolation,* 2011, ISBN 978-3-942036-04-7

201 Geleta, Habtamu Itefa: *Watershed Sediment Yield Modeling for Data Scarce Areas,* 2011, ISBN 978-3-942036-05-4

202 Franke, Jörg: *Einfluss der Überwachung auf die Versagenswahrscheinlichkeit von Staustufen,* 2011, ISBN 978-3-942036-06-1

203 Bakimchandra, Oinam: *Integrated Fuzzy-GIS approach for assessing regional soil erosion risks,* 2011, ISBN 978-3-942036-07-8

204 Alam, Muhammad Mahboob: *Statistical Downscaling of Extremes of Precipitation in Mesoscale Catchments from Different RCMs and Their Effects on Local Hydrology,* 2011, ISBN 978-3-942036-08-5

205 Hrsg.: Koschitzky, Hans-Peter; Braun, Jürgen: *VEGAS-Kolloquium 2011 Flache Geothermie - Perspektiven und Risiken,* Tagungsband zur Veranstaltung am 06. Oktober 2011 an der Universität Stuttgart, Campus Stuttgart-Vaihingen*,* 2011*,* ISBN 978-3-933761-09-2

206 Haslauer, Claus: *Analysis of Real-World Spatial Dependence of Subsurface Hydraulic Properties Using Copulas with a Focus on Solute Transport Behaviour,* 2011, ISBN 978-3-942036-10-8

207 Dung, Nguyen Viet: *Multi-objective automatic calibration of hydrodynamic models – development of the concept and an application in the Mekong Delta,* 2011, ISBN 978-3-942036-11-5

208 Hung, Nguyen Nghia: *Sediment dynamics in the floodplain of the Mekong Delta, Vietnam,* 2011, ISBN 978-3-942036-12-2

209 Kuhlmann, Anna: *Influence of soil structure and root water uptake on flow in the unsaturated zone,* 2012, ISBN 978-3-942036-13-9

210 Tuhtan, Jeffrey Andrew: *Including the Second Law Inequality in Aquatic Ecodynamics: A Modeling Approach for Alpine Rivers Impacted by Hydropeaking,* 2012, ISBN 978-3-942036-14-6

211 Tolossa, Habtamu: *Sediment Transport Computation Using a Data-Driven Adaptive Neuro-Fuzzy Modelling Approach,* 2012, ISBN 978-3-942036-15-3

212 Tatomir, Alexandru-Bodgan: *From Discrete to Continuum Concepts of Flow in Fractured Porous Media,* 2012, ISBN 978-3-942036-16-0

213 Erbertseder, Karin: *A Multi-Scale Model for Describing Cancer-Therapeutic Transport in the Human Lung,* 2012, ISBN 978-3-942036-17-7

214 Noack, Markus: *Modelling Approach for Interstitial Sediment Dynamics and Reproduction of Gravel Spawning Fish,* 2012, ISBN 978-3-942036-18-4

215 De Boer, Cjestmir Volkert: *Transport of Nano Sized Zero Valent Iron Colloids during Injection into the Subsurface*, 2012, ISBN 978-3-942036-19-1

216 Pfaff, Thomas: *Processing and Analysis of Weather Radar Data for Use in Hydrology*, 2013, ISBN 978-3-942036-20-7

217 Lebrenz, Hans-Henning: *Addressing the Input Uncertainty for Hydrological Modeling by a New Geostatistical Method*, 2013, ISBN 978-3-942036-21-4

218 Darcis, Melanie Yvonne: *Coupling Models of Different Complexity for the Simulation of CO_2 Storage in Deep Saline Aquifers*, 2013, ISBN 978-3-942036-22-1

219 Beck, Ferdinand: *Generation of Spatially Correlated Synthetic Rainfall Time Series in High Temporal Resolution - A Data Driven Approach*, 2013, ISBN 978-3-942036-23-8

220 Guthke, Philipp: *Non-multi-Gaussian spatial structures: Process-driven natural genesis, manifestation, modeling approaches, and influences on dependent processes*, 2013, ISBN 978-3-942036-24-5

221 Walter, Lena: *Uncertainty studies and risk assessment for CO_2 storage in geological formations*, 2013, ISBN 978-3-942036-25-2

222 Wolff, Markus: *Multi-scale modeling of two-phase flow in porous media including capillary pressure effects,* 2013, ISBN 978-3-942036-26-9

223 Mosthaf, Klaus Roland: *Modeling and analysis of coupled porous-medium and free flow with application to evaporation processes,* 2014, ISBN 978-3-942036-27-6

224 Leube, Philipp Christoph: *Methods for Physically-Based Model Reduction in Time: Analysis, Comparison of Methods and Application*, 2013, ISBN 978-3-942036-28-3

225 Rodríguez Fernández, Jhan Ignacio: *High Order Interactions among environmental variables: Diagnostics and initial steps towards modeling*, 2013, ISBN 978-3-942036-29-0

226 Eder, Maria Magdalena: *Climate Sensitivity of a Large Lake*, 2013, ISBN 978-3-942036-30-6

227 Greiner, Philipp: *Alkoholinjektion zur In-situ-Sanierung von CKW Schadensherden in Grundwasserleitern: Charakterisierung der relevanten Prozesse auf unterschiedlichen Skalen*, 2014, ISBN 978-3-942036-31-3

228 Lauser, Andreas: *Theory and Numerical Applications of Compositional Multi-Phase Flow in Porous Media*, 2014, ISBN 978-3-942036-32-0

229 Enzenhöfer, Rainer: *Risk Quantification and Management in Water Production and Supply Systems*, 2014, ISBN 978-3-942036-33-7

230 Faigle, Benjamin: *Adaptive modelling of compositional multi-phase flow with capillary pressure*, 2014, ISBN 978-3-942036-34-4

231 Oladyshkin, Sergey: *Efficient modeling of environmental systems in the face of complexity and uncertainty*, 2014, ISBN 978-3-942036-35-1

232 Sugimoto, Takayuki: *Copula based Stochastic Analysis of Discharge Time Series*, 2014, ISBN 978-3-942036-36-8

233 Koch, Jonas: *Simulation, Identification and Characterization of Contaminant Source Architectures in the Subsurface*, 2014, ISBN 978-3-942036-37-5

234 Zhang, Jin: *Investigations on Urban River Regulation and Ecological Rehabilitation Measures, Case of Shenzhen in China*, 2014, ISBN 978-3-942036-38-2

235 Siebel, Rüdiger: *Experimentelle Untersuchungen zur hydrodynamischen Belastung und Standsicherheit von Deckwerken an überströmbaren Erddämmen,* 2014, ISBN 978-3-942036-39-9

236 Baber, Katherina: *Coupling free flow and flow in porous media in biological and technical applications: From a simple to a complex interface description,* 2014, ISBN 978-3-942036-40-5

237 Nuske, Klaus Philipp: *Beyond Local Equilibrium — Relaxing local equilibrium assumptions in multiphase flow in porous media,* 2014, ISBN 978-3-942036-41-2

238 Geiges, Andreas: *Efficient concepts for optimal experimental design in nonlinear environmental systems*, 2014, ISBN 978-3-942036-42-9

239 Schwenck, Nicolas: *An XFEM-Based Model for Fluid Flow in Fractured Porous Media*, 2014, ISBN 978-3-942036-43-6

240 Chamorro Chávez, Alejandro: *Stochastic and hydrological modelling for climate change prediction in the Lima region, Peru*, 2015, ISBN 978-3-942036-44-3

241 Yulizar: *Investigation of Changes in Hydro-Meteorological Time Series Using a Depth-Based Approach*, 2015, ISBN 978-3-942036-45-0

242 Kretschmer, Nicole: *Impacts of the existing water allocation scheme on the Limarí watershed – Chile, an integrative approach*, 2015, ISBN 978-3-942036-46-7

243 Kramer, Matthias: *Luftbedarf von Freistrahlturbinen im Gegendruckbetrieb*, 2015, ISBN 978-3-942036-47-4

244 Hommel, Johannes: *Modeling biogeochemical and mass transport processes in the subsurface: Investigation of microbially induced calcite precipitation*, 2016, ISBN 978-3-942036-48-1

245 Germer, Kai: *Wasserinfiltration in die ungesättigte Zone eines makroporösen Hanges und deren Einfluss auf die Hangstabilität*, 2016, ISBN 978-3-942036-49-8

246 Hörning, Sebastian: *Process-oriented modeling of spatial random fields using copulas*, 2016, ISBN 978-3-942036-50-4

247 Jambhekar, Vishal: *Numerical modeling and analysis of evaporative salinization in a coupled free-flow porous-media system,* 2016, ISBN 978-3-942036-51-1

248 Huang, Yingchun: *Study on the spatial and temporal transferability of conceptual hydrological models*, 2016, ISBN 978-3-942036-52-8

249 Kleinknecht, Simon Matthias: *Migration and retention of a heavy NAPL vapor and remediation of the unsaturated zone*, 2016, ISBN 978-3-942036-53-5

250 Kwakye, Stephen Oppong: *Study on the effects of climate change on the hydrology of the West African sub-region*, 2016, ISBN 978-3-942036-54-2

251 Kissinger, Alexander: *Basin-Scale Site Screening and Investigation of Possible Impacts of CO_2 Storage on Subsurface Hydrosystems*, 2016, ISBN 978-3-942036-55-9

252 Müller, Thomas: *Generation of a Realistic Temporal Structure of Synthetic Precipitation Time Series for Sewer Applications*, 2017, ISBN 978-3-942036-56-6

253 Grüninger, Christoph: *Numerical Coupling of Navier-Stokes and Darcy Flow for Soil-Water Evaporation*, 2017, ISBN 978-3-942036-57-3

254 Suroso: *Asymmetric Dependence Based Spatial Copula Models: Empirical Investigations and Consequences on Precipitation Fields*, 2017, ISBN 978-3-942036-58-0

255 Müller, Thomas; Mosthaf, Tobias; Gunzenhauser, Sarah; Seidel, Jochen; Bárdossy, András: *Grundlagenbericht Niederschlags-Simulator (NiedSim3)*, 2017, ISBN 978-3-942036-59-7

256 Mosthaf, Tobias: *New Concepts for Regionalizing Temporal Distributions of Precipitation and for its Application in Spatial Rainfall Simulation,* 2017, ISBN 978-3-942036-60-3

257 Fenrich, Eva Katrin: *Entwicklung eines ökologisch-ökonomischen Vernetzungsmodells für Wasserkraftanlagen und Mehrzweckspeicher,* 2018, ISBN 978-3-942036-61-0

258 Schmidt, Holger: *Microbial stabilization of lotic fine sediments*, 2018, ISBN 978-3-942036-62-7

259 Fetzer, Thomas: *Coupled Free and Porous-Medium Flow Processes Affected by Turbulence and Roughness–Models, Concepts and Analysis*, 2018, ISBN 978-3-942036-63-4

260 Schröder, Hans Christoph: *Large-scale High Head Pico Hydropower Potential Assessment*, 2018, ISBN 978-3-942036-64-1

261 Bode, Felix: *Early-Warning Monitoring Systems for Improved Drinking Water Resource Protection*, 2018, ISBN 978-3-942036-65-8

262 Gebler, Tobias: *Statistische Auswertung von simulierten Talsperrenüberwachungsdaten zur Identifikation von Schadensprozessen an Gewichtsstaumauern*, 2018, ISBN 978-3-942036-66-5

263 Harten, Matthias von: *Analyse des Zuppinger-Wasserrades – Hydraulische Optimierungen unter Berücksichtigung ökologischer Aspekte*, 2018, ISBN 978-3-942036-67-2

264 Yan, Jieru: *Nonlinear estimation of short time precipitation using weather radar and surface observations*, 2018, ISBN 978-3-942036-68-9

265 Beck, Martin: *Conceptual approaches for the analysis of coupled hydraulic and geomechanical processes*, 2019, ISBN 978-3-942036-69-6

266 Haas, Jannik: *Optimal planning of hydropower and energy storage technologies for fully renewable power systems*, 2019, ISBN 978-3-942036-70-2

267 Schneider, Martin: *Nonlinear Finite Volume Schemes for Complex Flow Processes and Challenging Grids*, 2019, ISBN 978-3-942036-71-9

268 Most, Sebastian Christopher: *Analysis and Simulation of Anomalous Transport in Porous Media*, 2019, ISBN 978-3-942036-72-6

269 Buchta, Rocco: *Entwicklung eines Ziel- und Bewertungssystems zur Schaffung nachhaltiger naturnaher Strukturen in großen sandgeprägten Flüssen des norddeutschen Tieflandes*, 2019, ISBN 978-3-942036-73-3

270 Thom, Moritz: *Towards a Better Understanding of the Biostabilization Mechanisms of Sediment Beds*, 2019, ISBN 978-3-942036-74-0

271 Stolz, Daniel: *Die Nullspannungstemperatur in Gewichtsstaumauern unter Berücksichtigung der Festigkeitsentwicklung des Betons*, 2019, ISBN 978-3-942036-75-7

272 Rodriguez Pretelin, Abelardo: *Integrating transient flow conditions into groundwater well protection*, 2020, ISBN: 978-3-942036-76-4

273 Weishaupt, Kilian: *Model Concepts for Coupling Free Flow with Porous Medium Flow at the Pore-Network Scale: From Single-Phase Flow to Compositional Non-Isothermal Two-Phase Flow*, 2020, ISBN: 978-3-942036-77-1

274 Koch, Timo: *Mixed-dimension models for flow and transport processes in porous media with embedded tubular network systems*, 2020, ISBN: 978-3-942036-78-8

275 Gläser, Dennis: *Discrete fracture modeling of multi-phase flow and deformation in fractured poroelastic media*, 2020, ISBN: 978-3-942036-79-5

276 Seitz, Lydia: *Development of new methods to apply a multi-parameter approach – A first step towards the determination of colmation*, 2020, ISBN: 978-3-942036-80-1

277 Ebrahim Bakhshipour, Amin: *Optimizing hybrid decentralized systems for sustainable urban drainage infrastructures planning*, 2021, ISBN: 978-3-942036-81-8

278 Seitz, Gabriele: *Modeling Fixed-Bed Reactors for Thermochemical Heat Storage with the Reaction System CaO/Ca(OH)$_2$*, 2021, ISBN: 978-3-942036-82-5

279 Emmert, Simon: *Developing and Calibrating a Numerical Model for Microbially Enhanced Coal-Bed Methane Production*, 2021, ISBN: 978-3-942036-83-2

280 Heck, Katharina Klara: Modelling and analysis of multicomponent transport at the interface between free- and porous-medium flow - influenced by radiation and roughness, 2021, ISBN: 978-3-942036-84-9

281 Ackermann, Sina: *A multi-scale approach for drop/porous-medium interaction*, 2021, ISBN: 978-3-942036-85-6

282 Beckers, Felix: *Investigations on Functional Relationships between Cohesive Sediment Erosion and Sediment Characteristics*, 2021, ISBN: 978-3-942036-86-3

283 Schlabing, Dirk: *Generating Weather for Climate Impact Assessment on Lakes*, 2021, ISBN: 978-3-942036-87-0

284 Becker, Beatrix: *Efficient multiscale multiphysics models accounting for reversible flow at various subsurface energy storage sites*, 2021, ISBN: 978-3-942036-88-7

285 Reuschen, Sebastian: *Bayesian Inversion and Model Selection of Heterogeneities in Geo-statistical Subsurface Modeling*, 2021, ISBN: 978-3-942036-89-4

286 Michalkowski, Cynthia: *Modeling water transport at the interface between porous GDL and gas distributor of a PEM fuel cell cathode*, 2022, ISBN: 978-3-942036-90-0

287 Koca, Kaan: *Advanced experimental methods for investigating flow-biofilm-sediment interactions*, 2022, ISBN: 978-3-942036-91-7

288 Modiri, Ehsan: *Clustering simultaneous occurrences of extreme floods in the Neckar catchment*, 2022, ISBN: 978-3-942036-92-4

289 Mayar, Mohammad Assem: *High-resolution spatio-temporal measurements of the colmation phenomenon under laboratory conditions*, 2022, ISBN: 978-3-942036-93-1

290 Schäfer Rodrigues Silva, Aline: *Quantifying and Visualizing Model Similarities for Multi-Model Methods*, 2022, ISBN: 978-3-942036-94-8

291 Moreno Leiva, Simón: *Optimal planning of water and renewable energy systems for copper production processes with sector coupling and demand flexibility*, 2022, ISBN 978-3-942036-95-5

292 Schönau, Steffen: *Modellierung von Bodenerosion und Sedimentaustrag bei Hochwasserereignissen am Beispiel des Einzugsgebiets der Rems*, 2022, ISBN 978-3-942036-96-2

293 Glatz, Kumiko: *Upscaling of Nanoparticle Transport in Porous Media,* 2022, ISBN 978-3-942036-97-9

294 Pavía Santolamazza, Daniela: *Event-based flood estimation using a random forest algorithm for the regionalization in small catchments*, 2022, ISBN 978-3-942036-98-6

295 Haun, Stefan: *Advanced Methods for a Sustainable Sediment Management of Reservoirs*, 2022, ISBN 978-3-942036-99-3

296 Herma, Felix: *Data Processing and Model Choice for Flood Prediction*, 2022, ISBN 978-3-910293-00-7

297 Weinhardt, Felix: *Porosity and permeability alterations in processes of biomineralization in porous media - microfluidic investigations and their interpretation*, 2022, ISBN 978-3-910293-01-4

298 Sadid, Najibullah: *Bedload Transport Estimation in Mountainous Intermittent Rivers and Streams*, 2023, ISBN 978-3-910293-02-1

299 Mohammadi, Farid: *A Surrogate-Assisted Bayesian Framework for Uncertainty-Aware Validation Benchmarks*, 2023, ISBN 978-3-910293-03-8

300 Praditia, Timothy: *Physics-informed Neural Networks for Learning Dynamic, Distributed and Uncertain Systems*, 2023, ISBN 978-3-910293-04-5

301 Gyawali, Dhiraj Raj: *Development and parameter estimation of conceptual snow-melt models using MODIS snow-cover distribution*, 2023, ISBN 978-3-910293-05-2

302 Görtz, Jan: *Coupled modeling approach for physico-chemical processes during the deterioration of cement-based structures*, 2023, ISBN 978-3-910293-06-9

Die Mitteilungshefte ab der Nr. 134 (Jg. 2005) stehen als pdf-Datei über die Homepage des Instituts: www.iws.uni-stuttgart.de zur Verfügung.